

Mitigation of Methane and Carbon Dioxide Storage Issues for Transportation as well as Storage from the Gas Hydrate



Thesis submitted in partial fulfillment

for the Award of Degree

Doctor of Philosophy

By

BIDESH KUMAR HEMBRAM

Department of Petroleum Engineering and Geoengineering

RAJIV GANDHI INSTITUTE OF PETROLEUM TECHNOLOGY

JAIS – 229304

CERTIFICATE

It is certified that the work contained in the thesis titled "**Mitigation of Methane and Carbon Dioxide Storage Issues for Transportation as well as Storage from the Gas Hydrate**" by **BIDESH KUMAR HEMBRAM** has been carried out under our supervision and that this work has not been submitted elsewhere for a degree.

Signature: Supervisor
(Affiliation)

Co-Supervisor
(Affiliation)

DECLARATION BY THE CANDIDATE

I, **BIDESH KUMAR HEMBRAM**, certify that the work embodied in this thesis is my own bona fide work and carried out by me under the supervision of **DR. TUSHAR SHARMA** from "August 2020" to "April 2025", at the Rajiv Gandhi Institute of Petroleum Technology, Jais. The matter embodied in this thesis has not been submitted for the award of any other degree. I declare that I have faithfully acknowledged and given credits to the research workers wherever their works have been cited in my work in this thesis. I further declare that I have not wilfully copied any other's work, paragraphs, text, data, results, etc., reported in journals, books, magazines, reports dissertations, theses, etc., or available at websites and have not included them in this thesis and have not cited as my own work.

Date:

Place:

BIDESH KUMAR HEMBRAM

CERTIFICATE BY THE SUPERVISOR(S)

It is certified that the above statement made by the student is correct to the best of my/our knowledge.

**Supervisor
(Affiliation)**

**Co-Supervisor
(Affiliation)**

Signature of Head of Department

CERTIFICATE

CERTIFIED that the work contained in the thesis titled “**Mitigation of Methane and Carbon Dioxide Storage Issues for Transportation as well as Storage from the Gas Hydrate**” by Mr. **Bidesh Kumar Hembram** has been carried out under my/our supervision. It is also certified that he fulfilled the mandatory requirement of TWO quality publications arose out of his/her thesis work. It is further certified that the two publications (copies enclosed) of the aforesaid **Mr. BIDESH KUMAR HEMBRAM** have been published in the Journals indexed by

- a) SCI
- b) SCI Extended
- c) SCOPUS

Signature

Signature

Signature

()

()

()

DR. TUSHAR SHARMA

DR. VISHNU C. NAIR

Supervisor

Co-Supervisor

Convener, DPGC, SEAL

COPYRIGHT TRANSFER CERTIFICATE

Title of the Thesis: Mitigation of Methane and Carbon Dioxide Storage issues for Transportation as well as Storage from the Gas Hydrate

Name of the Student: Bidesh Kumar Hembram

Copyright Transfer

The undersigned hereby assigns to the Rajiv Gandhi Institute of Petroleum Technology Jais all rights under copyright that may exist in and for the above thesis submitted for the award of the "DOCTOR OF PHILOSOPHY ".

Date :

Signature of the Student

Place:

(Bidesh Kumar Hembram)

Note: However, the author may reproduce or authorize others to reproduce material extracted verbatim from the thesis or derivative of the thesis for author's personal use provided that the source and the Institute's copyright notice are indicated.

Dedicated To

My Beloved Parents & Wife

For their endless love, support and encouragement

Acknowledgment

Completing this PhD thesis has been a long and challenging journey, and it would not have been possible without the support and guidance of many individuals. First and foremost, I would like to express my deepest gratitude to my advisor, Dr. Tushar Sharma, for his unwavering support, invaluable insights, and constant encouragement throughout the research process. Their patience and wisdom have been instrumental in shaping this work.

I am also profoundly grateful to my RPEC committee members for their constructive feedback and invaluable suggestions that have enriched this research. I also want to thank Dr. Vishnu C. Nair of IIT Kharagpur for his Support and guidance. I am also grateful to Dr. Mahmood M. S. Abdullah of King Saud University for our collaborative work. I want to acknowledge PEGE department for allowing me to use their research facilities without which experimental work was impossible. My sincere thanks also go to the former director, Professor A. S. K. Sinha, and present director Professor Harish Hirani of Rajiv Gandhi Institute of Petroleum Technology (RGIPT), Jais, Amethi for availing research facility and financial support for my experimental work. Furthermore, I would also like to thank Dr. Satish Kumar Sinha (HoD) for providing excellent motivation and encouragement during my research work.

I am extremely thankful to be a part of the Enhanced Oil Recovery Lab under the Department of Petroleum Engineering and Geoengineering of RGIPT. I would also like to thank the past (Vivek Menna, Hari Prasad Shukla) and present (Manoj Kumar Yadav, Ramaswamy Gautam, Anirudh Bardhan, Darshan Halari, Ajeet Kumar Prajapati) lab members for all the questions and constructive criticism that I have received from them during our group meetings. These conversations were always helpful and improved my critical thinking. I am also duly grateful to all non-teaching

staff of RGIPT who help me directly or indirectly to contribute to my research work. I extend my gratitude towards the AI advanced tool for enhancing my research process, which streamlined my thesis work.

Lastly, I wish my parents for supporting me throughout this PhD thesis journey. I would like to take a moment to express my deepest gratitude to my wife, Namita. Your unwavering support, patience, and encouragement have been my foundation throughout this challenging journey. From the late nights spent together during my studies to your constant belief in my abilities, you have been my rock. You're understanding during difficult times and your ability to lift my spirits have made all the difference. I am truly grateful for your sacrifices and for always being by my side. Thank you for being my partner in this journey and for sharing in both the challenges and the triumphs. This accomplishment is as much yours as it is mine.

.....Bidesh Kumar Hembram

आचार्यात् पादमादत्ते पादम् शिष्यः स्वमेधया।

कालेन पादमादत्ते पादम् सब्रह्मचारिभिः।।

Table of Contents

Acknowledgment	i
Table of Contents	iii
List of Figures	ix
List of Tables	xv
List of Abbreviations	xvii
Preface	xix
Chapter 1: Introduction	1
1.1. Introduction	1
1.2. Properties of Gas hydrates	4
1.3. Hydrate structure	6
1.3.1. Structure I.....	9
1.3.2. Structure II	10
1.3.3. Structure H.....	10
1.4. Location of gas hydrate	10
1.5. Hydrates as a Potential Source of Energy.....	13
1.6. Gas hydrates — Greenhouse gas and climate change	15
1.7. Gas Hydrate Inhibitors and Promoters	17
1.7.1. Thermodynamics Inhibitor.....	19
1.7.2. Kinetic Inhibitors	20
1.8. Molecular Dynamics of Gas Hydrate	21
1.9. Molecular simulation and gas hydrate.....	21
1.10. Basic of molecular simulation.....	22
1.11. Research Motivation.....	27
1.12. Research Objective	27

1.13.	Thesis Organization.....	28
Chapter 2: Insights of Molecular Dynamics Simulation to Investigate the Impact of Ethylene Glycol on Methane Hydrate Dissociation		
31		
2.1.	Introduction.....	32
2.2.	Simulation Details.....	36
2.3.	Results and Discussion	39
2.3.1.	Radial distribution function (RDF)	40
2.3.2.	Impact of temperature	41
2.3.3.	Impact of concentration.....	45
2.3.4.	Total energy	49
2.3.5.	Diffusion Coefficient.....	51
2.4.	Conclusion and Summary	53
Chapter 3: Effects of Ethylene glycol and silica nanoparticles on methane hydrate formation		
55		
3.1.	Introduction.....	56
3.2.	Experimental section.....	59
3.2.1.	Materials.....	59
3.2.2.	Nanofluid synthesis	60
3.2.3.	Experimental setup.....	61
3.2.4.	Experimental procedure for hydrate studies.....	61
3.3.	Results and discussion	63
3.3.1.	Nanoparticle characterization.....	64
3.3.1.1.	Stability and zeta potential measurement of nanofluid	64
3.3.1.2.	UV- <i>vis</i> analysis of the nanofluids.....	66
3.3.2.	Hydrate formation experiments.....	68

3.3.2.1.	Effect of nanofluids on the phase stability of methane hydrate	69
3.3.2.2.	Impact of nanofluids on the methane hydrate induction time.....	70
3.3.2.3.	CH ₄ consumption during hydrate formation.....	73
3.3.2.4.	Rate of hydrate formation	75
3.3.2.5.	Methane storage capacity.....	77
3.3.3.	Future scope of the work.....	78
3.4.	Conclusion.....	79
Chapter 4: Effect of Single-Step Silica Nanofluid on Thermodynamic and Kinetics of Methane Hydrate Stabilized by Conventional Promoter		81
4.1.	Introduction	82
4.2.	Materials and methods.....	88
4.2.1.	Materials.....	88
4.2.2.	Nanofluid preparation and characterization	88
4.2.3.	Experimental set-up and hydrate preparation	89
4.3.	Results and discussion.....	92
4.3.1.	DLS and SEM analysis of nanofluid.....	92
4.3.1.	Effect of nanofluid on induction time	95
4.3.2.	Effect of nanofluid on gas consumption	99
4.3.3.	Effect of nanofluid on apparent rate constant of hydrate	103
4.3.4.	Determination of rate of gas consumption.....	106
4.3.5.	Storage capacity of hydrate samples.....	108
4.4.	Conclusion and Summary.....	111
Chapter 5: Examine the effect of ethylene glycol on the dissociation of hydrates (CH₄ & CO₂): A Molecular Dynamics Analysis		113
5.1.	Introduction	114

5.2. Simulation.....	118
5.2.1. Structure	118
5.2.2. MD simulation.....	119
5.3. Results & Discussion	121
5.3.1. Radial Distribution Function (RDF)	123
5.3.1.1. Effect of Temperature on Hydrate Structure	124
5.3.1.2. Effect of ethylene glycol concentration on Hydrate structure.....	126
5.3.2. Mean Square Displacement (MSD)	127
5.3.2.1. Effect of temperature.....	128
5.3.2.2. Effect of concentration	129
5.3.3. Total Energy	130
5.3.4. Diffusion Coefficient.....	132
5.4. Conclusion and Summary	133
 Chapter 6: Impact of single step-SiO₂ nanofluid on the kinetics of CO₂	
Hydrate formation Relevant for Carbon Capture and Storage	135
6.1. Introduction.....	136
6.2. Materials and Methods.....	140
6.2.1. Materials.....	140
6.2.2. Nanoparticle preparation and characterization.....	141
6.2.3. Hydrate formation studies	141
6.2.3.1. Experimental setup for hydrate studies	141
6.2.3.2. Experimental procedure for hydrate studies.....	142
6.2.4. CO ₂ absorption experiment	143
6.3. Results and discussion	143
6.3.1. Stability and DLS measurements	144

6.3.2.	CO ₂ absorption results with NPs.....	145
6.3.3.	CO ₂ hydrate formation kinetics in the presence of NPs.....	146
6.3.4.	CO ₂ gas consumption during hydrate formation.....	150
6.3.5.	Rate of hydrate formation	154
6.3.6.	CO ₂ storage capacity	155
6.3.7.	Dissociation kinetics of the hydrate in the presence of NPs	156
6.4.	Mechanism for the effect of NPs on the hydrate formation	158
6.5.	Conclusion and summary	159
	Chapter 7: Conclusion and Summary	161
7.1.	Conclusion and Summary.....	161
7.2.	Future Direction.....	162
	References.....	163
	PUBLICATION (IN THESIS).....	203

List of Figures

Figure 1.1: Gas hydrate structure [4].....	2
Figure 1.2: Various methods of gas hydrate extraction [6].....	2
Figure 1.3: The stable hydrate zone [10].....	4
Figure 1.4: Gas hydrate heat dissociation [12].....	5
Figure 1.5: Worldwide natural gas hydrate reservoir [20].....	11
Figure 1.6: Stability conditions for gas [25].....	12
Figure 1.7: The energy consumption of the 20th century [31].....	14
Figure 1.8: The timelines for gas hydrate projects [29].....	15
Figure 1.9: Hydrate management strategies [56].....	18
Figure 1.10: Different inhibitors.....	19
Figure 1.11: Edward summation method for calculating long-range Coulomb interaction.....	26
Figure 2.1: Workflow of MD simulation process.....	38
Figure 2.2: Dissociation of methane hydrate structure in the presence of 5 vol% of ethylene glycol at 300K (a) initial at time = 0 ps (b) time = 50 ps (c) time = 100 ps (d) time = 250 ps (e) time = 500 ps.....	39
Figure 2.3: Simulation box configuration at (a) 300K temperature and 2.5% ethylene glycol (b) 300K and 5% (c) 260K and 2.5% (d) 260K and 2.5%.....	41
Figure 2.4: RDF of methane and water molecules of hydrate at: (a) 260 K, (b) 280 K, and (c) 300 K with varying concentrations of ethylene glycol.....	42
Figure 2.5: The RDF of methane of hydrate and ethylene glycol at: (a) 260 K, (b) 280 K, and (c) 300 K with varying concentrations of ethylene glycol.....	43

Figure 2.6: The RDF of methane and water molecules of hydrate at different ethylene glycol concentrations: (a) 0 vol%, (b) 2.5 vol%, and (c) 5 vol% with varying temperatures.....	45
Figure 2.7: The RDF of methane of hydrate and ethylene glycol at different ethylene glycol concentrations: (a) 2.5 vol %, and (b) 5 vol % with varying temperature.....	46
Figure 2. 8: Total energy of hydrate system with (a) 5 vol% ethylene glycols at various temperatures, and (b) various concentrations of ethylene glycol at 300K and 50 bar.	49
Figure 3. 1: The actual setup consists of a hydrate autoclave, a water bath (to maintain the temperature), along a syringe pump to maintain the pressure inside the autoclave cell.....	61
Figure 3. 2: Pressure-temperature profile for gas hydrate formation	65
Figure 3. 3: Synthesize nanofluid image at 0 days and 30 days	65
Figure 3. 4: UV-vis analysis plots of A1, A2, and A3 as a function of storage period	67
Figure 3. 5: HVLE curve of various synthesized nanofluids along with pure water and pure ethylene glycol.....	68
Figure 3. 6: P-T cycle curves obtained in the presence of varying compositions (a) pure ethylene glycol (b) 0.5wt% nanofluids (c) 1.0wt% nanofluids (d) 1.5 wt% nanofluids	70
Figure 3. 7: Methane hydrate induction time for various synthesized samples.....	71
Figure 3. 8: CH ₄ gas consumption during hydrate formation for different samples...	73
Figure 3. 9: CH ₄ hydrate formation rate for various samples	76
Figure 3. 10: Methane storage capacity of different hydrate promoter formulations at 6.0 MPa and 278.15 K	77

Figure 4.1: Experimental set-up of gas hydrate (actual and schematic), along with essential accessories to record and monitor the progress of the process. The details of stirring geometry are also shown with important dimensions of the cell and stirrer..91

Figure 4.2: Visual appearance images of synthesized nanofluids of various concentrations (0.5-2 wt%) in the base fluid of polymer PAM.....94

Figure 4.3: SEM images of unsettled NPs and settled NPs from top and bottom layers of 0.5 wt% SiO₂ nanofluid after witnessing clear phase separation and NP settlement 94

Figure 4.4: Variation of pressure vs. temperature during hydrate experiment for sample composition S5, consisting of CH₄+DI water+1.5 wt% SiO₂ nanofluid95

Figure 4.5: Effect of nanofluid on induction time of DI water (S1), CTAB solution (S2), different nanofluids (S3-S6) at 6 MPa and 274.15 K96

Figure 4.6: Actual image of gas hydrate in reactor cell after the completion of experiment for sample composition S5 at 274.15 K99

Figure 4.7: The results of methane consumption vs. time for hydrates stabilized by DI water (S1), CTAB solution (S2), and SiO₂ nanofluids of varying NP concentration (S3-S6) at 6 MPa and 274.15 K..... 100

Figure 4.8: The results of methane consumption vs. time for hydrates stabilized by DI water (S1), CTAB solution (S2), and SiO₂ nanofluids of varying NP concentration (S3-S6) at 6 MPa and 277.15 K..... 101

Figure 4.9: Apparent rate constant for hydrates stabilized by DI water (S1), CTAB solution (S2), and SiO₂ nanofluids of varying NP concentration (S3-S6) at 6 MPa and 274.15 K 103

Figure 4. 10: Apparent rate constant for hydrates stabilized by DI water (S1), CTAB solution (S2), and SiO ₂ nanofluids of varying NP concentration (S3-S6) at 6 MPa and 277.15 K.....	104
Figure 4.11: Comparative performance to evaluate the rate of gas consumed for different hydrates stabilized by S1-S6 formulations at 274.15 K.....	107
Figure 4.12: Storage capacity of different hydrates stabilized by S1-S6 formulations at 6 MPa and 274.15 K	109
Figure 4.13: Storage capacity of different hydrates stabilized by S1-S6 formulations at 6 MPa and 277.15 K	109
Figure 5.1: The visualization of the molecules inside the simulation box.....	119
Figure 5.2: The visual appearance of the simulation box of 10% ethylene glycol concentration at 285.15K at (a) 0 ps and (b) 500 ps	122
Figure 5.3: Plots of RDF at 10% concentration of ethylene glycol. (a) oxygen-oxygen of hydrate (b) carbon-carbon of methane	124
Figure 5. 4: RDF at 10% concentration of ethylene glycol (a) carbon-carbon of CO ₂ (b) carbon (CO ₂)-oxygen of water	125
Figure 5. 5: Plots of RDF at 285.15K. (a) carbon-carbon of methane (b) oxygen-oxygen of water	126
Figure 5.6: Final configuration of simulation box of 10% ethylene glycol at (a) 270.15 K, (b) 275.15 K, (c) 280.15 K, (d) 285.15 K, and (e) 300 K.....	127
Figure 5.7: Plot of MSD of 10% concentration for (a) methane (b) CO ₂	128
Figure 5.8: Plot of MSD of 285.15 K for (a) methane (b) CO ₂ at various concentrations	129
Figure 5.9: Observations of the total energy of the simulation box (a) at 10% concentration (b) at 285.15 K	131

Figure 6.1: Schematic diagram of the hydrate system.....	142
Figure 6.2: Actual image of synthesized nanofluids in the lab (a) 0 day (b) 30 days	144
Figure 6.3: Molality results of CO ₂ for all synthesized nanofluids (S1, S2 and S3) at room temperature different equilibrium pressure	145
Figure 6.4: Pressure vs Temperature profile of the 0.5 wt% (S7) Nanofluid	146
Figure 6.5: Induction time for synthesizing NPs concentration-wise	149
Figure 6.6: CO ₂ consumption for all NPs.....	151
Figure 6.7: Final amount of CO ₂ consumption for during 120 mins of hydrate growth	151
Figure 6.8: Rate of hydrate Formation for various concentrations of NPs.....	154
Figure 6.9: Storage capacity of different hydrate promoter formulations at 3.5 MPa and 275.15 K.....	156
Figure 6.10: Gas released during methane hydrate dissociation for (a) S0, S1, S2, S3 and (b) S4, S5, S6, S7, S8 and S9 samples.....	157
Figure 6.11: Schematic diagram mechanism of NP hydrate formation.....	158

List of Table

Table 1.1: Properties of different hydrates [12].....	4
Table 1.2: Properties of gas hydrate compared with ice [12]	5
Table 1.3: Hydrate cell Structure International Table of Crystallography [16].....	8
Table 1.4: Guest molecules and hydrate cages	9
Table 2.1: The number of molecules of ethylene glycol in hydrate structure	40
Table 2.2: Diffusion coefficient of methane and water molecules at P = 50 bar.....	52
Table 3.1: Chemical details used in the experiment	59
Table 3.2: DLS measurements along with induction time of synthesized nanofluids	65
Table 4.1: DLS measurements [size and zeta-potential] of synthesized nanofluids ..	93
Table 4.2: The compositional details, nomenclature, and induction time of hydrates prepared with CTAB and different concentrations of nanofluids.....	104
Table 4.3: Apparent rate constant of hydrates stabilized by nanofluids of different concentrations.....	106
Table 5.1: Observations of molecules used in the simulation	120
Table 5.2: Values of force field used in this investigation.....	121
Table 5.3: Diffusion coefficients of methane and carbon dioxide molecules.....	133
Table 6.1: Chemical details used in the experiment	141
Table 6.2: DLS measurements of synthesized nanofluids at room temperature	144
Table 6.3: Induction time for at 3.5MPa and 275.15K	147

List of Abbreviations

CTAB	Cetrimonium Bromide
DLS	Dynamics Light Scattering
EtOH	Ethanol
EGY	Ethylene Glycol
FESEM	Field Emission Scanning Microscope
KHI	Kinetic hydrate inhibitor
MD Simulation	Molecular Dynamics Simulation
NH₄OH	Ammonium Hydroxide
PAM	Polyacrylamide
SDS	Sodium Dodecyl Sulfate
TEOS	Tetraethyl Orthosilicate
THI	Thermodynamic hydrate inhibitor

Preface

Gas hydrates, also known as clathrate hydrates, have emerged as one of the most intriguing topics in modern energy and environmental research. These crystalline compounds form when gas molecules—commonly methane—become trapped within a lattice of hydrogen-bonded water molecules under conditions of low temperature and high pressure. Gas hydrates occur naturally in permafrost regions and deep marine sediments, representing a vast and largely untapped reservoir of methane. Their unique physicochemical properties and their relevance to energy security, climate change, and geotechnical stability have positioned them at the centre of interdisciplinary scientific investigations.

Methane hydrates are estimated to contain more carbon than all known conventional fossil fuel reserves combined, which makes them a potential alternative energy source for future generations. However, despite this promise, the safe and efficient exploitation of gas hydrates remains a formidable challenge. Hydrate-bearing sediments are highly sensitive to pressure and temperature variations, and hydrate dissociation can cause seafloor instability, uncontrolled gas release, and environmental risks. Moreover, the kinetics of hydrate formation and dissociation are inherently slow, often limiting their practical utilisation in energy recovery, gas storage, and transportation. Addressing these challenges requires innovative approaches to enhance hydrate formation rates, improve thermal conductivity, and ensure system stability—fields in which nanotechnology has recently shown great potential.

The introduction of nanoparticles into gas hydrate research has opened a new frontier in understanding and manipulating hydrate systems. Nanoparticles, owing to their extremely high surface area-to-volume ratio, can significantly influence the nucleation and growth of gas hydrates. Various studies have demonstrated that

nanoparticles such as alumina (Al_2O_3), copper oxide (CuO), and carbon-based nanomaterials can serve as effective promoters for gas hydrate formation. They enhance thermal conductivity, provide additional nucleation sites, and modify interfacial characteristics, resulting in faster formation kinetics and greater gas storage capacity.

While nanoparticle-assisted hydrate formation could facilitate carbon capture and sequestration through CO_2 hydrate formation, it is also essential to assess the environmental fate and long-term stability of nanoparticles in marine and permafrost environments. Therefore, contemporary hydrate research increasingly focuses not only on improving performance metrics but also on ensuring environmental safety and sustainability. The combination of hydrate science and nanotechnology exemplifies the evolution of multidisciplinary approaches aimed at addressing global energy and environmental issues.

Advancements in experimental techniques, molecular simulations, and in-situ measurements have deepened our understanding of hydrate systems at both macroscopic and molecular scales. The synergy between nanotechnology and gas hydrate research has expanded the scope of hydrate applications beyond traditional energy recovery and storage. Such developments underscore the importance of integrating thermodynamics and environmental engineering to design efficient and sustainable hydrate-based technologies.

This thesis is inspired by the growing recognition that the future of gas hydrate research lies in innovation through materials engineering and nanoscale control. By examining the influence of nanoparticles on hydrate formation and dissociation behaviour, this work seeks to contribute to the ongoing efforts to make hydrate-based technologies more viable, efficient, and environmentally sustainable. The

investigation focuses on understanding the mechanisms through which nanoparticles alter hydrate kinetics and thermodynamics to bridge the gap between laboratory findings and practical applications. Also, a molecular simulation was performed.

In conclusion, this exploration is not only about enhancing energy security but also about ensuring sustainable practices that protect our planet. We hope this work inspires further research and innovation in this exciting and vital area, encouraging collaboration across disciplines to unlock the full potential of gas hydrates while addressing the pressing challenges of our time.

1.1. Introduction

Gas hydrate is a solid ice-like crystalline compound formed by hydrocarbon molecules, encaged inside a solid structure formed by the hydrogen bond of the water [1]. The gas molecules are entrapped inside the empty lattice of the water molecules, which helps in lattice stabilization. The gas molecules can be of various compounds and/or elements: methane, ethane, propane, iso-butane, nitrogen, and carbon dioxide [1]. There is no chemical bond between their gas and water molecules, only Van der Waals [2]. In the literature, gas hydrates are formed at high pressure and temperature. Gas hydrate consists of three different structures: sI, sII, sH. Each structure is a different size and structure [3]. The structure I (sI) have a center cubic structure, mainly formed by smaller gases like methane, ethane, and carbon dioxide. Structure II (sII) has a diamond lattice within a cubic framework with a gas size larger than ethane and smaller than pentane. Structure H (sH) has a hexagonal framework that can accommodate larger molecules like naphtha and gasoline [1]. Figure 1.1 shows the type of structures sI, sII, and sH. With 46 water molecules in total, the structure sI is made up of six huge tetrakaidecahedron ($5^{12}6^2$) cavities and two small pentagonal dodecahedron (5^{12}) cavities. Similarly, structure II has 16 small (5^{12}) cavities and 8 large hexakaidecahedron ($5^{12}6^4$) cavities with a total of 136 water molecules. Structure H is made up of three small pentagonal dodecahedron (5^{12}) cavities along with two irregular-shaped cavities with 34 water molecules.

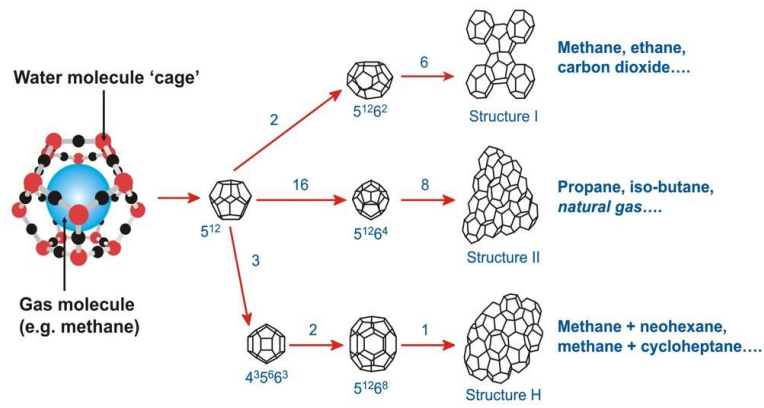


Figure 1.1: Gas hydrate structure [4]

These hydrates form at high pressure and low temperature. Such conditions are found only in subsea sediment, permafrost, and near-polar regions. As pressure increases and temperature decreases, water molecules trap the gas molecules (mainly methane) and freeze, forming a solid hydrate structure [5]. The methane hydrate in nature, pressure, and temperature must be in a hydrate-stable zone. This methane can be extracted from these reservoirs by altering the pressure and temperature. There are three different methods: thermal injection, depressurization, and inhibitor injection, for separating the methane from the hydrate. Figure 1.2 illustrates the different methods of extraction.

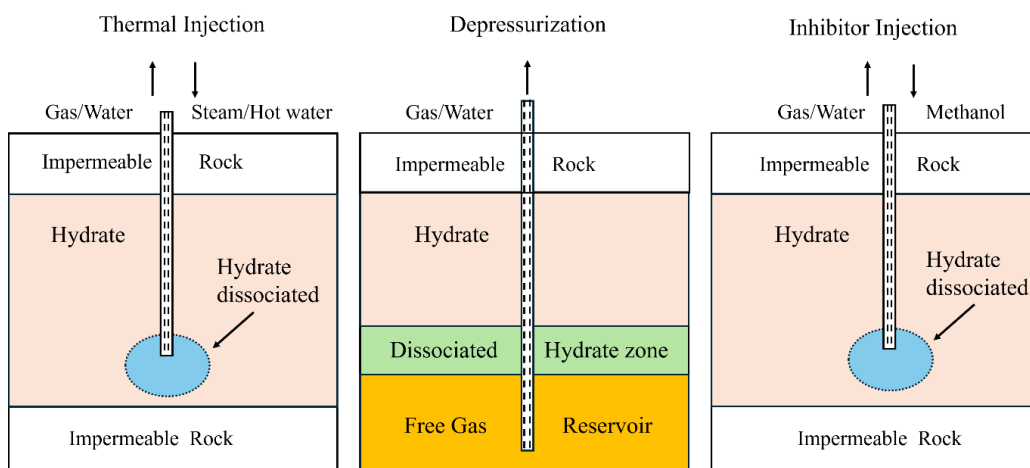


Figure 1.2: Various methods of gas hydrate extraction [6]

In depressurization, the pump reduces the reservoir pressure, resulting in the dissociation of gas hydrate. A pump is lower in the downhole to achieve this pressure

reduction. As the pressure reduces, the temperature also decreases. Together, these two help dissociate the solid hydrate into methane and water. The dissociation stops when the reservoir reaches a 3-phase equilibrium temperature equivalent to reservoir pressure, as shown in Figure 1.3. The methane recovery is only 60% by depressurization due to various reservoir properties [7]. Next is thermal injection. As the name suggests, the hydrate dissociation takes place as the temperature increases. Here, the reservoir temperature increases using thermal stimulation or thermal flooding. In thermal stimulation, the temperature near the wellbore is increased by circulating hot water. In thermal flooding, hot water is injected into the reservoir. This increases the bottom-hole temperature, leading to methane recovery [8,9]. A very small percentage of methane recovery is expected since water circulation requires a bottom-hole pressure higher than the reservoir pressure. The thermal methods required energy. Since the energy requirement is large, the quality of thermal recovery is very questionable. The injector injection method is a common method to extract methane from methane hydrate reservoirs. But continuous supply is very difficult due to its expense. Also, it is challenging to inject into a shallow, effective permeable reservoir. Hence, injecting inhibitors is not a viable option for hydrate recovery from these reservoirs.

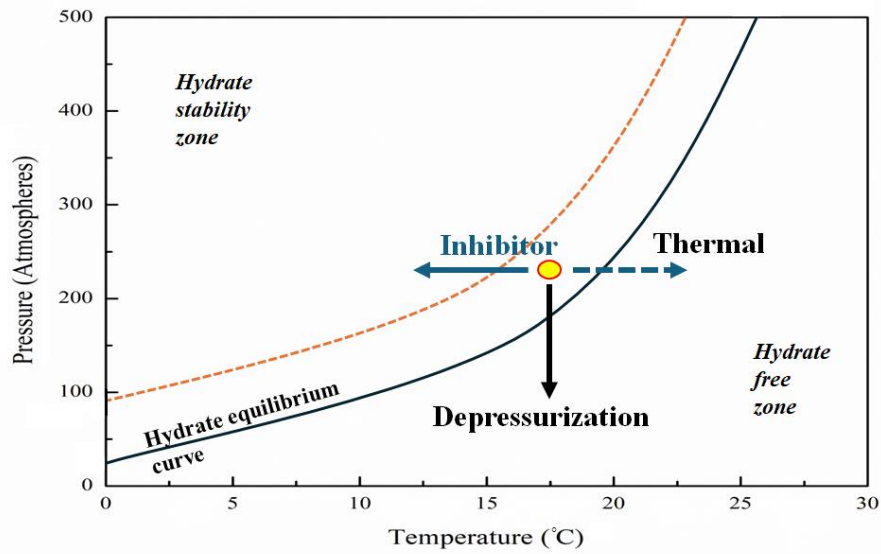


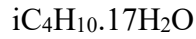
Figure 1.3: The stable hydrate zone [10]

1.2. Properties of Gas hydrate

Gas hydrates are an ice-like compound, first discovered by Sir Humphry Davy in 1810. But it was still in the 20th century that this hydrate was considered due to the flow assurance problem in the oil and gas industry. Apart from this disadvantage, there is one major advantage, i.e. storage and transportation. This gas hydrate can store a larger volume of gas inside. One cubic meter of hydrate can store approximately 165 cubic meters of methane in compressed form at standard pressure and temperature [11]. The property of gas hydrate varies with the composition of the gas. Hydrate dissociation is an endothermic reaction. Figure 1.4 [12] shows the heat of dissociation of different hydrates.

Table 1.1: Properties of different hydrates [12]

Gas	Formula of Hydrate	Hydrate density @ 273K(gr/cm^3)
CH_4	$\text{CH}_4 \cdot 6\text{H}_2\text{O}$	0.910
CO_2	$\text{CO}_2 \cdot 6\text{H}_2\text{O}$	1.117
C_2H_6	$\text{C}_2\text{H}_6 \cdot 7\text{H}_2\text{O}$	0.959
C_3H_8	$\text{C}_3\text{H}_8 \cdot 17\text{H}_2\text{O}$	0.866



0.901

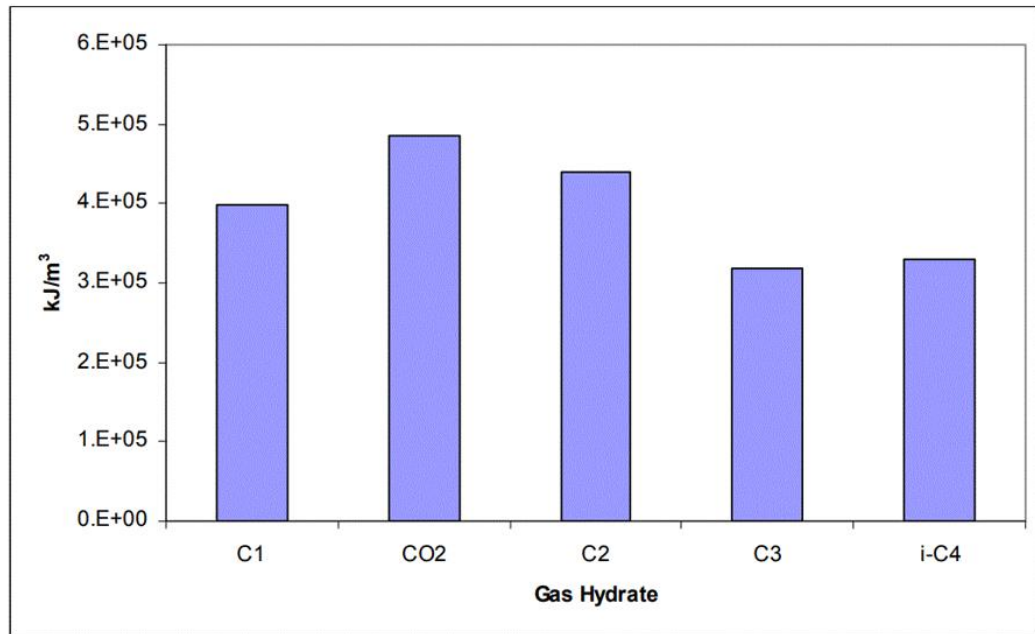


Figure 1.1: Gas hydrate heat dissociation [12]

Table 1.2: Properties of gas hydrate compared with ice [12]

Property	Water	Ice	sI	sII
Thermal conductivity (W/m-K)	0.58 (283K)	2.21 (283K)	0.57 (263K)	0.51 (261K)
Heat capacity (J/kg-K)	4192 (283K)	2051 (270K)	2031 (263K)	2020 (261K)
Linear thermal expansion at 200K (K ⁻¹)	-	56×10 ⁻⁶	77×10 ⁻⁶	52×10 ⁻⁶
Compressional wave velocity, V _p (km/s)	4.5	3.87	3.77	3.821

Shear wave velocity, V_s (km/s)	0	7.94	7.96	2.001
Bulk modulus, K (GPa)	0.015	9.09	8.41	8.48
Shear modulus, G (GPa)	0	3.49	3.54	3.66
Density (kg/m^3)	999.7	917	929	971

Table 1.2 summarises the solid structure using Brillouin spectroscopy. Waite et al. tested dense polycrystalline methane hydrate and pulse wave transmission to obtain results [13]. Triaxial experiments on dense polycrystalline methane hydrate were carried out by Durham [14], and the results indicated that methane hydrate was, on average, 20–30 times stronger than ice. This high strength of hydrate compared to water ice has significant implications for the mechanical behaviour of hydrate-bearing sediments.

1.3. Hydrate structure

A Gas hydrate is formed when guest gas is encapsulated inside the hydrate structure. The structure consists of pentagonal and hexagonal faces. Combining various parts of these faces leads to diverse hydrate structures, highlighting the importance of geometric arrangements in understanding the nature of hydrates. The two most prevalent hydrate structures are structure I (sI) and structure II (sII). Another less common structure compared to structures I and II is structure H. The shared characteristic of the three hydrate structures is the tetrahedral arrangement of water molecules, bonded together by a hydrogen bond. This tetrahedral arrangement of water molecules in hydrate molecules in hydrate mirrors the same positioning found in ice formation. Due to the different sizes of guest gas molecules, the structure has a different arrangement. Hydrate only forms if the temperature

above the freezing point (273.15 K) is maintained. Also, sufficient gas and water is required to form hydrate [15]. Figure 1.1 shows the different structures. hydrate mirrors the same positioning found in ice formation. Due to the different sizes of guest gas molecules, the structure has a different arrangement. Hydrate only forms if the temperature above freezing point (273.15 K) is maintained. Also, sufficient gas and water is required to form hydrate [15].

Table 1.3: Hydrate cell structure international table of Crystallography [16]

Structure	I		II		H		
Crystal system	Cubic		Cubic		Hexagonal		
Space group	Pm3n (No. 223)		Fd3m (No. 227)		P6/mmm(No. 191)		
Ideal unit cell	$2 (5^{12})6(5^{12}6^2) \times 46$		$16 (5^{12})8(5^{12}6^4) \times 136$		$3 (5^{12})2(4^35^{16}6^3) \times 34 \text{ H}_2\text{O}$		
Ideal cell	H ₂ O		H ₂ O				
Ideal Hydration number	5.750		5.667		5.667		
Cages	Small	Large	Small	Large	Small	Medium	Large
Average cavity radius (Å)	3.95	4.33	3.91	4.73	3.94	4.04	5.79
Variation in radius (%)	3.4	14.4	5.55	1.71	4.0	8.5	15.1
Water molecules per cavity	20	24	20	28	20	20	36

Hydration number (n) is the ratio of water to gas molecules in the unit cell. Cage occupancy (Θ) is defined as the amount of gas captured in hydrate [9]. Sometimes two or more gases can also be present inside the lattice structure of the hydrate. The structure is influenced by both the size of the gas as well as the concentration of the gas molecules. For

example, methane is a single gas that can be both sI and sII. Similarly, ethane also forms sI and sII. If both methane and ethane are present together, both can form sI and sII depending upon the temperature, pressure, and relative concentration of the gas potential.

Table 1.4: Guest molecules and hydrate cages

Guest molecule		sI	sII	sI	sII
Molecule	Diameter(Å)	SC	LC	SC	LC
N ₂	4.1	0.804	0.7	0.817	0.616
O ₂	4.2	0.824	0.717	0.837	0.631
CH ₄	4.36	0.855	0.744	0.868	0.655
H ₂ S	4.58	0.898	0.782	0.912	0.687
CO ₂	5.12	1.00	0.834	1.02	0.769
C ₂ H ₆	5.5	1.08	0.939	1.10	0.826
C ₃ H ₈	6.28	1.23	1.07	1.25	0.943
i-C ₄ H ₁₀	6.5	1.27	1.11	1.29	0.976
n-C ₄ H ₁₀	7.1	1.39	1.21	1.41	1.07

1.3.1. Structure I

Structure I has 46 water molecules per unit cell, with 2 dodecahedral voids and 6 tetrakaidecahedral voids that can host up to 8 gas molecules. The hydration number varies from 5.75 to 7.67, with an average of 6. The hydrate number varies according to gas occupancy. A higher hydration number indicates that all the cages are filled with gas molecules. Lower value of hydration means there are empty cages. This sI structure hydrate typically forms with gases like methane, ethane, carbon dioxide, and hydrogen sulfide [1,17,18].

1.3.2. Structure II

Structure II has 136 water molecules per unit cell, organized into 16 Dodecahedral voids and 8 Hexakiadecahedral voids, with a capacity up to 24 gas molecules to accommodate into the structure. Structure II has a hydration number of 5.67 when all the units are filled with gas molecules. Sometimes its hydration number is 17, when larger guest molecules cannot occupy the smaller cages. This configuration permits the inclusion of propane and iso-butane, along with methane and ethane, but excludes pentane [1,17,18].

1.3.3. Structure H

The less common structure H was discovered by Ripmesster et al. in 1987 [4]. Gas hydrate comprises 34 water molecules per unit cell, arranged in 3 pentagonal dodecahedral voids, 2 irregular dodecahedral voids, and icosahedral voids, allowing them to accommodate larger guest molecules like iso-pentane. These hydrate structures feature three 5^{12} , two $4^35^66^3$, and one $5^{12}6^8$ crystal units within a single-unit cube. There will be 6 gas molecules per 34 water molecules [1,17,18]. The formation of this structure requires smaller guest molecules, such as methane, nitrogen, or carbon dioxide, for the 5^{12} and $4^35^66^3$ cages. However, the molecules in the $5^{12}6^8$ cages need to be between 0.7 nm and 0.9 nm, like methylcyclohexane.

1.4. Location of gas hydrate

The hydrate was discovered in 1820, but the problem began after the 1920s when methane was transported in a pipeline from gas reservoirs. Due to the formation of solid hydrates inside the pipeline due to low temperatures, the gas flow was stopped. Initially, it was thought to be frozen water. However as the pressure was reduced, the flow became normal. Hence, in the 1930s, the recommended term for these impediments was identified as hydrate. Russian experts asserted in 1946 that natural circumstances and resources exist in permafrost-covered areas for hydrate formation and stability, with Western Antarctica

being the first location they suggested for a discovery [12,19]. The hydrate location throughout the world is shown in Figure 1.5. Most gas hydrate resources—roughly 98%—are found in marine sediments, with the remaining 2% being found in permafrost. Gas hydrate accumulations (red) and found gas hydrates (blue) are caused by seismic processes and scientific drilling operations, respectively [20].

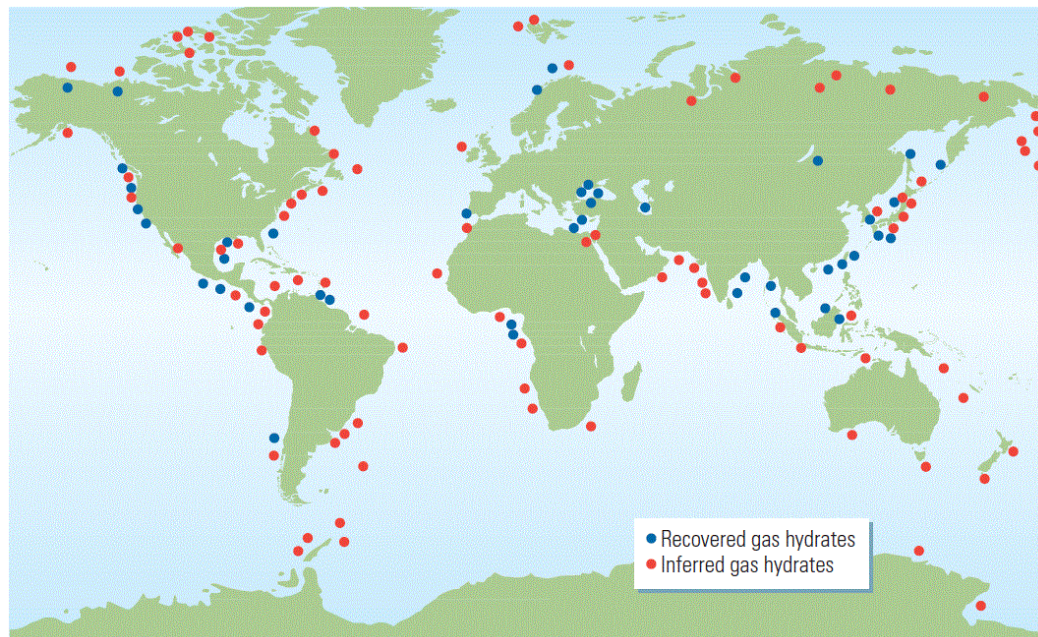


Figure 1.5: Worldwide natural gas hydrate reservoir [20]

Some other regions are Japan, India, China, the Gulf of Mexico, and Alaska, where hydrate reservoirs have been located. The hydrate reservoir can be classified into four categories. They are classified based on geological and lithological hydrate-bearing zones. The four categories are: sand-dominated reservoir, fractured clay-dominated reservoir, hydrate formation on the sea floor and low-concentrated hydrate in clay. Because methanogenesis in marine sediments actively produces methane, the bulk of hydrates is found in oceanic sediments [21]. When a certain pressure and temperature are reached, the methane that has been generated subsequently combines with the water to form methane hydrate. Gas hydrate occurs only in deep ocean and permafrost environments with tectonic and sedimentary characteristics. Makogon first published the estimation and occurrence of

methane in hydrate in 1966 [22]. He also generates methods to estimate hydrate in the subsurface. A detailed hydrate resource estimation was given by Milkov [23]. In offshore, the hydrate is generally found at a depth of 200 to 600 meters, depending on gas composition and geothermal gradient [24]. Figure 1.6 shows the temperature vs depth in the hydrate stable zone [25].

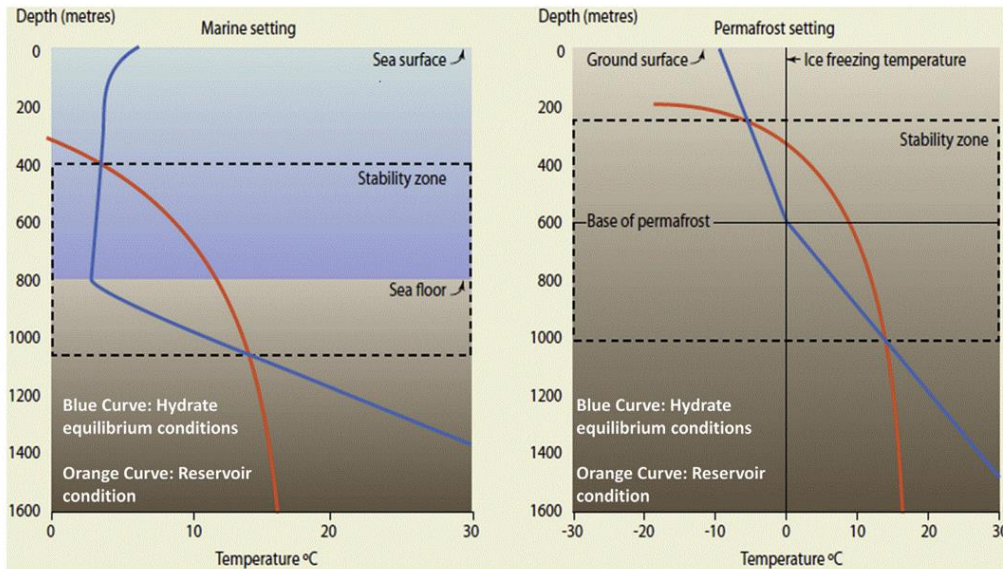


Figure 1.2: Stability conditions for gas [25]

The equilibrium curve, called the “methane-water-hydrate curve”, depends on water salinity and gas composition. HSZ (hydrate stability zone) means that hydrates are more likely to form in that region than always being present there. Besides pressure, temperature, gas composition, and salinity, methane supply is another factor that determines the formation of hydrates in marine sediments. Hydrates are formed when methane is above its solubility limit at specified pressures and temperatures.

The HSZ varies with the depth of the ocean due to the following factors:

- The HSZ's thickness varies depending on the global variations in ocean depth; a thicker HSZ corresponds to a deeper water body.
- Chemical properties of the guest molecule have a significant impact on the stability region. A study conducted in the Gulf of Mexico, where the gas is not

pure methane, found that the base of the HSZ exists at temperatures 2°C higher than a pure methane deposit [26]

To develop hydrate, it is important to have a gas supply and a source that coincides with proper thermobaric conditions. In oceanic and permafrost environments, the methane has two origins: biogenic or thermogenic [21]. When microorganisms are buried in an anoxic environment, biogenic methane is produced. When this methane is saturated in water, a hydrate forms. This biogenic methane is formed in relatively shallow-depth sediment. This methane travels hundreds of meters before hydrate formation [27]. Thermogenic methane is produced by the degradation of organic matter due to the Earth's heat. They are found in greater depth and can travel very long distances before hydrate formation. This hydrate is generally found along faults [28], mud volcanoes [23], and structurally deformed carrier beds [27].

1.5. Hydrates as a Potential Source of Energy

Hydrate is identified as a problem in the oil and gas industry. However, it can be used as an energy source because of the methane present in the gas hydrate. Throughout the world, more than 220 gas hydrate reservoirs have been discovered. One cubic meter of gas hydrate contains around 170 cubic meters of methane. It is estimated that over $1.5 \times 10^{16} \text{ m}^3$ gas hydrate reserves are distributed both onshore and offshore. Hence, the volume of gas in that $1.5 \times 10^{16} \text{ m}^3$ reserve is enormous. 15% recovery from these reservoirs can supply energy for 200 years [29]. As the rate of population and development increases, the energy demands also increase. So, this energy demand can be fulfilled by extracting the methane and then using the methane as a cleaner source of fuel [30]. Figure 1.7 shows the energy consumption of the 20th century. [31]

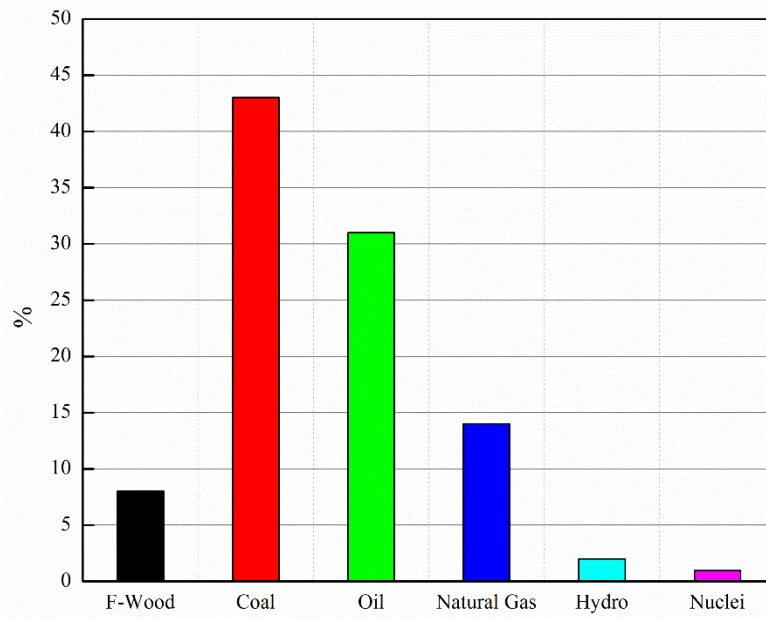


Figure 1.7: The energy consumption of the 20th century [31]

Currently, oil and gas are the primary sources of energy. Natural gas extraction from hydrates has the potential to support global political stability and the long-term economic growth of nations. Extraction and commercial methane production from gas hydrate deposits are challenges for the 21st century. Methane is a cleaner fuel; it generates less carbon dioxide per mole when burned than any other fossil fuel. Thus, it reduces carbon dioxide emissions, reducing the greenhouse effect. Moreover, methane is a more potent greenhouse gas, having four times the effect of carbon dioxide. It is also to be noted that methane present in the hydrate form is twice in quantity as all other fossil fuels combined [32]. Figure 1.8 illustrates the timelines for the world's gas hydrate projects.

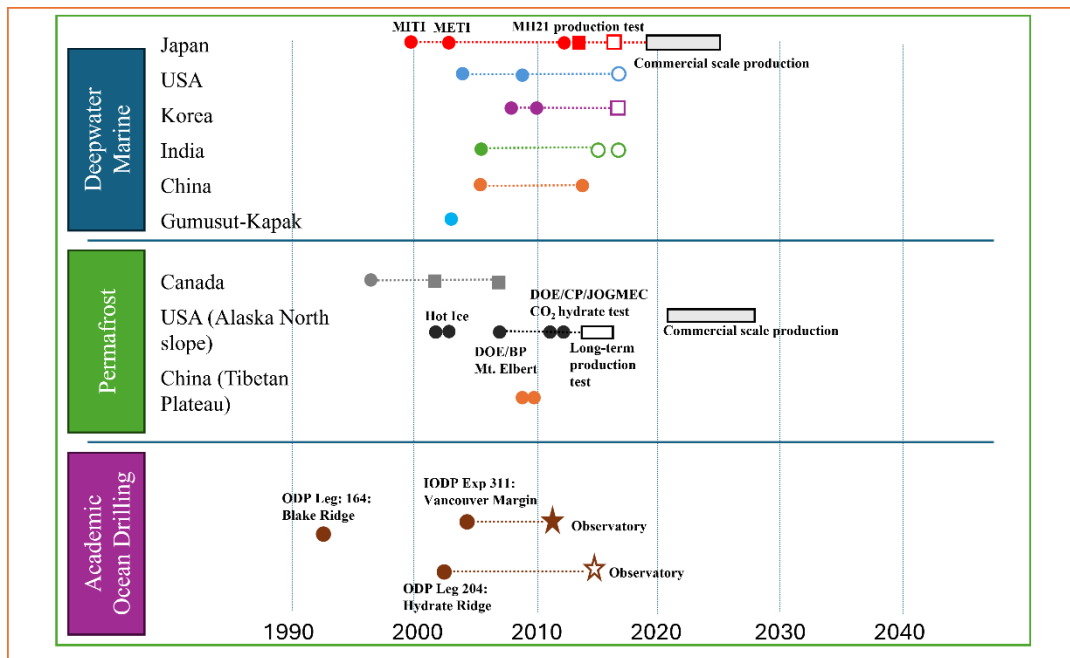


Figure 1.3: The timelines for gas hydrate projects [29]

Compared with hydrocarbon sources, [29]natural gas hydrates are more evenly distributed globally. The creation of extremely efficient methods for converting natural gas from its solid condition into free gas is the main source of concern [29].

1.6. Gas hydrates — Greenhouse gas and climate change

Despite the significant uncertainty in global estimates of methane contained in gas hydrates, these hydrates serve as a substantial natural reservoir for methane, preventing it from being released into the ocean or atmosphere. Methane leakage from gas hydrates into the atmosphere might have a major effect on global climate change since it is a more potent greenhouse gas than CO₂ [33]. However, the impact of global warming on gas hydrate deposits varies significantly across different regions. Ocean water is added by melting glaciers and ice caps due to global warming. The hydrostatic pressure corresponding to the rising water level stabilizes submerged gas-hydrate deposits and thickens the stability zone downward. In addition to increasing air temperatures, water temperatures also rise during global warming, although deepwater bottoms are less affected by global warming thanks to the ocean's high heat capacity. Due to this, for deepwater deposits in depths greater than

500 m, the increase in stable gas hydrates caused by rising sea levels may counterbalance any destabilization caused by an increase in water temperatures, thus resulting in less dissociation [34]. Nonetheless, gas-hydrate deposits are particularly susceptible to variations in ocean circulation and bottom-water temperature at a key depth of roughly 500m [35]. During these warmings, methane could be released, leading to global warming, which might outpace the rise in sea level. As the methane rapidly escapes from these reserves, this will increase the atmosphere's temperature, resulting in global warming.

Hydrates are also geohazards because it is very sensitive to temperature and pressure. A significant impact of gas hydrate formation and dissociation on the marine sediments. The porosity and permeability of the sediments decrease as dissociation occurs [36]. Consequently, during gas-hydrate dissociation, free gas and water are liberated, lowering the sediment's strength. Solid gas hydrate usually occupies less space in the pore space than water or free gas released. Thus affecting the pore pressure [37]. As a result, either pressure increases or volume increases. Sediment can become weaker as pore pressure increases, sediment volume expands, and free gas bubbles form.

The presence of gas hydrate near the sub-surface sediment (a few hundred feet) poses a geo-hazard to oil and gas production. The safety concerns associated with drilling for hydrocarbons (from greater depths) from shallow gas-hydrate accumulations have been reported [38,39]. However up until now, we haven't had much experience creating gas from gas-hydrate deposits and dealing with any potential risk. Production test in 2008 at the Mallik well had safety issues in terms of water and sand production during gas extraction [40,41]. The most recent research on energy from gas hydrates provides a more thorough analysis of the safety concerns associated with gas-hydrate production[40].

1.7. Gas Hydrate Inhibitors and Promoters

Hydrate is one of the major problems in the oil and gas industry. It raises problems in the wellbore during drilling [42], well completion [43,44] as well as transportation in pipelines [45,46]. One way to tackle the hydrate problem is by adding thermodynamics inhibitors and/or Low Dose Hydrate Inhibitors (LDHI) [47].

The science of hydrate formation kinetics is always important and deserves further investigation. The hydrate formation mechanism is poorly understood, resulting in various theories and models. In literature, different models and correlations are predicted for hydrate production by Elgibaly and Elkamel [48]. This correlation can be divided into five main processes, namely: the K-value method [49], Gas-Gravity plot, empirical correlations formulated by Holder [50] and Makogon [51], expansion chart of natural gas by Katz [52], the statistical thermodynamic approach developed by van der Waals and Platteeuw [53]. To predict hydrate formation conditions, the K-value method is based on the vapor-solid equilibrium constants. The second method developed by Katz, the Gas Gravity plot. In the third method, empirical correlations are developed based on pure gases selected by Holder and Makogon. In the Fourth method, hydrate-formation charts are provided to show the extent to which natural gas can expand without forming hydrates. Using the Joule Thomson cooling curves and the gas gravity charts, these charts were redrawn. The fifth method shows the interaction between gas and water molecules and was developed by van der Waals and Platteeuw in 1958. Besides all these methods, one more idea was given by Ostegaard et al. [54] in 2000. It is like a gas gravity plot, but applies to all reservoir fluids. It also considers the impact of non-hydrocarbon gases like CO₂ and N₂ in the petroleum fluid.

Using freshwater helps in hydrate formation during drilling wells in water-based drilling fluid when the temperature is low [55]. If hydrate forms during the drilling

operation, it “plugs” the wellbore. Another problem of hydrate occurs during the transportation of gas through pipelines in low-temperature zones, a flow assurance problem. So, these hydrate occurrences can be stopped by either hydrate avoidance or hydrate management. Figure 1.9 shows hydrate management [56].

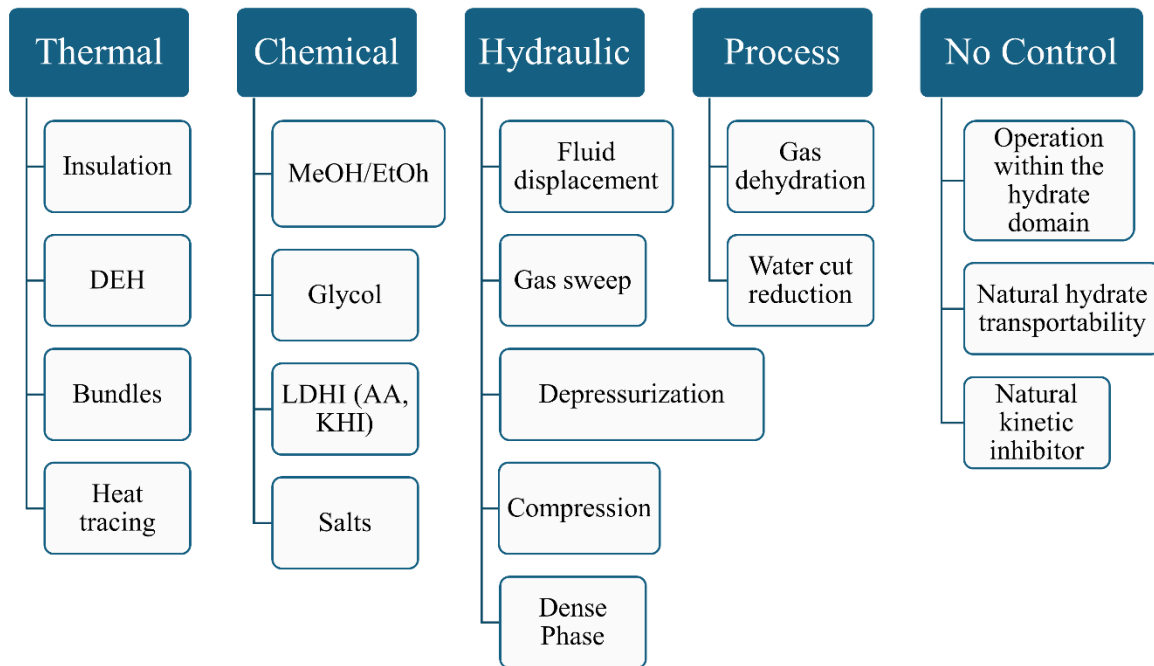


Figure 1.4: Hydrate management strategies [56]

All the above methods sometimes work, sometimes do not. For example, Dehydration is a less effective approach for subsea wells. Heating and insulation are used together for effective hydrate management. Out of all these strategies, chemical inhibition is the most used method for hydrate management [57]. The two primary types of chemical approaches are thermodynamic inhibitors and low-dosage inhibitors. Organic compounds are such as Methanol, Mono-ethylene glycol, and Di-ethylene glycol used most widely as thermodynamic inhibitors [58]. Salts like NaCl, KCl, CaCl₂, etc, are some other inhibitors [59]. low-dosage inhibitors are of two types: kinetic inhibitors (KHIs) and anti-agglomerants (AAs). Kinetic inhibitors can be polymers (PVA), amino acids, and salts with more than two n-butyl, n-pentyl, and iso-pentyl groups, etc [60,61]. Anti-agglomeration is

generally a surfactant that can be anionic(LABSA), cationic(DAM) or non-ionic(Ethoxylate) [62]. Figure 1.10 shows hydrate inhibitors

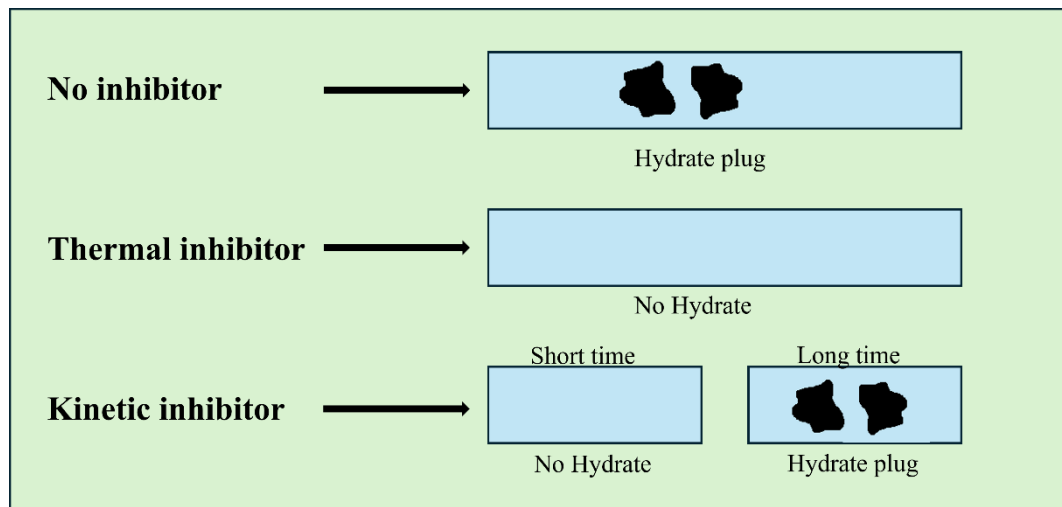


Figure 1.10: Different inhibitors

1.7.1. Thermodynamics Inhibitor

THI is a chemical agent designed to regulate the interactions between hydrocarbons and water that lead to the creation of solid crystalline compounds. It achieves this by altering the hydrate equilibrium curve, effectively lowering the reaction temperature to a point that prevents hydrate formation. The use of a thermodynamic hydrate inhibitor as an additive helps minimize hydrate buildup in pipelines. Methanol is a more common inhibitor used in the oil and gas industry. Methanol works by reducing the fugacity of water, this allows hydrates to form at lower temperatures and higher pressures than would occur without adding methanol [63]. THIs operates by shifting the phase limits for hydrate formation away from the temperature and pressure conditions, hence increasing the driving force needed for hydrate generation [64,65]. Glycol, salts are also inhibitors commonly used for hydrate inhibitors [66]. Quigley and Hubbar [67] explained that thermodynamic inhibitors such as methanol or glycol show much better thermodynamic properties than salts [67]. NaCl, NaBr, and CaCl₂ are used by Kotkoskie et al. [68] as a thermodynamic inhibitor for hydrate inhibition. Out of three salts, CaCl₂ was found to be the most effective

in the inhibition of hydrate. Ebeltoft et al. evaluated the salt polymer system for hydrate inhibition [69]. The best results were using 10wt % EGY with 15 wt% of NaCl and 5 wt% of KCL. Mohammadi et al. have used NaBr, KBr, CaBr₂, K₂CO₃, and MgCl₂ for hydrate dissociation [70]. Experiments were performed at various temperatures and concentrations. All salts exhibited similar behavior under dissociation conditions, except for MgCl₂, which showed distinct behavior at higher concentrations.

1.7.2. Kinetic Inhibitors

KHI is an inhibitor that embeds itself into the lattice of a hydrate crystal and prevents its growth or nucleation. KHIs are low-dosage inhibitors (LDIs) that act at low concentrations (lower than 1 wt%) without affecting hydrate thermodynamics [71]. Mostly, KHIs are soluble in water. KHIs delays a system's hydrate formation by delaying the formation of nucleation and growth [72]. The first nucleation of the hydrate crystal is called the induction time [73]. For different reservoir fluids, KHIs have shown better performance in hydrate inhibition [74]. In literature, various KHIs inhibitors have been explored. For example, ionic liquids (ILs) [75,76], antifreeze proteins (AFPs)[77,78], and Tetrahydrofuran (THF) or cyclopentane [79]. Polymers such as Poly-N-vinyl-lactam [80,81], polyaspartamides [82], N-Isopropylmethacrylamid [83] are also used as KHIs. Chong et al. (2015) explained that NaCl has kinetic inhibitor properties in hydrate formation in porous media by slowing the rate of hydrate growth.

Amino acids have become notable for their role as kinetic inhibitors, but their application has largely been confined to lab environments. Glycine, L-alanine, and L-valine are hydrophobic amino acids utilized as thermodynamic hydrate inhibitors [84]. Sa et al. have illustrated the effect of amino acids (L-proline, L-serine, L-alanine, glycine) on methane and carbon dioxide inhibition [85]. L-serine is the most effective KHI among amino acids in inhibiting the development and nucleation of hydrates. EGY is an inhibitor used widely

in the oil and gas industry to prevent hydrate formation during production and transportation in pipelines. The use of EGY can shift the equilibrium curve of hydrates toward higher pressures and lower temperatures (thermodynamic conditions), which is outside the conditions required for hydrate formation, therefore offshore flowlines can operate normally. EGY has hydroxyl group in its structure, which helps in excellent interface with water, making it difficult to bind water molecules to form a hydrate. Hence, it prevents hydrate formation. The EGY is preferred over other inhibitors due to Health, Safety, and Environmental (HSE) issues. Apart from HSE issues, EGY can be produced economically and recycled with relatively low losses, resulting in less operational cost. EGY has been used as an inhibitor in the Gulf of Mexico since 2007.

1.8. Molecular Dynamics of Gas Hydrate

Using computer simulation to study a molecular system's physical properties has become common practice. Most of these studies use Monte Carlo simulations (MC) and MD simulations. MD simulation integrates Newton's equations over time for each molecule. In addition to calculating thermodynamic properties, MD simulation is capable of calculating time-dependent phenomena. The integration algorithm updates the positions and velocities of each molecule over time. A molecule's configuration and the potential model selected determine its net force. The force and acceleration acting on each molecule are corrected by using the force and acceleration of the previous step. It is possible to calculate macroscopic properties based on the time-averaged trajectories of molecules after integrating forces over several time steps.

1.9. Molecular simulation and gas hydrate

Tes et al. used MD simulation for the first time to study gas hydrate behavior [86]. They explained that through the calculation of vibrational frequency, it is possible to explain the differences and similarities between ice and hydrate. Using MD simulation, the vdWp

statistical theory was applied to calculate three-phase equilibria of hydrate. This theory is given by van der Waals [53,87]. A Monte Carlo simulation study has shown that including long-range guest-host interactions will improve the physical significance of vdWP theory without affecting its accuracy [88]. MD simulations revealed that the repulsion interaction between gas and hydrate lattice is crucial for stabilizing the whole structure [89].

The mechanism of hydrate formation can be explained using MD simulation. The mechanism includes nucleation and growth. This nucleation and growth are very hard to find experimentally. The nucleation and growth mechanism information is gained from MD simulation. Walsh et al. [90] explained methane hydrate nucleation and growth. They found out that during the initial few microseconds, the hydrate network (formed by water) forms around the methane molecules, only to disappear. Only after 1 microsecond, spontaneous nucleation took place to form the hydrate structure. Both sI and sII are formed after the growth of the hydrate structure.

Driving force is an important parameter for hydrate formation. It depends on sub-cooling and over-pressurization of hydrate formation. Hence, this driving force should be well-defined when the simulation runs. To successfully and accurately run the simulation, knowledge of hydrate phase boundary is essential. There are models to calculate the phase equilibria of liquid water-methane gas-methane hydrate. Walshe et al. have used a potential model for nucleation and growth simulation [90]. This helps calculate the thermodynamic properties of the simulation. This model can be used since both sI and sII structures coexist in the MD simulation. Additionally, one can use the Clapeyron equation and simulations to calculate the enthalpy of hydrate dissociation.

1.10. Basics of molecular simulation

Two ensembles are instrumental in MD simulation. NPT (isothermal-isobaric ensemble) and NVT (canonical ensemble). N, P, V, and T represent the number of molecules, pressure,

volume, and temperature of the system. Either pressure or temperature was kept constant during the simulation. The NVT ensembles exhibit Helmholtz free energy related to partition functions, (Q) and is given by the following equation:

$$= -k_B T \ln(Q(NVT))$$

$$= \left(-k_B T \ln \left[\frac{q^n}{N!} \times \int \exp -\beta U(r_1, \omega_1, \dots, r_n, \omega_n) dl \dots dN \right] \right) \quad (1.1)$$

where, $\beta = 1/k_B T$, and k_B is Boltzmann's constant, q is the molecular partition function, dl stands for $dr_i d\omega_1 = dx_i dy_i dz_i. d\omega_1$. For molecules i the coordinates are $r_i(x_i, y_i, z_i)$ with the angle of orientation of ω_i . In the case of a nonlinear molecule, the molecular partition function can be represented as:

$$q = q_{t'} q_r q_v q_e \quad (1.2)$$

$q_{t'} = \frac{q_t}{V}$ is the translational function. q_r , q_v , and q_e are the rotational, vibrational, and electronic partition functions, respectively. These are all dimensions and coexist during phase equilibrium. $q_{t'}$ is commonly expressed as inverse thermal wavelength ($\frac{1}{\Lambda^3}$), $\Lambda = h / \sqrt{2\pi m k_b T}$ where h is Planck's constant and m is molecular mass.

For NPT ensemble, the Gibbs free energy is a necessary parameter. It is obtained as:

$$G = -k_b T \ln(Q(NPT)) \quad (1.3)$$

Where Q given as

$$Q(NPT) = \frac{q^N \beta P}{N!}$$

$$\left[\int \exp(-\beta PV) dV \times \int \exp[(-\beta U)(\omega_1, s_1, \dots, s_n, \omega_n; H)] V^n \times (ds_1 d\omega_1 ds_1 d\omega_n) \right] \quad (1.4)$$

s_i are the coordinate of molecules i in the simulation.

Only the potential energy is taken into account in MC simulations, as opposed to MD simulations, which incorporate both kinetic and potential energies in the acceptance

criterion. The potential energy, U_{Pot} is necessary to interact energy between all molecules in the system:

$$U_{Pot} = \frac{1}{2} \sum_{i,j,n} u(|r_{ij} + nL|) \quad (1.5)$$

Where, L is the length of the simulation box, n is an arbitrary vector of three integer numbers, $u(r)$ is the intermolecular potential between two molecules. To exclude self-interactions, the term where $i = j$ is excluded when $n = 0$. Lennard-Jones (LJ) potential, u_{LJ} , is widely used in molecular simulation for non-polar molecules, expressed by the following equation:

$$u(r)_{LJ} = 4\varepsilon \left[\left(\frac{\sigma}{r} \right)^{12} - \left(\frac{\sigma}{r} \right)^6 \right] \quad (1.6)$$

Where, ε , σ , and r is the depth of the potential well, the diameter of the molecules, and the distance between the molecules, respectively.

In theory, when calculating the intermolecular energy of a system with N molecules, all molecules should be considered. But in practice, $N - 1$ molecules do not have any effect on the molecules. Hence, in molecular simulation, only a certain distance is taken into consideration for simulation; this distance is called the cut-off distance. The maximum cut-off distance can only be, $L/2$ where L is the length of the simulation box. The cut-off radius of 2.5σ is sufficient to obtain simulation results [91], since the LJ potential drops rapidly beyond this distance. Because the LJ potential drops rapidly, two present errors are introduced [92]. This error can be corrected by adding a long-range correction term to Equation 5 [93]. The log-range correction assumes a pairwise distribution function, $g(r)$, is 1 beyond the 2.5σ cut-off distance and long-range potential, u^{long} and is calculated by following the equation:

$$u^{long} = 2\pi\rho \int_{r_c}^{\infty} u(r)r^2 dr \quad (1.7)$$

Where, ρ is the average density inside the simulation box. The presence of polar molecules causes problems during simulation. Hence Coulomb interaction comes into the picture. Coulomb interactions decay at a rate of $-1/r$, and the errors caused by long-range contributions remain significant, even when using a cutoff radius of several angstroms. It is generally accepted that the long-range contribution diverges unless $u(r)$ decays faster than $1/r^3$ [94]. Among the methods for calculating potential energy after boundary conditions, the Ewald summation method is the most commonly used [95]. Coulomb interactions with the potential energy are given by

$$u(r)_{Coul} = \frac{1}{2} \sum_{i=1}^N q_i \phi(r_i) \quad (1.8)$$

q_i is the particle charge and $\phi(r_i)$ is the electrostatic potential at the position of i^{th} particle

$$\phi(r) = \sum_{j,n}' \frac{q_j}{|r_{i,j} + nL|} \quad (1.9)$$

Where, whenever $n = 0$, the sum is over all periodic images n and overall particles j with the exception that $j = i$, if $n = 0$.

In equation 1.8, the sum of electrostatic energies is not well-converging, which makes it unusable as a method of calculating electrostatic energy. To improve the equation 1.8, each particle having q_i charge is surrounded by the opposite charge of Gaussian charge distribution. This total charge helps to cancel the q_i charge. As a result of these charge distributions, the charge becomes short-range, resulting in shorter interactions. It is essential to make necessary corrections to the added potential; this is done by adding the opposite charge of the same sign.

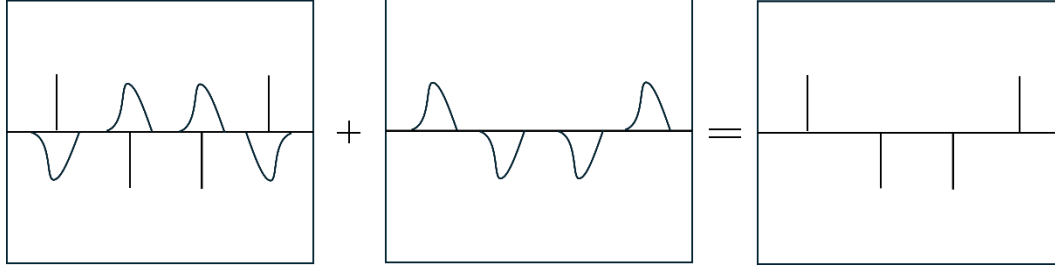


Figure 1.11: Edward summation method for calculating long-range Coulomb interaction

This addition of compensating charge distribution is represented by the Fourier series. The Coulomb interaction for potential energy for compensating charge distribution is given by

$$\begin{aligned}
 U_{Coul} = & \frac{1}{2V} \sum_{k \neq 0} \frac{4\pi}{k^2} |\rho(\mathbf{k})|^2 \exp \frac{-k^2}{4\alpha} & (1.10) \\
 & - \left(\frac{\alpha}{\pi}\right)^{\frac{1}{2}} \sum_{i=1}^N (q_i)^2 \\
 & + \frac{1}{2} \sum_{i \neq j}^N \frac{q_i q_j \operatorname{erfc}(\sqrt{\alpha} r_{ij})}{r_{ij}} + \frac{2\pi}{(2\kappa' + 1)V} \left| \sum_{i=1}^n \mathbf{r}_i q_i \right|^2
 \end{aligned}$$

$$\begin{aligned}
 U_{Coul} = & \text{Fourier contribution} - \text{Self potential correction} + \\
 & \text{Real space contribution} + \text{Boundary effects} & (1.11)
 \end{aligned}$$

Where $k = \left(\frac{2\pi}{L}\right)I$ and $I = I_x, I_y, I_z$ are lattice vectors, α is convergence parameter for compensating Gaussian charge distribution, κ' is dielectric constant, erfc is the error function. Short simulations can determine α by considering computational efficiency and accuracy [96]. For a larger system, the traditional Ewald summation becomes unaffordable due to its computational effort scaling as $N^{3/2}$. When in the systems have more than 105 molecules ($N > 10^5$), other methods may be used, such as particle-particle/particle-mesh (scaled by $N \log N$).

1.11. Research Motivation

As the world progresses into the 21st century, the energy demand continues to rise at an unprecedented rate. Most of the energy is from non-renewable resources. This emits CO₂, a greenhouse gas. Due to this global temperature is increasing. This results in a warmer atmosphere. Gas hydrate is one of the potential cleaner energy sources. Its quantity is twice the quantity of fossil fuel. Also, this hydrate can be used as a storage of CO₂ inside the hydrate reservoir, i.e. CO₂ capture and sequestration. This means that gas hydrates can be used to trap carbon dioxide and store it safely, reducing its release into the atmosphere and combating climate change.

Nanoparticles are nano-sized particles (<100nm). These nanoparticles are a relatively new technology that improves the storage capacity and faster hydrate formation. Forming a gas hydrate with nanoparticles enhances its process by improving the rate at which the hydrate forms and ensuring its stability.

In summary, the exploration of gas hydrates is driven by their potential as an energy resource and their role in carbon storage.

1.12. Research Objective

Synthesis and performance of nanoparticles in hydrate formation, storage, and to study the MD simulation of the hydrate dissociation. Key goals include:

- Enhancing the induction time and rate of hydrate formation by using single-step SiO₂ nanoparticles, as nanoparticles act as promoters, accelerating nucleation and growth of hydrates.
- Increasing gas consumption and hydrate storage capacity.
- Studying single-step SiO₂ nanoparticle impact on storage capacity, water conversion, gas consumption, and induction time under different temperatures and pressures.

- Understanding the effects of inhibitors on hydrate stability and dissociation, including how chemicals (ethylene glycol) influence molecular interactions and hydrate decomposition kinetics.

1.13. Thesis Organization

Creating a clear and logical arrangement for my thesis chapters is essential for conveying my research effectively. This thesis comprises seven chapters.

Chapter 1 introduces gas hydrates, including their formation mechanisms, natural sources, and the various challenges associated with their extraction. The chapter also reviews the different inhibitors reported in the literature that delay hydrate formation. This background establishes the motivation for using molecular dynamics (MD) simulations, which are introduced toward the end of the chapter. Their working principles and relevance to hydrate structure analysis are also discussed, forming the foundation for the simulation studies in the following chapters.

Chapter 2 builds on the simulation concepts introduced in Chapter 1 by exploring the effect of ethylene glycol on gas hydrate dissociation using MD simulations. Various concentrations of ethylene glycol were examined at different temperatures. The analysis includes radial distribution functions (RDF), diffusion coefficients, and total energy evaluations, providing insight into the dissociation behavior of hydrates in the presence of ethylene glycol.

Chapter 3 extends the findings of Chapter 2 by examining the combined effect of ethylene glycol and nanofluids on hydrate formation. The nanofluid was laboratory-synthesized, and their influence on both the thermodynamics and kinetics properties of hydrate was evaluated. Hydrates were synthesized using pure water, pure ethylene glycol, and mixtures of ethylene glycol–nanofluid at different concentrations. The results from all

these solutions provide a comparative understanding of how inhibitors and nanofluids interact during hydrate formation.

Chapter 4 continues the experimental investigation by focusing specifically on single-step synthesized silica nanofluids and their role in methane hydrate formation inside an autoclave. The presence of nanoparticles was shown to accelerate hydrate formation, enhance gas consumption, and increase the overall methane storage capacity. This chapter further reinforces the potential of nanofluids as hydrate promoters, complementing the observations made in Chapter 3.

Chapter 5 revisits MD simulations to deepen the understanding of hydrate behavior in mixed gas systems. In this chapter, the radial distribution function, diffusion coefficient, and mean square displacement for CH₄-CO₂ hydrates were analyzed in the presence of ethylene glycol. These analyses help verify the dissociation mechanisms discussed earlier and link simulation results to experimental trends observed in previous chapters.

Chapter 6 expands on the role of nanofluids introduced in Chapters 3 and 4 by investigating CO₂ hydrate formation in the presence of single-step silica nanofluids. Various nanoparticle concentrations were introduced into the system to evaluate their impact on hydrate formation. The study highlights how nanoparticles reduce induction time, increase gas consumption, and enhance the rate of hydrate formation, thus supporting and extending the earlier findings.

Chapter 7 concludes the thesis by summarizing the combined effects of inhibitors and nanofluids on hydrate dissociation and formation, integrating insights from both MD simulations and experimental studies. The chapter also outlines potential directions for future research and provides recommendations based on the outcomes of the presented work.

Chapter 2: Insights of Molecular Dynamics Simulation to Investigate the Impact of Ethylene Glycol on Methane Hydrate Dissociation

Abstract

Gas hydrate is a tremendous source of clean energy found across the world. The controllable extraction of natural gas for commercial applications from gas hydrate is a challenging task. In the oil and gas industry, hydrate inhibitors are crucial for flow assurance, especially in subsea and deepwater operations. These hydrates can block pipelines and equipment, leading to flow restrictions, reduced efficiency, and potential safety hazards. Therefore, managing hydrate formation is a key concern in the industry. Also, designing better hydrate inhibitor formulations is becoming the need of the hour as the world is moving towards a more gas-based economy. So, it's very important to understand these additives' effect on the methane hydrate. However, the mechanism and extent of hydrate inhibition with additives such as alcohol are yet to be fully understood. Hence, understanding the CH₄ hydrate dissociation process and various thermodynamic parameters under the influence of these additives is very important. In this study, an investigation was done to see the effect of ethylene glycol concentration on CH₄ hydrate dissociation by molecular dynamic simulation under varying thermodynamic conditions. The water cage integrity is investigated at different times, temperatures, and pressures. To be able to quantify the decomposition and mechanism of CH₄ hydrate, the radial distribution function (RDF) and total energy were studied. The result of the radial distribution function and mean square displacement of water and ethylene glycol shows that the hydrate cages decrease with increasing temperature. When the ethylene glycol concentration was increased from 0% to 5%, gas hydrate dissociation increased. Dissociation of the hydrate system is enhanced by both increasing concentration and

temperature, or both respectively. According to the results of this study and previous research findings, such a work would aim to offer effective tips/guidelines for processing hydrate formations and dissociations.

2.1. Introduction

Gas hydrates are ice-like Clathrate crystalline substances, formed by water (host) trapping hydrocarbon molecules (guest). Methane gets entrapped inside cages that are formed by the water molecules through hydrogen bonds; entrapped hydrocarbon gas molecules can be small gases such as methane, ethane, carbon dioxide, etc, or larger gases like pentane, isopentane, and isobutene. The gas inside the structure is held by a weaker intermolecular force, van der Waals forces. Gas hydrate is a stable compound under particular temperature and pressure conditions. There are different structures of gas hydrates that exist like structure I (sI), structure II (sII), and structure H [5]. Among these; sI one is the most commonly occurring gas hydrate structure [97]. It is estimated that 10^{13} and $20 \times 10^{15} \text{ m}^3$ (standard condition) of methane gas are present in both onshore and offshore areas, respectively [98]. Gas hydrate moreover has other practical applications, like gas storage [30], and transportation of gas [99], gas separation [100], and water desalination [101].

The natural gas hydrate mostly consists of methane, Hence, it is also called methane hydrate. These methane hydrates are generally found in ocean permafrost, continental margins, and the Arctic regions. This methane gas, entrapped in a gas hydrate, can in addition be used as a source of energy [30]. One-meter cube of methane gas hydrate can hold approximately 170 cubic meters of methane under standard conditions [17]. The total methane present in methane hydrate is approximately twice the amount of total conventional energy (oil, coal, and natural gas, etc.) put together [102]. So, if extracted, it will be a huge energy source.

Carbon dioxide (CO₂) and methane (CH₄) are both very potent greenhouse gases. However if we compare, methane's greenhouse gas potential is more than 30 times that of CO₂. Moreover, methane has a "Global Warming Potential" GWP of 120 [103]. Therefore, uncontrolled liberation of methane from these hydrate reservoirs is environmentally harmful and may lead to many catastrophic events [104],[105].

The methane extraction process is very challenging because of its sensitivity to temperature and pressure. If the extraction of this methane goes wrong, it leads to serious environmental impacts. Therefore, extracting methane in a controlled manner from hydrate reservoirs is beneficial for environmental protection as well as future clean energy. There are some common methods for hydrate extraction: depressurization method [106,107], gas replacement method [108,109], chemical injection method [110,111], thermal stimulation method [106,112], and sometimes a mixture of these methods. Out of these methods, the depressurization method is the easiest one; however, hydrate reformation and ice formation can happen and hinder the process [113]. The thermal stimulation process requires a high amount of heat and is largely uneconomical. The gas replacement method is prone to low replacement efficiency and injectivity issues. Another method, such as chemical injection, has low energy requirements, however high gas productivity and injection volume can be controlled as per the requirement, except for the low sweep efficiency and requirement of huge quantities of chemicals (hydrate inhibitors). The application of chemical hydrate inhibitors is well known in the petroleum industry for the flow assurance purpose. In addition, it can be a very promising method combined with any other methods mentioned above. The chemical method has a good potential for methane extraction from the hydrate reservoir.

Various simulation, modelling, and experimental studies were conducted on the dissociation of methane hydrate [114–117]. The addition of chemical additives can alter the

decomposition or formation of gas hydrate [5]. These additives (chemicals) change the hydrate equilibrium phase of gas hydrate. So, it is very important to understand the additive's role in both the formation and dissociation of gas hydrate for gas recovery or any other gas hydrate application. In the case of gas recovery from hydrates, the chemical additives are thermodynamic/kinetic inhibitors. The most used hydrate inhibitors are salts, alcohols, and glycols. There are lots of experimental studies available in the literature to understand chemical inhibitors. A recent study shows that various chemicals/additives/salts assist the decomposition of gas hydrate [118]. They studied the effect of ammonium salt in the dissociation of gas hydrate. The performance of different inhibitors (e.g., serine, glycine, and alanine) on hydrate growth was illustrated [119]. The amino acid, as an inhibitor, was examined in methane hydrate dissociation [120]. The effect of biologically active inhibitors, which reduced hydrate formation *via* accelerating dissociation, was also reported in literature [121]. Other studies subsequently studied and reported the important impacts of different inhibitors, such as nuclear magnetic resonance, used for dissociation mechanism of hydrate [122], the effect of ethanol and sodium chloride on CO₂ hydrate [123].

The molecular-level understanding cannot be derived from lab-scale experiments. However, the molecular level understanding of the behaviour of these hydrate inhibitors is very much essential for the development of better inhibitors and fine-tuning the existing inhibitors. MD simulation is an excellent application to see the response of molecules/atoms in each given system. The simulation tells how the molecules/atoms behave at a certain given temperature and pressure, which is impossible to see in an experiment. The trajectory of these molecules/atoms is governed by Newton's laws of motion. Over the last decade, MD simulations have helped study microscopic studies of

gas hydrates. These studies include hydrate growth [124], stability [125], nucleation [126], and thermodynamic properties [127].

Walsh et al. [90] conducted an experiment on nucleation of hydrate and the change of the methane hydrate structure. The use of alcohol in dissociation of hydrate was studied by Hoa-Li et al. [128] Adding alcohol reduces the three-phase temperature because of the chemical potential. This chemical potential is lower in water-alcohol than in pure water. English et al. [129] studied hydrate growth in the presence of an electromagnetic field, where the molecule mobility increases with an increase in the electromagnetic field. Yagasaki et al. [130] illustrated the effect of NaCl on gas hydrate (both acceleration and dissociation). Zhang & Pan [124] has reported both structural and dynamic properties with the help of the displacement density profile & radial distribution function. Sakemoto et al. [131] studied both mechanical and thermodynamic characteristics of methane hydrate structure. According to Sun et al. [132], methanol is effective in decomposing methane hydrate as it promotes methane hydrate dissociation.

Myshakin et al. [133] used MD simulation to investigate the effect of methanol, ethanol and glycerine on the stability of sII hydrate structure, the result shows decomposition rate is inversely proportional to cage occupancy. English et al. [134] showed that dissociation rate controls the diffusion of methane on the surface of the gas hydrate. Qi et al. [135] simulated dissociation of hydrate in electrolytic solution. Mean square displacement to calculate the diffusion coefficient of both methane and hydrate water was reported by Zhang et al. [136] The microscopic process of methane hydrate dissociation was studied using MD simulation. However, the authors have not extended the study to understand the effect of both temperature and concentration.

Although various thermodynamic properties of hydrate in the presence of ethylene glycol as a hydrate inhibitor have been studied by several researchers. But MD simulation

has not been used for analysing the effect of ethylene glycol on methane hydrate dissociation with different operational parameters such as temperature and concentration. Hence, to understand the characteristics of methane hydrate under various temperatures and ethylene glycol concentrations MD simulation and thermodynamics model tools are used in this study. In this paper, we studied the effect of the concentration of ethylene glycol on the dissociation of hydrates. The simulation was performed at different temperatures. Both thermodynamics and structural properties of the hydrate were also studied at different temperature and pressure conditions. radial distribution function (RDF) and thermodynamic properties were investigated in this research paper at various thermodynamic conditions, along with the presence and absence of ethylene glycol. The results give a very good understanding of the molecular-level behaviour of ethylene glycol on methane hydrate. It shall help with the development of novel hydrate inhibitors and optimisation of hydrate inhibitors for the flow assurance applications and gas recovery from hydrate reservoirs.

2.2. Simulation Details

The initial state of a simulation system was created with solid and liquid components. The solid part of the system was gas hydrate sI (structure I), which is a clathrate compound consisting of water molecules that form cages around methane molecules. To build the solid system, the positions of the methane and water molecules in a unit cell of the gas hydrate sI structure were determined using x-ray diffraction [137]. The unit cell was then replicated to create a larger supercell that measures $37 \times 37 \times 37$ cubic angstroms, which contains 1248 water molecules and 216 methane molecules. To include the ethylene glycol molecules in the simulation, the simulation box was resized to $37 \times 37 \times 90$ cubic angstroms. This increased the z-dimension of the box to accommodate the larger molecule. The simulations were run using periodic boundary conditions, which means that when a

molecule crosses one boundary of the simulation box, it reappears on the opposite side of the box, creating an infinite system. This is necessary because it allows the simulation to accurately represent a bulk system, rather than a finite system with artificial boundary effects. Periodic boundary conditions also allow for the simulation of large-scale systems that would be very difficult to study otherwise. Overall, the initial state of the simulation was carefully designed to represent a real-world system of a hydrate plug, and the simulations were run under controlled conditions to accurately model the behavior of the system.

For this study, GROMACS [138], an open-source program widely used for MD simulations, was employed. MD simulations involve the use of various water models [139,140]. In our study, we utilized the TIP4P [141] model for water and the OPLS-AA [142] model for methane. For Ethylene glycol, the OPLS-AA [143] force field was used. The Lennard-Jones parameters between different types of atoms were managed using Lorentz-Berthelot combination rules, and the cutoff radius for Lennard-Jones interactions was set at 15 Å. Long-range electrostatics were handled using Particle Mesh Ewald summation for particle meshes, with a Coulomb force cutoff of 12 Å. The Leapfrog algorithm was employed for conducting simulations. Temperature and pressure were regulated using Berendsen thermostat and barostat [144] respectively, with a thermostat decay of 0.2 ps and a barostat decay of 0.1 ps. by 0.2ps and barostat by 0.1 ps. During the simulation process, the initial configuration was relaxed by using energy minimization. This was achieved by using the Steepest Descent algorithm. Next step, NVT ensemble at constant pressure and constant temperature was performed for 50ps. This is to achieve the targeted temperature of the system. The final step, NPT ensemble, is conducted to study the decomposition process at different pressures and temperatures. The run time was 500ps. Figure 2.1 represents the workflow of simulation process. Simulations were run at different

temperatures ranging from 260 to 300 K while pressure remained constant at 50 bar with different volumes of ethylene glycol (0%, 2.5%, 3.5% and 5%). Here, 2.5% vol is 1.042 g/cc, 3.5% is 1.018 g/cc, 5% vol is 1.014 g/cc.

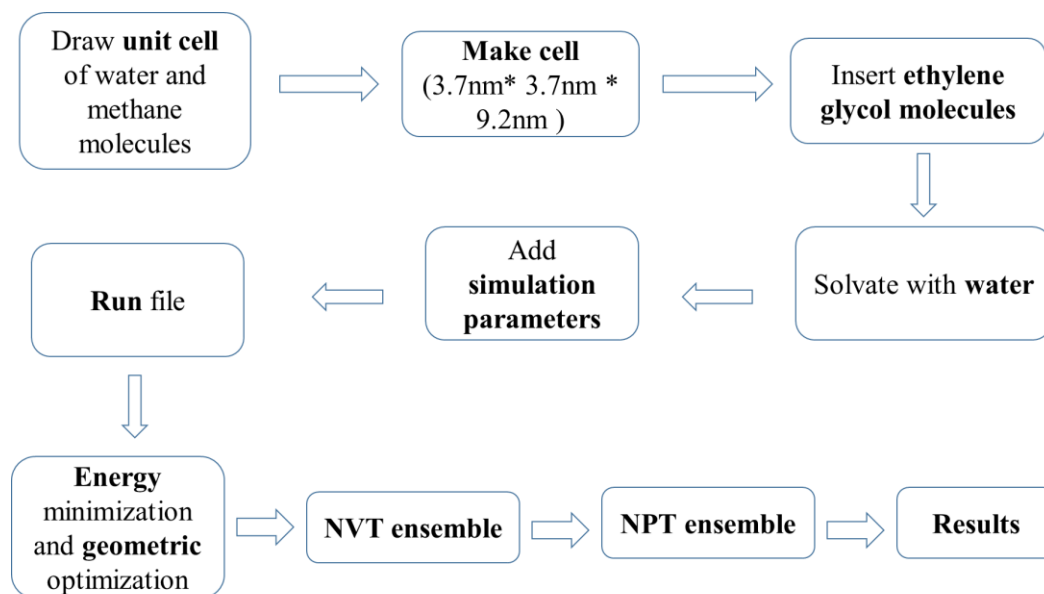


Figure 2.1: Workflow of MD simulation process

2.3. Results and Discussion

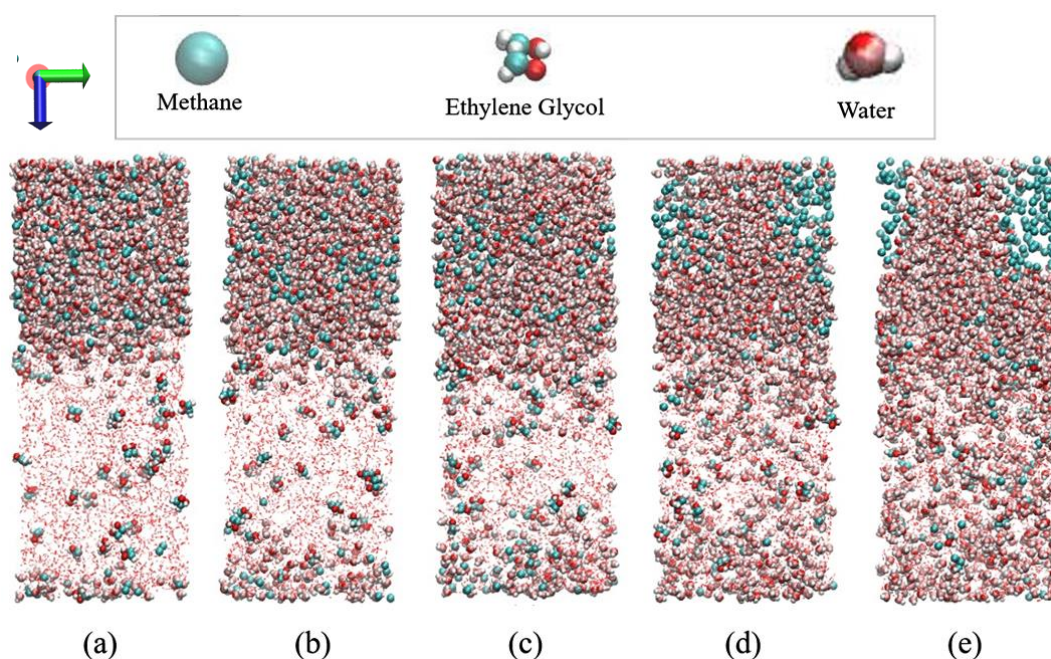


Figure 2.2: Dissociation of methane hydrate structure in the presence of 5 vol% of ethylene glycol at 300K (a) initial at time = 0 ps (b) time = 50 ps (c) time = 100 ps (d) time = 250 ps (e) time = 500 ps

This study aimed to investigate the molecular effects of different concentrations of ethylene glycol at various temperatures in the system. Figure 2.2 illustrates the system configuration at 300K over time. The simulation box contained 5% v/v of ethylene glycol with methane hydrate. Figure 2.2(a) depicts the initial configuration of the simulation box at time 0 ps, where the hydrate structure appeared intact. However, as the simulation progressed, the structure began to disintegrate, leading to the dissociation of the hydrate structure, as shown in the Figure. 2.2(b), 2.2(c), 2.2(d), 2.2(e), and 2.2(f), at 50 ps, 100 ps, 250 ps, and 500 ps, respectively. With time, methane escaped more easily from the cages, and the hydrate dissociated more readily, leading to the absence of an intact hydrate structure towards the end of the simulation run, with only methane and water clusters visible. Figure 2.1 provides insight into the simulation workflow, with the hydrate initially intact in the top portion of the image, and the glycol-water mixture visible below it. As time

progressed, the glycol interacted with the water molecules of the gas hydrate, leading to its dissociation. At the end of the simulation (Figure 2.1e), the hydrate had completely dissociated, with the released methane gas aggregating at the left and right top sides of the simulation box, leading to gas-liquid separation. Table 2.1 displays the number of water and ethylene glycol molecules in the simulation box with different concentrations. The simulation results were analyzed using three different tools, namely Radial Distribution Function (RDF), total energy, and diffusion coefficient.

Table 2.1: The number of molecules of ethylene glycol in hydrate structure

Concentration (vol%)	Number of water molecules	Number of ethylene glycol
0	2610	0
2.5	2537	19
3.5	2584	26
5	2455	37

2.3.1. Radial distribution function (RDF)

The Radial Distribution Function (RDF) is a crucial parameter for characterizing the microstructure of gas hydrate/ethylene glycol systems and provides insight into the dissociation effect of ethylene glycol on the hydrate structure. RDF is utilized to determine the probability distributions of similar particles in the vicinity of a given particle in space.

The expression of RDF is

$$g_{\alpha\beta}(r) = \frac{V_s}{N_\alpha N_\beta} \left(\sum_{i=1}^{N_\alpha} \frac{n_i \beta(r)}{4\pi r^2 \Delta r} \right) \quad (2.1)$$

where, $g_{\alpha\beta}(r)$ is the average probability of a particle β within the distance of r and $r + \Delta r$ away from the i th particle α ; N_α is the number of particles α and N_β is the number of

particles β ; V_s is volume of simulation box; $N_{i\beta}(r)$ is number of particle β within the distance of r and $r + \Delta r$ away from i th particle α .

The RDF can be represented as the plot between the average probability of a particle vs distance. From the RDF plot, the probability of the average distance between two similar atoms can be obtained from the peaks. The RDF methane was calculated and plotted with the centre of mass of ethylene glycol and water molecules [145].

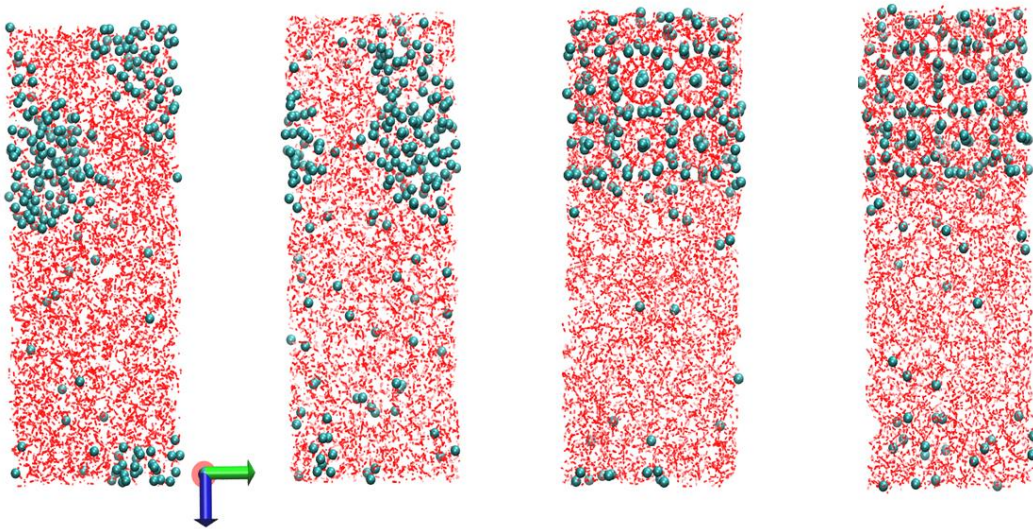


Figure 2.3: Simulation box configuration at (a) 300K temperature and 2.5% ethylene glycol (b) 300K and 5% (c) 260K and 2.5% (d) 260K and 2.5%

2.3.2. Impact of temperature

There is a primary peak at 4.1\AA , which is the distance represents the hydrogen bond connecting the oxygen molecules of water particles of hydrate and methane present in the hydrate. In Figure 4(a), there is no change in the RDF value (4.1\AA) as the concentration increases. This is because at this temperature the hydrate structure is still not dissociated. Since no change was found in RDF values, it can be concluded that the hydrate is stable or did not dissociate. Figure 4(b) shows that peak decrease, i.e., the probability of finding methane and water of hydrate is less; this is due to the fact that at 280K the hydrates are not stable and start to dissociate but not yet fully. As the concentration of ethylene glycol

is 5 vol%, the RDF is even less. That indicates more dissociation than 0 vol% and 2.5 vol% but in Figure 4(c) there is no peak or valley left in the RDF meaning is no structure left at this temperature; the hydrate has completely dissociated. Figure 2.3 concludes that, as temperature increases, the peak decreases. This shows that the increase in temperature disestablishes the hydrate structure. The above figure moreover illustrates that as the temperature increases, it breaks the hydrogen bond easily, resulting in dissociation of the hydrate structure. Table 2.1 shows the number of both water and ethylene glycol molecules in the simulation box with different concentrations.

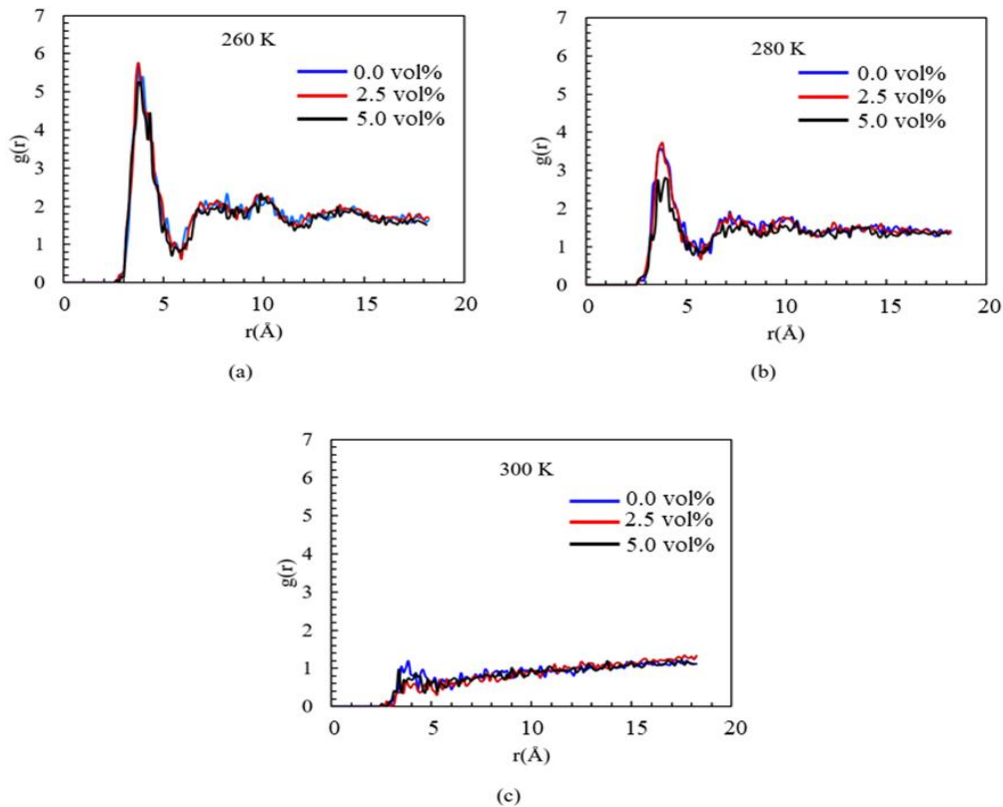


Figure 2.4: RDF of methane and water molecules of hydrate at: (a) 260 K, (b) 280 K, and (c) 300 K with varying concentrations of ethylene glycol

Figure 2.4(a), (b), and (c) demonstrate the radial distribution function (RDF) at 500ps between methane atoms and water molecules in a hydrate system box containing different concentrations of ethylene glycol at various temperatures. The primary peak in

the RDF appears at 4.1Å, which represents the distance of the hydrogen-bonded oxygen molecules of water particles in the hydrate and methane present in the hydrate [146]. Figure 2.4(a) indicates that there is no change in the RDF value (4.1Å) as the concentration increases, which is due to the stable hydrate structure at this temperature that is not dissociated.

In Figure 2.4(b), the peak decreases because the hydrates are not stable and start to dissociate at 280K, but not completely. The RDF is even lower at a concentration of 5 vol%, indicating a higher dissociation than at 0 vol% and 2.5 vol%. Figure 2.4(c) shows no peak or valley remaining in the RDF, indicating that no structure is left at this temperature, and the hydrate has completely dissociated. The results of Figure 2.4 suggest that as there is an increase in temperature, the peak decreases, demonstrating that the hydrate structure is destabilized by the temperature increase. Moreover, as the temperature increases, the hydrogen bond in the hydrate easily breaks, resulting in hydrate dissociation.

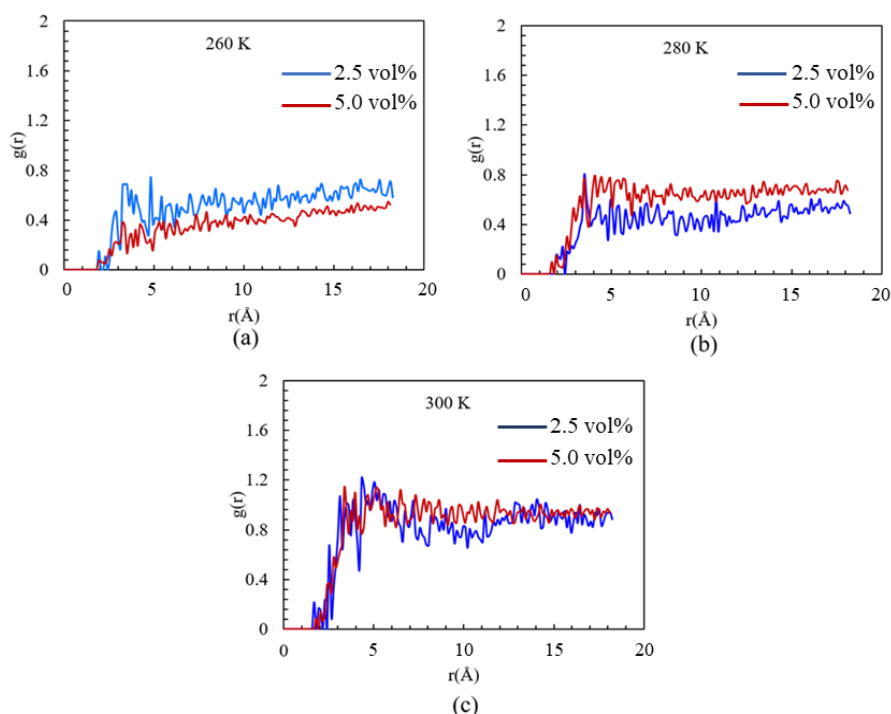


Figure 2.5: The RDF of methane of hydrate and ethylene glycol at: (a) 260 K, (b) 280 K, and (c) 300 K with varying concentrations of ethylene glycol

RDF of methane and ethylene glycol at 50 bar and different temperatures with two different concentrations (2.5 vol% and 5 vol%) is shown in Figure 2.5(a), (b), and (c). In Figure 2.5(a), the RDF value is higher in 2.5 vol% than in 5 vol%. This is because the fewer molecules of 2.5 vol% move more freely inside the simulation box. At this temperature, the hydrate is still intact, and therefore, there is less or no interaction between methane and ethylene glycol molecules. Similarly, Figure 2.5(b) shows that as the temperature and concentration increase, the hydrate dissociates, resulting in more interaction between these two molecules. The RDF value is higher in 5 vol% than in 2.5 vol% due to a higher concentration of ethylene glycol molecules to move around inside the simulation box. In Figure 2.5(c), the hydrate is completely dissociated at a temperature of 300K, resulting in a higher interaction between methane and ethylene glycol, as evident from the higher RDF values for both concentrations. At 260 K and 280 K, the RDF value is lower than 300K; the very minimal interaction between methane and ethylene glycol is the primary reason, which is credited to the non-dissociation of the hydrate structure at lower temperature, as evident from Figure 2.5 (also verified from Figure 2.4). Hence, a lesser value of RDF was obtained. However, at 300 K, the hydrogen bond between oxygen atoms breaks, leading to hydrate dissociation and an increase in the probability of methane and ethylene glycol, as shown in the Figure. 2.5. Figure 2.5 also illustrates that a higher value of RDF is obtained with an increase in concentration and temperature.

2.3.3. Impact of concentration

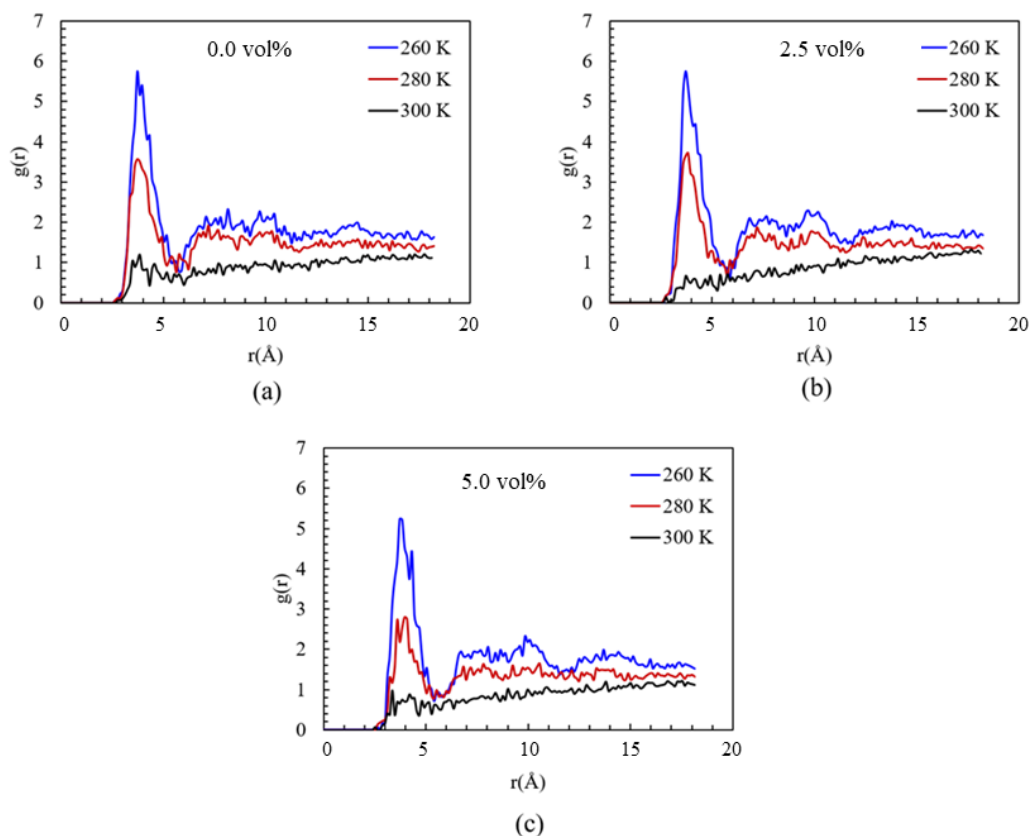


Figure 2.6: The RDF of methane and water molecules of hydrate at different ethylene glycol concentrations: (a) 0 vol%, (b) 2.5 vol%, and (c) 5 vol% with varying temperatures

RDF of methane and water molecules of hydrate with varying ethylene glycol concentrations and temperatures is shown in Figure 2.6(a), (b), and (c). Figure 2.6(a) represents the effect of temperature with 0 vol% of ethylene glycol. The peak values follow the order of $260\text{K} > 280\text{K} > 300\text{K}$. At 260K, the structure is stable, resulting in a higher RDF value of 5.85 at 4.1 Å. At 280K, the less stable structure leads to more hydrate dissociation, and the RDF value decreases to 3.76. At 300K, the RDF value is 1.12, indicating complete dissociation of the hydrate structure. This suggests that an increase in temperature leads to the destruction of the structure, releasing methane molecules into the system. Figure 2.6(b) shows similar results for 2.5 vol% of ethylene glycol in the system. As the temperature increases, more dissociation occurs. In Figure 2.6(c), there is a slight decrease in the peak at all temperatures due to the presence of 5 vol% ethylene glycol,

indicating that both temperature and ethylene glycol have a combined effect on the hydrate structure, leading to faster dissociation.

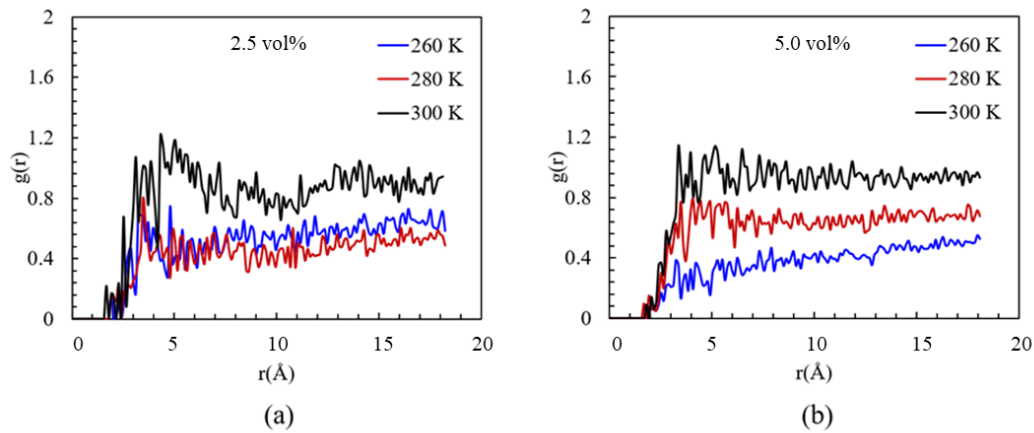


Figure 2.7: The RDF of methane of hydrate and ethylene glycol at different ethylene glycol concentrations: (a) 2.5 vol%, and (b) 5 vol% % with varying temperature

Figure 2.7(a) represents the radial distribution function (RDF) between ethylene glycol and methane molecules at various concentrations within the simulation box. As mentioned earlier, the RDF measures the probability of finding a certain molecule (methane in this case) at a given distance from another molecule (ethylene glycol). At a concentration of 2.5 vol%, the RDF values for methane and ethylene glycol are similar for both 280K and 260K, indicating that the probability of finding methane molecules near ethylene glycol molecules is comparable at these temperatures. This suggests that the behavior of methane is relatively stable, and it doesn't escape the structure or form clusters significantly. However, at 300K, the RDF value for methane is higher, indicating an increased probability of finding methane molecules near ethylene glycol molecules. This suggests that at higher temperatures, methane molecules have a higher tendency to escape the structure, or the hydrate dissociates, leading to an increased presence of methane near ethylene glycol molecules. In Figure 2.7(b), the RDF is shown for a concentration of 5 vol% at different temperatures. From the figure, it is clear that at 300K, the RDF values are higher compared

to the other temperatures, indicating a stronger effect or interaction between methane and ethylene glycol. This suggests that at 300K, the presence of methane has a more significant impact on the behavior or distribution of ethylene glycol molecules compared to the lower temperatures. From these results, one can say that at 2.5 vol%, the RDF values for methane and ethylene glycol are similar at 280K and 260K, indicating comparable probabilities of finding methane molecules near ethylene glycol. However, at 300K, the RDF value for methane is higher, suggesting a higher probability of methane escaping the structure. In Figure 2.7(b), at a concentration of 5 vol%, the RDF values are higher at 300K compared to the other temperatures, suggesting higher dissociation of the hydrate.

The results suggest, as the concentration of ethylene glycol increases, the peak value in the radial distribution function (RDF) decreases. This observation indicates that at higher concentrations, the hydrate structure of the system becomes more easily dissociated. When the concentration of ethylene glycol is higher, the RDF steadily diminishes. This decrease in the RDF peak implies that the hydrate is becoming less stable and more prone to dissociation. In other words, the presence of a higher concentration of ethylene glycol disrupts the integrity of the hydrate structure, making it easier for methane to escape from the solid structure of the hydrate. At lower concentrations, ethylene glycol exhibits a lower breaking capacity of hydrogen bonds between the water molecules of the hydrate cage. This means a weaker ability to disrupt the hydrogen bonds that hold the hydrate structure together. As a result, the hydrate structure remains relatively stable, and the probability of finding methane molecules within the structure remains higher. However, as the concentration of ethylene glycol increases, it allows ethylene glycol to disrupt the hydrogen bonds more easily within the hydrate structure, leading to its dissociation. Consequently, as the concentration of ethylene glycol increases, the hydrate structure becomes more

susceptible to breaking apart, resulting in a decrease in the probability of finding methane molecules within the structure.

Overall, these results suggest that both the temperature and concentration of ethylene glycol play a significant role in the stability of the hydrate structure. Firstly, let's consider the role of temperature. As the temperature increases, the energy of the system also increases (Detailed analysis of total energy is given in section 2.3.4). This increased energy can disrupt the intermolecular forces, such as hydrogen bonds, that hold the hydrate structure together. The increased thermal energy provides more kinetic energy to the molecules, making them move more vigorously and facilitating the breakage of hydrogen bonds. Consequently, higher temperatures can lead to the destabilization and dissociation of the hydrate structure. Secondly, the concentration of ethylene glycol also plays a significant role in hydrate stability. Ethylene glycol can form hydrogen bonds with water molecules of the hydrate, and the hydrogen-bonded water molecules contribute to the formation and stability of the hydrate structure. At lower concentrations, there are fewer ethylene glycol molecules available to participate in hydrogen bonding with water molecules, resulting in a weaker influence on the hydrate structure. The hydrogen bonding network within the hydrate is mainly maintained by water molecules. However, as the concentration of ethylene glycol increases, more ethylene glycol molecules are present to participate in hydrogen bonding with water molecules. This leads to the formation of new hydrogen bonds between ethylene glycol and water, which can replace some of the original hydrogen bonds among water molecules within the hydrate structure. The formation of these new hydrogen bonds alters the stability of the hydrate, potentially weakening the original structure and making it more susceptible to dissociation.

In summary, both temperature and concentration have significant effects on the stability of the hydrate structure. Higher temperatures increase the energy of the system,

facilitating the breakage of hydrogen bonds and destabilizing the structure. Increasing the concentration of ethylene glycol can alter the hydrogen bonding network within the hydrate, potentially leading to the dissociation of the structure. Therefore, the combined influence of temperature and concentration determines the overall stability and integrity of the hydrate structure.

2.3.4. Total energy

When methane hydrate dissociates, it undergoes an endothermic process, meaning it absorbs energy for decomposition. As a result, increase in the total energy of the system during dissociation. However, as the dissociation progresses, the total energy stabilizes with time. This suggests that the system reaches a new equilibrium state as the hydrate structure breaks down. Before decomposition occurs, the water molecules within the hydrate cage maintain their hydrogen bonds, keeping the structure intact. Initially, during the simulation, the total energy varies around its equilibrium values, indicating that the hydrate cage remains intact and the hydrogen bonds within the structure are maintained.

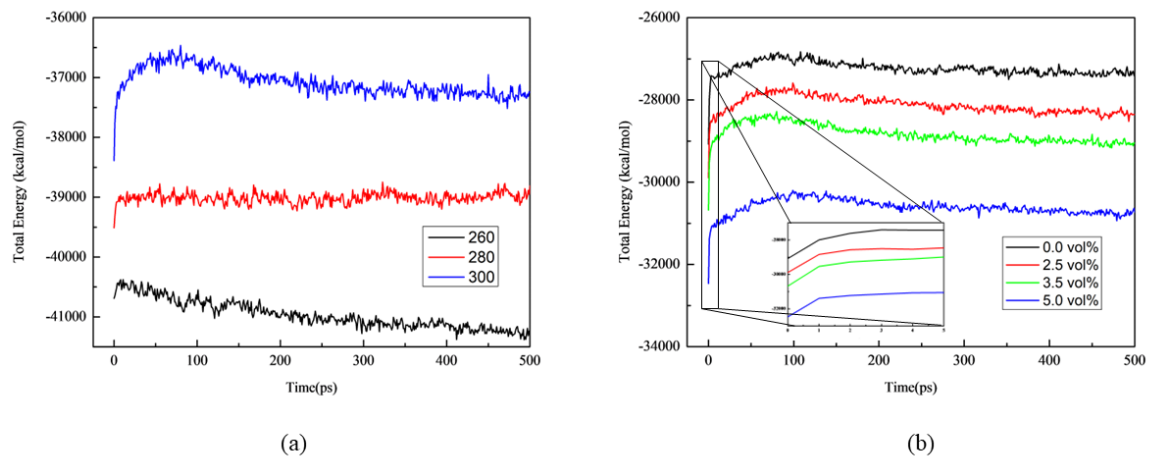


Figure 2. 8: Total energy of hydrate system with (a)5 vol% ethylene glycol at various temperatures, and (b) various concentrations of ethylene glycol at 300K and 50 bar

Figure 2.8(a) illustrates the total energy at 50 bar pressure for different temperatures. It shows as the temperature increases, the less time required by total energy

to reach the maximum value. This indicates that higher temperatures lead to faster dissociation of the methane hydrate. At higher temperatures, the kinetic energy of molecules increases, making it easier for them to break through the cage structure and initiate dissociation. As shown in the figure, the total energy increases rapidly during a specific time interval, typically between 0.05ps and 1.05ps. This increase in total energy signifies the breakdown of hydrogen bonds present in the water molecules within the hydrate cage, indicating the dissociation process. From the analysis of Fig., the conclusion can be drawn that the hydrate structure remains stable initially around 0.05ps. However, all the dissociations take place within approximately 1.05ps. After this time, there is no further change in the total energy, suggesting that dissociation is complete, and the system has reached a new stable state.

In summary, the information provided highlights that as the temperature increases, the dissociation of methane hydrate occurs more rapidly. The total energy of the system increases during dissociation, reflecting the breakdown of hydrogen bonds within the hydrate structure. Once dissociation is complete, the total energy becomes stable, indicating the system has reached a new equilibrium state.

Figure 2.8(b) focuses on the total energy at a temperature of 300K and a pressure of 50 bar, considering various concentrations of ethylene glycol. The results demonstrate that the total energy increases with simulation time (at the initial stage), indicating the destabilization and dissociation of the gas hydrate structure. In the presence of ethylene glycol, the hydroxyl group (-OH) plays a crucial role in breaking the hydrogen bonds between water molecules within the gas hydrate structure. The hydroxyl group formed new hydrogen bonds with water molecules, disrupting the existing hydrogen bonding network of the hydrate structure. These newly formed hydrogen bonds contribute to the destabilization of the gas hydrate structure, ultimately leading to its dissociation. As the

concentration of ethylene glycol increases, more hydroxyl groups are available to form hydrogen bonds with water molecules. Consequently, a greater number of hydrogen bonds are formed, and the dissociation occurs more rapidly of the hydrate structure. Increased concentration of ethylene glycol amplifies the effect of breaking the hydrogen bonds within the hydrate, resulting in a faster breakdown of the structure. It is worth noting that ethylene glycol plays a significant role in the dissociation process of the gas hydrate structure. The hydroxyl groups of ethylene glycol introduce instability to the structure by disrupting the hydrogen bonding network. This disruption prompts the water molecules to break away from the original hydrate structure and form clusters or aggregates, leading to the dissociation of the gas hydrate. As a result, the total energy of the system increases with simulation time, indicating the destabilization and dissociation of the gas hydrate structure. The hydroxyl groups present in ethylene glycol play a crucial role in breaking the hydrogen bonds within the hydrate, leading to its dissociation. The concentration of ethylene glycol influences the rate of dissociation, with higher concentrations accelerating the breakdown of the gas hydrate structure.

2.3.5. Diffusion Coefficient

Simulation run information is provided by the diffusion coefficient in the MD simulation. The average of the pressure and temperature simulation at certain nodes is described by this variable. The calculation diffusion coefficient of water and methane molecules within the hydrate structure can be used to explain the dissociation of the hydrate structure. The equation is given by [147]

$$6Dt = MSD \quad (2.2)$$

D is the diffusion coefficient, t is the simulation time, and MSD is mean mean-squared displacement.

Table 2.2: Diffusion coefficient of methane and water molecules at P = 50 bar

Ethylene glycol concentration (%)	Temperature (K)	Pressure (bar)	Methane diffusion coefficient ($\times 10^{-9}$ m ² /s)	Hydrate's water diffusion coefficient ($\times 10^{-9}$ m ² /s)
2.5	300	50	2.8049	3.7828
3.5			2.8675	4.1073
5			2.9031	4.3791
2.5	280	50	1.2626	0.9900
3.5			1.2910	1.2228
5			1.3057	1.2360
2.5	260	50	0.1570	0.2328
3.5			0.2396	0.2772
5			0.2532	0.2925

Table 2.2 summarized the diffusion coefficient of water and methane at 300K temperatures and 50 bar pressures. It is clear from the table that diffusion coefficient values of 260K and 280K were very low, indicating a stable system. As concentration increases, the diffusion coefficient becomes smaller; that means an increase in dissociation rate [148]. As a comparison of both hydrate water and methane, the diffusion coefficient of hydrate water molecules is higher than methane molecules. As the concept of MSD, at a given temperature, a stable structure allows vibration of water molecules around the hydrate cage. There are more water molecules surrounding the methane in a given structure. As the temperature or/and concentration increases, these water molecules vibrate more violently before dissociation. This explains that the diffusion coefficient is high for hydrate water

molecules and low for methane molecules at lower temperatures. The more the temperature, the faster the movements in molecules. Methane's diffusion coefficient increases as dissociation takes place, and the value increases till it is the same as the diffusion coefficient in a gas/liquid system. Since the dissociation occurs, methane that escapes from the lattice of the hydrate forms bubbles at the interface of the hydrate-liquid. This has been observed in early simulation studies [149],[150]. Since methane bubbles form, these increase the dissociation rate because the bubbles absorb surrounding methane molecules [151].

Diffusion coefficient is a function of time. Therefore, it is necessary to simulate the dissociation process for different temperatures within the same time frame. Both dissociation coefficients of methane and hydrate water explain the dissociation process of the hydrate system.

2.4. Conclusion and Summary

An MD simulation is used to understand and investigate the mechanism of dissociation of methane hydrate due to ethylene glycol concentration. MD simulation uses parameters like RDF, diffusion coefficient, and total energy to dissociate the hydrating process. This helps in quantitatively determining the degradation of hydrate structure under various ethylene glycol concentrations, as well as temperature and pressure conditions. To achieve the results, numerous simulation runs are performed at various temperatures, pressures, and with different concentrations. As the temperature increases in the methane hydrate system, there is a decrease in the height of peaks (from RDF of 6 to 1) and a decrease in the width of peaks; the trend was verified in the literature [146]. Hence, the system exhibits reduced stability. As the concentration increases from 0% to 5% vol, the structure dissociation can be seen in the RDF between methane and ethylene, also verified in the literature [146]. The

total energy also increases with temperature, indicating the destruction of the solid hydrate structure[152].

There are two steps in hydrate dissociation. As the temperature and concentration increase, water molecules start vibrating; due to this methane molecule present inside the cages also starts vibrating; this is continuous till the hydrogen bonds between the water molecules break, resulting in the breaking of the hydrate structure [153]. In the second step, the escape of methane from the water cage of the dissociated hydrate structure occurs. Increasing temperature speeds methane hydrate dissociation, as at higher temperatures, kinetic energy is higher. Hence, the more unstable the structure is, the easier the dissociation. Moreover, the obtained results gave new insight into how methane hydrates decompose, allowing the use of alcohols and other additives efficiently for hydrate development, thereby promoting controllable hydrate exploitation

Chapter 3: Effects of Ethylene glycol and silica nanoparticles on methane hydrate formation

Abstract

Methane hydrate in nanofluid systems has garnered significant attention due to its potential applications in energy storage, natural gas transportation, and CO₂ sequestration. This study explores the behavior of methane hydrate in the presence of nanofluids—colloidal suspensions of nanoparticles in liquids. The primary focus is on understanding how the addition of various nanoparticles influences the formation and dissociation of methane hydrate. Nanoparticles have been observed to alter the nucleation process, accelerate the growth of hydrate crystals, and potentially enhance the stability of methane hydrates under subzero conditions. Nanofluid (20-90 nm) prepared by the sol-gel method. In addition, ethylene glycol was used for hydrate formation and compared with pure water hydrate formation. This research examined a range of nanofluid solutions with 0.5, 1.0, and 1.5 wt% SiO₂ nanoparticles. The results indicate that 1.0 wt% nanofluid-based methane hydrate systems exhibit improved heat transfer characteristics, potentially making them more efficient for practical applications like methane storage and transport. Additionally, the interaction between nanofluid and the hydrate structure can modify the thermodynamic properties of the system, which may offer pathways for optimizing methane storage. With 1 wt% of nanofluids, the storage capacity and quantity of methane uptake increased by 275% to water. Investigating the hydrate growth rate at the start of the hydrate formation process shows that nanoparticles and their mixture increased the induction time, consumption rate, and storage capacity considerably. This research contributes to the understanding of the complex interactions between methane hydrates and nanofluids, paving the way for future innovations in energy and environmental technologies. Thus, nanofluids with greater (optimal) concentrations of single-step SiO₂ NPs increase CH₄

hydrate formation kinetics, thermodynamics, and storage potential.

3.1. Introduction

A gas hydrate is a solid ice-like structure where smaller gas molecules are entrapped inside the clathrate structure formed by hydrogen-bonded water molecules. Methane hydrate is stable at higher pressure and low temperature. This hydrate forms during the transportation of fluid in a pipeline, causing accidents that may result in catastrophic losses [17]. As a result, hydrate mitigation is crucial for flow assurance in oil and gas production. As a standard practice, operators have used “total hydrate avoidance”, maintaining the pipeline operational pressure and temperature levels outside the hydrate deposition envelope. Typically, some salt is present in the produced water in the pipeline in modest concentrations, which is insufficient to prevent the hydrate formation. In the quest for more effective hydrate inhibition, the majority has focused on experimental and simulations of the MD of hydrate extraction [154]. The three types of hydrate inhibitors are anti-agglomerants, low-dosage, and THI, each having distinct mechanisms [155]. THI generally include alcohols and salts, the latter inhibiting the hydrate formation depending on the salt solution ionization. Predicting the gas hydrate phase equilibrium data in an aqueous solution including salt and alcohol, is crucial to optimize the concentration of salts/THIs and their efficiency of hydrate inhibition. For example, the inclusion of 10 wt% NaCl reduces the equilibrium temperature by 2.5 to 4.0 °C [156]. Methanol, ethylene glycol etc., are thermodynamic inhibitors that are traditionally injected into the pipeline to prevent hydrate formation [157,158]. By shifting the hydrate phase equilibrium border to higher pressures and lower temperatures, increasing THI loading makes it possible to produce without blockage under such circumstances [17,159].

An important consideration when using THIs is that the generated water directly correlates to the injection rates [160]. If a reservoir produces more water, adding more THI

into the reservoir increases the capital and operational costs [161][162]. THI shifts the hydrate phase equilibrium boundary [163–165], hydrate growth rate [166,167]. However, some studies show that THI has increased the hydrate growth rate [168]. The study conducted by Di Lorenzo et al. [169] found a reduction in hydrate growth rates with EGY concentration from 0 to 30 wt%, owing to a decreased driving force. Kinetic inhibitors such as surfactant are sometimes added in the system to encourage hydrate formation (growth rate [170], induction time [171,172], and storage capacity [173,174]). Additionally, it reduces the induction time by reducing the surface tension between the gas and the liquid, leading to an increased mass transfer through the gas-water interface [174–176]. Nevertheless, the formation of foam in the presence of surfactants makes it undesirable to be employed as a promoter for industrial scale. In the past decades, nanoparticles have also been used to study their effects on hydrate formation.

Nanoparticles are metallic, conductive, and enhance the hydrate formation by increasing the hydrate nucleation and crystal growth [177–180]. Researchers use different nanoparticles, like Cu nanoparticles [181], Zn nanoparticles [182], and Ag nanoparticles [178,183]. Li et al. [181] observed that the copper nanoparticle promotes R134a hydrate formation. Arjang et al. [178] explain that including silver nanoparticles in hydrate formation enhances methane consumption by 33.7% than pure water. These nanoparticles are kinetic promoters owing to the high surface energy and higher area-to-volume ratio [184]. In their investigation of the impact of commercially available graphite nanoparticles on gas hydrate formation, Sloan and Koh [17] and Zhou et al. [185] found a greater potential for hydrate growth. The effect of carbon nanotubes on the amount of hydrate stored and the induction time is highlighted by Park et al. [177], where the authors observed an increase in gas storage by over 300%. Pahlavanzadeh et al. [186] observed an ~63.3% increase in methane consumption compared to pure water, in the presence of 0.157 M copper oxide,

owing to enhanced heat transfer in the presence of nanoparticles. Interestingly, nanoparticles are likely to aggregate and settle due to high surface energy, contributing to the reduced effectiveness of nanofluid for its intended applications. To increase stability and distribute nanoparticles in the base fluid, surfactants are sometimes used [187]. Najibi et al. [180] report the effect of copper oxide (CuO) mixed with Sodium dodecyl sulfate (SDS) on methane hydrate formation. They concluded that the combination of SDS and CuO considerably increases gas consumption as well as water-to-hydrate conversion. Abedi-Farizhendi et al. [188] found that carbon nanostructure, along with SDS improves hydrate formation nucleation and hydrate growth. Kakati et al. [189] observed the enhanced gas consumption during hydrate formation by 150% and 158%, in the presence of Zn nanoparticles and Al₂O₃ (both 0.8 wt%) mixed with SDS (0.03 wt%), respectively, compared to pure water. Zhou et al. [190] have studied the thermodynamics and kinetics of hydrate formation in the presence of graphite nanoparticles with tetra-n-butyl ammonium halides (TBAH). The result explains that there is a slight thermodynamic inhibition in hydrate formation however shows a positive effect in kinetic behavior.

In the literature, studies on the promoter plus inhibitors effect together in a system are scarce. Inhibitors prevent the hydrate formation; similarly, promoters enhance faster hydrate formation by providing suitable conditions for nucleolus. When used together could modify the behaviour of the hydrate zone. The use of promoters and inhibitors together provides increased flexibility and regulation over the process of methane hydrate formation. Promoters facilitate the formation of targeted hydrate (for extraction, storage, or gas exchange), while inhibitors prevent the formation of unwanted hydrates in transport or storage systems. By controlling the use of both, efficiency is maximized, safety is enhanced, and operational risk is reduced in both transport and extraction operations. This research presents the findings of our investigation into the impact of SiO₂ nanofluid

solutions (with single-step silica nanoparticles) on the thermodynamics and kinetics of CH₄ hydrate formation. Sol-gel method was used to synthesize the single-step SiO₂ nanofluid (0.5, 1.0, and 1.5 wt% SiO₂) with nanoparticle sizes ranging from 20 to 90 nm, and stability tests were carried out. Along with the pure nanofluids, studies were performed on hydrate formation in the presence of a mixed system (ethylene glycol and nanofluid-ethylene glycol). The characteristics, including mole consumption, consumption rate, and storage capacity, were determined at 6.0 MPa and 278.15 K. The findings were compared for hydrate storage applications. In addition, it was determined how both inhibitors and promoters can influence the rate and stability of the hydrate formation.

3.2. Experimental section

3.2.1. Materials

Ammonium hydroxide and tetraethyl orthosilicate (TEOS) were obtained from Sisco Research Laboratories Pvt. Sigma Ltd. of India supplied the polyacrylamide (PAM). China's Changshu Hongsheng Fine Chemical Ltd. purchased the ethanol. Millipore® Elix-10 supplied the DI water used to synthesize the nanofluid. Methane with ~99.9% purity was obtained from Purusottam gas suppliers (Rae Bareli). To mix and prepare the NPs, a magnetic stirrer manufactured by D-Lab (MS-H280-Pro) was used. The materials used in this experiment are listed in Table 3.1.

Table 3.1 : Chemical details used in the experiment

Chemical name	Name of the company	CAS number	Purity
Ammonium hydroxide	SRL chemical	1336-21-6	99.9%
Tetethylorthosilicate (TEOS)	SRL chemical	78-10-4	98%
Ethanol	Changshu China	64-17-5	99.9%

Polyacrylamide (PAM)	Sigma-Aldrich	9003-05-8	98%
----------------------	---------------	-----------	-----

3.2.2. Nanofluid synthesis

The nanofluid synthesis is based on the sol-gel method. The base fluid was initially prepared using the PAM solution (1000 ppm) for all nanofluid solutions. The next step involved mixing 80 mL of PAM solution with 20 mL of ethanol for 100 minutes at 800 rpm. Further, 1.5 mL of TEOS was added dropwise (for 0.5wt%), and the stirrer was run continuously for 250 mins. The last stage was to add a certain quantity (2ml) of ammonium hydroxide to the mixture and agitate it for another 100 mins. As the stirrer continued to run, white precipitation inside the solution confirmed the synthesis of nanoparticles. For size distribution and stability analyses, the Dynamics Light Scattering (DLS) equipment (SZ-100, Horiba Scientific, Singapore). These nanofluids are of different concentrations: 0.5 wt%, 1.0 wt% and 1.5 wt%. For preparation of the 1.0wt % nanofluid, the 3 mL TEOS concentration is added. Similarly, for 1.5wt%, 4.5mL of TEOS is added. Adding ammonium hydroxide influences the size of the nanoparticles. The characterization of the nanofluid has been explained in our previous studies [191]. A similar observation was made by Bailey and McCartney [192]. To avoid the formation of polymer aggregates, the necessary precautions were taken. The quantity of chemicals is added precisely and uniformly, thus there are no lump forms during the formation of the nanofluids. According to Vajihinejad et al. [193], adding non-uniform chemicals leads to the formation of the cluster and thus forms an aggregate. This aggregate may either float to the top of the surface or settle to the bottom of the solution during the process. In order to prevent the formation of aggregates, the chemicals were gradually introduced to base fluids and stirred well using a laboratory stirrer.

3.2.3. Experimental setup

The stirred reactor setup for hydrate studies (D-cam Engineering, Ahmedabad, India) (Figure 3.1) is made of SS 316 with a 250 mL volume. A chiller is used to maintain the experimental temperature by circulating the glycol-water mixture through the reactor water jacket. The reactor has two PT-100 temperature sensors (± 0.01 MPa accuracy) and a pressure sensor (HD20V4T, Delta Ohm, Italy, ± 0.01 MPa accuracy) that can measure temperatures from 250 to 400 K and 0.05 to 120 MPa, respectively.

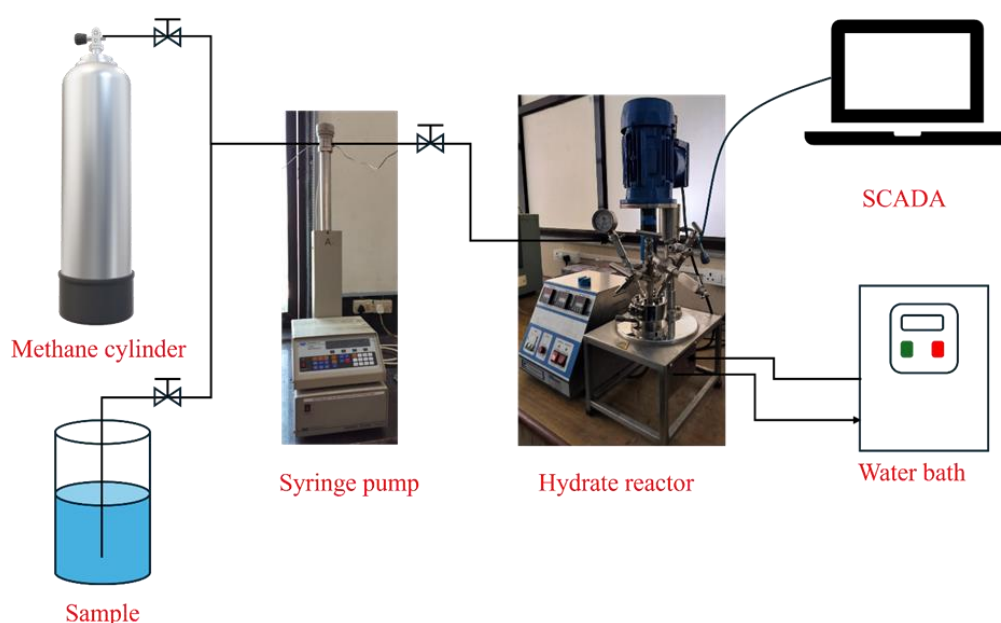


Figure 3. 1: The actual setup consists of a hydrate autoclave, a water bath (to maintain the temperature), along a syringe pump to maintain the pressure inside the autoclave cell

3.2.4. Experimental procedure for hydrate studies

For hydrate studies, the required amount of aqueous solution was injected inside the reactor. Upon the leak test (for ~8 hrs), the reactor was purged 4-5 times at low pressure with methane gas to remove atmospheric air removal from inside the reactor. Methane gas was then injected at the required pressure, the chiller was started, and the stirrer was set at 500 rpm (consistent across every experiment).

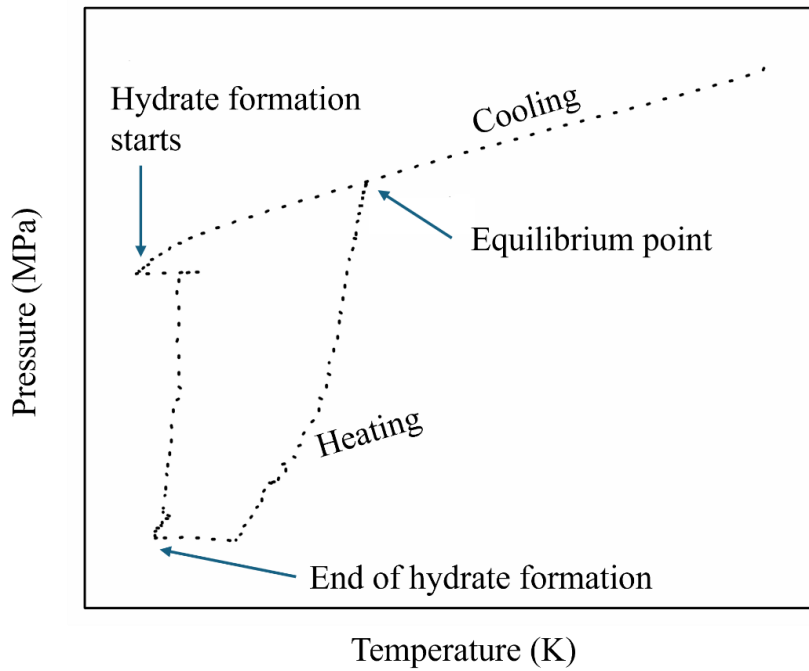


Figure 3. 2: Pressure-temperature profile for gas hydrate formation

Figure 3.2 shows the isochoric pressure search diagram (pressure vs temperature) through the phase stability experimental duration. Hydrate synthesis is divided into four stages (1) cooling stage; (2) nucleation point and hydrate formation; (3) hydrate stabilization; and (4) heating [194]. The cooling stage is the initial stage where the gas dissolves in the aqueous solution. According to Gay-Lussac's Law, gas pressure drops as temperature drops. Research conducted by Kvamme et al. [194] confirms that CH_4 continues to dissolve in water up to a certain extent, as its solubility in water rises with the temperature decrease. This is because, as the temperature drops, the kinetic energy of water molecules decreases, which allows more methane molecules to be trapped in the water, leading to an increase in solubility. Their results verify that methane solubility increases as temperatures decrease from 283.13 K to 275.11 K. The induction time, shown by the rise in temperature on the P vs T graph, is the point at which the visible drastic pressure decrease ensues (gas consumption in hydrate formation), accompanied by a spike in the temperature (exothermic nature of hydrate formation). After the hydrate formation stage, there is not much change in pressure, which is due to the saturation of hydrate in the system and a reduction in the

driving force required for hydrate growth. For hydrate dissociation, heating is started till the temperature reaches 3K more than the formation temperature. Next, the temperature is ramped to 0.5 K/hr. After 3-4 hrs, the hydrate dissociates, and the pressure reaches initial values. When the pressure intersects the cooling values, this value is noted and is called Hydrate-Vapor-liquid equilibrium (HVLE). This value is important to determine the hydrate stable zone in any aqueous solution. Experiments were repeated 3 times with fresh aqueous samples to ensure the reliability of the results.

Induction time is the time when the first crystal of hydrate forms inside the reactor. There are three stages of hydrate formation: dissolution, growth, and stabilization. When the stirrer starts inside the reactor, a continuous mixing of gas and aqueous phase occurs. Hence, the gas dissolves. Formation and dissolution of unstable water happen. This continues until there is a spike in temperature reading along with a reduction in pressure reading, indicating the first nucleus of the hydrate formation (exothermic reaction of hydrate formation). The hydrate growth starts after the induction time. There is rapid gas consumption inside the hydrate structure, resulting in a further decrease in the pressure. This decrease in pressure is also due to the reduction in mass transfer of gas-liquid. Once the full hydrate crystal forms, both temperature and pressure do not change, indicating that the gas and liquid inside the reactor are stable, and no further hydrate will form inside the reactor.

3.3. Results and discussion

The study report examined the kinetic and thermodynamic influence of a single-step silica nanofluid on methane hydrate formation in the presence of ethylene glycol. Research into HVLE, gas consumption, gas consumption rate, induction time, and storage capacity was carried out by synthesizing hydrate with different concentrations of nanofluid.

3.3.1. Nanoparticle characterization

3.3.1.1. Stability and zeta potential measurement of nanofluid

Some quantities of nanoparticles were taken for stability measurements upon preparation, and some were kept inside a transparent culture tube (see Figure 3.3). The size and zeta potential range of the synthesized nanofluid are provided in Table 3.2. With time, the nanofluid tends to settle, like in our previous studies [195]. These settlements are found to be critical in different applications. The size and zeta potential values were 32nm, 25nm, 54 nm, and -34.1 mV, -46.3 mV, and -39.1 mV for samples A1, A2, and A3, respectively. As the nanoparticle concentration increases, more settlement occurs inside the culture tube. A3 with 1.5 wt% concentration has more settlement than A1 (0.5 wt%) and A2 (1.0 wt%). The increased concentration causes more particles to clump together and form agglomerates, leading to the nanoparticle settlement at the bottom of the culture tube. Sample A1 with the lowest nanoparticle concentration was more stable with zeta potential at -34.1 mV (day 0) and -30.6 mV (30 days) (see Table 3.2). Sample A2 exhibits -46.3 mV and -38.2 mV while A3 exhibit -39.1 mV and -31.6 mV for 0 and 30 days, respectively. Figure 3.3 moreover confirms that A1 nanofluid exhibits more stability and fewer sediments than A2 while A3 has the least stability, leading to nanoparticle settlement. The zeta potential values were observed to be outside the -30 mV to 30 mV range (a prerequisite for a stable colloidal particle suspension), even after 30 days. The obtained particle sizes also corroborate the zeta potential results. As the nanofluids are freshly synthesized the particles are well dispersed inside the base fluids. Due to the surface charger, the particles form clusters and agglomerate. Hence, there is a significant change in the particle size. The conclusion is drawn from these results that A1 and A2 have less agglomeration and are more stable than A3.

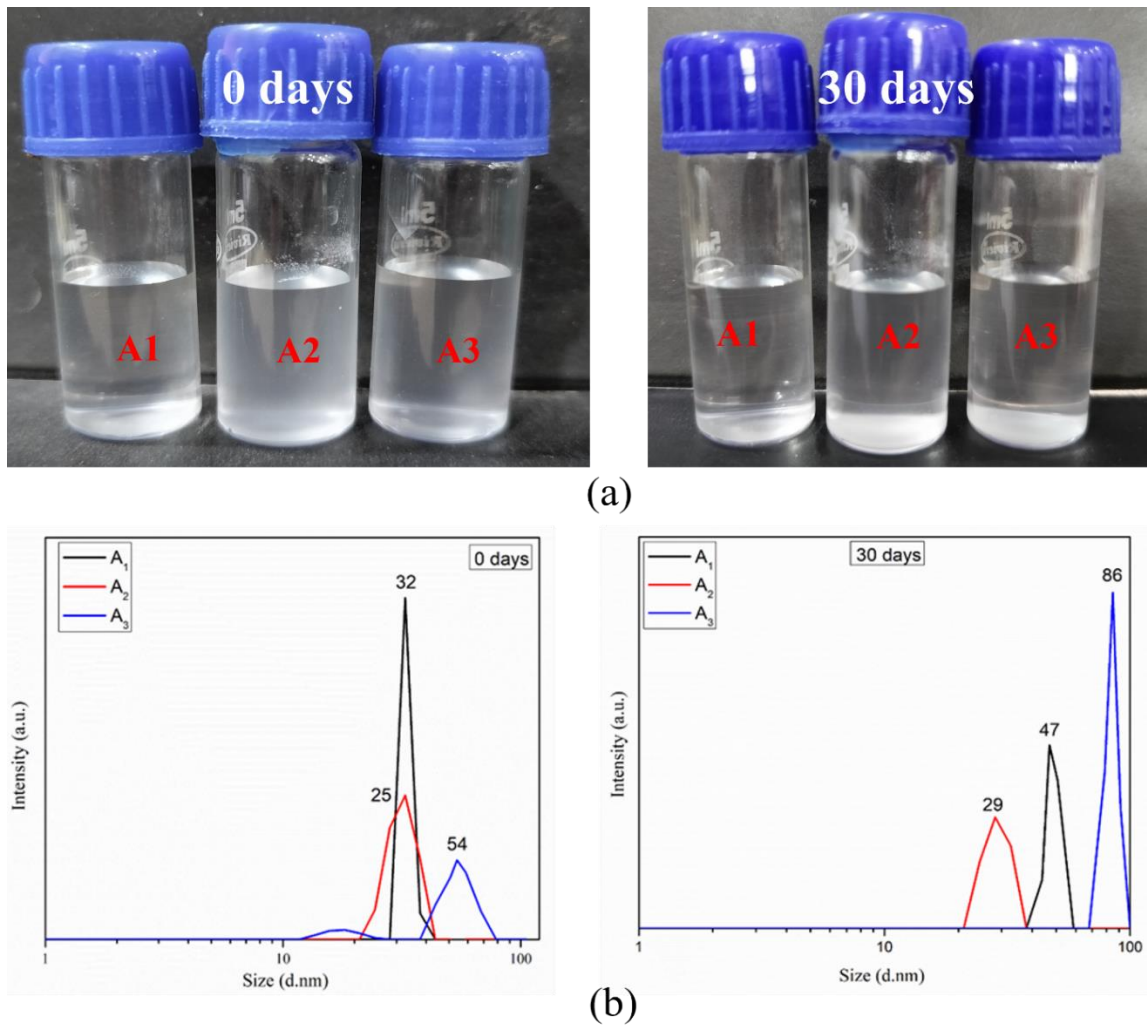


Figure 3. 1: Synthesize nanofluid image at 0 days and 30 days

Table 3.2: DLS measurements along with the induction time of synthesized nanofluids

Sample name	Nomenclature	Zeta Potential (mV)		Particle Size (nm)		Induction time (mins)	Average Induction time (mins)
		0 days	30 days	0 days	30 days		
DI water (130ml)	A0					181.6	159
						144.8	
						150.6	
Ethylene Glycol (EGY) (130ml)	A'0					214.8	206.5
						210.4	
						194.3	
0.5 wt% (130ml)	A1	-34.1	-30.6	32	47	88.1	90.6
						93.6	
						90.1	

1.0 wt% (130ml)	A2	-46.3	-38.2	25	29	103.4 93.9 97.3	98.2
1.5 wt% (130ml)	A3	-39.1	-31.6	54	86	91.1 92.5 95.4	93
DI (50ml) + EGY (30ml) + A1(50ml)	A4					118.3 104.6 111.9	111.6
DI (50ml) + EGY (30ml) + A2(50ml)	A5					128.7 106.1 122.5	119.1
DI (50ml) + EGY (30ml) + A3(50ml)	A6					129.1 108.6 112.7	116.8
DI (50ml) + EGY (50ml) + A1(30ml)	A6		NA			135.1 120.1 114.1	123.1
DI (50ml) + EGY (50ml) + A2 (30ml)	A8					146.9 138.4 124.8	136.7
DI (50ml) + EGY (50ml) + A3 (30ml)	A9					137.1 124.6 117.8	126.5

3.3.1.2. UV-vis analysis of the nanofluids

UV-vis (Ultraviolet-Visible) spectroscopy is one of the most common analytical methods applied in material characterization, especially for nanofluid studies. The interaction between the nanoparticles inside the nanofluids, as well as their optical characteristics, is thoroughly examined in the characterization of nanofluids. UV-vis spectroscopy is used in this situation for the same. In order to characterize nanofluids, it is necessary to conduct a comprehensive investigation into the optical characteristics of the nanoparticles and the way in which they interact with the nanofluids. The absorbance spectra that are produced from UV-vis analysis can be used to determine essential

information on the optical properties of nanofluids. This information includes particle size, concentration, surface modification of nanoparticles, and the kind of material.

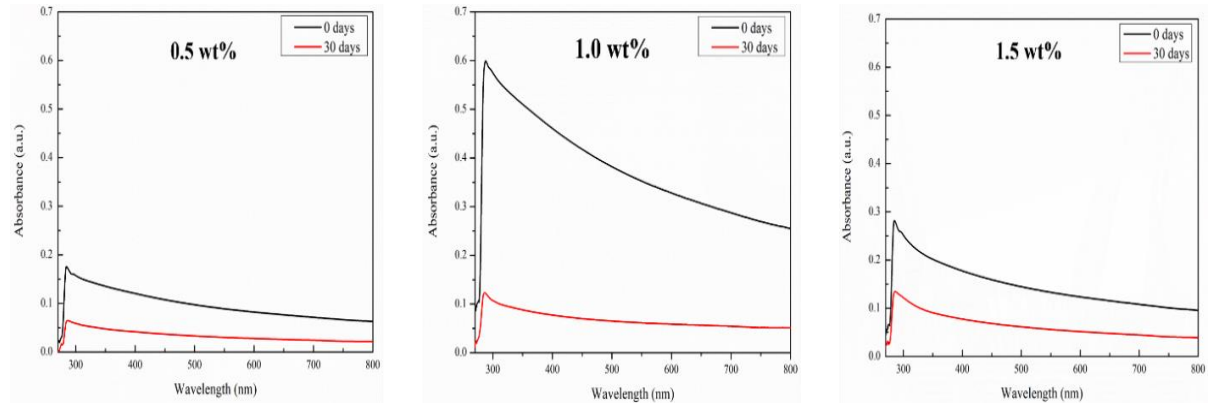


Figure 3. 2: UV-*vis* analysis plots of A₁, A₂, and A₃ as a function of storage period

Figure 3.4 shows the UV-*vis* for 0 and 30 days. For UV-*vis*, the wavelength for SiO₂ varies from 273-285 nm. Samples A1, A2, and A3 have a wavelength of 283.1 nm, 284.6 nm, and 284.9 nm, confirming that the synthesized sample is SiO₂. Samples A1, A2, and A3 exhibit peak absorbance values of 0.17, 0.58 and 0.28, respectively (0 days). The nanofluid A2 has a higher absorbance peak value due to the well-dispersed nanoparticle inside the nanofluid. A higher peak value indicates more interaction with the light. The observation validates the DLS results of the nanofluids (Table 3.2). Figure 3.4 in addition gives the time dependency of absorbance. After 30 days, the absorbance reduces to 0.06, 0.12, and 0.135 for A1, A2, and A3, respectively, due to the nanoparticle settlement, of the absorbance decreases. There is a reduction of 64.7% for sample A1. For A2 and A3, the reduction is 79.3% and 51.7%, respectively.

The conclusion, absorption properties that are detected in the UV-*vis* spectrum are heavily influenced by the concentration of nanoparticles that are present in the nanofluid. Because there are more particles available to interact with light, absorption peaks tend to be stronger when there are higher amounts of nanoparticles. This can be verified from

Figure 3.4, as the concentration increases from 0.5wt % to 1.5wt % (for 0 days), the peak increases. UV-vis moreover provide the stability of a nanofluid. A stable nanofluid will typically exhibit a distinct and consistent absorption peak over time, whereas instability may cause this peak to migrate or vanish as a result of nanoparticle aggregation. Hence, in 30 days absorbance, there peak is higher for 1.0 wt% than its counterpart due to its stability, indicating a more stable nanofluid.

3.3.2. Hydrate formation experiments

3.3.2.1. Effect of nanofluids on the phase stability of methane hydrate

Hydrogen-Vapour-Liquid Equilibria, abbreviated as HVLE, is a term that describes the equilibrium that exists between the gas phase (vapor), the liquid phase, and the hydrate phase in systems that contain water molecules and gas molecules. HVLE is a system that typically consists of three phases: the hydrate phase, the liquid phase, and the vapor phase. The equilibrium describes the balance between the formation and dissociation of hydrates, as well as the coexistence of gas and liquid phases. This equilibrium is important for understanding and controlling hydrate formation.

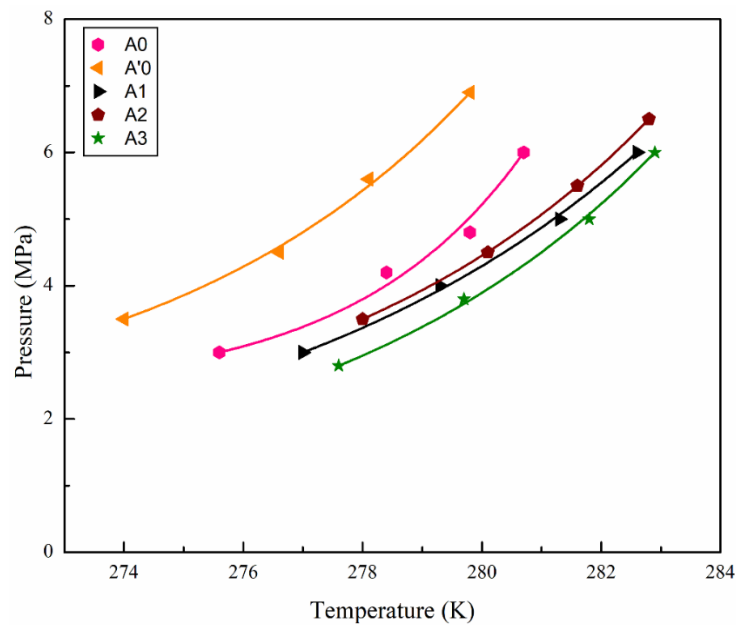


Figure 3. 5: HVLE curve of various synthesized nanofluids along with pure water and pure

ethylene glycol

Figure 3.5 explains the hydrate-vapor-liquid equilibrium (HVLE) diagram. The hydrate phase equilibrium curve is a graphical representation that shows the boundary conditions (temperature vs. pressure) within which gas hydrates can exist in equilibrium, i.e., the conditions under which gas hydrates can form or dissociate. This phase diagram is essential to explain the hydrate zone vs the non-hydrate zone. For gas hydrates to form and remain stable, high-pressure and low-temperature conditions are typically required. Above the curve (at lower temperatures or higher pressures), gas hydrates are stable, and below the curve (at higher temperatures or lower pressures), gas hydrates are unstable and dissociate into gas and water. In the presence of an inhibitor, the phase equilibrium curve shifts toward low-temperature and high-pressure regions, reducing the hydrate stable zone. As the nanofluid is introduced inside the system, the HVLE curve shifts towards higher temperature, increasing the hydrate stable zone and hence promoting the hydrate formation. Figure 3.6 depicts the pressure and temperature profile for various samples (ethylene glycol, pure water and 100% nanofluids).

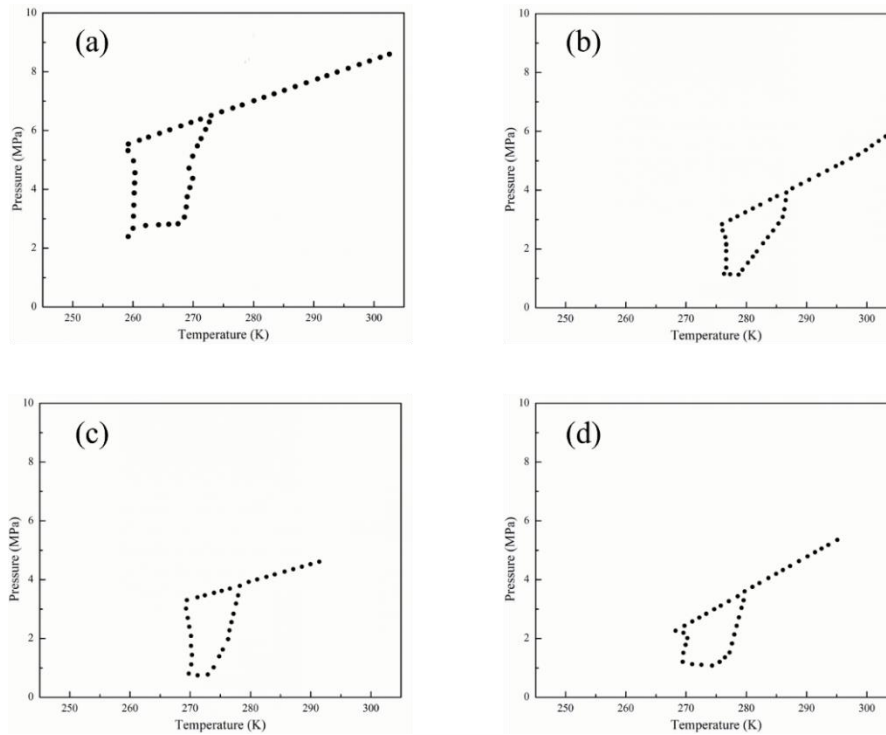


Figure 3. 6: P-T cycle curves obtained in the presence of varying compositions (a) pure ethylene glycol, (b) 0.5 wt% nanofluids, (c) 1.0 wt% nanofluids, (d) 1.5 wt% nanofluids

In conclusion, the hydrate equilibrium curve is crucial for understanding the conditions under which gas hydrates form and remain stable, which is particularly important in the context of gas hydrate research, CH₄ storage, and energy production. The nanofluid inside the aqueous solution plays an important role in changing the phase equilibria. The mechanism can be explained as the pure nanofluids help in better heat and mass transfer due to the presence of the nanoparticles. In addition, due to its high surface area, it provides hydrate molecules for accumulation. The presence of nanoparticles in the system affects the interaction between gas and nanoparticles by shifting the equilibrium temperature and pressure.

3.3.2.2. Impact of nanofluids on the methane hydrate induction time

By utilizing nanofluids, the amount of time needed to induce methane hydrate can be reduced, which is of great relevance in terms of the practical implications of this development. Increased hydrate production can aid methane storage and transit, which

could lead to denser and more secure storage solutions, which is good news for natural gas transportation. An increase in the pace at which methane hydrates are produced can be facilitated through the utilization of nanofluids in carbon capture and storage (CCS). Because of this, it would be possible for CH₄ and other greenhouse gases to be absorbed and stored in geological or undersea rocks. The utilization of nanofluids may also lead to the development of processes that are more efficient inside energy storage systems that are based on hydrates.

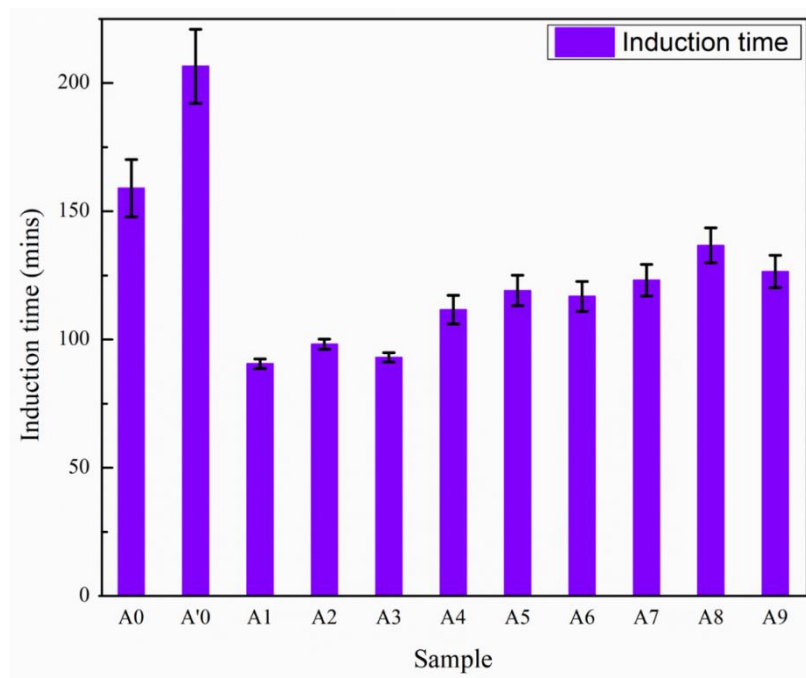


Figure 3. 7: Methane hydrate induction time for various synthesized samples

Figure 3.7 shows the methane hydrate induction time for different systems with the nanofluids (for nomenclature, please see Table 3.2). The experimental temperature and the injection pressure were kept at 278.15 K and 6.0 MPa, respectively. Out of all the systems with nanofluids and different combinations of ethylene glycol and nanofluids, the sample containing 1.0 wt% indicates a better performance than their counterparts. For pure water, the induction time is 159 mins. As the nanoparticle increases in the aqueous phase, the induction time reduces. A1 (0.5 wt%) has an induction time of 90.6 mins. Sample A2 (1.0 wt%) exhibits 98.2 minutes induction time. A3 (1.5wt%) has 93 mins induction time. It is

observed that there is a reduction in 43%, 38.2%, and 41.5% in samples A1, A2, and A3 as compared to A0. For pure ethylene glycol aqueous phase (sample A'0), the induction time was found to be 206.5 mins. The nanoparticles, because of their size, have a higher thermal conductivity. This thermal conductivity helps in better heat transfer within the system, resulting in faster hydrate formation. Moreover, due to the presence of nanoparticles, the nucleation site for hydrate formation inside the system increases. This increase in nucleation ultimately increases the mass transfer. Hence, by combining both mass and heat transfer of these nanoparticles, the induction time was reduced, forming a faster hydrate. Several experiments were conducted to verify that these nanofluids help reduce the induction time. A4, A5 and A6 correspond to different

Samples A4, A5, A6, A7, A8, and A9 have induction times of 111.6 mins, 119.1 mins, 116.8 mins, 123.3 mins, 136.7 mins, and 126.5 mins, respectively. The results indicate that the average induction time is best for 1.0 wt%. So, it can be stated that the optimum concentration for this SiO₂ nanofluid is 1.0 wt%. After optimum concentration, nanoparticles tend to agglomerate, resulting in fewer nucleation sites and less surface area to form hydrate. In conclusion, nanofluids have an effect on the amount of time it takes to induce methane hydrates by increasing the pace of heat transfer, promoting gas dispersion, and stabilizing the formation of hydrates. The incorporation of nanoparticles into the base fluid has the potential to accelerate the formation process, resulting in a reduction in the induction time. This finding has the potential to be advantageous in a variety of industrial applications, including natural gas transportation, carbon capture and storage, and energy storage systems.

3.3.2.3. CH₄ consumption during hydrate formation

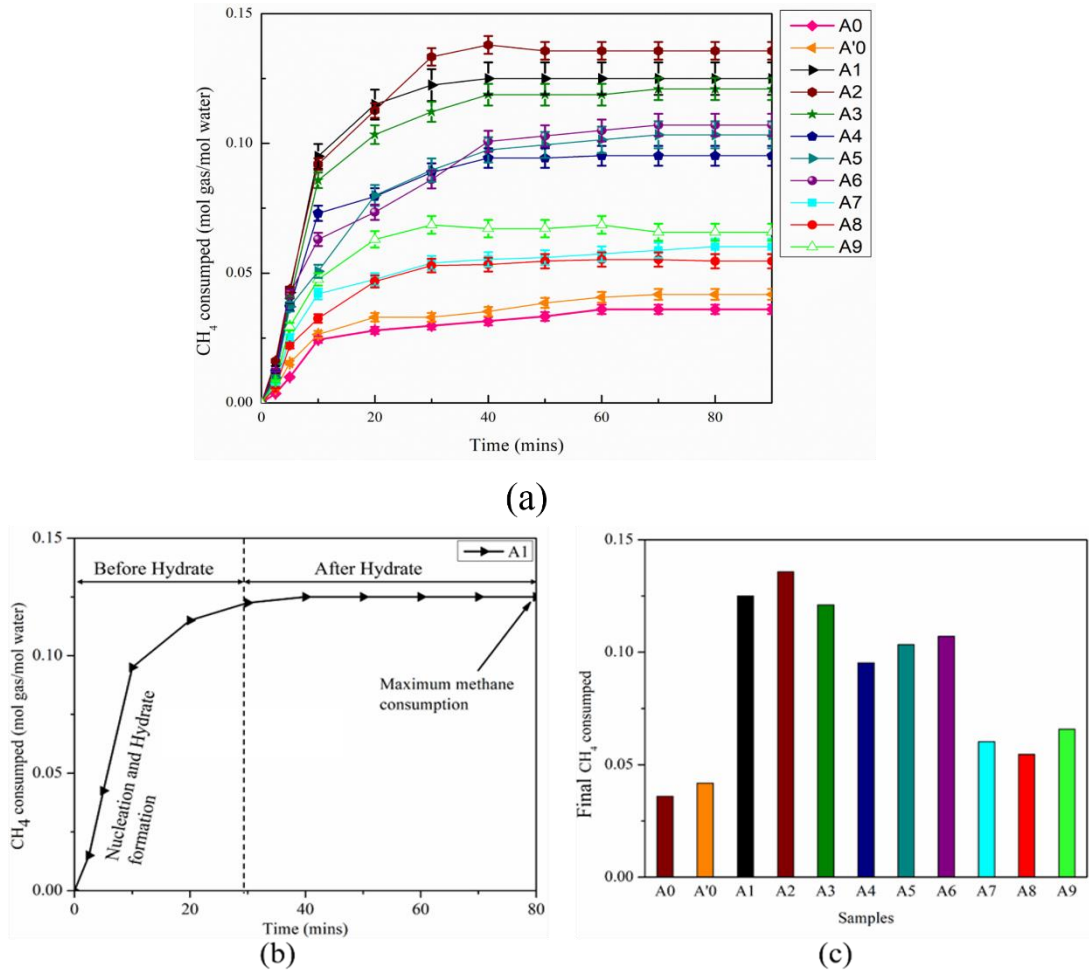


Figure 3. 8: CH₄ gas consumption during hydrate formation for different samples

The temperature and pressure were maintained at 278.15K and 6.0 MPa at 500 rpm.

The following equation is used to calculate the moles of CH₄ consumed in hydrate formation [196,197],

$$\Delta n_{CH_4} = \frac{1}{R} V \left(\frac{P_0}{Z_0 T_0} - \frac{P_t}{Z_t T_t} \right) \quad (3.1)$$

where R is the universal gas constant, P₀, and T₀ are the reactor's initial pressure and temperature, P_t, and T_t are the reactor's final pressure and temperature. Compressibility is given by Z₀ and Z_t (calculated by the Peng-Robinson equation), and V is the gas phase volume.

Figure 8 indicates both the trend and amount of methane consumption during the hydrate

formation in the aqueous phase of a solvent. The pressure and temperature data were recorded every 20 s, and hence, methane consumption was calculated after every 20 s till the entire duration of 80 min. It is evident from Figure 3.8 that as the concentration increases, the gas consumption of methane increases. As explained earlier, the presence of nanoparticles in the nanofluids helps in faster hydrate formation. The gas consumed is plotted after the induction times. It can be seen that after the induction time, the gas consumption increases rapidly. This is due to the hydrate formation as soon as the induction time. There is a rapid entrapment of gas inside the hydrate structure. As time goes on, consumption reaches a constant level. This indicates that no more hydrate formation occurs. Hydrate forms within the initial 10 minutes after reaching the induction time. The max mole consumption is observed in 1.0 wt% (A2) of 0.0.135. For pure water, the mole consumption was 0.036. The mole consumption for pure ethylene glycol was calculated to be 0.0418. It is more than 16.13 % of pure water. The gas consumption was 0.125, 0.135, and 0.121 for pure nanofluid samples for A1, A2, and A3. Compared to pure water, there is an increase of 247.2 %, 275.0%, and 236.1%. The mole consumption is 0.095, 0.103, and 0.107 for samples A4, A5, and A6. Adding ethylene glycol and nanofluid has increased the gas consumption in the hydrate as compared to pure water. In comparison to pure water, methane consumption increases by 164%, 186.1%, and 197.2%, respectively. Samples A7, A8, and A9 had corresponding mole consumptions of 0.060, 0.054, and 0.065 moles. Figure. 3.8 (b) shows the typical trend of methane consumption as a function of time for sample A1. Initially, at the beginning of the experiment, the methane consumption was zero. As the stirrer forced methane diffusion into the aqueous phase, the rate of consumption increased. The amount of methane consumption further increased with the development of the hydrate in the system. Finally, the methane consumption showed a plateau, which indicated the saturation limit of methane consumption in the hydrate. In this

case, after 28 min (Figure 3.8b), sample A1 showed no change in methane consumption. The total amount of methane consumed by different samples is shown in the Figure. 3.8c, where A1-A3 samples exhibited a superior impact on the amount of methane consumption in a hydrate.

When hydrate forms, it releases heat (exothermic reaction). Hence, if nanoparticles are present in the aqueous solution help in dissipating the heat, enhancing faster hydrate formation. Numerous nucleation sites where hydrate develops are also a result of the aqueous solution's heterogeneous composition. Nanoparticles boost the driving force during hydrate formation, resulting in a greater mole consumption. As already explained earlier, due to the higher surface area of nanoparticles, the mass transfer rate increases between liquid and gas inside the reactor.

3.3.2.4. Rate of hydrate formation

The equation used to calculate the rate of hydrate formation $r(t)$ is given by A Mohammadi. [198].

$$r(t) = \frac{n_{CH_4,i-1} - n_{CH_4,i+1}}{(t_{i+1} - t_{i-1}) n_{W_0}} \quad (3.2)$$

where $n_{CH_4,i-1}$ is the amount of mole methane in the gas phase at t_{i-1} time. $n_{CH_4,i+1}$ is the mole amount of methane in the gas phase at t_{i+1} time. The real gas equation calculates the number of methane moles. n_{W_0} is an initial mole of water. Figure 3.9 illustrates the formation rate. Similar to the mole of gas consumption, the formation rate is calculated after accounting for the induction time. As soon as induction times reach, hydrate starts to form. The gas, which is in a free state, starts to get trapped inside the hydrate [184]. The hydrate formation is completed in the initial 15-20 minutes after reaching the induction time. It is evident from the figure that there is a rapid formation rate initially, and then the rate of formation decreases over time. Nanofluid inside the system helps in faster hydrate formation, which promotes gas initial gas consumption. For water, the initial consumption

rate is 0.01 mol of gas/mol of water/min. For nanofluid, it is found to be 0.017 mol of gas/mol of water/min (0.5wt%), 0.026 mol of gas/mol of water/min (1.0wt%), and 0.022 mol of gas/mol of water/min (1.5wt%). For ethylene glycol, the rate is 0.009 mol of gas/mol of water/min. There is an increment of 70 % (0.5wt%), 160% (1.0wt%), and 120% (1.5wt%) over DI water's rate. The consumption rate also increases to 62 % (A5 sample), 60 % (A6 sample), 70 % (A7 sample), 80 % (A8 sample), and 65 % (A9 sample). As a result, a higher concentration of nanofluids promotes faster hydrate.

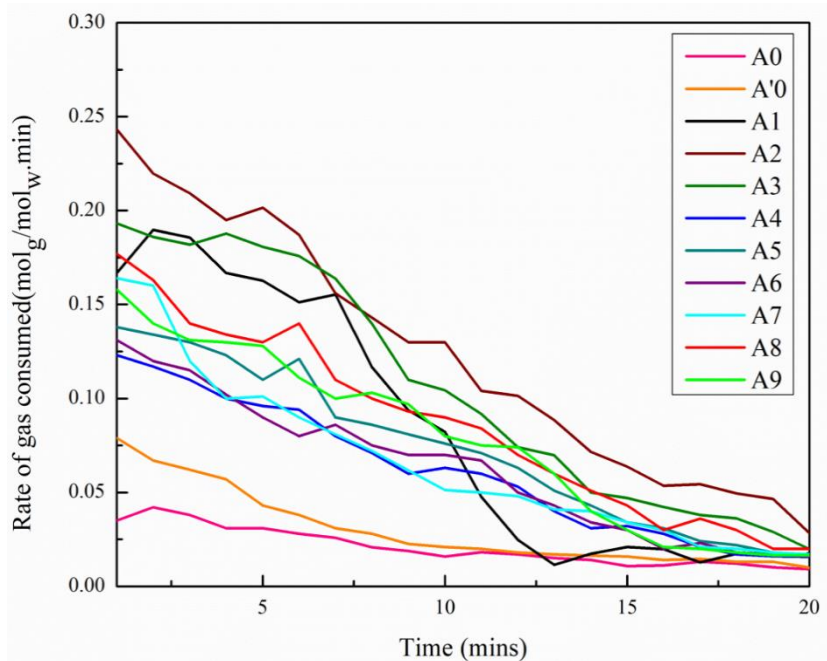


Figure 3. 9: CH₄ hydrate formation rate for various samples

Due to their nanoscale size, these nanoparticles are highly dispersed within the aqueous solution, covering a larger surface area and promoting nucleation. These nanoparticles' excellent thermal conductivity facilitates effective heat and mass transmission, which speeds up induction times and improves formation kinetics. Additionally, the nanosized of the nanoparticles makes it easier for tiny gas bubbles to develop all throughout the solution, which in turn increases the gas diffusivity at the interface. As the diffusivity of the gas rises, the rate at which the gas is consumed also increases

3.3.2.5. Methane storage capacity

The volume of gas contained within the solid hydrate structure is its storage capacity in the hydrate phase and is given by [174,199].

$$SC = \frac{\frac{\Delta nRT_{STP}}{P_{STP}}}{V_H} \quad (3.3)$$

STD is the standard condition V_H is the volume of gas hydrate at the end of the reaction. The amount of gas trapped under standard conditions is known as storage capacity. Figure 3.10 shows the storage capacity of the methane hydrate.

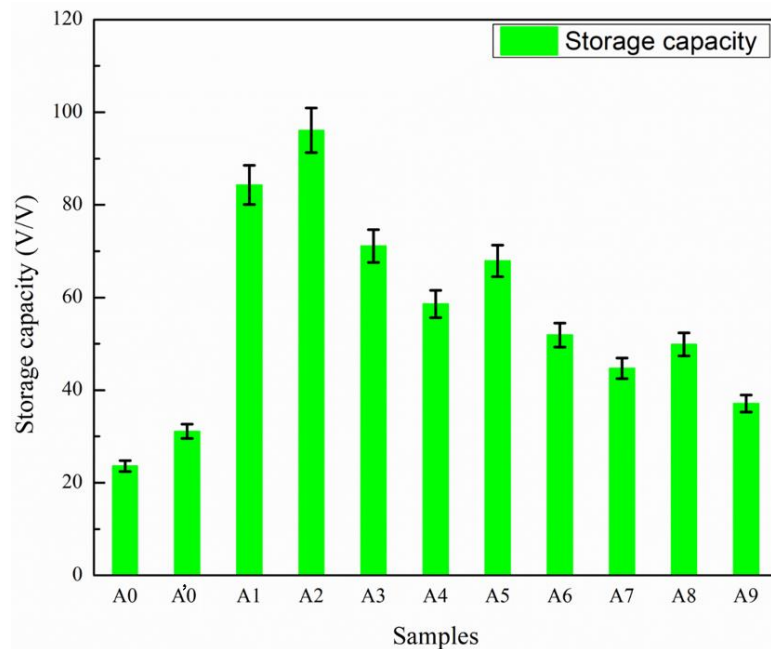


Figure 3. 10: Methane storage capacity of different hydrates promoter formulations at 6.0 MPa and 278.15 K

SC of methane hydrate for pure water is 22.2 v/v. For the ethylene glycol system, the SC is 31.1 v/v. The system with nanofluid has 84.3 v/v (A1), 96.1 v/v (A2), and 71.1 v/v (A3). In comparison to pure water, there is an increment of ~280 % for A1, ~332 % for A2, and ~220 % for A3. Hence, this can be said that a concentration of 1.0 wt% of NPs has a greater ability to store CH₄ than the other samples. In comparison to pure water, this data confirms that the nanoparticle in the aqueous solution holds more gas. Therefore, it may be

concluded that NPs enhance the gas hydrate's kinetic characteristics. In addition, the system having both nanofluid and ethylene glycol has a better SC than pure water. Sample A4, A5, A6, A7, A8, and A9 have SC of 58.6 v/v, 67.9 v/v, 51.9 v/v, 44.7 v/v, 49.9 v/v, and 37.1 v/v. The nanoparticle inside the nanofluids helps in better storage and faster hydrate formation. The optimum concentration of the nanoparticle helps in the uniform distribution of the nanoparticle in the aqueous phase.

3.3.3. Future scope of the work

There is significant potential for the application of nanoparticles in gas hydrate research and applications. Gas hydrates are crystalline compounds that combine water with gas, typically methane or other lower hydrocarbons. They exist in subsea environments and permafrost areas, where they have been considered and presented both as an energy resource and a problem that creates instability, is difficult to extract, and poses a risk to the environment. Nanoparticles, with unique properties such as small sizes and large surface areas, therefore, provide opportunities to counter the challenges and problems associated with gas hydrate formation, extraction, and stability. Nanoparticles could be used as nucleation sites and, thus, may facilitate the production of gas hydrates. In this way, incorporating nanoparticles into a system may make it possible to control the development rate and the structure of crystals of hydrates. It could be extremely useful for artificial methods for producing hydrates for energy storage or CO₂ sequestration. Nanomaterials might also be developed for novel methods of storing and transporting gas hydrates. These materials could stabilize hydrates, making them easier to transport and store at ambient conditions. This opens new possibilities for using gas hydrates as a medium for energy storage and transportation. Possible new ways to store and transport gas hydrates might be made possible by nanomaterials. Gas hydrates might be stored in more practical forms, including transportable solid-state containers, if nanoparticles stabilize them under milder

circumstances. In areas without conventional power grids, such as offshore or in isolated areas, gas hydrates may become a more attractive energy storage alternative.

3.4. Conclusion

This study examined the kinetic characteristics of methane hydrate production (induction time, SC, and growth rate) in an autoclave stirrer reactor using SiO₂ nanofluid of different concentrations, ethylene glycol, and a combination of ethylene glycol and nanofluid. According to the findings, the employment of the evaluated additives significantly reduced the amount of time required for the formation of methane hydrate. The investigation of methane uptake over 0–215 minutes at 278.15 K and 6.0 MPa indicates that the addition of nanofluids and a mixture of ethylene glycol and nanofluids significantly enhances methane uptake compared to pure water. Methane consumption increases by 275% compared to pure water when 1.0 wt% SiO₂ is added, consistent with reports in the literature [200]. Additives that have been evaluated affect the amount of methane consumption that is comparable to their effect on the storage capacity. Pure ethylene glycol shows an induction time of 206.5 minutes. It is also observed that as the concentration of nanofluid increases the kinetic parameters increase. Increasing the nanofluid dosage from 30 mL to 50 mL of 0.5 wt%, 1.0 wt%, and 1.5 wt% decreases the induction time by 9.2%, 12.9%, and 7.6%, respectively, which is the same as previously reported findings [201]. Similarly, there is an increment of 21%, 47% and 23% respectively for the mole of gas consumption (30mL nanofluid to 50mL nanofluid). It is also observed that the rate of gas consumption is higher for all the pure nanofluid samples. For pure nanofluid 0.5 wt%, 1.0 wt%, and 1.5 wt%, the rate of consumption was found to be 231.4%, 564%, and 451% respectively in comparison to water. Pure nanofluid samples also have an increased storage capacity as the concentration rises. It was calculated to be 84.3, 96.1, and 71.1 v/v for pure samples. As the concentration of the nanofluid increases, storage capacity also increases.

From 44.7 v/v (30 mL) to 58.6 v/v (50 mL) for 0.5 wt% i.e. increment of 31%. Similarly, an increase of 36% for 1.0 wt% and 39.9% for 1.5 wt%.

Chapter 4: Effect of Single-Step Silica Nanofluid on Thermodynamic and Kinetics of Methane Hydrate Stabilized by Conventional Promoter

Abstract

Stable synthesis of methane hydrate is the best technique to store an ample amount of methane during storage and transportation. However, the use of a conventional promoter is limited by marginal improvement in the kinetics of hydrate, which can be addressed by the use of solid particles synthesized by a single-step technique. Single-step facilitates control on the size of synthesized NPs, which is not possible with the two-step technique or commercial NPs. Thus, in this study, a single-step technique was used to synthesize silica nanofluids of different NP size (5-100 nm) and concentration (0.5-2 wt%) and compared their impact on the kinetics of hydrate, stabilized by conventional surfactant, CTAB. Nanofluids exhibited superior stability with zeta-potential in between -36 to -48 mV. Properties such as mole consumption, gas consumed, rate of gas consumed, and apparent rate constant were studied at 6 MPa and two test temperatures: 274.15 and 277.15 K. NP offered significant improvements in kinetic properties of CTAB based hydrates resulting induction time improved by 56% while mole of gas consumption and apparent rate constant increased by 88.4% and 184% with NP inclusion of 1.5 wt% at 274.15 K. With increase in test temperature by 3 K, these properties marginally reduced at 277.15 K however remained 36.84% higher (in storage capacity) than that of conventional CTAB. NP concentration of 1.5 wt% was found to be optimum in hydrate stabilized by solid particles, as further NP addition showed reverse behaviour and was considered uneconomical, as evident from the results of sample composition of 2 wt% SiO₂. It is in addition important to highlight that the single-step technique is able to synthesize NP of desired size, which is difficult to achieve with the two-step technique, where particles are

externally procured, followed by mixing with intensive energy. The insights of the study are extremely useful for the use of promoters in effective energy storage during transportation.

4.1. Introduction

Gas hydrate is a solid ice-like crystalline substance in which methane is trapped inside a cage-shaped crystal. This makes hydrate an unconventional source of energy, which typically exists at the condition of low temperatures and high pressures. Apart from energy resources, hydrate can also be used for cost-effective storage and transportation of natural gas, as one unit of volume can store 164 units of methane, which is significantly higher than any form of storage [202]. There are three types of hydrate structures *viz.*, structure I(sI), structure II(sII), and hexagonal structure (sH)[4] in which guest molecules (CH₄, C₂H₆, CO₂, and N₂ *etc.*) are typically trapped within a cage built from hydrogen bonds of the host molecule (water). Since the energy demands are rapidly increasing on a global scale, an imbalance in the supply of continuous and clean energy is evident, which will moreover impose a significant burden on current greenhouse gas emissions. Thus, it becomes imperative for the scientists/industrialists to focus on finding alternative solutions for reducing these emissions, along with a constant supply of energy. Natural gas is known as the cleanest fossil fuel, in great supply in nature [203,204], having much less effect on the environment when burned. The other methods (compressed natural gas, liquified natural gas, and adsorbed natural gas) of natural gas storage and transportation are not effective on a large scale, which leaves no choice however to store and transport natural gas through hydrate. During hydrate formation, the primary hurdle is the slow rate of formation and lower gas consumption. These problems usually arise due to irregular heat and mass transfer during the formation and dissociation of the hydrate. The high stirring rate influences the rate of heat and mass transfer, which often promotes the reaction of hydrate

formation. An increase in turbulence, caused by high stirring, affects mass transfer at the gas-liquid interface, which helps in hydrate formation [205]. With an increase in heat and mass transfer, gas enters the water molecule cavity, which causes a significant change in temperature between the cooling bath and the crystallizer, resulting in faster formation of hydrate. Additionally, stirring can quicken the nucleation of hydrates by shortening the induction time that accelerates the hydrate formation [205]. Hence, stirring significantly affects the development of gas hydrates, and enhancement in mass and heat transfer is the primary requisite for the promising use of promoters in hydrate formation or inhibitors in case of dissociation [206]. These challenges need to be addressed for gas hydrate to be a viable technology in the sustainable supply of future energy, especially for the area of bulk storage and transportation of natural gas, when liquefaction technology is not feasible. In addition, it has been found that a slower rate of hydrate formation is another important hurdle in effective and faster transportation of natural gas, which can be improved through the inclusion of a suitable promoter. The promoters are moreover referred to as thermodynamic and kinetic promoters, which mechanistically target phase equilibrium conditions of gas hydrate, followed by their shift towards moderate pressures and ambient temperature [207]. The role of a kinetic promoter is appreciated by the increase in the rate of hydrate formation with a simultaneous decrease in the time required for the growth of crystals [186].

In literature, several methods such as agitation [208], spraying [209] and bubbling [210] have been reported to enhance the rate of kinetic and thermodynamic, however they are very expensive for commercializing at an industrial scale. Therefore, chemical methods can be an alternative to these methods, where different chemicals can be used to alter the promotion of the hydrate structure. Various chemicals like tetrahydrofuran, acetone, 1,4-dioxane, tetrahydropyran, tetra-n-butyl ammonium halides, cyclopentane, and cyclohexane

have been reported in the literature for promoting hydrate formation [211,212]. The main advantage of the chemical method over other processes is moreover cost-effectiveness. The impact of different geometries, which are the sources of stirring, is moreover important for the rate of hydrate formation, stability of hydrate, and storage capacity in a hydrate [213]. In literature, different geometries such as pitched blade and paddle stirrers were used for the hydrate experiments [213]. The results indicated that paddle and pitched blade stirrers, at 300 rpm, provided Reynolds numbers of 3101 and 3740, respectively. The impact of axial and radial flow patterns, produced by these stirrers, is also investigated for hydrate experiments. DuQuesnay et al. [205] explained a novel hydrate reactor design in which hydrate formation occurred faster than in the conventional reactors. Stoporev et al. [213] explained the impact of reactor material on the hydrate process; the steel reactor suggested hydrate formation in 32.7 min, while it took 55.3 min for the glass reactor. Gootam et al. [214] modelled hydrate growth in a stirred tank of two different reactors (overhead and bottom-mounted stirrers), where the top-mounted stirrer demonstrated a faster onset of reaction and more methane absorption. The mole of water consumed to form a hydrate for the top stirrer was 200% more than bottom bottom-mounted stirrer. Linga et al. [215] have illustrated the use of a gas-inducing impeller for hydrate formation. In comparison to regular laboratory apparatus, this novel apparatus enhances the gas/water interaction, leading to a considerable increase in gas uptake during hydrate crystallization. Similarly, surfactants have received significant attention in hydrate formation, and the most common surfactant, which works as a kinetic promoter, is sodium dodecyl sulfate (SDS) [216]. Surfactants can additionally facilitate a reduction in surface tension of the aqueous phase, which mechanistically results in a higher rate of mass transfer from gas to aqueous phase. According to Yoslim et al. [217]. SDS decreased the induction time, resulting gas storage capacity increased by 14 times that of pure water. Like SDS, cationic surfactant *e.g.*, CTAB

[218] was also used in hydrate promotion experiments. Ganji et al. [216] have illustrated that CTAB is a good promoter in hydrate formation, and their results indicated that 1000 ppm CTAB showed better performance. Pahlavanzadeh et al. [186] studied the effect of CTAB along copper NPs, where CTAB with a higher concentration offered more impact on the hydrate formation process. However, these surfactant-based promoters were toxic in nature when used in larger quantities as demonstrated [219]. Therefore, their usage should be minimal, and the remaining effect should be compensated for by the use of another suitable promoter.

Adding a nanoparticle (NP) is one of the solutions to improve the performance of conventional hydrates [218]. NPs can enhance the rate of heat and mass transfer at the solid-liquid interface of hydrate and create appropriate conditions for heterogeneous nucleation [178]. To increase rate of hydrate formation, Sloan and Koh [16] and Zhou et al. [185] verified that graphite NPs were superior thermodynamic and kinetic promoters in decreasing induction time by 80.8% to pure water. The impact of copper NP on HFC-134a hydrates was explored to address heat and mass transfer issues during formation and dissociation of hydrate [181]. The effect of carbon nanotubes (size = 15 nm) on the volume of gas stored and induction time was presented by Park et al. [177], who highlighted that the volume of gas stored increased by 300%. Additionally, the induction time exhibited a significant decrease of 52%, which was only 14% with the CTAB-based promoter. A significant increase in the heat transfer rate of water was observed when copper oxide NPs of size 40 nm were used [180]. Their inclusion moreover facilitated faster hydrate formation with an increase in mole consumption as well as storage capacity. For the stable growth of CO₂ hydrates, the effect of iron oxide NP (size = 40 nm) was investigated on SDS-stabilized hydrates [220], and the results demonstrated a significant decrease in induction time (70%) along with greater (by 160%) consumption of moles. Su et al. [221] have studied the effect

of coated surfaces on hydrate formation and its properties. The author has compared three surface coatings, namely PTFE/PPS composite, epoxy resin E-51, and polyurea, on hydrate formation. The results showed that the PTFE/PPS composite coating provided more resistance to hydrate development in the pipeline. Particularly at lower sub-cooling circumstances, both polyurea and epoxy resin E-51 coatings showed some resistance to hydrate adherence. Filarsky et al. [222] have investigated the effect of modified silica beads on hydrate formation, where untreated glass beads of diameter 1.15 mm showed faster hydrate formation. The hydrate formed within the first 100 min with a water-to-hydrate conversion ratio of 71.67%. The impact of the glass surface on the morphological characterization of hydrate was presented by Beltran and Servio [223]. It was discovered that initial nucleation occurred on the periphery film; however, second nucleation took place on the water's edge. Em et al. [224] developed a special surface-active coating for hydrate promotion *via* investigation on kinetic and gas storage capacity results of hydrate. In this study, three distinct silanes with progressively longer carbon chains were explored. The silane decreased the surface tension. Additionally, it created a gas-enriched layer that promoted the production of hydrate. Em et al. [224] moreover demonstrated the formation of methane hydrate in the presence of halloysite clay nanotubes. These results indicated more hydrate formation in pores smaller than 10 nm than in their larger counterparts. In addition, up to 70% water-to-hydrate conversion was observed within 3 h in the pores smaller than 10 nm. Silica sand particles of 329 μm were used for hydrate formation, where sand particles facilitated a 74-78.5% increase in water-to-hydrate ratio [225]. Esmail and Beltran [226] demonstrated the impact of varying surface wettability on methane hydrate propagation. Three surfaces *e.g.*, glass, sapphire, and polyvinyl chloride, were used, and the glass surface exhibited lower wettability as compared to both sapphire and polyvinyl chloride during hydrate formation. The research findings of Arjang et al. [178] and

Dongliang et al. [183] demonstrated that hydrate will form faster and quicker in the presence of a suitable dispersant, such as silver nano-silica of 75 nm and carbon nanotubes of 20 nm. Their presence in the hydrate scheme can considerably increase methane hydrate yield and rate of heat transfer, respectively. The role of L-Arginine (as promoter) was investigated in the hydrate scheme of methane-tetrahydrofuran system [227]. One of the main conclusions from these research works pointed high surface energy of NPs as an important trait in the promotion of gas hydrate. However, the use of solid NPs is always associated with their tendency to agglomerate, followed by settlement after a certain period. Therefore, it is important to keep NPs stable against agglomeration and settlement, which is difficult to obtain when NPs are mixed externally [228,229]. Thus, the novelty of this research work lies in the utilization of NPs, which originate within in aqueous phase through the addition of suitable precursor and accelerator under adjusted pH, temperature, and drying conditions. Single-step method facilitates the development of size-controlled, independent, and agglomeration-free NPs, which will help in more heat and mass transfer. On the other hand, the two-step method will require intensive energy to break agglomerated NPs into smaller particles; thus, the single-step method simplifies the synthesis procedure.

As far as we are aware, the single-step method has not been investigated in thermodynamic and kinetic studies of surfactant-based gas hydrates. Thus, we report the role of single-step based silica nanofluids of different concentration (0.5-2 wt%) and size (5-100 nm) on the kinetics of hydrate stabilized by conventional promoters such as CTAB. The parameters, such as moles of gas consumption, storage capacity, and apparent rate constant, were determined at two test temperatures (274.15 and 277.15 K) and 6 MPa and the results are suitably compared to promote single-step nanotechnology in hydrate formation for storage and transportation applications.

4.2. Materials and methods

4.2.1. Materials

Chemicals *viz.*, cetyltrimethylammonium bromide, tetraethylorthosilicate, ethanol, and ammonium hydroxide, were supplied by Sisco Research Laboratories Pvt. Ltd., India. Polyacrylamide (PAM) was supplied by Sigma Ltd., India, and it was used as received during the synthesis of the nanofluid as a base solution. Ethanol was purchased from Changshu Hongsheng Fine Chemical Ltd., China. Digital weighing balance (Mettler Toledo, ME204/A04; repeatability approximately 0.01 mg) was used to measure the weight of chemicals. The synthesis of all aqueous solutions and base solution for nanofluid was done using deionized (DI) water, obtained from laboratory laboratory-installed Millipore[®] Elix-10 water purification apparatus. For CH₄ availability, a stainless steel cylinder (Purushottam gas suppliers, India), equipped with a pressure regulator, was used.

4.2.2. Nanofluid preparation and characterization

A single-step silica nanofluid was used in this study, where NPs were prepared using the standard sol-gel method. The details of nanofluid preparation using a single-step route are also provided in our previous works [229]. However, some details are moreover provided in this study for brevity. To prepare the nanofluid, a base solution of 1000 ppm PAM was prepared after mixing 1 g of PAM powder in 1000 mL of DI water. Next, a certain amount of 20mL of ethanol was taken in a beaker and kept on a magnetic stirrer (MS-H280-Pro, procure from D-Lab) with a stirring speed of 800 rpm. PAM solution of the required amount 80mL was added drop-wise with the help of a dropper while the stirring was kept on for 200 min. Next, TOES of 3 mL was added drop-wise into the solution. After 500 min of stirring, ammonium hydroxide was added and the solution was stirred for a further 200 min. The development of silica NPs was confirmed by the appearance of white precipitate inside the beaker. In addition, an aqueous phase of 300 ppm was prepared by mixing 0.3

wt% CTAB powder in 1000 mL of PAM solution. A CTAB solution was prepared to compare its performance with surface-active nanofluid and establish single-step nanotechnology as an effective promoter in hydrate development.

In addition, the development of NP was confirmed by the dynamic light scattering (DLS) method, and for that, a zeta sizer (SZ-100, Horiba Scientific, Singapore) was used. To visualize NP distribution in the bulk phase, scanning electron microscope (SEM) images were captured using a JEOL-based instrument (JSM-7900F). For SEM images, a glass slide was covered with a drop of nanofluid and dried in a lab oven at 70 °C for SEM investigation. This was necessary to remove any liquid or moisture from the nanofluid, which left a dry impression of solid NPs on the glass slide.

4.2.3. Experimental set-up and hydrate preparation

The syringe pump, water bath, and experimental setup of hydrate were procured from an Indian manufacturer: D-CAM Engineering, Ahmedabad. Figure 4.1 shows a schematic diagram of the entire setup used for the synthesis of hydrate and for the determination of different kinetic parameters such as induction time, moles of gas consumption, apparent gas constant, rate of gas consumption, and storage capacity. The system moreover includes a temperature and pressure sensor, high high-pressure autoclave, and a data acquisition system. The reactor of the equipment was made of SS316 with a volume of 250 mL, where operating temperature and pressure of the reactor range from 260 to 375 K and 0.5 to 120 MPa, respectively. The autoclave was 12.75 cm in height and had a diameter of 5 cm with a volume of 250 mL. The blade, used in this stirrer, was a pitched blade exhibiting four blades with a diameter of 4 cm. The height of the stirrer was 9.75 cm. The volume of aqueous solution was 130 mL (height = 6.63 cm), where the remaining volume (120 mL, height = 6.12 cm) was occupied by methane gas. In literature, geometric studies on stirrers have been explored by Filarsky et al. [230]. The geometry of the stirrer helps to explain the

flow condition using a dimensionless parameter, the Reynolds number. Reynolds number is calculated with the help of Eq. 4.1, where N is the rotation frequency (1/s), d is the diameter of the stirrer (m), and ν is the kinematic viscosity of water (m^2/s)

$$\text{Reynolds no.} = \frac{N \times d^2}{\nu} = \frac{8.33 \times 0.04^2}{1.61 \times 10^{-6}} = 8278 \quad (4.1)$$

The rpm carried out in this experiment was 500. Hence, the Reynolds number for turbulent flow in DI water was determined as 8278. In addition, Reynolds no of 94475 was calculated for the gas phase at 274.15 K. Reynolds number is a dimensionless number and it is used to understand the amplitude of turbulence. A higher value of the Reynolds number is the result of an increase in the initial rate of hydrate development [205]. In addition, it is difficult to calculate the Reynolds number with a hydrate in the system, as the viscosity of aqueous media is not well-defined. Therefore, it is to be noted here that Reynolds no is subjected to change during the hydrate experiment as viscosity varies with hydrate formation [215]. The sensor, which was used to measure temperature, consisted of two platinum (Pt100) resistance sensors with an accuracy of +/- 0.01 K. Similarly, the pressure sensor model (HD20V4T, Delta Ohm, Italy) exhibited an accuracy of ± 0.01 MPa.

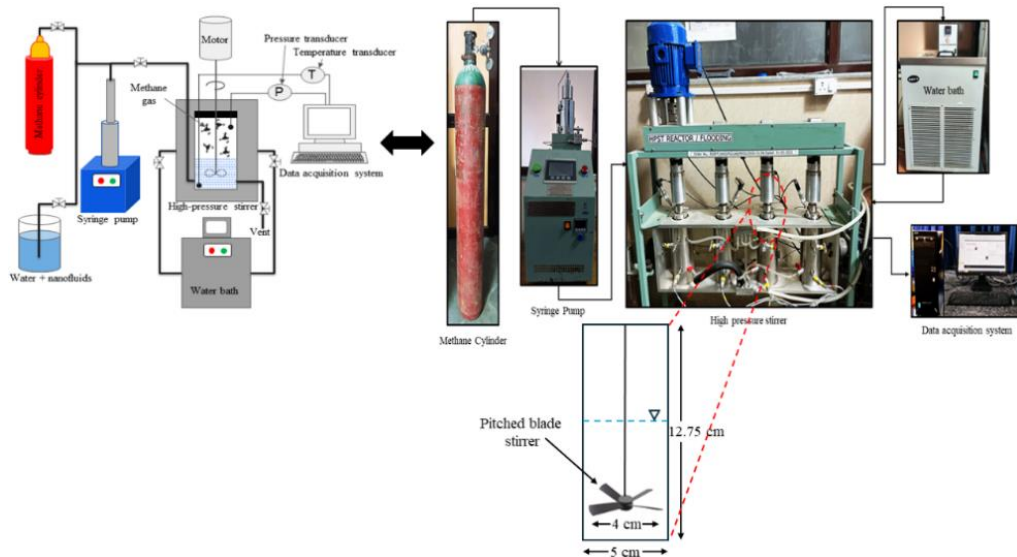


Figure 4.1: Experimental set-up of gas hydrate (actual and schematic), along with essential accessories to record and monitor the progress of the process. The details of stirring geometry are also shown, with important dimensions of the cell and the stirrer

Before each experiment, the reactor was first washed with DI water, followed by thorough cleaning with solvent ethanol. For residual particles, we made sure to clean every part of the reactor repetitively, followed by drying. The reactor was then sealed and checked to envisage leaks by pressurizing it with nitrogen. Nitrogen was removed, and the required amount of water with and without nanofluid was filled into the reactor. The initial temperature was set to the desired temperature, and methane (also procured from Purushottam Gas Suppliers, India) was charged into the reactor till 0.1 MPa was reached on dial. Methane was released from the reactor after 5-6 min. The same process was repeated 3-4 times that no atmospheric air was retained in the reactor. After purging, methane was charged at the rate of 0.2 MPa/s till it reached the level of 6 MPa. The system was ready to run once all the operating conditions of the experiment were set to the desired values. For repeatability, the tests were performed at least three times. The induction was calculated at the development of the first crystal structure of the hydrate in the reactor, which was filled with the sample along with CH₄. The development of the first crystal

structure is determined by the pressure and temperature graph. All parameters, such as induction time, rate of gas consumption, and moles of consumption, were calculated using pressure and temperature readings from the SCADA software of the hydrate system.

4.3. Results and discussion

Hydrate formation involves three phases, *e.g.*, dissolution, induction, and growth phase [231]. The induction phase has significant importance in hydrate formation and thus, different tests such as DLS/SEM, induction time trend, gas consumption in moles, apparent rate constant, rate of gas consumption, and storage capacity were conducted to investigate the role of nanofluid on hydrate formation and presented the results accordingly.

4.3.1. DLS and SEM analysis of nanofluid

DLS measurements were conducted as soon as white precipitate appeared in the solution. DLS analysis provided the average NP size in the nanofluid, whose details are provided in Table 4.1 for different NP concentrations. With increasing concentration, particles tend to agglomerate and form larger clusters of size greater than the original NP [232]. Thus, it increases the overall NP size in the nanofluid. Therefore, SiO₂ nanofluids of higher concentration exhibited greater NP size than those of lower NP concentration. The actual appearance images of synthesized nanofluids and the CTAB solution of 300 ppm are provided in Figure 4.2. 0.5 wt% SiO₂ nanofluid exhibited NP size in the range of 5-10 nm, while 10-20 nm NP size was found with 1 wt% SiO₂ nanofluid (Table 4.1). Similarly, NP sizes of 60-85 and 90-100 nm were associated with 1.5 and 2 wt% SiO₂ nanofluids, respectively. The nanofluids were stable colloidal suspensions as they exhibited zeta-potential values greater than -30 mV [233] In addition, zeta-potential values did not decrease much over the storage period of 15 d and their value sustained around -40 mV. All nanofluids remained stable till a storage period of more than 4 months, before showing any sign of phase separation and settlement.

Table 4. 1: DLS measurements [size and zeta-potential] of synthesized nanofluids

Nanofluid and concentration	Average size (nm)	Zeta-potential (mV)
SiO ₂ (0.5 wt%)	5-10	-48
SiO ₂ (1 wt%)	10-20	-42
SiO ₂ (1.5 wt%)	60-85	-39
SiO ₂ (2 wt%)	90-100	-36

For morphology validation, SEM images were purposefully captured after phase separation in nanofluid so that morphological characteristics of both (1) NPs in dispersion and (2) NPs settled can be shown. SEM image of SiO₂ NPs in 0.5 wt% nanofluid is produced in Figure 4.3 from top and bottom layers of phase separation and NP settlement, respectively. It was observed that, even after settlement, some NPs stayed back in suspension however, they were sparsely distributed than the densely ones settled in the bottom (see Figure 4.3). Additionally, from images, it can be seen that NPs are irregular in shape and size as evident from NP clusters of different size. It indicates that NPs tend to agglomerate and develop clusters of different shape and size, which also supports the results of varying rate of NP settlement and phase separation in synthesized nanofluids. This observation is in accordance with DLS results of nanofluids.



Figure 4.2: Visual appearance images of synthesized nanofluids of various concentrations (0.5-2 wt%) in the base fluid of polymer PAM

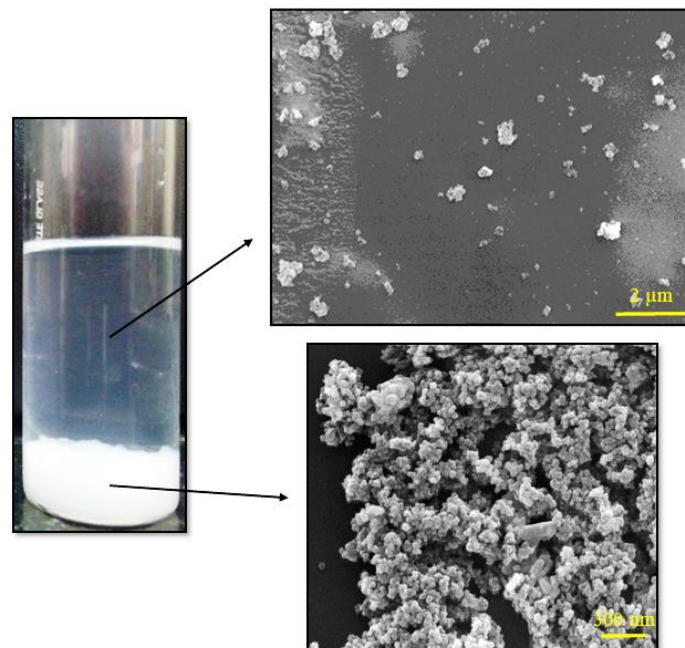


Figure 4.3: SEM images of unsettled NPs and settled NPs from the top and bottom layers of 0.5 wt% SiO₂ nanofluid after witnessing clear phase separation and NP settlement

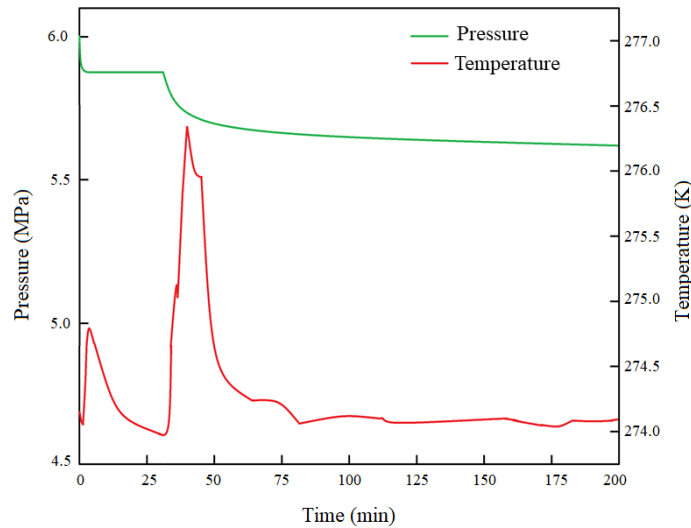


Figure 4.4: Variation of pressure vs. temperature during hydrate experiment for sample composition S5, consisting of CH₄+DI water+1.5 wt% SiO₂ nanofluid

4.3.1. Effect of nanofluid on induction time

Induction time is a part of a kinetic study for gas hydrate, which is determined by the temperature and pressure variations in the reactor. The time taken between the injection of CH₄ into the cell and the production of the first hydrate nucleus is known as the induction time [17]. Nanofluid samples of Table 4.1 were used to investigate the impact of NP on the induction time of surfactant-based hydrate, prepared with CH₄ and 300 ppm CTAB. The details of different compositions along with nomenclature are provided in Table 4.2, where induction times are provided for conventional (DI water and CTAB surfactant-based) and nanofluid (concentration: 0.5-2 wt%) based hydrates. The variations of pressure and temperature during a typical hydrate experiment are provided for CH₄+water+1.5 wt% SiO₂ nanofluid (S5) in Figure 4.4. The first peak (0-5 min) of rapid temperature increase and pressure drop corresponds to initial gas dissolution in the aqueous phase, caused by the start of the stirrer inside the reactor. The second peak refers to hydrate nucleation, which continues till the pressure and temperature attain constant values. In addition, it can be stated that rapid migration of gas molecules to hydrate cages usually causes a sharp reduction in pressure at the induction time (first crystal formation) [234]. The temperature

curve moreover showed supporting trends, and its value increased as soon as dissolution of methane takes place in solution and reached to maximum level of 0.8 K. The temperature drops from 274.8 K to 273.8 K (a difference of 1 K) till it reaches the induction time. Since crystallization is an exothermic reaction, the temperature of the reactor rises substantially by around 2-3 K. When the formation of the hydrate is over, the temperature starts to decrease. In all hydrate formation tests, the induction time was measured using a similar method. All experiments were performed three times to minimise the error, as pressure and temperature kept changing till the formation of the hydrate. Once the hydrate is fully formed, no change in pressure and temperature was observed however a constant value. The results of induction time for all experiments are provided in both Table 4.2 and Figure 4.5, which clearly indicate that the induction time reduced with increasing NP concentration, which might be credited to the NP. NP induced a greater rate of driving force to form a hydrate. For DI water, the formation of hydrate was observed at an induction time of 71 min (274.15 K, Figure 4.5) and 76.1 min (277.15 K, Table 4.2). With the DI water + CTAB (300 ppm) system (S2), the induction time was found to be 51.4 and 52.7 min at 274.15 and 277.15 K, respectively. The induction time significantly reduced after the inclusion of NP in the system (Table 4.2).

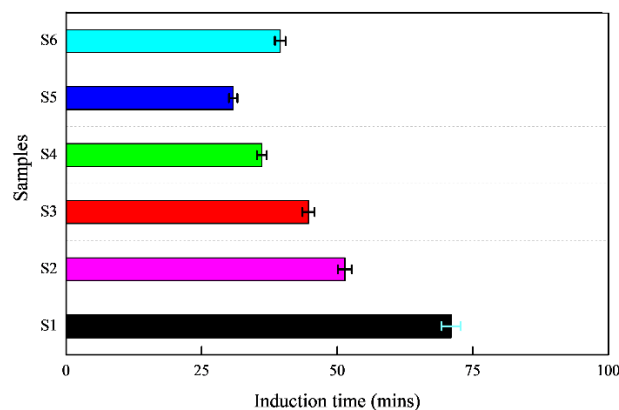


Figure 4.5: Effect of nanofluid on induction time of DI water (S1), CTAB solution (S2) different nanofluids (S3-S6) at 6 MPa and 274.15 K

Table 4.2: The compositional details, nomenclature, and induction time of hydrates prepared with CTAB and different concentrations of nanofluids

Aqueous phase	Surfactant, CTAB (ppm)	Polymer, PAM (ppm)	SiO ₂ nanofluid (wt%)	Nomenclature	Pressure (MPa)	Temperature (K)	Induction time (min)	Water to hydrate conversion (mole%)
-DI water	----	----	----	S1	6	274.15	71	12.3
	300	1000	----	S2			51.4	14.1
			0.5	S3			44.7	23.4
			1.0	S4			36.1	26.1
	----		1.5	S5			30.8	38.1
			2.0	S6			39.5	25.6
	----		----	----	S1	76.1	11.6	
	300	1000	----	S2	52.7	13.2		
			0.5	S3	47.6	21.4		
			1.0	S4	39.0	23.8		
	----		1.5	S5	32.8	29.1		
			2.0	S6	40.4	22.4		
						277.15		

Therefore, the shortest induction time (30.8 min: 274.15 K and 32.8 min: 277.15 K) occurred when NP concentration was 1.5 wt% (S5), ~56% lower than that of DI water. In addition, as compared to DI water, the induction time was ~37% lower for 0.5 wt% SiO₂ nanofluid (S3) (see Figure 4.5). Similarly, it was ~49% and ~44% lower for 1 (S4) and 2 wt% (S6) SiO₂ nanofluid, respectively. The high conductivity of SiO₂ NPs probably enhanced the heat transfer ability of the fluid. Furthermore, the traits of Brownian motion and high specific surface area increased the number of nucleation sites in the fluid, which has increased the rate of heterogeneity and mass transfer in the system [235]. The observations of these factors are in line with research findings in literature [235,236] and therefore, they can be considered as possible reasons for significantly reducing the induction time in NP based hydrates. It is moreover interesting to note that the value of induction time did not decrease after a certain concentration of NP in the system, as shown in Figure 4.5, which is 1.5 wt% in this study. It can be seen from Table 4.2 and Figure 4.5 that induction time reached to minimum level at 1.5 wt% for both the tested temperatures, followed by an increase at 2 wt%. Thus, induction time was around 28% (274.15 K) and 23% (277.15 K) higher at 2 wt% than at 1.5 wt%. This indicates that saturation was achieved at 1.5 wt%, resulting in further NP inclusion could not occupy enough space in the aqueous phase and therefore, its impact on induction time and hydrate scheme was unnoticeable. It is also to be noted here that induction has a direct relation with the temperature of the reactor. At higher temperature (277.15 K), it is expected that it took more time to release the heat when the hydrate crystals form in the reactor. Therefore, a delay in induction time was seen at 277.15 K than 274.15 K. For example, a delay of ~7% was determined for induction time (76.1 min) when reactor temperature increased by 3 K (see Table 4.2). Similarly, for nanofluid-based hydrate (S5: 1.5 wt% SiO₂), the induction

time delayed by 6.5% at 277.15 K. The actual image of S5 based hydrate sample (received after opening of reactor cell) is moreover captured and shown in Figure 4.6.

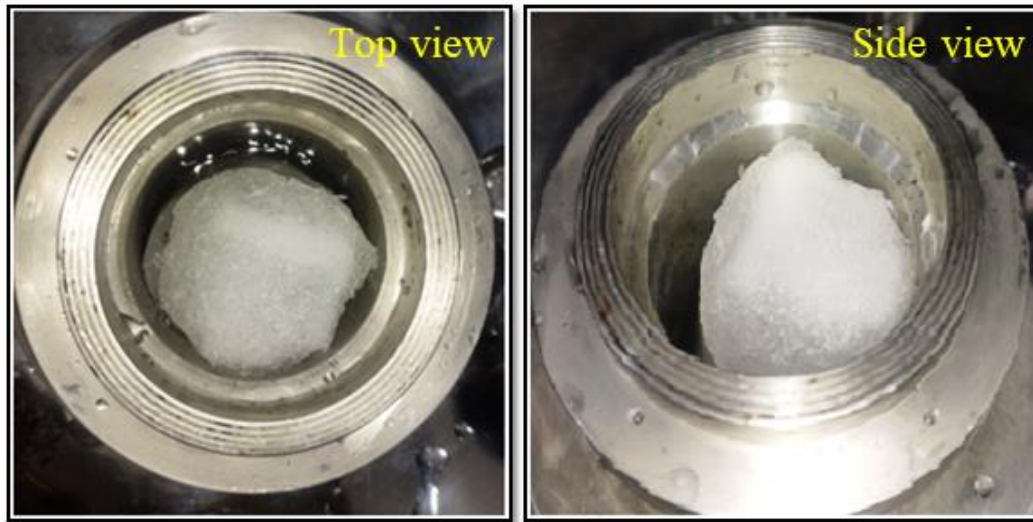


Figure 4.6: Actual image of gas hydrate in reactor cell after the completion of experiment for sample composition S5 at 274.15 K

4.3.2. Effect of nanofluid on gas consumption

Gas consumption is one of the important parameters and can be calculated by Eq. 4.2 [237]

$$\Delta n_{CH_4} = \frac{1}{R} \left(\frac{P_0 V_0}{Z_0 T_0} - \frac{P_t V_t}{Z_t T_t} \right) \quad (4.2)$$

where, n_{CH_4} = methane gas consumption in mole, P = pressure of the reactor, T = temperature of the reactor, V = volume of the reactor, R = universal gas constant, Z = compressibility factor of methane. Subscript '0' and 't' represent initial and final time, respectively. The compressibility factor of methane is calculated by following the Peng-Robinson equation of state (Eq. 4.3) [238]

$$Z^3 - (1 - B)Z^2 + (A - 3B^2 - 2B)Z - (AB - B^2 - B^3) = 0 \quad (4.3)$$

$$A = \frac{(a_c a)P}{(RT)^2} \quad (4.4)$$

$$B = \frac{bP}{RT} \quad (4.5)$$

$$a_c = 0.45724 \left(\frac{RT_c}{P_c} \right)^2 \quad (4.6)$$

$$b = 0.07780 \left(\frac{RT_c}{P_c} \right) \quad (4.7)$$

P_c and T_c are the critical pressure and temperature of methane, respectively. a and m were taken from literature [239].

$$a = (1 + m(1 - T_r^{0.5}))^2 \quad (4.8)$$

$$m = 0.3746 + 1.5423\omega - 0.2669\omega^2 \quad (4.9)$$

where, ω is acentric factor = 0.0114

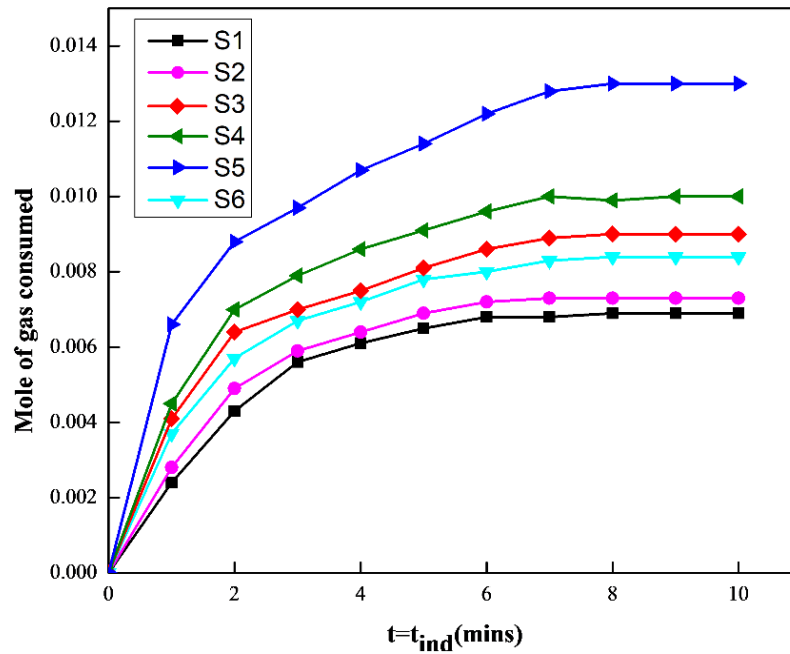


Figure 4.7: The results of methane consumption vs. time for hydrates stabilized by DI water (S1), CTAB solution (S2), and SiO₂ nanofluids of varying NP concentration (S3-S6) at 6 MPa and 274.15 K

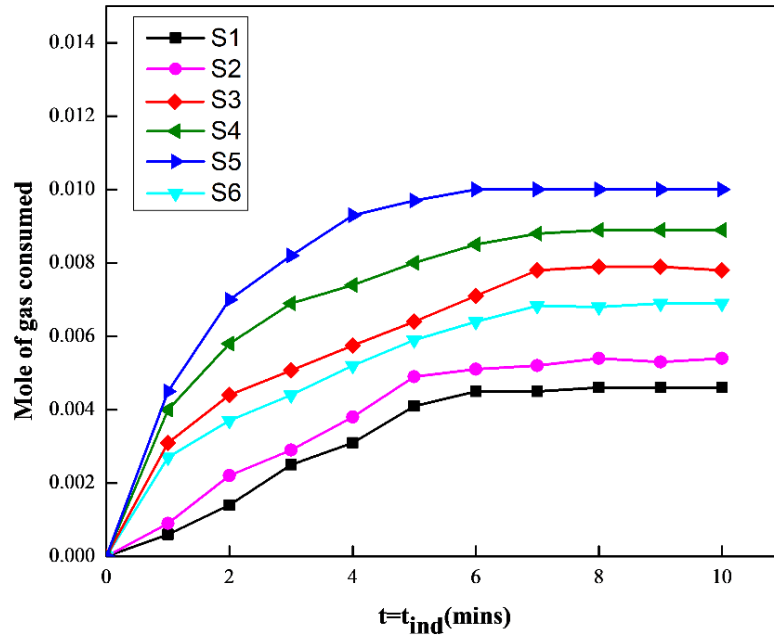


Figure 4.8: The results of methane consumption vs. time for hydrates stabilized by DI water (S1), CTAB solution (S2), and SiO₂ nanofluids of varying NP concentration (S3-S6) at 6 MPa and 277.15 K

The results of methane consumption vs. time are shown in Figure 4.7 and Figure 4.8 for the following scenarios: DI water (S1), 300 ppm CTAB (S2), and SiO₂ nanofluids of varying NP concentration (S3-S6) at 6 MPa and different temperatures (274.15 and 277.15 K). It was observed that the consumption of methane was larger when a nanofluid was introduced in the system than that of DI water (S1) or 300 ppm CTAB (S2). It is also to be noted here that the amount of consumed gas increases with increasing concentration of NP till 1.5 wt% (S5) for both the tested temperatures (Figures 4.7 and 4.8). It is well established that NP has a higher surface area, and with the combination of Brownian motion, these nanofluids can reduce mass transfer that occurs at the liquid-gas interface [240]. In addition, the increase in gas consumption may be the inclusion of CTAB surfactant, which helped to increase mass transfer from gas to liquid phase. Moreover, NPs can affect hydrate equilibrium by increasing the driving force in hydrate development, which ultimately leads to higher moles of methane consumption. However, the rate of gas

consumption did not increase after a certain concentration of NP (1.5 wt%), and this can be the saturation limit of the NP population in the system. It might be possible that NPs, beyond 1.5 wt%, saturated the available space in the aqueous phase and at the liquid-gas interface. Consequently, it left limited space for the consumption and transfer of gas molecules in the aqueous phase. Therefore, gas consumption was found least for the S6 sample (NP concentration > 1.5 wt%) at both temperatures. From Figures 4.7 and 4.8, it is moreover to be noted here that moles of consumption rapidly increased within a few minutes (3-4 min) of the experiment, followed by a sustained increase till the induction time was reached. Additionally, it is also clear from the images that the nanofluid worked better at 274.15 K and a greater number of moles were consumed in the cages of nanofluid-based hydrate samples (S3-S6). For example, mole consumption reduced by ~23% when the temperature of the hydrate experiment increased by 3 K (from 277.15 K to 274.15 K). Similar behaviour was shown by other nanofluid samples, and they exhibited 13.33% (S3), 11% (S4), and 17.85% (S6) reduction in mole consumption at 277.15 K.

In literature [241], it has been proven that NPs have higher thermal conductivity than water and as a result, it facilitate heat dissipation more effectively when the hydrate forms. Therefore, it can be expected that the inclusion of NP up to 1.5 wt% suggested faster kinetics in hydrate formation. Mechanistically, there was an increase of 88.4% in mole consumption with 1.5 wt% SiO₂ (S5) than DI water (S1) at 274.15 K (Figure 4.7). Similarly, 0.5 wt% (S3), 1 wt% (S4), and 2 wt% (S6) provided an increase of 30.4%, 45%, and 21.7%, respectively, at 274.15 K (Figure 4.7). Figure 4.8 shows mole consumption data at 277.15 K, where results showed similar behaviour with 117.39% increase for 1.5 wt% SiO₂ (S5). S3, S4, and S6 suggested 69.56%, 93.47%, and 50%, respectively, increase in mole consumption. A conclusion can also be drawn that the mole of gas consumption slightly decreased with an increase in temperature. Overall, a reduction of 23% was determined

with a temperature rise by 3 K. Even, it can be highlighted that the inclusion of surfactant CTAB improved gas consumption of DI water and mole consumption of 0.0073 per mole of water obtained with the S2 sample at 274.15 K, which was 5.8% greater than that of S1. Moreover, these results suggested that a single-step TiO₂ nanofluid of a certain concentration (1.5 wt%) and size (60-85 nm) should be designed to improve the gas consumption value of conventional surfactant-based hydrates.

4.3.3. Effect of nanofluid on apparent rate constant of hydrate

Apparent rate constant can be calculated by following Eq. 4.9

$$k_{app} = \frac{n_{G,i-1} - n_{G,i+1}}{(t_{i+1} - t_{i-1})n_{w0}} (f_g - f_{eq})_{t_i} \quad (4.9)$$

Where, k_{app} is apparent rate constant, n_{w0} is mole of water, $n_{G,i-1}$ mole of CH₄ at time $t_{(i-1)}$, $n_{G,i+1}$ is the mole of CH₄ at time t_{i+1} .

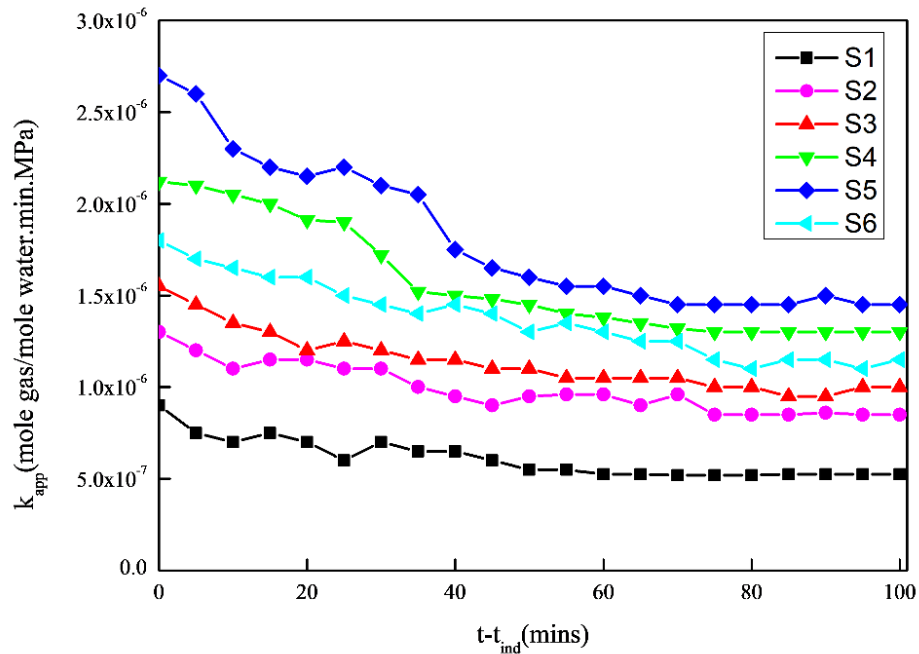


Figure 4.9: Apparent rate constant for hydrates stabilized by DI water (S1), CTAB solution (S2), and SiO₂ nanofluids of varying NP concentration (S3-S6) at 6 MPa and 274.15 K

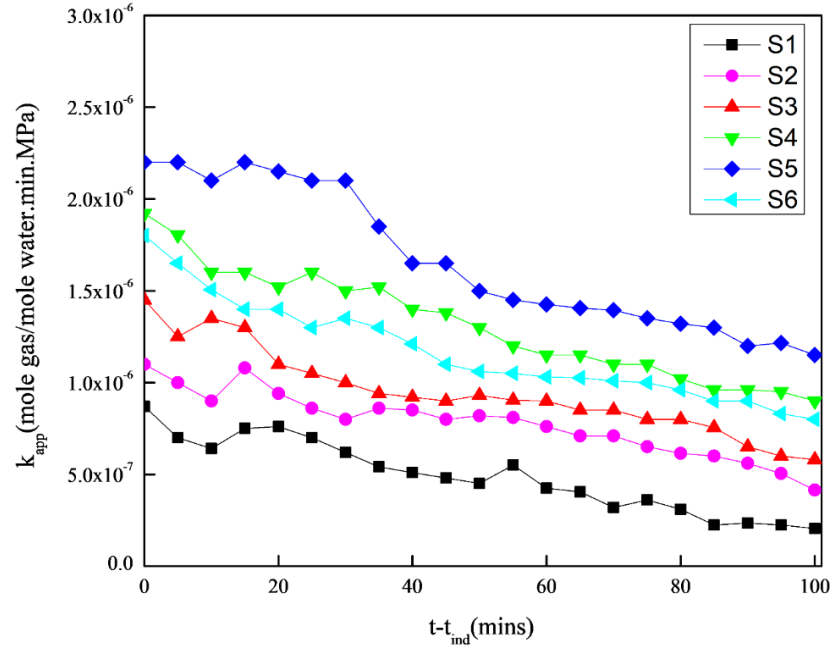


Figure 4. 10: Apparent rate constant for hydrates stabilized by DI water (S1), CTAB solution (S2), and SiO₂ nanofluids of varying NP concentration (S3-S6) at 6 MPa and 277.15 K

The apparent rate constant is an important parameter to compare rate of hydrate growth at different conditions, which is based on Eq. 4.4. Figure 4.9 illustrates the impact of nanofluid on apparent rate constant of DI water and CTAB based hydrates at 6 MPa and 274.15 K. It was observed that apparent rate decreased with increase in time for all samples, which signifies the growth of hydrate inside reactor. The initial value of the apparent rate constant for S1 and S2 was determined as 9×10^{-7} and 1.3×10^{-6} mole gas/mole water.min.MPa, respectively, which decreased with time and reached to minimum level of 5.25×10^{-7} and 8.5×10^{-7} mole gas/mole water.min.MPa at 100 min. The inclusion of nanofluid showed a remarkable jump in the apparent rate constant of S1/S2-based hydrates. As a result, it reached to maximum level of 2.7×10^{-6} mole gas/mole water.min.MPa ($t = 0$) for the S5 sample, which is consistent with the gas consumption result of this nanofluid. At $t = 100$ min, the value of the apparent rate constant for S5 was determined as 1.4×10^{-6} mole gas/mole water.min.MPa, higher than the values associated with S3 (1×10^{-6}), S4 (1.3×10^{-6})

⁶), and S6 (1.15×10^{-6}) samples. Thus, it is evident that NP concentration ~ 1.5 wt% is the optimum concentration to affect the rate of hydrate growth in this study. As expected, the apparent rate constant of S1 increased by 184% in the presence of 1.5 wt% SiO₂. Similarly, with NP concentration of 0.5 wt% (S3), 1 wt% (S4), and 2 wt% (S6), the apparent rate constant of S1 increased by 74.19%, 27.35%, and 50%, respectively. In addition, the reason for the significant jump in the initial value of the apparent rate constant is the indication of an exothermic reaction during hydrate formation and the decrease in driving force [242]. It was moreover observed that the apparent rate constant decreased with an increase in temperature and these results are provided in Table 4.2 and Figure 4.10 for 277.15 K. It was observed that the apparent rate constant of S1 (DI water) was found to be 0.87×10^{-7} mole gas/mole water.min.MPa. The subsequent level of apparent rate constant was determined as 1.10×10^{-7} mole gas/mole water.min.MPa for S2. With increasing NP concentration, it was observed that the apparent rate constant increased. Therefore, its value was determined as 1.40×10^{-7} , 1.97×10^{-7} , and 2.2×10^{-7} mole gas/mole water.min.MPa for S3, S4, and S5, respectively. From Figures 4.9 and 4.10, it can be concluded that the apparent rate constant decreased by $\sim 9.5\%$ with a 3 K increase in test temperature. Similarly, a decrease of 15.3%, 9.6%, 7%, 18.5%, 3.88% was reported for S2, S3, S4, S5 and S6 samples, respectively. Even at high temperature, nanofluid-based hydrates exhibited a higher apparent rate constant than S1/S2-based hydrates (Table 4.2). As explained earlier, NP inclusion is advantageous for the increment in gas consumption and rate of heat transfer. Therefore, it is expected that the peak value of the apparent rate constant will be achieved at the induction time. Since the driving force is maximum at the beginning of hydrate growth, a higher number of stable nuclei of gas hydrate is possible in the presence of NPs inside the reactor.

Table 4.3: Apparent rate constant of hydrates stabilized by nanofluids of different concentrations

Nomenclature	Pressure (MPa)	Temperature (K)	Apparent rate constant K_{app} at $t=t_{ind}$
S1	6	274.15	0.95×10^{-7}
S2			1.30×10^{-7}
S3			1.55×10^{-7}
S4			2.12×10^{-7}
S5			2.70×10^{-7}
S6			1.80×10^{-7}
S1	6	277.15	0.86×10^{-7}
S2			1.10×10^{-7}
S3			1.40×10^{-7}
S4			1.97×10^{-7}
S5			2.20×10^{-7}
S6			1.73×10^{-7}

4.3.4. Determination of rate of gas consumption

The results of the rate of gas consumption vs. time for various samples (S1-S6) at 274.15 K are shown in Figure 4.11. It can be stated that a sharp decline in the rate of gas consumption in the initial few minutes is an indication of the onset of reaction. As soon as induction time is reached, a sharp increase in the rate of gas consumption occurs, which is likely due to the formation of a hydrate crystal. It is to be noted here that the rate of gas consumption was faster for S5 of 1.5 wt% NP: the rate of gas consumption was determined as 0.016 $n_g/n_w.min$, which was calculated as 0.014, 0.013, and 0.012 $n_g/n_w.min$ for S3, S4,

and S6, respectively. With the growth of crystallisation, more methane gets entrapped inside and as a result, the rate of gas consumption reached to further heights. No change in the rate of gas consumption indicates full growth of the hydrate. From Figure 4.11, it can moreover be noticed that gas consumption started early in between 28-55 minutes for S3-S6 samples, which was significantly delayed (~ 70 min) in the case of DI water (S1) at 274.15 K. The credit is attributed to the inclusion of SiO₂ nanofluid of 1.5 wt% (S5) which increased the rate of gas consumption by 60%.

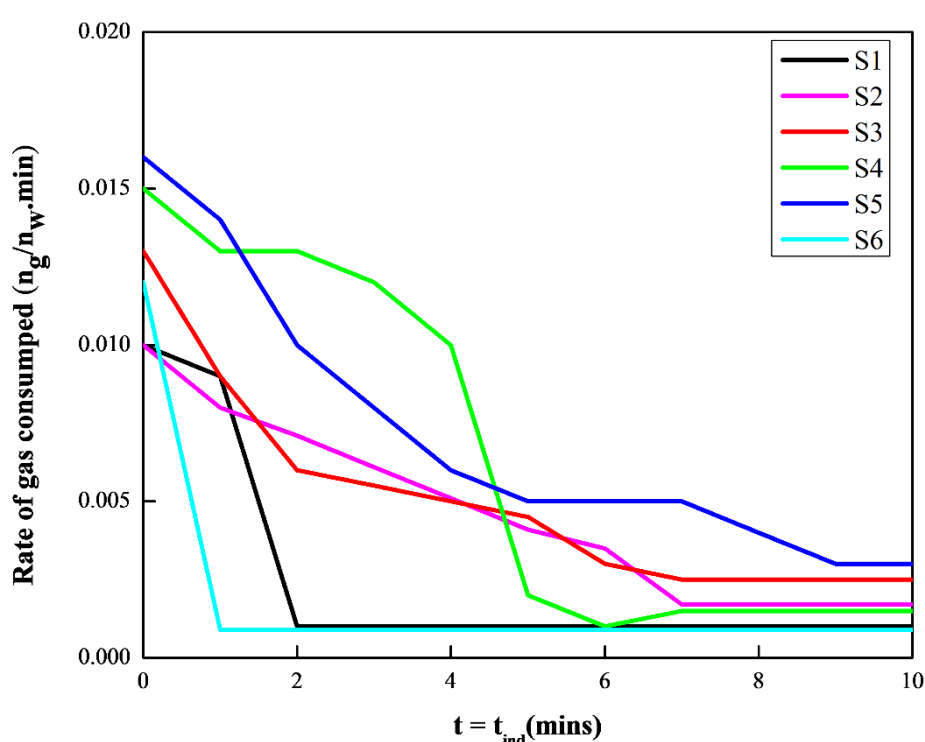


Figure 4.11: Comparative performance to evaluate rate of gas consumed for different hydrates stabilized by S1-S6 formulations at 274.15 K

Thus, the role of nanofluid on the rate of gas consumption is further explained as follows:

- NPs were independent and possessed more surface area than conventional two-step nanofluid, and therefore, the high thermal conductivity of these nanofluids helped in efficient heat removal during the formation of hydrate at induction time. With the

increase in temperature, the driving force decreased, which resulted in a delay in induction time.

- It is expected that NPs reduce the liquid-gas interface and make it a thinner interface. As a result, the motion of NPs facilitated significant heat and mass transfer across the interface of the hydrate.
- Nanofluid exhibited smaller particles that possess a smaller surface area, and consequently, they developed tiny gas bubbles. These bubbles possessed better heat and mass transfer characteristics than larger bubbles, usually the case with hydrates stabilized by two-step nanofluids or commercial NPs. It can also be stated that these smaller bubbles positively increased gas diffusivity at the liquid-gas interface.

4.3.5. Storage capacity of hydrate samples

Storage capacity can be determined as the volume of gas entrapped inside the solid cage of the hydrate. It is estimated as per volume of gas entrapped at standard conditions. Eq. 4.10 illustrates the expression for storage capacity [174]

$$SC = \frac{V_{STP}}{V_H} = \frac{\frac{\Delta nRT_{STP}}{P_{STP}}}{V_H} \quad (4.10)$$

Where, STD stands for standard condition (273.15 K and 0.1MPa).

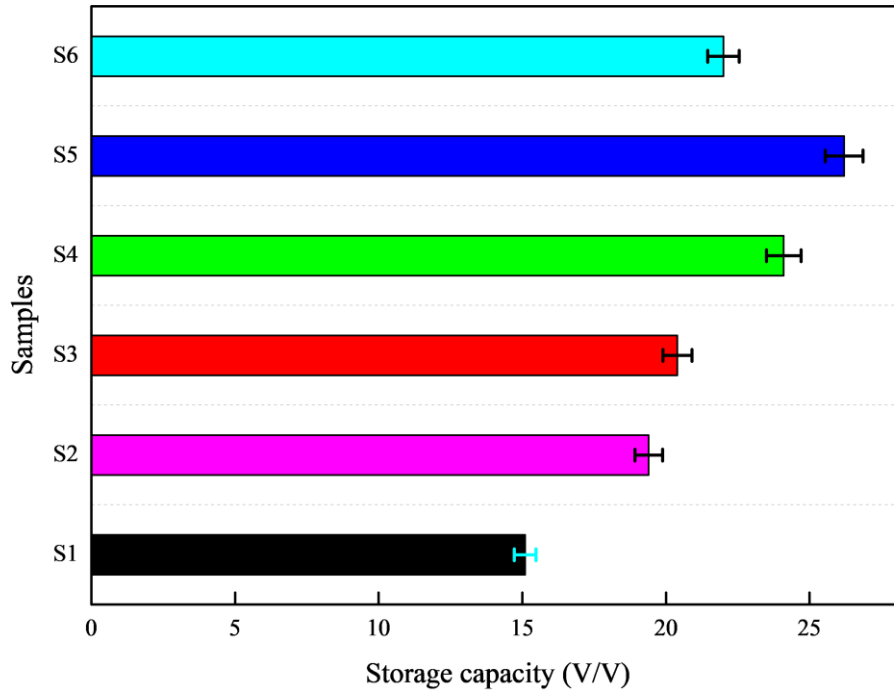


Figure 4.12: Storage capacity of different hydrates stabilized by S1-S6 formulations at 6 MPa and 274.15 K

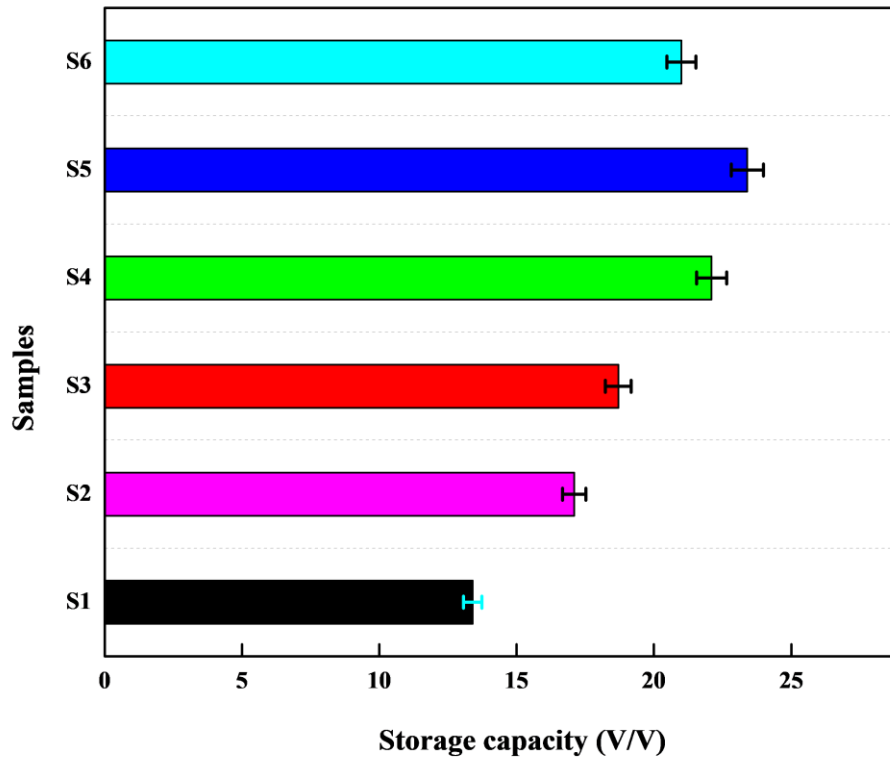


Figure 4.13: Storage capacity of different hydrates stabilized by S1-S6 formulations at 6 MPa and 277.15 K

The results of storage capacity for all samples are provided in Figure 4.12, which was prepared for methane hydrates at 6 MPa and 274.15 K. It is clear from Figure 4.12 that the storage capacity of nanofluid-based hydrates was significantly higher than that of S1/S2 samples. The storage capacity of S1 and S2 samples was determined as 15 and 18.2 v/v, respectively, which increased to 20.2(S3), 24.1(S4), 26.8(S5), and 22.3(S6) v/v when a nanofluid of different concentrations was introduced in the system. Thus, the storage capacity of hydrate, stabilized by NP concentration of 1.5 wt%, was superior to other nanofluid-based hydrates, and it was measured that inclusion of 1.5 wt% enhanced the storage capacity of DI water (S1) by 78.66%. Even low NP concentration suggested greater storage capacity (than S1) for the application when high NP concentration is not economical to use or nanofluid synthesis of 1.5 wt% is not feasible. Storage capacity greater than 60% can be obtained with the inclusion of 1 wt% SiO₂ nanofluid (S4) in DI water, which was determined to be 34.66% with 0.5 wt% (S3) and 49% with 2 wt% (S6). This is remarkable for the storage and transportation applications, when a single unit of hydrate can store more gas than that of conventional water-based hydrate. Figure 4.13 shows storage capacity results at 277.15 K. The storage capacity of sample S1 was calculated as 13.4 v/v at 277.15 K. Similarly, S2, S3, S4, S5, and S6 exhibited storage capacities of 17.1, 18.7, 22.1, 23.4, and 21 v/v, respectively. These results moreover suggest that an increase in test temperature also reduced the amount of storage capacity, as evident from Figures 4.12 and 4.13. Mechanistically, storage capacity decreased by 12.9%, 14.5%, 3.6%, 10.5%, 13.3% and 4.5% for S1, S2, S3, S4, S5, and S6, respectively, when test temperature increased from 274.15 to 277.15 K. Here, it is important to note that nanofluids of desired size were synthesized than procuring them externally followed by extensive mixing in base fluid. Thus, maintaining desired NP size becomes difficult when NPs are externally added, and this challenge can be addressed if NPs are synthesized in single-step. This study

moreover aims to highlight that NPs of other sizes can also be synthesized to make (1) a single-step method applicable for greater applications and (2) a nanofluid a promoter in hydrate formation on a global scale.

4.4. Conclusion and Summary

In this study, the effect of the single-step technique was explored through the development of nanofluids of desired NP size and investigating their role as promoters in the kinetics of the conventional hydrate of surfactant, CTAB. For the kinetic study, the pressure was chosen as 6 MPa with two different test temperatures of 274.15 and 277.15 K. Four nanofluids of different NP concentration (0.5-2 wt%) and size (5-100 nm) were synthesized. Nanofluids were stable colloidal suspensions with varying size distribution, as confirmed by size and zeta-potential measurements; however, they exhibit time-dependent NP agglomeration followed by settlement as demonstrated by SEM analysis. As compared to CTAB, the inclusion of nanofluid was more advantageous, as confirmed by the increased rate of gas consumption. Results moreover showed that NP concentration ~1.5 wt% was the inversion point and had the greatest impact on the kinetics of methane hydrate. As a result, a significant reduction of 56.6% was obtained in induction time at 274.15 K and 1.5 wt% was considered as the optimum NP concentration in hydrate formation. In addition, the mole of gas consumption and apparent rate constant were found to be 88.4% and 184% higher than those of DI water. All nanofluids (S3-S6) showed less induction time, mole consumed, and apparent rate constant than DI water (S1) and CTAB solution (S2). It was understood that NP concentration above a certain limit is affected by the saturation limit, as NPs tend to saturate the liquid-gas interface, and further addition hardly affects the kinetic properties of the hydrate. Similar was observed with NP concentration of 2 wt% as induction time, rate of gas consumed, and apparent rate constant displayed a reverse effect and therefore, 1.5 wt% was concluded as the best particle concentration for promoting the

kinetics of a hydrate. Finally, it can be concluded that storing methane, after extraction from hydrate, is vital for transportation followed by its subsequent usage. Since methane offers a viable option for clean energy, its immediate utilization after extraction may not be required or feasible, and thus, storage methods of superior efficiency are important. However, conventional storage methods either demand considerable space or sophisticated manufacturing. Synthesis of these nanofluids/nanoparticles does not consume any expensive or rare chemicals; moreover, the method of manufacturing is simple (sol-gel), available in literature, and a standard for large-scale implementation in industry. Thus, the use of single-step silica nanofluids can provide better improvement in methane storage efficiency than conventional nanoparticles (which are first procured and then mixed in a base fluid), enabling greater quantities to be stored within the same constraints. These nanoparticles can be recycled for approximately 80 days following decomposition, which is of key importance in ensuring stability for reuse.

Chapter 5: Examination of the effect of ethylene glycol on the dissociation of hydrates (CH₄ & CO₂): A Molecular Dynamics Analysis

Abstract

Gas hydrates is a source of energy and causes pipeline flow assurance issue risking shutdowns, equipment damage, and safety hazards in oil and gas operations due to its solid crystalline structure. To mitigate these issues, flow assurance strategies often involve using hydrate inhibitors (like ethylene glycol), insulation, and heating systems to maintain conditions that prevent hydrate formation, ensuring safe and continuous gas transport. MD simulations offer a powerful tool to investigate the behaviour of gas hydrates at the atomic level, providing insights into their formation, stability, and interactions. This study explores the impact of ethylene glycol (EG) on the dissociation and stability of CO₂ and methane hydrates together in a system through MD simulations. While inhibitors are commonly used in the industry to prevent hydrate formation and assist in dissociation, their precise role in this gas exchange mechanism demands more detailed exploration. In this study, we investigated the potential of ethylene glycol as a chemical additive to promote gas hydrate dissociation, though its effects are not yet fully understood. Using MD simulations, we explored parameters such as radial distribution function (RDF), mean square displacement (MSD), and diffusion coefficients to examine the impact of ethylene glycol across various temperatures (270.15 K to 300 K) and concentrations (0-15% V/V). The results indicate that gas dissociation accelerates by 150 % with rising temperatures, allowing methane to escape more rapidly into the simulation box, thereby enabling controlled gas production. Additionally, a 10% increase in glycol concentration destabilizes the hydrate structure. Based on these findings, we recommend using ethylene glycol at 10% V/V for gas hydrate dissociation at 280 K.

5.1. Introduction

The rapidly increasing carbon dioxide (CO₂) level in the atmosphere and the resultant global climate change concerns have intensified the search for effective strategies to mitigate anthropogenic emissions to achieve net-zero [243]. Net zero refers to the balance between the amount of greenhouse gas emissions produced and the amount removed from the atmosphere. Countries commit to net zero to mitigate climate change by reducing emissions and enhancing carbon removal efforts. The commitment to net zero involves technology such as carbon capture and storage, transitioning towards cleaner energy, and improving energy efficiency to offset emissions [243]. Achieving net zero requires a comprehensive approach, including policy changes, technological advancements, and international collaboration [244]. One promising avenue involves capturing and storing CO₂ within natural gas hydrates (NGH), which are crystalline structures formed by water molecules encapsulating guest molecules such as methane under low temperature and high-pressure conditions. Like methane, CO₂ can moreover form hydrates under relatively low pressure and high temperature, making it a viable option for CO₂ sequestration. The CO₂-CH₄ exchange in hydrate not only addresses environmental concerns however also offers a potential source for natural gas production. It is worth noting that compared to NGH, CO₂ hydrates have a more stable structure [245,246]. The hydrate reserves are plenty around the world; generally found in permafrost, continental margin, and subsea sediments. One cubic meter of NGH holds 170 cubic meters of methane under standard conditions [17]. It is estimated that the methane available in these reserves is around 2500-20000 trillion cubic meters [247]. The amount of methane present in the hydrate is twice the non-renewable sources put together [248].

Hydrates are non-stoichiometric substances that primarily exist in three different structures: sI, sII, and sH [5]. This structure depends on the shape and size of gas molecules

[5]. sI is the smaller structure consisting of small gas molecules like methane, ethane, and carbon dioxide [16]. Out of the three structures, sI is more frequently occurring in nature [97]. The trapped gas inside the water cages is held by van der Waals forces, a very weak intermolecular force. The formation and dissociation of various hydrates have been well explored in the literature. CO₂ storage in hydrate is a well-researched topic. However, a comprehensive understanding of the CH₄-CO₂ exchange process remains elusive due to its complex nature, particularly concerning the phase behavior and its interaction with other reservoir gases [17]. The validity of this process has been established in several previous works that have explored the kinetic and thermodynamic properties of the process, which prove that the exchange can occur in certain temperature and pressure conditions [249–252].

The fundamentals of CH₄-CO₂ exchange mechanisms are essential to understanding both thermodynamic and kinetic behavior for hydrates [253],[254]. The stability of these hydrates was checked by Okano and Yasuoka et al. [125], who has explained that the nucleation of gas hydrates does not depend on the potential energy of the hydrate structure. In a separate study, Wei and Hong [127] calculated the thermodynamic property and the density of the hydrate structure, which is essential to understand before leveraging NGH for methane recovery and illustrated that Bernal Fowler ice rules satisfied the dissociation of the hydrate structure. Tariq et al. [255] have illustrated the formation and dissociation of the CO₂ hydrate at constant pressure, the result shows that hydrate formation depends on several factors, like initial pressure, subcooling, cooling rate, and heating rate.

However, the practical application of gas hydrates for CO₂ storage and energy production is fraught with challenges, primarily related to the controlled dissociation of these structures [256]. Gas hydrates are known for their instability, making it essential to develop methods for their targeted dissociation [257]. This work thus seeks to explore and

address these challenges, focusing on the role of ethylene glycol as a dissociation agent. Ethylene glycol is often considered a more useful chemical inhibitor for gas hydrate dissociation compared to others due to its unique properties [258]. Ethylene glycol has a high affinity for water molecules, disrupting the hydrogen bonding network crucial for gas hydrate stability. Moreover, ethylene glycol as a hydrate inhibitor is commonly available, cost-effective, and environmentally less harmful than some alternatives [259]. These characteristics contribute to ethylene glycol's practicality and efficiency in mitigating gas hydrate formation and promoting dissociation in various industrial applications. By examining the interactions between ethylene glycol and gas hydrate structure, the objective of this work is to elucidate the underlying mechanisms of the extraction of methane.

This study can be achieved by either high-end in-situ analytical instruments at hydrate stable conditions (high pressure and low temperature). The designing and performing of this experiment are highly challenging because of the extreme hydrate conditions. These experiments are also time-consuming. So, another alternative to experiments is MD simulation, a computational technique that simulates the motion of atoms and molecules over time at a given pressure and temperature, which provides invaluable information in unravelling the interactions that dictate gas hydrate behavior.

Previously, utilizing MD simulation [260] English et al. [134] performed a simulated dissociation of methane hydrate and found that dissolution occurred within 400ps of the simulation run and was due to the stochastic nature of hydrate structure, with initial decay followed by plateaus [261]. Li et al. [111] elaborate on the formation of hydrate in the presence/absence of kinetic inhibitors using MD simulation. They concluded that PVP-A exhibits better inhibition than PVA and PVA-E. Bai et al. [262] illustrated CO₂ hydrate formation by MD simulation, the results show hydrate formation takes place on the solid surface i.e. at the interface of liquid and solid & it moreover gives the impression that

nucleation occurs in three different stages. In the first stage, the ice-like structure formed at the interface at nanoseconds. In the second stage, at the sub-microsecond time level a thin layer of the structure formed around the ice-like layer, and the third stage of microsecond level nucleation formed from the intermediate structure [263]. Bai et al. [264] examined the MD simulation of CH₄-CO₂ exchange, where the CH₄ hydrate was in contact with water, and then CO₂ gas was inserted in the system, and then checked the growth of the CO₂ hydrate. Dashti et al. [265] illustrate the modelling of CO₂ capture in hydrate with nucleation stage and induction time prediction. In literature, the memory effect of the gas hydrate was studied for CO₂ capturing and CH₄ recovery [266]. Tian et al. [267] evaluated the recovery potential of CH₄ from the hydrate reservoir by injecting CO₂. In a different study, Liang et al. [268] explored the diffusion of gas in carbon dioxide hydrate and concluded that a vacant cage in the hydrate structure is necessary to store CO₂ gas in hydrate form. Apart from mechanisms, plenty of studies were conducted to understand the CH₄-CO₂ exchange process. Geng et al. [269] investigated the CH₄-CO₂ exchange process and found that methane reoccupies its cage after dissociation and forms a mixed hydrate of both CH₄ and CO₂ that is more stable. Sun et al. [132] examine the dissociation of hydrate structure using various alcohol additives by MD simulation. It concluded that adding methanol promotes hydrate dissociation. Zhang et al. [136] calculated the water's diffusion coefficient using MD simulation. The findings demonstrated that the structure of water and the creation of H-bonds between water molecules are mostly unaffected by the concentration of methane [270].

Thus, given the intricacies of methane recovery by gas hydrate dissociation and CO₂ sequestration, the integration of ethylene glycol and MD simulation offers a synergistic approach. Hembram et al [271]. has performed a simulation on methane hydrate with ethylene glycol. Although there are various studies of dissociation conducted in the

literature, very few studies have been done in a system having both CH₄ hydrate and CO₂ hydrate. In this paper, we have used ethylene glycol as a hydrate inhibitor to dissociate both structures. Simulations were performed at various temperatures from 270 K to 310 K and with the concentration of ethylene glycol of 1% V/V to 15% V/V. Investigations were performed for both the thermodynamics and structural properties in reported simulations with Radial distribution function (RDF) and mean square displacement (MSD) data. This parameter helps in exploring the dissociation of methane from hydrate structure, addressing environmental challenges, and advancing toward sustainable energy solutions.

5.2. Simulation

The MD simulation was performed using GROMACS, an open-source software that has been widely used in previous studies [138,272]. GROMACS is used in MD simulations to study the interaction among atoms and molecules. The simulation was performed at the High-Performance Computing (HPC) Cluster. The HPC cluster has nine (one master and eight compute) nodes (Fujitsu PR3000), and each node has dual processors with 20 cores/processor (with a total of 180 cores).

5.2.1. Structure

To perform MD simulations, a well-defined system structure is essential. The system under study comprises various molecules, including two different hydrate structures: CH₄ hydrate and CO₂ hydrate. Each hydrate structure is prepared individually before being combined into a unified system.

For both CH₄ and CO₂ hydrates, unit cell structures of the sI hydrate type were constructed separately. These unit cells were then used to form supercells with dimensions of 3.7 nm × 3.7 nm × 3.7 nm, containing 1,248 water molecules and 216 methane or carbon dioxide molecules, respectively. PACKMOL software was employed to integrate these supercells into a larger superstructure with dimensions of 3.7 nm × 3.7 nm × 10.9 nm [273].

In this arrangement, the methane hydrate is positioned at the top, while the carbon dioxide hydrate is located at the bottom, separated by a distance of 37 Å. The intervening space within the structure is occupied by water and ethylene glycol. Figure 5.1 illustrates the simulation box, showing the detailed arrangement of the methane and carbon dioxide hydrates along with the separating water and ethylene glycol layers.

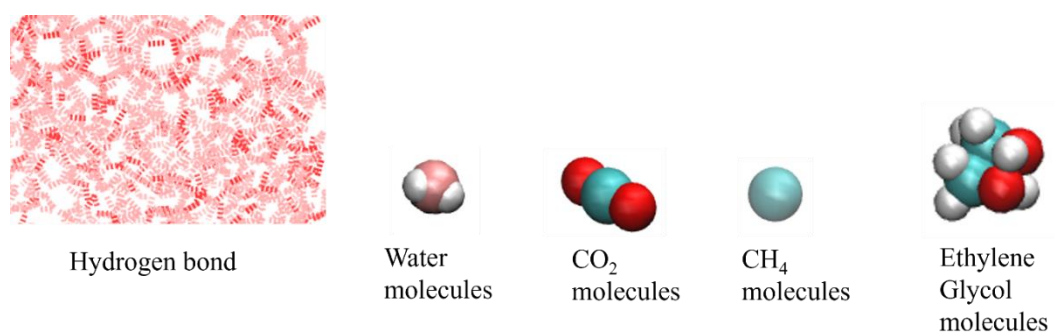


Figure 5.1: The visualization of the molecules inside the simulation box

5.2.2. MD simulation

A mixture of water and ethylene glycol molecules was inserted into the vacant space of the superstructure (between CO₂ and CH₄ hydrate). Periodic boundary conditions were applied during the run. While several water models are reported in the literature [142,144]. This study used the TIP4P [141] model, as this model can help best replicate experimental values. OPLS-AA (Optimized Potentials for Liquid Simulations – All Atom) was used to model CO₂. OPLS-UA (Optimized Potentials for Liquid Simulations – United Atom) was used to model CH₄ [142]. The cut-off radius of short-range interaction (Lennard-Jones potential action) is 1.5 nm. Long-range Coulomb interactions were processed using the PME (Particle-mesh Ewald) method. The steepest descent integrator was used in energy minimizations. The Leapfrog algorithm was used for the simulation run (energy minimization and final simulation algorithm). The Berendsen thermostat is used to regulate the temperature, while the Berendsen barostat is used for pressure [144]. The initial configuration of the hydrate structure is relaxed

using energy minimization at the start of the simulation. This is done to ensure that the system does not have any steric clashes or inappropriate geometry. The steepest descent algorithm is used in energy minimization. In the next step, to achieve the required temperature of the system, NVT (constant-particle, constant-volume, constant-temperature) ensemble was performed for 50 ps. The final step is to perform NPT (constant-particle, constant-pressure, constant-temperature) ensemble, which is done to achieve the required pressure and to study the whole dissociation process. NPT ensemble was performed at 500 ps. The pressure is kept at 50 bar throughout the experiment. Table 5.1 indicates the different molecules that are inside the simulation box. The top of the superstructure consists of carbon dioxide hydrate, and the bottom consists of methane structure. With each increase in ethylene glycol concentration, the water concentration reduces. Mole concentration for 2.5%, 5%, 10% and 15% are 0.4485 M, 0.897 M, 1.79 M and 2.69 M.

Table 5.1: Observations of molecules used in the simulation

Concentration (%)	Number of water molecules	Number of ethylene glycol	Number of methane	Number of carbon dioxide
0	2610	0		
2.5	2535	19		
5	2455	37	216	216
10	2310	74		
15	2036	148		

5.3. Results & Discussion

Hydrate dissociation is a phase change process from solid to liquid. The solid structure dissociates from a rigid hydrate structure into a random disorder stage, and the guest molecules are released to the fluid phase. To observe the dissociation of both CO₂ and CH₄ hydrate in the presence of ethylene glycol, a dissociation study was performed for 500 ps. Figure 5.2 represents the different molecules used in this simulation.

Table 5.2: Values of the force field used in this investigation.

Molecules	Atom	$q(e)$	$\sigma(\text{\AA})$	$\epsilon(\text{KJ/mol})$
H ₂ O	OW	0.0	$3.16557e^{-01}$	$6.50170e^{-01}$
	HW	0.52	0.0000	0.00000
	MW	-1.04	0.0000	0.00000
CH ₄	CH	0.0	$3.73000e^{-01}$	$1.23010e^{+00}$
CH ₂ OHCH ₂ OH	C	0.050	$3.50000e^{-01}$	$2.34144e^{-01}$
	HC	0.090	$2.38000e^{-01}$	$1.14620e^{-01}$
	O	-0.650	$3.14000e^{-01}$	$8.04280e^{-01}$
	HO	0.420	$0.04000e^{+00}$	$0.19200e^{+00}$
CO ₂	CC	0.700	$2.8000e^{-01}$	$2.244780e^{-01}$
	OC	-0.350	$3.05000e^{-01}$	$6.56806e^{-01}$

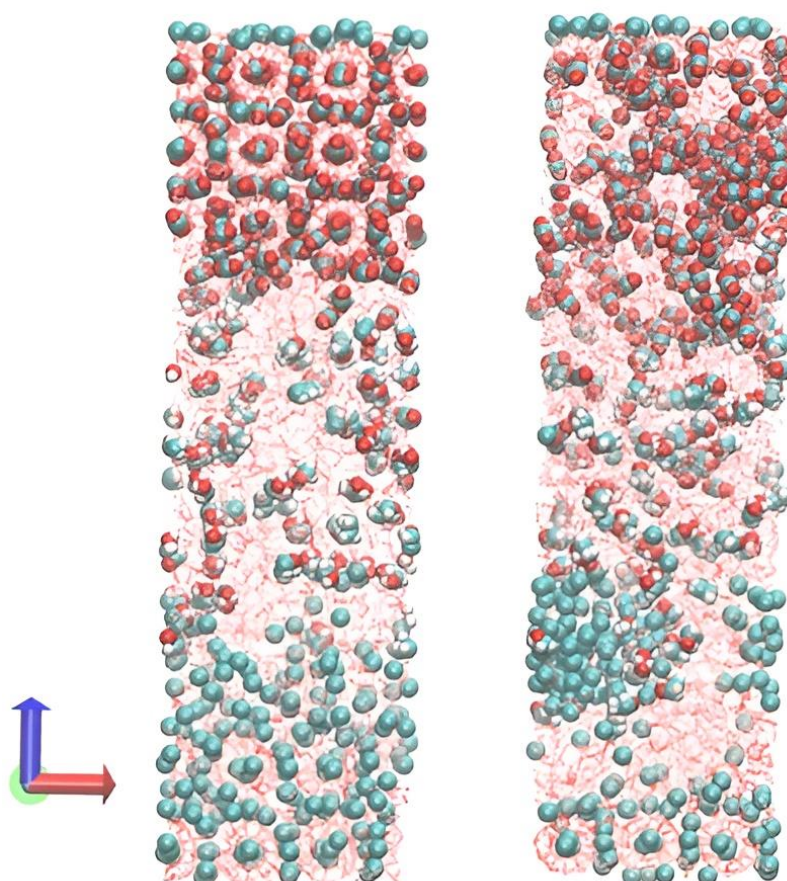


Figure 5.2: The visual appearance of the simulation box of 10% ethylene glycol concentration at 285.15K at (a) 0 ps and (b) 500 ps

These results provide insight into the dissociation of the hydrate structure. Figure 5.2 represents the final simulation system over 500ps at 50 bar and 285.15K. The system consists of 10% V/V ethylene glycol with both methane hydrate and carbon dioxide hydrate. Figure 5.2(a) shows the initial structure of the system at the beginning, and Figure 5.2(b) shows the system after the simulation completes (after 500ps). At the end of the specified simulation time, the hydrate structure dissociated. Figure 5.2 observations indicate that methane and carbon dioxide are released from the hydrate's rigid structure as time increases at 285.15K. The dissociation starts from the liquid-solid interface of the hydrate structure. Over time, dissociation causes the solid phase to completely disappear. Once dissociation is complete, the gases gather at the top and bottom of the simulation box,

leading to a separation into two phases: liquid and gas. This accumulated gas can then be extracted in a controlled manner and subsequently used as an alternative fuel. Table 5.2 displays the number of molecules present during the simulation. The results of the dissociation were analysed by three major tools: Radial Distribution Function (RDF), total energy, and diffusion coefficient.

5.3.1. Radial Distribution Function (RDF)

RDF [274] is a parameter to describe the molecular arrangement in a system by calculating the probability of finding similar particles from a certain particle in a given space system. RDF values can be used to understand the structural integrity of the hydrate structure and help in characterizing the hydrate microstructure. It provides the interaction between the guest molecules and host molecules [275]. When the RDF is observed, the existence of a peak exists at a certain distance. The existence of this peak depends on the type of molecules in the system and the distance between adjacent molecules in the hydrate structure, plotted between average probability vs. distance. The result reveals information in the form of heights and the shape of the peak [274]. The equation that calculates the RDF is

$$g_{\alpha\beta}(r) = \frac{V_s}{N_\alpha N_\beta} \left(\sum_{i=1}^{N_\alpha} \frac{n_i \beta(r)}{4\pi r^2 \Delta r} \right) \quad (5.1)$$

Where, $N_i \beta(r)$ is the number of β at distance r and $r + \Delta r$ away from i th particle α . N represents the number of particles inside the simulation box, and V is the box's volume.

In RDF, the first peak between carbon-carbon in methane represents the distance between two different carbon atoms present in the nearest cage structure. Similarly, RDF's first peak in oxygen atoms represents the average distance between the nearest oxygen molecules of water [276], and RDF second peak shows the crystal structure of hydrate sl with hydrogen bonding.

5.3.1.1. Effect of Temperature on Hydrate Structure

The RDF of oxygen-oxygen of water in the simulation is shown in Figure 5.3(a). There are three peaks at 2.76 Å, which donate the distance between oxygen-oxygen to the nearest water molecules that form hydrogen bonds. At lower temperatures, the peak is higher, indicating the hydrate structure expansion [276]. This is due to the guest molecules occupying the lattice of the hydrate, which increases the average distance between the two molecules. However, at higher temperatures, the peak reduction indicates the dissociation of the hydrate structure due to an increase in thermal energy in the molecules. As the temperature increases, molecules vibrate by gaining energy, and this elevated energy facilitates the dissociation of hydrates. This directly affects the stability of the structure. The lower peak indicates that both guest and host molecules leave the original position to form two separate phases. The second and third peaks at 4.57 and 6.56 Å. almost disappear, respectively indicating the complete dissociation of the hydrate structure. Due to dissociation, there is an increase in water disorder, from solid to liquid.

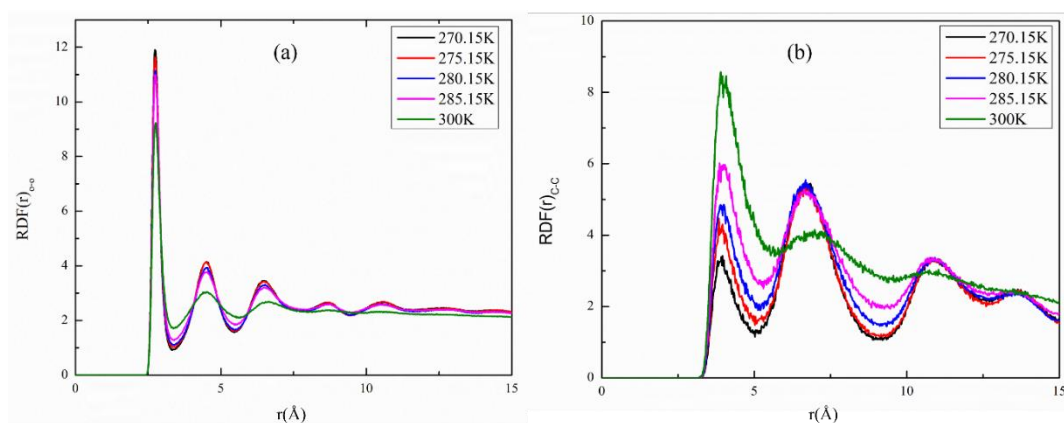


Figure 5.3: Plots of RDF at 10% concentration of ethylene glycol. (a) oxygen-oxygen of hydrate (b) carbon-carbon of methane

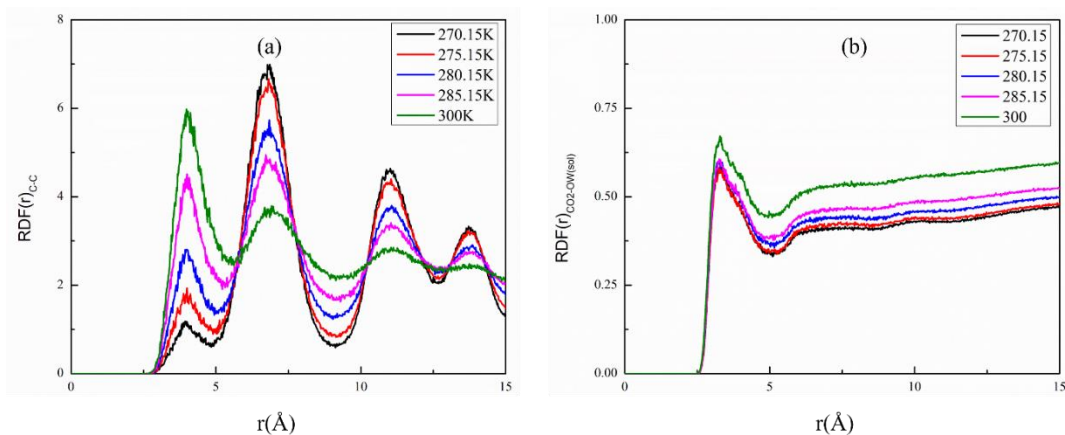


Figure 5. 4: RDF at 10% concentration of ethylene glycol (a) carbon-carbon of CO₂ (b) carbon (CO₂)-oxygen of water

The RDF of carbon-carbon of methane molecules is shown in Figure 5.3(b). The graph shows the highest peak at 300K indicates more water dispersed i.e. due to the dissociation of the hydrate structure at higher temperature, more molecules escape from the rigid structure to two different phases. As the temperature increases, the molecules vibrate, gaining kinetic energy. Hence, dissociation of NGH takes place. Figure 5.4(a) shows the RDF of carbon of carbon-carbon of carbon dioxide. The primary peak can be seen at 4 Å. This indicates the distance between two carbon molecules of CO₂. In this graph, the RDF peak reduces as the temperature increases. This indicates there is 4 Å is the distance between two carbon molecules of CO₂. As the temperature rises, dissociation occurs. This indicates that at higher temperatures, the probability of finding methane and water molecules becomes less, hence it can be said that at higher temperatures, the hydrate structure is not stable, and hence dissociation of the hydrate takes place. This indicates that more methane molecules are escaping from the lattice of the hydrate structure. The lower the temperature, the higher the probability of methane being found. This verifies that at lower temperatures, the structure is stable and is thus too tough to dissociate [246].

In Figure 5.4(b) c-o RDF of carbon of CO₂ and oxygen of hydrate, it can be observed that there is a rapid increment in the RDF values with the temperature. This

denotes that at higher temperatures, there is a probability of the CO₂ molecules forming clusters once they escape from the hydrate cage, making hydrate dissociation rapid. The second peak is around 6.61 Å, which is the distance between two CO₂ molecules in the nearest cage. On temperature increase, the second peak moreover increases, portending the escape of CO₂ from the structure. These escaped CO₂ molecules form a cluster at 4.1 Å. From these results, it can be observed that as temperature increases, the first peak increases and the second peak decreases (almost disappears) for C-O, indicating the complete hydrate dissociation in the system [152].

5.3.1.2. Effect of ethylene glycol concentration on Hydrate structure

Figure 5.5 illustrates the RDF at 285.15K with the variation of concentration. Figure 5.5(a) is the carbon-carbon RDF of methane. There is a decrease in the peak of RDF as the concentration increases. Since the concentration of the ethylene glycol increases, it breaks the hydrogen bond of the hydrate, making its structure weak. The guest molecules escape as the structures weaken. Hence, at 15% fewer water molecules will be found as compared to 10% or less. With 0%, the RDF was 8.14. Since 15% ethylene glycol injection reduces the RDF value to 4.7, observations indicate that hydrate dissociation increases with an increase in concentration, something which is also observed in previous studies [152].

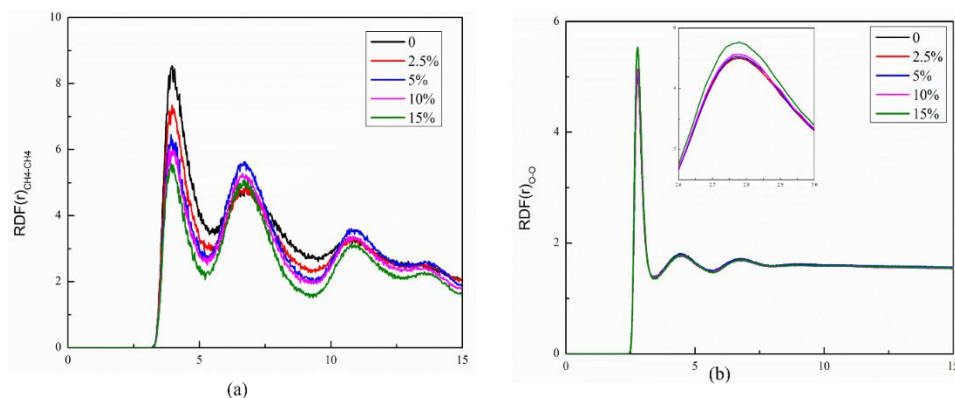


Figure 5. 5: Plots of RDF at 285.15K. (a) carbon-carbon of methane (b) oxygen-oxygen of water

Figure 5.5(b) indicates the RDF of oxygen-oxygen of water molecules. Since the concentration increases, more water molecules are found forming a cluster. This happens because of the structural failure of the hydrate. This also verifies that as the concentration increases, the hydrate dissociates rapidly.

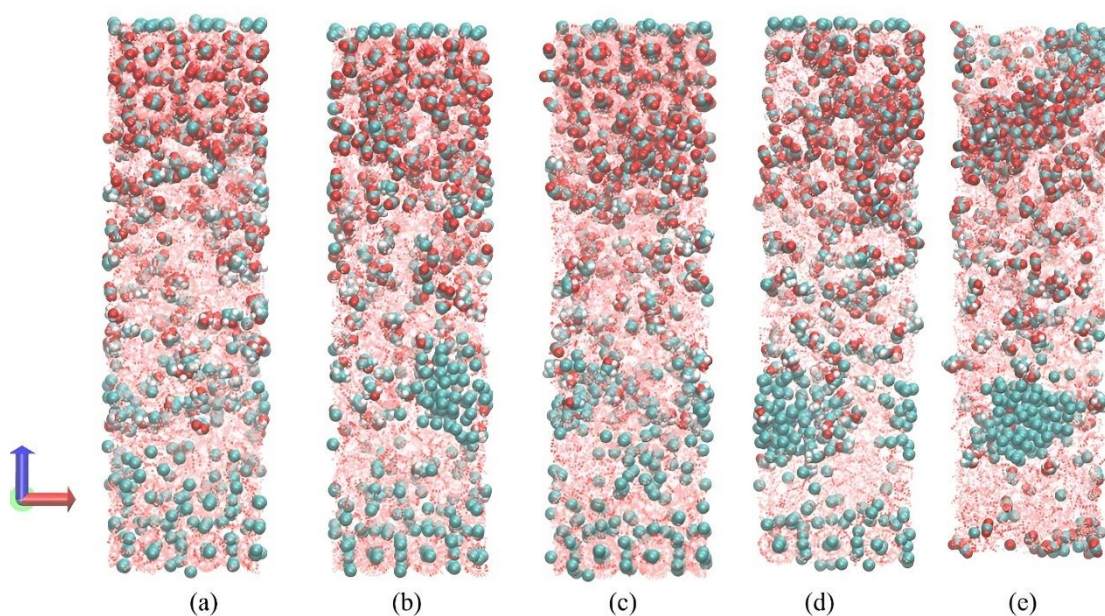


Figure 5.6: Final configuration of simulation box of 10% ethylene glycol at (a) 270.15 K, (b) 275.15 K, (c) 280.15 K, (d) 285.15 K, and (e) 300 K

5.3.2. Mean Square Displacement (MSD)

MSD is another parameter that analyses the dynamic property of molecules present in the system. It determines the average displacement of an atom, which is a function of time. It also explains the diffusion of molecules [152]. In MSD, each molecule's motions are separately modelled within the structure. It is defined as the average square displacement of a molecule from its original position over a given time. MSD moreover provides information about the diffusivity of the guest molecules within the hydrate [152]. It is essential to understand the behavior of these gases to develop the technology to extract them from hydrate reservoirs. The MSD can be expressed by the following equation [277]

$$MSD = \frac{1}{N} \sum_{i=1}^N (|R_i(t) - R_i(t_0)|^2) \quad (5.2)$$

Where N is the total number of particles, $R_i(t)$ is the position of the particle at time t, $R_i(t_0)$ is the initial position of the particles.

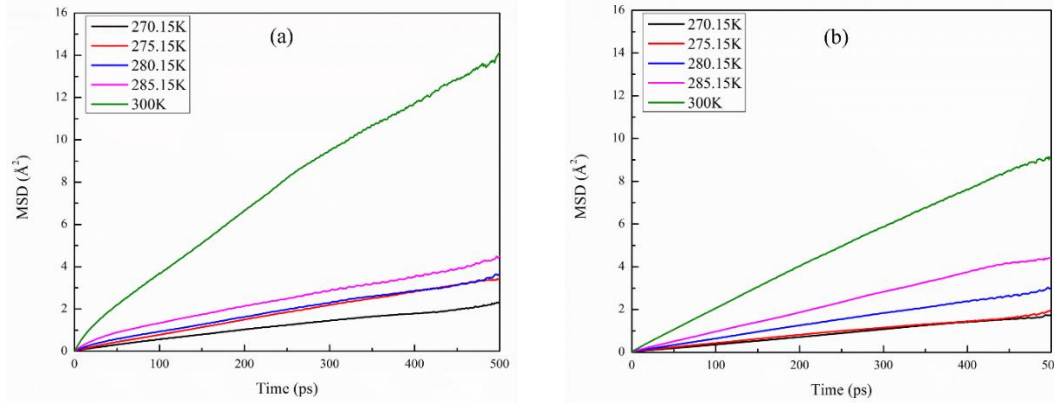


Figure 5.7: Plot of MSD of 10% concentration for (a) methane (b) CO₂

5.3.2.1. Effect of temperature

Figure 5.7 (a) shows the MSD of methane gas in the system; it is evident that at lower temperatures, the MSD changes very little. This means that the methane is still trapped inside the clathrate, and hence the hydrate structure is stable. At lower temperatures, initial MSD is very low, indicating the host molecules are still trapped inside the lattice of the hydrate. At lower temperatures, the molecules vibrate at their original position as they do not get enough energy to dissociate, making the structure stable. The order of MSD is 300K>285.15K>280.15K>275.15K>270.15K. As the temperature increases, the first breakage of the hydrate structure occurs around the phase boundary/interface between the solid and liquid. Then it extends toward the simulation box. It is seen from the graph that 300K has a higher MSD. The higher the temperature, the more the MSD, as the dissociation is faster.

Figure 5.7(b) shows the carbon dioxide MSD, which is in line with previous results. Here, the MSD of the system rises slowly initially, however after a period, it rises sharply

with an increase in simulation time. This indicates that the carbon dioxide entrapped inside the confined state changes to the free state, as the hydrate dissociates. MSD at higher temperatures is higher; it is easier for the carbon dioxide molecules to escape from the rigid hydrate structure. The movement of the molecules is due to the mass transfer in the gas hydrate; this happens due to the diffusion mechanism [152]. The diffusion coefficient of hydrate is a complex phenomenon mainly depending on the composition and condition of the hydrate. Temperature is also an important factor, as the temperature rises, the mobility of the guest molecules increases (Figure 5.6).

5.3.2.2. Effect of concentration

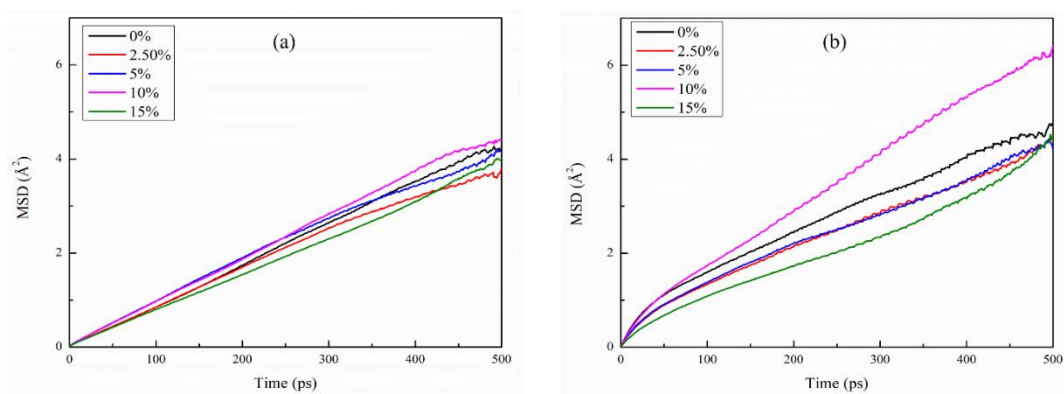


Figure 5.8: Plot of MSD of 285.15 K for (a) methane, (b) CO₂ at various concentrations

The MSD of methane is shown in Figure 5.8(a), which moreover indicates that as the simulation time increases, MSD rises slowly and then rises very sharply. The MSD of the 10% system was the highest. Figure 5.8(b) shows the MSD of CO₂ molecules for different concentrations. The graph clearly shows that as the concentration increases, the MSD in addition increases. With the increase in simulation time, the MSD initially rises slowly till 100 ps, then the rise is quick. The reason for less MSD in the initial stage is that the carbon dioxide molecules are still vibrating and trapped inside the lattice of the hydrate. As the dissociation happens, these molecules escape, giving the higher MSD into the simulation box (Also evident in Figure 5.2). The MSD is higher at 10% V/V, which means

that the solution having 10% EGY in the system dissociates the hydrate faster. It is evident from Figs 5.8(a) and (b) that the 10% ethylene glycol system was higher, indicating the decomposition of the hydrate in that system was faster. The conclusion obtained from this is that 10% of the ethylene glycol system had more impact on the dissociation of the hydrates. From these observations, it can be observed that ethylene glycol helps in breaking the hydrogen bond of the hydrates and affects the mass transfer of the carbon dioxide molecules.

5.3.3. Total Energy

Total energy analysis of the hydrate structure during the phase change transition of the hydrate stability, and how the gas and liquid interaction takes place. The total energy is simulated as a function of time [152]. Hydrate dissociation is an energy-absorbing process because it is an endothermic reaction. As the methane and carbon dioxide escape from the hydrate, the structure completely dissociates. Hence, the total energy tends to stabilize with time. The faster the scale of dissociation, the peak will be reached faster, as moreover observed in previous works [152]. The speed of these dissociations can be tracked by the total energy throughout the simulation time. Figure 5.9(a) and (b) show the total energy with various concentrations and temperatures, respectively. Figure 5.9(a) shows the total energy at 10% concentration at various temperatures. Here, figures suggest that as the concentration increases, total energy also rises with simulation time, indicating the dissociation of the hydrate. As the ethylene glycol concentration increases, the hydroxyl group present in it breaks the hydrogen bonds of the hydrate to destabilize the structure. This destabilization helps in faster dissociation [278]. Moreover, some of the hydroxyl groups form hydrogen bonds with water molecules [152]. This ultimately helps in completely dissolving the hydrate structure. Increased concentration helps more rapid dissociation. This results in faster breaking of the hydrate structure. Once the structure is

unstable, the guest molecules escape from the lattice, forming clusters of guest molecules. Hence, it can be said that the presence of ethylene glycol influences the dissociation rate.

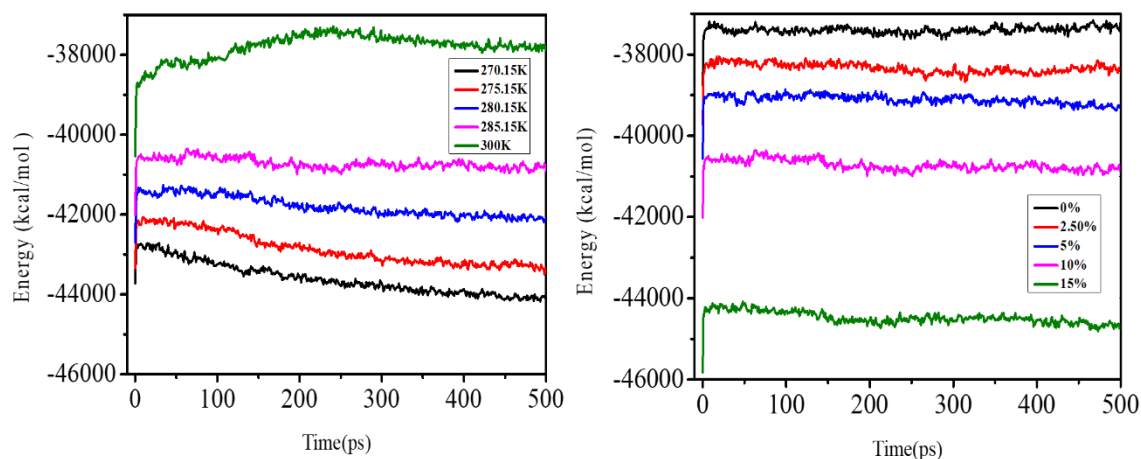


Figure 5.9: Observations of the total energy of the simulation box (a) at 10% concentration (b) at 285.15 K

Figure 5.9(b) illustrates the effect of temperature. As the temperature increases, the total energy takes very little time to reach the maximum value. This is due to the kinetic energy of the molecules increasing as the temperature increases [152]. This makes the structure vulnerable to dissociation and releases the guest molecules. The graph indicates that the total energy increased rapidly from 0.04ps to 1ps. As the energy increases, this helps the breaking of the hydrogen bonding in the hydrate, starting the dissociation process instantly. The structure remains stable approximately till 0.04ps. Between 0.04ps to 1ps, the total energy increases rapidly. During this time, the hydrate structure breaks and forms two distinct phases (liquid and gas). As the structure dissociates, the total energy becomes stable. After 1ps, there is no change in total energy, indicating the system is stable; no further hydrate structure is left for dissociation. From the values of total energy, it can be understood that as the temperature rises, dissociation occurs rapidly. The total energy increases and becomes constant, which shows that the system has reached equilibrium [152].

5.3.4. Diffusion Coefficient

The diffusion coefficient is defined as the average MSD at a certain point in the simulation box at a certain temperature and/or concentration, and is a measure of the pace of a molecule's diffusion in a medium [152]. Hydrate dissociation can be quantified through the diffusion coefficient; the equation for the same is provided by [147]

$$6Dt = MSD \quad (5.3)$$

Where D is the diffusion coefficient, t is the simulation time and MSD is the mean squared displacement. Table 5.2 summarizes the diffusion coefficient of water and carbon dioxide at various temperatures and concentrations. The table indicates that the diffusion coefficient of 270.15K & 275.15K is a deficient value of diffusion coefficient, this is due to the guest molecules moving and vibrating inside the hydrate cage structure without dissociating at this temperature. As the temperature increases, the hydrate structure breaks and hence rises in the diffusion coefficient. The dissociation takes place at the interface of solid and liquid. A liquid film will form near the interface. The higher the concentration, the more will be the thickness of the layer. This will affect the diffusion of the guest molecules. It is to be noted that the dissociation happens more in 10% V/V ethylene glycol solution as compared to 15% V/V solution. The diffusion coefficient is a function of time; thus, it needs to be a simulation decomposition process. The dissociation hydrate structure can be explained by the diffusion coefficient of methane and carbon dioxide at different points in the simulation box. Diffusion coefficient obtained from the velocity auto-correlation function.

Table 5.3: Diffusion coefficients of methane and carbon dioxide molecules

Concentration of ethylene glycol (%)	T (K)	Methane diffusion coefficient ($\times 10^{-5}$ cm ² /s)	Carbon dioxide coefficient ($\times 10^{-5}$ cm ² /s)
2.5	270.15	0.593	0.587
5		0.632	0.586
10		0.683	0.687
15		0.662	0.427
2.5	275.15	1.165	0.565
5		1.225	0.830
10		1.242	0.907
15		0.775	0.775
2.5	280.15	1.234	0.900
5		1.359	0.964
10		1.355	1.024
15		0.950	0.944
2.5	285.15	1.294	1.147
5		1.360	1.210
10		1.711	1.299
15		1.175	1.282
2.5	300	3.947	1.901
5		4.392	2.916
10		4.506	3.290
15		4.358	3.013

5.4. Conclusion and Summary

In this study, MD simulations were explored to quantify the dissociation of both CO₂-CH₄ hydrate cages in the presence of ethylene glycol. Uniquely, these investigations were performed for a system that contains both methane and carbon dioxide gas hydrates, to

better mimic a natural hydrate accumulation undergoing carbon sequestration and methane recovery. These simulations were performed using Gromacs. The NPT (isobaric isothermal) ensemble was performed to understand the hydrate stability and dissociation process. The simulations were run at different concentrations (0%, 2.5%, 5%, 10% & 15%) and temperature (270.156K, 275.15K, 280.15K & 285.15K) to better mimic the field conditions. The RDF and MSD were used to study the dissociation process, as these help in quantifying the dissociation of the hydrate structure. Next, the Diffusion coefficient was analyzed to understand the molecular diffusion in the system. From the results of the RDF, it was observed that the methane curve decreases as the temperature increases, indicating the unstable structure of the hydrate. The RDF of carbon dioxide with water shows an increase in peak, indicating the dissociation of the structure [279]. Similarly, the peak of methane in water reduces with an increase in temperature, which shows that the methane gas has escaped from the lattice of the hydrate structure. RDF curve of carbon-carbon shows a change in peaks, indicating an unstable structure and pointing to the dissociation of the hydrate structure. It is also to be noted that the width of the curve increases. This verifies the dissociation process. The MSD and diffusion coefficient also increase with time, indicating the dissociation process [279]. The results illustrate that the optimum concentration of ethylene glycol in this simulation system is 10% V/V for both CO₂ and CH₄ hydrate dissociation when they coexist in the simulation system. The findings provide a very excellent knowledge of how ethylene glycol interacts with both CO₂ hydrate and CH₄ hydrate at the molecular level. It will aid in the creation of new hydrate inhibitors and their optimization for use in flow assurance applications and the extraction of methane gas from hydrate reservoirs.

Chapter 6: Impact of single-step SiO₂ nanofluid on the kinetics of CO₂ Hydrate formation Relevant for Carbon Capture and Storage

Abstract

Increased greenhouse gases (GHGs) emissions have led to global warming, and the adverse effects of increased atmospheric CO₂ concentration on the entire ecosystem necessitates the rapid development of carbon capture and storage (CCS) solutions. Out of many initiatives, capturing and storing CO₂ in hydrate form seems attractive as it can ensure long-term storage. The process kinetics are, however, slow, necessitating the development of additives/methods to accelerate the hydrate formation. Metallic nanoparticles (NPs) stand out as promising due to increased surface area, enhanced heat, and mass transfer. Literature regarding the effect of the single-step nanoparticles on the hydrate formation kinetics is scarce. This study investigates the impact of nanofluid solutions containing single-step SiO₂ NPs on the CO₂ hydrate formation kinetics and the storage capacity, crucial for CCS applications. Single-step SiO₂ NPs (~5 to 150 nm) were synthesized through the sol-gel process, and stability studies were conducted. Different nanofluid solutions were considered in this study (20, 40, and 100 % v/v in the aqueous phase, each with three different NPs concentrations of 0.5, 1.0, and 1.5 wt% SiO₂). It was observed that increased NPs concentration in the nanofluid up to 1 wt% resulted in an enhanced CO₂ capture capacity due to a higher available surface area for CO₂ absorption, and interfacial area for mass transfer through the gas-liquid interface. Additionally, at the same NPs concentration, the CO₂ hydrate formation kinetics is enhanced due to heat-mass transfer, surface area and system homogeneity. Further increase in the NPs concentration (> 1 wt%), hindered the hydrate formation kinetics due to nanoparticles agglomeration and development of heterogeneity in the system. It can be concluded that a nanofluid with a higher (optimum)

concentration of single-step SiO₂ NPs is more effective (as promoters) for CO₂ hydrate formation kinetics and the storage potential

6.1. Introduction

Climate change is one of the most significant concerns in the 21st century. Increased fossil fuel consumption has led to a significant rise in greenhouse gas (GHG) emissions, raising the earth's average surface temperature and endangering the lives of all living beings. Of all the greenhouse gases, CO₂ is the major contributor [280]. Based on the annual National increasing carbon dioxide (CO₂) level in the atmosphere and the resultant global climate change concerns have intensified the search for effective al the Oceanic and Atmospheric Administration (NOAA) report, the average annual atmospheric CO₂ concentration rose to ~419.3 ppm in 2023 [281] due to ~36.6 billion tonnes CO₂ emission. The oil and gas industry is a major contributor to the GHG emissions, with up to ~5.1 billion tonnes (gigatonnes or Gt) CO₂-eq in 2022 (~66.7% through crude oil and the rest through natural gas), which is just below ~15% of the total energy-related GHG emissions [282]. The annual rate of rise in CO₂ concentration in the past 60 years has been more than ~100 times the previous natural causes [281]. With the current rate, the threshold of ~1.5°C is likely to be crossed by 2030 [283]. This will lead to rising sea levels and unpredictable weather, disturbing the entire ecosystem [284]. Ocean acidification is seen as the major culprit behind the disruption in the ecosystem. Oceans have absorbed enough CO₂, resulting in a reduction of pH by 0.1 (equivalent to 30% increase in acidity) [281].

As evident from the above discussion, reducing the atmospheric CO₂ level is a pressing issue that would ultimately help improve environmental, social, and economic aspects in the long run. Climate change was first addressed in 1992 at the UN Conference on Environment and Development by adopting the “United Nations Framework Convention on Climate Change (UNFCCC)” [285]. Since then, mitigation strategies for

the increased anthropogenic CO₂ concentration have drawn wide attention from the research and industry communities. Another crucial initiative in this regard is the “Paris Agreement” or the UN Climate Change Conference (COP 21) in 2015, which aims to limit the global temperature below ~2°C, compared with the pre-industrialization level [286]. India’s cumulative CO₂ emissions (1850 - 2019) amount to less than 4 % of the world from the pre-industrial era. India launched the National Action Plan for Climate Change (NAPCC) in 2008 to mitigate and adapt to climate change, consisting of various missions, some of which focus on renewables, sustainable habitat and agriculture, and enhanced energy efficiency. In addition, India has adopted a net-zero emissions target by 2070. Even the aggressive CO₂ reduction measures could take ~ 80 or more years to limit to 1.5°C [287], highlighting the severity of the issue.

One of the ways to mitigate the increased atmospheric CO₂ level is carbon capture and storage [280], which essentially aims to reduce CO₂ discharge into the environment. The approach involves three stages: a) CO₂ capture from a large point source; b) Treatment and transportation to a long-term storage location; c) injecting it into the site for long-term sequestration. The geological storage of CO₂ can be realised through various trapping mechanisms, including structural, mineral, residual, and solubility trapping [288,289]. For facilitating carbon capture and storage, various materials (absorbents) have been used by industrial processes, including amines [290], zeolites [291], metal-organic frameworks [292], and solid absorbents [293]. Compared to solid absorbents, storage of this CO₂ can be maximized if it is injected in the sub-surface geological formations, which include depleted oil and gas reservoirs, saline aquifers, deep coal seams, and hydrate deposits [294–297] Worldwide efforts have been encouraged in recent years by the sequestration of CO₂.

A promising way of storing CO₂ is through solid clathrate hydrates in subsurface environments (discussed previously), where it can be stored for a longer period, resulting

in less greenhouse gas emission [298]. A cubic meter of gas hydrate can hold ~160-180 cubic meters of gas at standard temperature and pressure [106,299]. CO₂ hydrate CO₂·nH₂O consists of 46 H₂O molecules and up to 8 CO₂ molecules (assuming a complete cage occupancy, which has been hypothesized at sufficiently high pressure) [300,301]. The formation of CO₂ hydrate has been studied by NMR spectroscopy [302,303], Neutron diffraction [304,305], and X-ray diffraction [306]. The complicated mechanism involving heat and mass transfer at low temperatures and high pressure limits the creation of CO₂ hydrate. As a result, a significant amount of energy is used in the cooling and pressurization process, apart from other challenges, such as low rates and low gas consumption. Hence, developing efficient and low-energy capture is necessary to overcome these challenges [307].

Various methods have been used to facilitate hydrate formation, viz. agitation, spraying, and bubbling [208–210,308]. These processes are relatively expensive on an industrial scale. So, various additives (thermodynamics and kinetics) have been explored as a possible CO₂ hydrate storage solution [309]. In literature, thermodynamics additives like tetrahydrofuran (THF) [310], tetrabutylammonium-bromide (TBAB) [311], cyclopentane (CP) [312] were used to form hydrate at increased temperature and reduced pressure. Kang et al. [211] investigated the impact of 1-3 mol% THF on the phase equilibrium of CO₂/N₂ gas. The results concluded a shift in the phase equilibrium to higher temperature and lower pressure. It is also noted that introducing 5.56 mole% of THF inhibits the hydrate formation. Li et al. [313] and Fan et al. [314] examined the effect of TBAB and CP on CO₂ hydrate, respectively, and both reports reduced energy consumption and enhanced hydrate formation kinetics. Kinetic additives such as sodium dodecyl sulfate (SDS) [176,315] decrease induction time with an increase in gas storage capacity by 14 times. Nahri et al. [220], explores SDS with an increase in 70% of induction time and 160%

mole consumption during hydrate formation. Cetrimonium bromide CTAB [174,186,316] moreover increases the hydrate promotion. Chemical additives lower the gas-liquid surface tension and quicken the guest molecule's dissolution, thus increasing gas consumption. Ganji et al. [216] have examined CTAB, and their results conclude that 1000 ppm works better than other concentrations. The impact of CTAB along cooper NPs was investigated by Pahlavanzadeh et al. [186], who found that higher concentrations of CTAB had a greater effect on the process of hydrate formation. Using larger quantities of this surfactant is toxic [219]. As a result, their use should be kept to a minimum, with any remaining impact being offset by the employment of another qualified promoter.

Adding nanoparticles (NPs) is a new trend in hydrate-based CO₂ capture. NPs have a large surface-to-volume ratio, aiding in the CO₂ absorption. Moreover, these NPs are metallic and conductive. Since these NPs are in a metallic form, they enhance the hydrate formation kinetics due to enhanced heat and mass transfer, for example, Cu NPs [181]. Sloan and Koh [17] and Zhou et al. [185] have examined the effect of graphite NP in gas hydrate formation and observed an enhanced hydrate formation tendency (~81 % reduction in induction time). Park et al. [177] highlight the impact of carbon nanotubes on the volume of hydrate storage and induction time. The results indicate a ~300% increase in the volume of stored gas. Arjang et al. [178] and Dongliang et al. [183] have used silver nanoparticles (75nm size) and carbon nanotubes (20nm size) for faster hydrate formation, respectively. Najibi et al. [180] noted that the heat transfer rate is increased by introducing 40 nm copper NPs into the system, which ultimately results in more gas consumption and storage capacity. Kumar et al. [227] explored the L-arginine as a promoter in the methane hydrate system. The primary finding indicates that NPs' high surface energy was a crucial characteristic in the promotion of gas hydrate. Apart from all these advantages, there is one major disadvantage of using these NPs: they tend to agglomerate and settle when mixed

externally [228,317], thus necessitating their synthesis. These NPs are aqueous phase by adding the precursor and accelerator while adjusting the pH and temperature. These are called single-step NPs, which have a more controlled particle size distribution and are agglomeration-free, resulting in enhanced heat and mass transfer, crucial for hydrate formation. However, the data regarding the effect of single-step nanoparticles on the hydrate formation is scarce, which is the focus of this investigation.

In this research paper, we have studied the impact of different nanofluid solutions containing single-step silica NPs on the CO₂ absorption and the hydrate formation kinetics. Single-step SiO₂ NPs (varying sizes of 5 to 150 nm) were synthesized through a sol-gel process, and stability studies were conducted. Different nanofluid solutions (20, 40, and 100 % v/v nanofluid) were synthesized with three different NPs concentrations of 0.5, 1.0, and 1.5 wt% of SiO₂. The parameters, such as moles of gas consumption and storage capacity were determined at ~275.15 K temperatures and ~3.5 MPa, and the results were compared for hydrate storage applications.

6.2. Materials and Methods

6.2.1. Materials

Ammonium hydroxide and tetraethylorthosilicate (TEOS) were sourced from Sisco Research Laboratories Pvt. Ltd., while Sigma Ltd. (India) provided Polyacrylamide (PAM), the base solution for the preparation of nanofluid. Ethanol was procured from Changshu Hongsheng Fine Chemical Ltd., China. The DI water for nanofluid preparation was obtained from Millipore[®] Elix-10. For CO₂, a stainless-steel cylinder 47.6 litres (Purushottam gas suppliers, India), equipped with a pressure regulator, was used. D-Lab magnetic stirrer (model no MS-H280-Pro) was used for mixing and preparation of NPs. Table 6.1 provides the list of chemicals use in this experiment.

Table 6.1: Chemical details used in the experiment

Chemical Name	Name of the company	CAS number	Purity
Ammonium hydroxide	SRL chemical	1336-21-6	99.9%
Tetraethylorthosilicate (TEOS)	SRL chemical	78-10-4	98%
Ethanol	Changshu China	64-17-5	99.9%
Polyacrylamide (PAM)	Sigma-Aldrich	9003-05-8	98%
CO ₂ gas	Sigma	75-21-8	99.9%

6.2.2. Nanoparticle preparation and characterization

Sol-gel method was used for NPs preparation. The first step was the base fluid preparation (1000 ppm of PAM in 1000 mL of DI water). In the second step, 80 mL of PAM solution was added to 20 mL of Ethanol in a dropwise manner at 800 rpm for 100 min. Next, 3mL TEOS was added to the solution dropwise for another 250 min. In the final step, a certain amount of ammonium hydroxide was added to the solution and further stirred for 100 min. The appearance of white precipitates confirmed the NPs formation. NPs zeta potential measurement and particle size distribution were obtained from DLS measurement (SZ-100, Horiba Scientific, Singapore).

6.2.3. Hydrate formation studies

6.2.3.1. Experimental setup for hydrate studies

The hydrate setup (shown in Figure 6.1) consists of a SS-316 stainless steel stirred reactor with ~250 mL volume, a syringe pump, and a water bath (D-cam Engineering, Ahmedabad). The reactor is made of SS316. The reactor is equipped with a pressure (HD20V4T, Delta Ohm, Italy, ±0.01 MPa accuracy) and two PT-100 temperature sensors (±0.01 MPa accuracy) with an operating range of 0.05-120 MPa and 250-400 K,

respectively. The experimental temperature is maintained by circulating a glycol-water mixture through the reactor water jacket (with the help of a water bath).

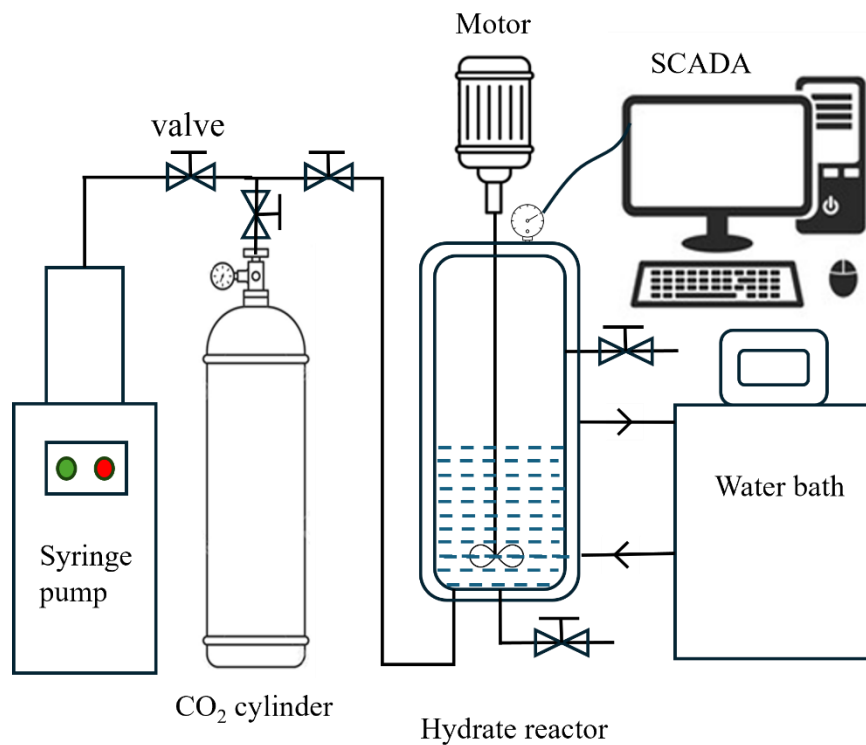


Figure 6.1: Schematic diagram of the hydrate system

6.2.3.2. Experimental procedure for hydrate studies

Before every experiment, the reactor is rinsed clean with DI water. The required amount of aqueous solution is then injected into the reactor, and it is closed tightly, followed by a leakage test. The reactor is purged 3-4 times with the hydrate former gas (CO_2) at a low pressure of 0.1 MPa. After injecting CO_2 at the desired pressure (~ 3.5 MPa), the stirrer is switched on and set at 500 rpm (maintained throughout all experiments), ensuring minimum possible heat and mass-transfer resistance through the hydrate formation. The hydrate nucleation was indicated by a temperature increase (exothermic nature of hydrate formation) and a corresponding sudden pressure decrease (CO_2 consumption during hydrate formation). The data logger records the data every 10 sec. All the experiments are performed three times for repeatability. The fresh sample is introduced

in each experiment into the autoclave for repeatability. This was done to eliminate the memory effect of the gas hydrate. The obtained temperature and pressure data through SCADA software are used to calculate all the necessary parameters, like induction time, rate of gas consumption, and moles of consumption.

6.2.4. CO₂ absorption experiment

CO₂ gets trapped inside the nanofluids, which have been investigated by the same setup as used in hydrate formation experiments (Figure 6.1). After injecting the required solution and applying the pressure at 3.5 MPa (with the help of a syringe pump), the stirrer is switched on. As the CO₂ gets absorbed into the solution, pressure reduction ensues, which continues till the equilibrium pressure indicating no further absorption. This CO₂-entrapped solution is taken out of the autoclave for further analysis. The molality is calculated by following the equation [318]

$$n_{\text{CO}_2}^{\text{abs}} = \frac{n_{\text{CO}_2}^i}{n_{\text{CO}_2}^f} = \frac{\frac{P_i V_{gc}}{Z_{\text{CO}_2}^i RT_i}}{\frac{P_f (V_{\text{cell}} - V_{\text{nf}})}{Z_{\text{CO}_2}^f RT_f}} \quad (6.1)$$

When *i* and *f* represent the initial and final value corresponding value. P is pressure, T is temperature, R is the gas constant, and Z is the compressibility factor. $n_{\text{CO}_2}^{\text{abs}}$ is the CO₂ moles absorbed. V_{gc} , V_{nf} and V_{cell} is the volume of the gas, the volume of the nanofluid, and the volume of the cell, respectively.

6.3. Results and discussion

The kinetic effect of single-step silica nanofluid on carbon dioxide hydrate formation was studied in the research paper. Hydrate was synthesized with varying nanofluid concentrations to find the gas consumption, gas consumption rate, induction time, and storage capacity. Moreover, the nanofluid's stability and size were explored in this study.

6.3.1. Stability and DLS measurements

Upon preparation, each sample of nanofluids was kept in a transparent cell culture tube undisturbed for 45 days (see Figure 6.2). It is clear from the figure that with time, there is a slight settlement of NPs at the bottom of the cell culture tube. It can be observed that the sample S₃ has a higher settlement than S₁ and S₂. Table 6.2 illustrates the zeta potential and particle sizes of the synthesized nanofluids.

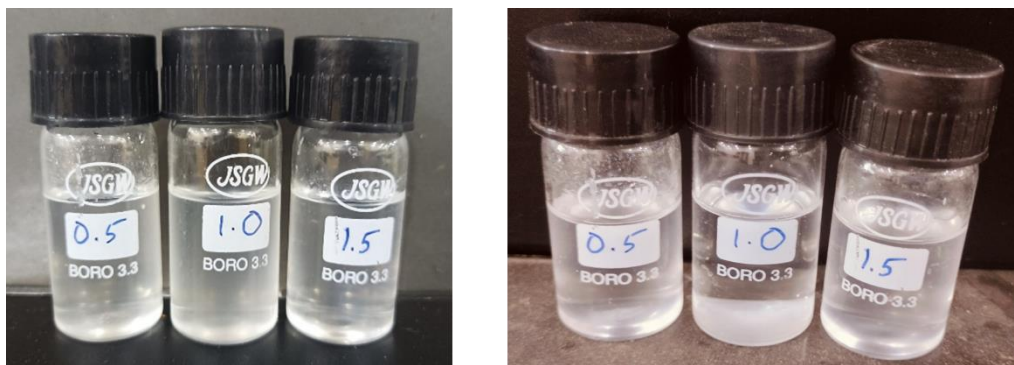


Figure 6.2: Actual image of synthesized nanofluids in the lab (a) 0 day (b) 30 days

Table 6. 2: DLS measurements of synthesized nanofluids at room temperature

Sample name	Nomenclature	Zeta Potential (mV)		Particle size (nm)	
		0 days	30 days	0 days	30 days
DI water	S ₀	NA		NA	
0.5 wt% (SiO ₂)	S ₁	-56.1	-42.4	21	38
1.0 wt% (SiO ₂)	S ₂	-41.3	-31.6	46	61
1.5 wt% (SiO ₂)	S ₃	-64.1	-47.7	86	104

The measured zeta potential for S₁ (0.5 wt% of SiO₂ NPs) is around 56.1 mV on the day of preparation, and for samples S₂ and S₃, it is ~ 41.3 mV and ~64.1 mV, respectively. This value is well above the unstable value between 30 mV to -30 mV [319]. As time goes by, the zeta potential changes. This is due to NPs present inside the sample getting agglomerated, forming a large cluster of NPs, reducing the overall stability. Experiment data indicate small changes in the zeta potential after 30 days. S₁ has ~42.4 mV, whereas S₂ and S₃ have ~31.6 mV and ~47.7 mV, respectively. The particle size distribution is an indicative of sample stability. NPs in S₁, S₂, and S₃ have an average particle size of 21 nm, 46 nm, and 86 nm, respectively. After 30 days, the particle size increases, indicating the NPs inside the system agglomerate and increase its size to 38 nm (S₁), 61 nm(S₂), and 104 nm(S₃).

6.3.2. CO₂ absorption results with NPs

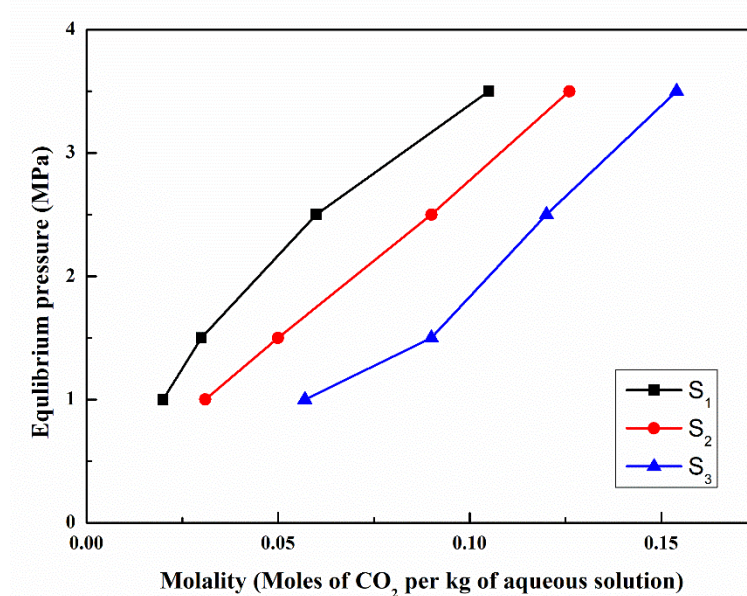


Figure 6.3: Molality results of CO₂ for all synthesized nanofluids (S₁, S₂ and S₃) at room temperature different equilibrium pressure

CO₂ absorption results (equilibrium pressure vs molality) for the three nanofluids (S₁, S₂, and S₃) are shown in Figure 6.3. It is observed that as the concentration of NPs increases (from S₁ to S₃), CO₂ absorption increases significantly (19.6% and 44.1% for S₂

and S_3 , respectively, compared to S_1 . Nanofluid exhibits higher CO_2 absorption than pure water [320], due to factors such as higher surface area, enhanced mass transfer, etc. Higher surface area leads to more contact of CO_2 with the aqueous phase, leading to faster absorption [321]. Nanoparticles moreover enhance the mass transfer properties [235], leading to more CO_2 molecules being transferred from the gas phase to the liquid phase. These NPs act as surfactants and can also prevent the agglomeration of gas bubbles, helping to maintain a high interfacial area between two phases and promoting CO_2 absorption [322]. Combining all the parameters, it can be said that CO_2 absorption is better compared to pure water.

6.3.3. CO_2 hydrate formation kinetics in the presence of NPs

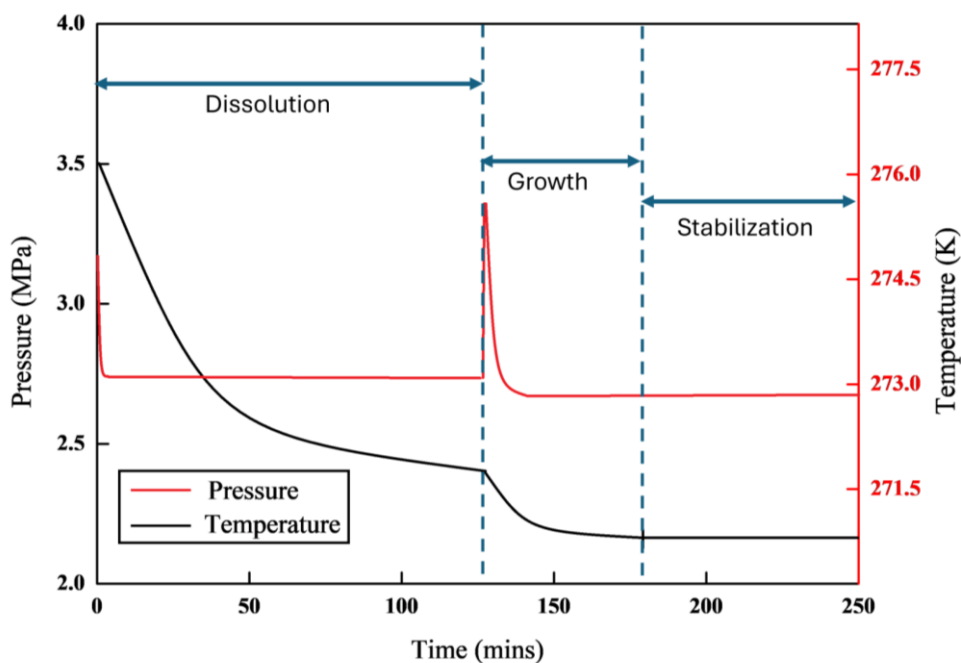


Figure 6.4: Pressure vs Temperature profile of the 0.5 wt% (S_7) Nanofluid

Figure 6.4 indicates the pressure and temperature variation through the hydrate formation experiment (3.5 MPa and 275.15 K), starting from injection to steady-state pressure and temperature with 0.5 wt% concentration S_7 (40% Nanofluids + 60% DI water) along with time at 3.5 MPa pressure and 275.15 K temperature. As observed in the figure, the CO_2 hydrate system is divided into three stages: dissolution, growth, and stabilization.

In the Dissolution stage, the CO₂ gas is absorbed into the aqueous solution as indicated by the reduced pressure (~1 MPa within ~139 min). However, the temperature remains almost constant throughout the first stage. Hydrate nucleation theory [90] states that during the first stage, recurrent formation and dissolution of unstable water clusters happen simultaneously, which does not affect the system's temperature. In the next phase (~139 min), a sudden spike is observed in temperature (exothermic hydrate formation nature) along with a corresponding pressure reduction (gas consumed in hydrate formation) due to hydrate induction. As soon as the induction time is achieved, rapid hydrate formation and gas consumption take place, resulting in a decrease in the pressure profile. As the hydrate formation proceeds, the driving force as well as mass transfer between gas-liquid reduces due to a decrease in the pressure (~0.15 MPa). After ~179 min, pressure and temperature have been observed to reach a steady state, indicating a hydrate saturation in the system.

Table 6.3: Induction time for at 3.5MPa and 275.15K

Aqueous phase	Nomenclature	Induction time	Average Induction time
		197.5	
DI Water	S ₀	166.3	175.4
		162.4	
		63.8	
100% Nanofluids	S ₁ (0.5 wt%)	48.2	51.1
		41.3	
	S ₂ (1.0 wt%)	40.4	36.3

		30.8	
		38.6	
		46.2	
	S ₃ (1.5 wt%)	45.8	44.8
		42.4	
		154.6	
	S ₄ (0.5 wt%)	141.3	146.3
		143.0	
		124.4	
20% Nanofluids + 80% DI water	S ₅ (1.0 wt%)	117.1	111.8
		93.9	
		141.9	
	S ₆ (1.5 wt%)	126.8	129.6
		120.1	
		139.5	
	S ₇ (0.5 wt%)	120.7	121.3
40% Nanofluids + 60% DI water		103.7	
		83.0	
	S ₈ (1.0 wt%)	86.7	84.6
		84.1	

110.8

S₉(1.5 wt%)

91.1

101.3

102

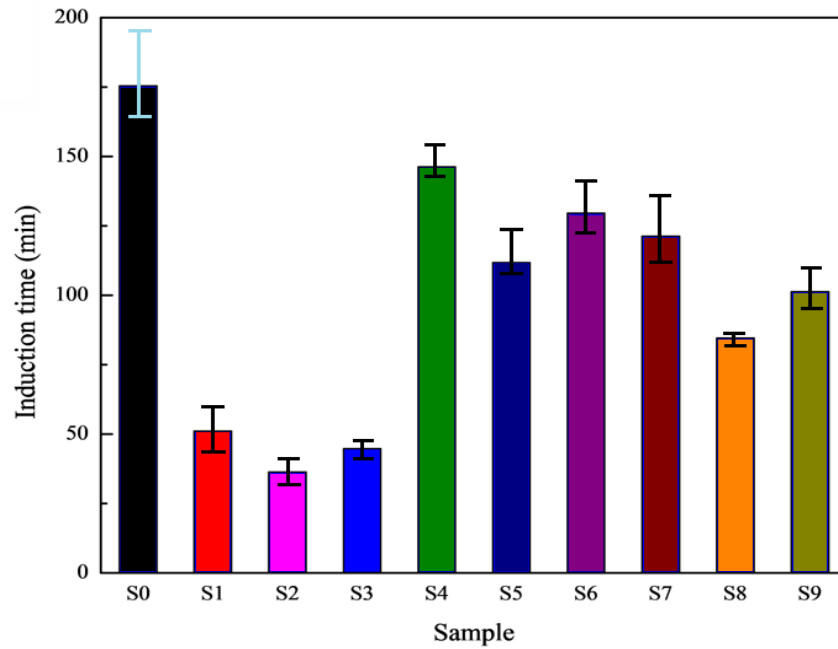


Figure 6.5: Induction time for synthesizing NPs concentration-wise

Figure 6.5 and Table 6.3 show the average CO₂ hydrate induction time for all systems. It is evident that as the concentration of the NPs increases, the average induction time first reduces for systems with 1 wt% NPs before an observed slight increase for 1.5 wt% case. From Table 6.3, there is an observed decrease in the induction time of ~70.9%, ~79.3%, and ~74.4% for S₁, S₂, and S₃ samples, respectively, compared to pure water. A decrease in induction time indicates fast heat and mass transfer within the system. As explained earlier, metallic NPs have higher thermal conductivity which enhances the heat transfer during hydrate formation. Additionally, an increased surface area enhances the hydrate nucleation. They moreover enhance the mass transfer required for forming hydrate [235]. The reason for the increase in the induction time from 1 to 1.5 wt% is due to the fact that after the

optimum concentration of the NPs, there is a particle agglomeration tendency which hinders the formation of the hydrate in the system by making the system heterogeneous [323]. So, it can be said that the optimum concentration is ~1.0 wt% for the temperature ~275.15 K. To verify the effect of NPs, several more experiments have been conducted. The samples S₄, S₅, and S₆, have 20% (v/v) Nanofluid and 80% (v/v) DI water whereas S₇, S₈, and S₉ have 40% nanofluid and 60% DI water. Sample S₄ has an average hydrate induction time of ~146.3 min, S₅ shows 111.8 min, and S₆ gives 129.6 min. For S₇, S₈, and S₉, the average induction time varies from ~121.3 to ~84.6 and ~101.3 min. From Table 6.3, it can be concluded that as the NPs concentration increases, the average CO₂ hydrate induction time decreases up to 1 wt%, followed by an increase for 1.5 wt%, probably due to a less homogeneous solution of nanofluid in the system.

6.3.4. CO₂ gas consumption during hydrate formation

The temperature and pressure were maintained at 275.15K and 3.5 MPa at 500 rpm. The following equation is used to calculate the mol of CO₂ consumed in hydrate formation

$$\Delta n_{CO_2} = \frac{1}{R} V \left(\frac{P_0}{Z_0 T_0} - \frac{P_t}{Z_t T_t} \right) \quad (6.2)$$

where R is the universal gas constant, P and T are reactor pressure and temperature, Z is the CO₂ compressibility (calculated by Peng-Robinson equation), and V represents the gas phase volume above the solution. Subscripts '0' and 't' represent initial and elapsed time from the hydrate induction.

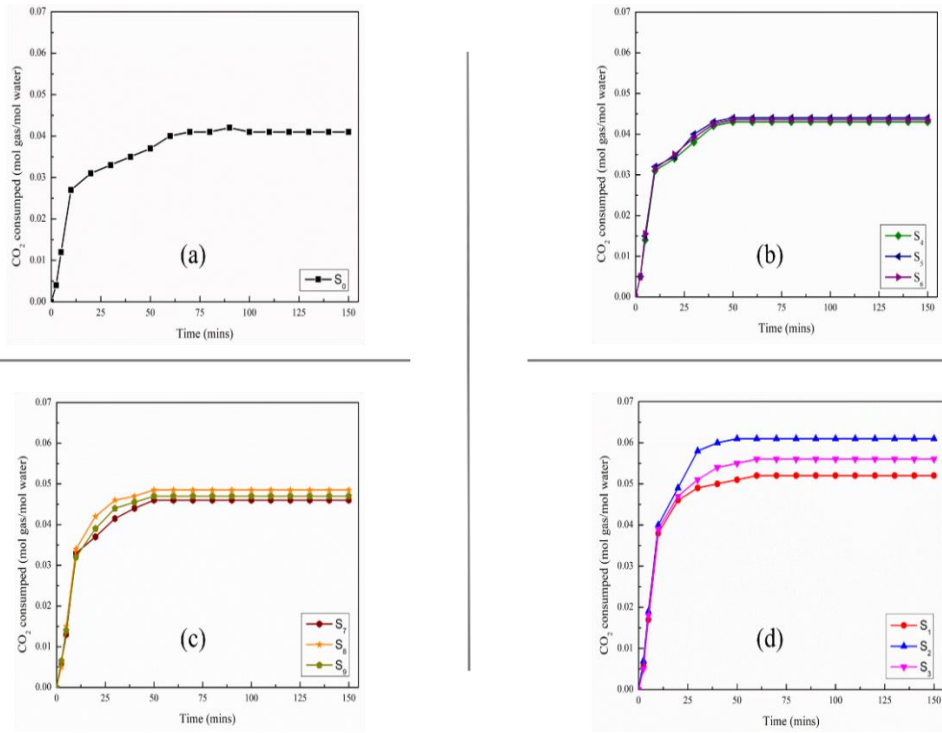


Figure 6.6: CO₂ consumption for all NPs

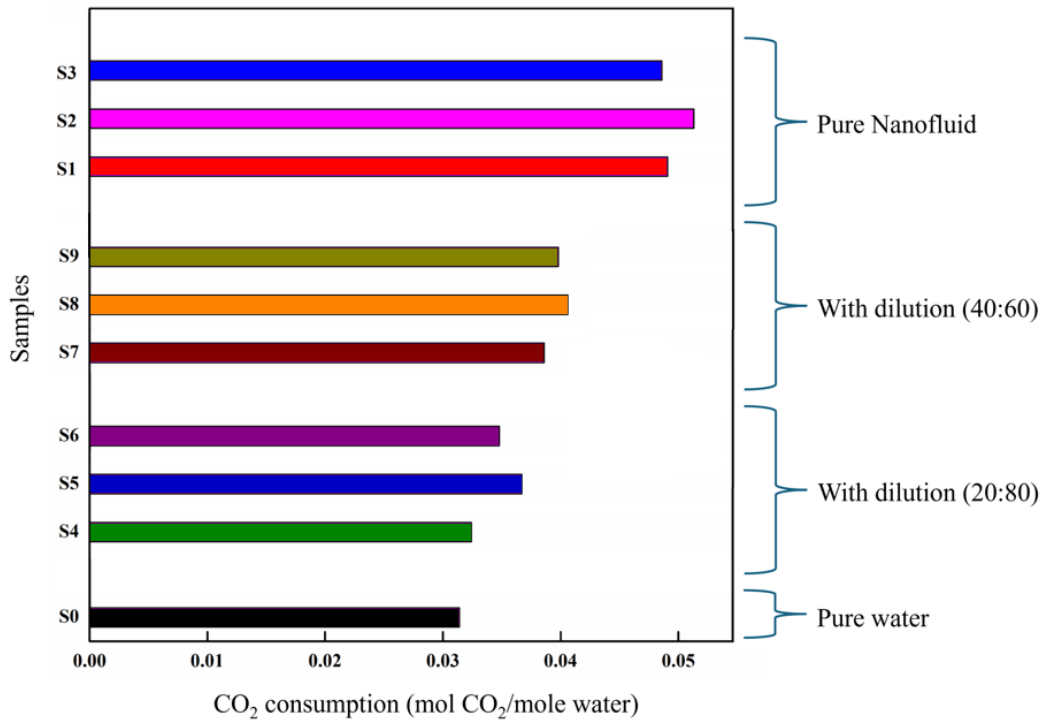


Figure 6.7: Final amount of CO₂ consumption for during 120 mins of hydrate growth

Figure 6.6 represents the mol of CO₂ consumption during the hydrate formation (mol for all the systems. It is visible from the figure that the presence of NPs in the system

has a positive effect on the amount of CO₂ consumption in the hydrate formation (reasons explained in the previous section). The amount of CO₂ consumption for the initial time is found to be approximately 0.041 mol for pure water. Figure 6.7 indicates the cumulative gas consumption at the end of hydrate formation. The maximum gas consumption is observed in the presence of 1.0 wt% (S₂) concentration. This indicates as the NPs concentration increases, more CO₂ gets absorbed inside the system, thereby enhancing the chances of hydrate nucleation sites. Additionally, compared to pure water, S₁, S₂, and S₃ have an increased gas consumption by ~26.8 %, 48.8 %, and 36.5%, respectively. For other samples like S₄, it is found to be 0.043 mole. Similarly, for S₅ and S₆, the consumption was 0.441 moles and 0.435 moles of CO₂ in the system. The mole consumption was 0.0464 moles, 0.0485 moles, and 0.474 moles for samples S₇, S₈, and S₉, respectively. Heat and mass transfer are crucial for hydrate growth. It is well established that NPs have a higher surface area, resulting in increased mass transfer occurring between liquid and gas inside the system. NPs increase the driving force during hydrate formation and hence lead to higher mole consumption. Moreover, hydrate formation is an exothermic reaction. This exothermic reaction can also affect the growth process of hydrate. The presence of NPs in the system enhances heat transfer by extracting heat from the hydrate system effectively, which enhances the exothermic reaction.

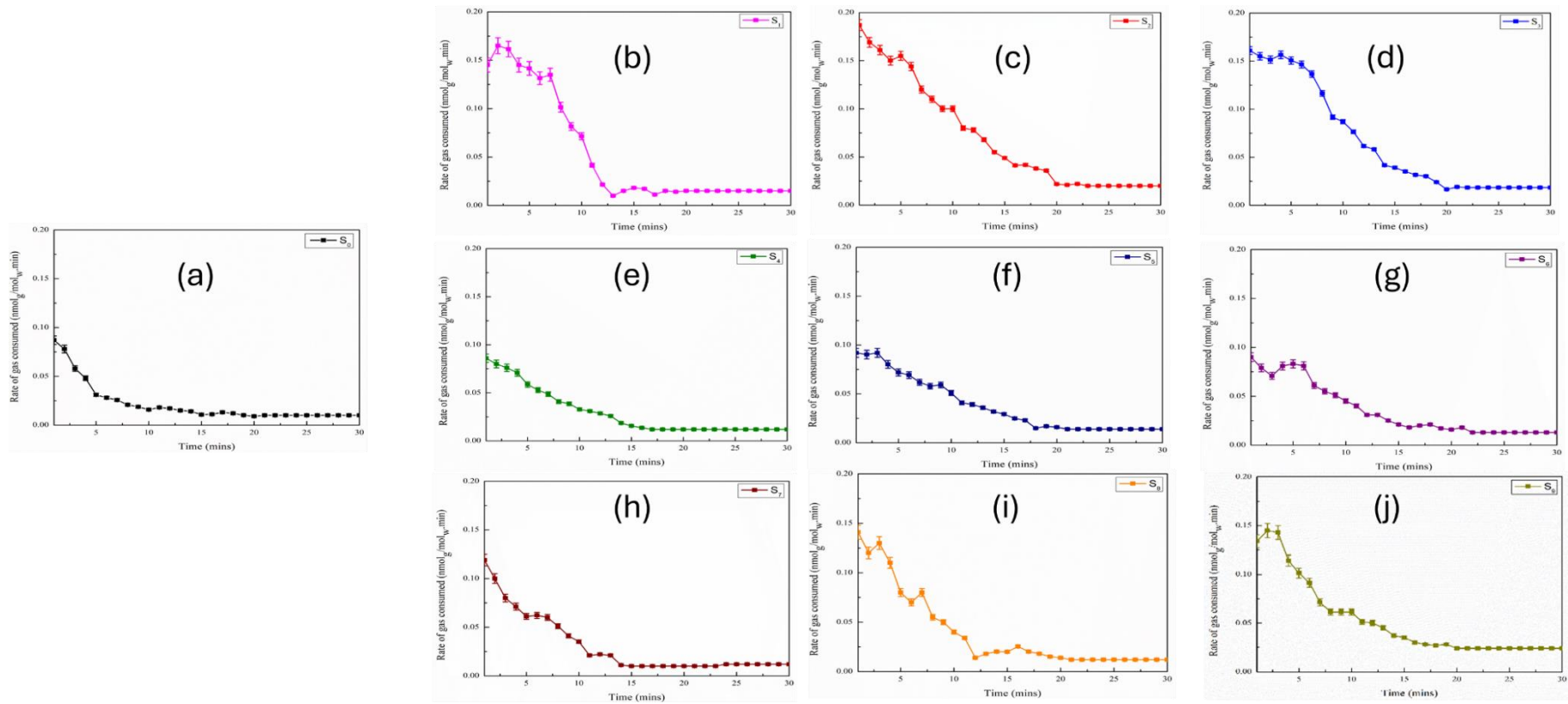


Figure 6.8: Rate of hydrate Formation for various concentrations of NPs

6.3.5. Rate of hydrate formation

The equation used to calculate the rate of hydrate formation $r(t)$ is given by Mohammadi [198]

$$r(t) = \frac{n_{CH_4,i-1} - n_{CH_4,i+1}}{(t_{i+1} - t_{i-1}) n_{W_0}} \quad (6.3)$$

where $n_{CH_4,i-1}$ is the amount of moles of carbon dioxide in the gas phase at t_{i-1} time. $n_{CH_4,i+1}$ is the mole number of carbon dioxide in the gas phase at t_{i+1} time. The number of carbon dioxide moles is calculated by the real gas equation. n_{W_0} is the initial mole of water.

Figure 6.8 shows the CO₂ hydrate formation rate of up to ~30 minutes (starting from the induction point) for various systems. The main concentration of the formation is the initial 30 minutes. The gas is rapidly trapped inside the hydrate crystal structure cavity as the nucleation forms. Due to more nuclei formation, sudden nucleation occurs, resulting in rapid gas consumption during this period [184]. As the hydrate continues to form, it gets stable, and the rate of hydrate starts to reduce. The rate of hydrate changes faster initially, then slowly within 30 minutes of the nucleation, thus accelerating the hydrate formation. The same has been verified in the literature [324]. This promotes gas consumption. As the NPs introduce the system, the gas consumption is higher than DI water. The rate of consumption for pure water was found to be 0.089 mol/mol/min (fig 6.8 (a)). For example, the initial rate of S₁ (0.5 wt%) of NPs was found to be 0.145 mol/mol/min. 0.187 mol/mol/min (fig 6.8(b)) and 0.161 mol/mol/min for S₂ (fig 6.8(c)) and S₃ (fig 6.8(d)) respectively. S₁, S₂, and S₃ have increments of 62.9 %, 110.1%, and 80.9% than DI water's hydrate formation rate. It is also noted that as the concentration increases from 20 % to 40% to 100% the rate of hydrate formation increases. There is increase of 59.3%, 94.7% and 73.1% of S₁, S₂, and S₃ than S₄, S₅, and S₆ (fig 6.8(e-g)) respectively. Moreover,

increment of 20.1%, 32.6% and 21.8% of S₁, S₂, and S₃ than S₇, S₈, and S₉ (fig 8(h-j)). Thus, an increase in the concentration helps in the faster formation of the hydrate.

Due to their nano size, these NPs are well dispersed inside the aqueous solution. They are well dispersed and cover more surface area for nucleation formation. Fast heat and mass transfer occur because of the high thermal conductivity of these NPs. This results in a faster induction time and the formation kinetics. These NPs in addition reduce the gas-liquid interface inside the reactor. This moreover helps increase the heat and mass transfer across the interface, forming hydrate faster. Because of the nano size of the NPs, tiny gas bubbles develop throughout the aqueous solution. These bubbles also help increase the gas diffusivity at the interface. As gas diffusivity increases, gas consumption occurs faster.

6.3.6. CO₂ storage capacity

The storage capacity of gas in the hydrate phase is the volume stored inside the solid hydrate structure and is governed by the following equation [174,199]

$$SC = \frac{\Delta nRT_{STP}}{P_{STP}V_H} \quad (6.4)$$

STD is the standard condition (273.15 K and 0.1 MPa). V_H is the volume of gas hydrate. Storage capacity is defined as the volume of the gas entrapped under standard conditions. The results are described in Figure 6.9. It is clear from Figure 6.9 that, as the NPs concentration in the system increases, the SC increases. The CO₂ storage capacity, as calculated in the present study for pure water, is 12.8 v/v. For example, S₁, S₂, and S₃ have CO₂ SC values 18.6, 21.3, and 19.1 v/v, respectively, giving an increase of 45.3%, 66.4 %, and 49.2 %, compared to pure water. The general trend has been that within each aqueous phase, NPs concentration of 1.0 wt% provides an enhanced CO₂ storage capacity, compared to the rest of the samples. The optimum concentration of maximum storage capacity is 1.0 wt%. The optimum. This result verifies that the nanoparticle contained in the aqueous

solution stores more gas as compared to pure water. Hence, it can be said that NPs improve the kinetic parameters of the gas hydrate.

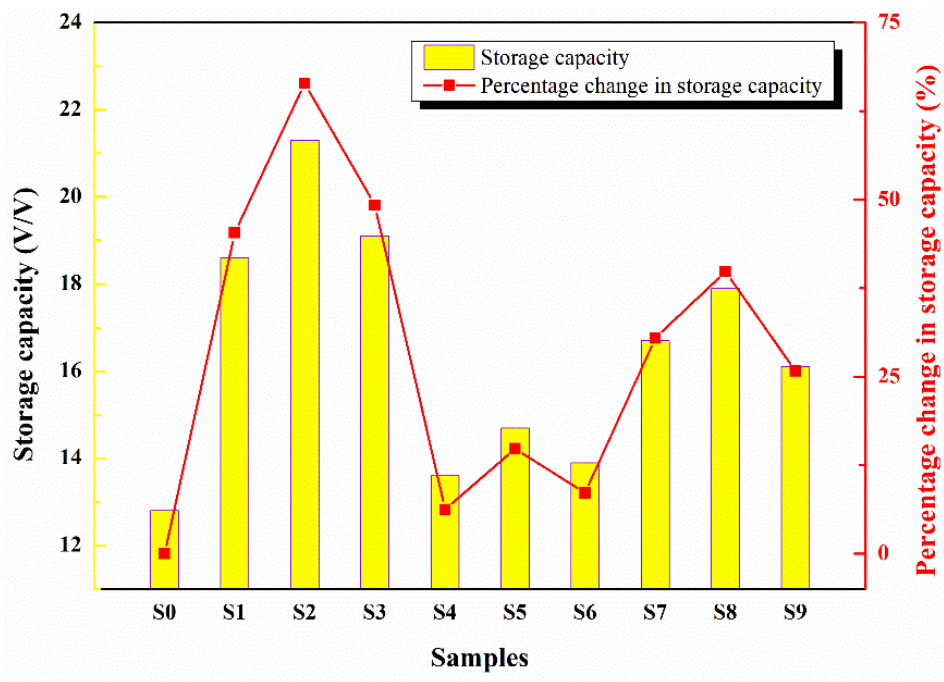


Figure 6.9: Storage capacity of different hydrates promoter formulations at 3.5 MPa and 275.15 K

6.3.7. Dissociation kinetics of the hydrate in the presence of NPs

The following equation is used to calculate the moles of CO₂ dissociated in hydrate formation

$$\Delta n_{CO_2} = \frac{1}{R} V \left(\frac{P_0}{Z_0 T_0} - \frac{P_t}{Z_t T_t} \right) \quad (6.5)$$

All symbols have usual meaning.

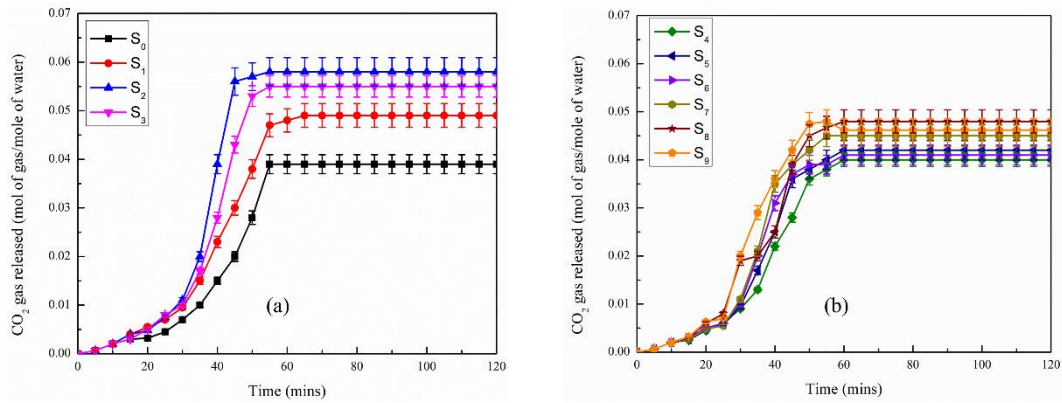


Figure 6.10: Gas released during methane hydrate dissociation for (a) S₀, S₁, S₂, S₃ and (b) S₄, S₅, S₆, S₇, S₈ and S₉ samples

The hydrate was dissociated from 275.15 K to 290 K. The ramping rate was kept at 10 ± 0.5 K/hr. Figure 6.10 shows the number of gas moles released per water mole. It is clear from the figure that the maximum gas is released from the S₂ system. The figure illustrates that as the concentration of the nanofluids increases, more moles of gas are released from the hydrate. Figure 6.10 (a) explains the moles of gas released for S₀, S₁, S₂, and S₃. For pure water (S₀), it has slower dissociation among all the samples around 20 mins. Due to the presence of the nanofluid, the complete dissociation of hydrate in all these samples are similar around 45-50 mins. As the temperature increases the system gets heat, and the hydrate starts to dissociate. The nanoparticle present in the sample helps in faster heat transfer within the system. Sample S₂ dissociation starts around 15 mins, and it continues till 45 mins. Since more gas consumption takes place for the S₂ sample, it has higher gas release during dissociation. S₂ was followed by S₁ and S₃. For both S₁ and S₃, the dissociation starts ~19 mins and 14 mins respectively. And dissociation for both ends at 50 mins. Figure 6.10 (b) illustrates for samples S₄, S₅, S₆, S₇, S₈ and S₉. The figure indicates that the dissociation rate is faster than the previous corresponding sample when the nanofluid concentration increases. Due to the presence of the nanoparticle in the system, the dissociation occurs faster than in pure water. For S₅, the dissociation occurs between 15

to 45 minutes. Dissociation starts around 20 mins both S₄ and S₆ & ends at approximately 50 mins. For, S₇, S₈, and S₉ the total dissociation occurs near 45 minutes. Hydrate dissociates at a given temperature and pressure. Before that, the hydrate structure remains stable. This is the reason why hydrate does not dissociate initial 15 mins. Once sufficient temperature and pressure are reached, the hydrate structure starts to disintegrate. Hence, the gas that is entrapped inside the solid structure escapes. This results in an increase of the gas mole after 15 minutes. The gas escapes from the solid structure exponentially throughout the next 50 minutes. Meanwhile, the gas release has not changed after 50 minutes, suggesting that the structure has dissociated completely.

6.4. Mechanism for the effect of NPs on the hydrate formation

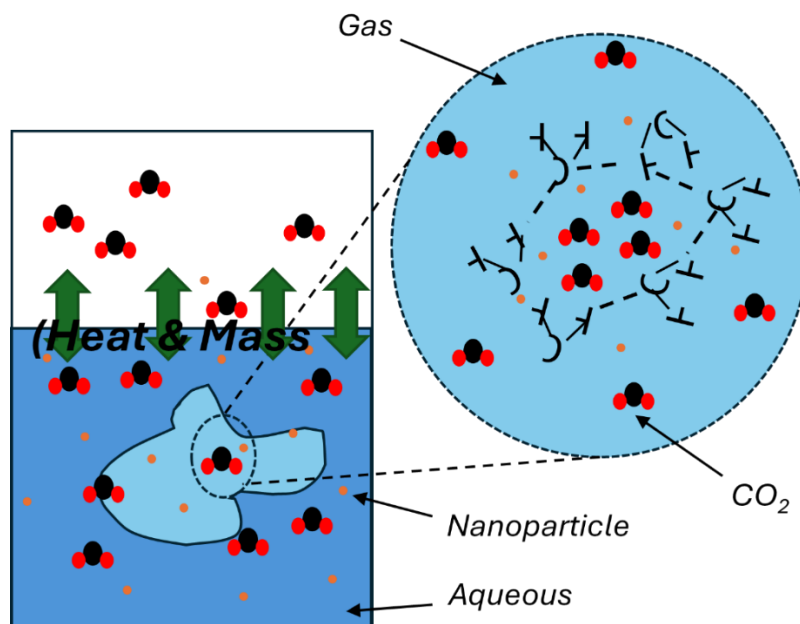


Figure 6.11: Schematic diagram mechanism of NP hydrate formation.

As discussed in previous sections, the system containing a single-step SiO₂ nanofluid enhances the CO₂ hydrate formation kinetics. As the nanofluid concentration increases up to a certain optimum concentration, these NPs are uniformly dispersed in the aqueous solution, making a heterogeneous solution. A uniform distribution allows for a larger number of hydrate nucleation sites and reduced barrier energy for hydrate formation

[325,326][326]. Figure 6.11 explains the mechanism of gas hydrate formation in the presence of nanofluids. As the pressure and temperature for the hydrate condition are achieved, the motor starts. Due to the motion, the pressure reduces inside the reactor as the gas adsorbs inside the liquid NPs solution. This absorption happens because of the mass transfer of gas into an aqueous solution. The presence of NPs drastically improves the heat transfer, enhancing the hydrate formation kinetics. These NPs make for a heterogeneous solution, forming more nuclei sites to start the nucleation process of hydrate growth. More nucleation means faster hydrate growth. As the hydrate grows, CO₂ gets entrapped inside the hollow cavity. Hence, the gas hydrate has wider applications from storage to transportation and helps in carbon capture.

6.5. Conclusion and summary

The present study investigates the impact of single-step nano-fluids on the CO₂ hydrate formation kinetics and the storage capacity, which are crucial for CO₂ capture and storage applications. Nanofluids with NPs concentrations of 0.5, 1.0, and 1.5 wt% and varying sizes between 5 to 150 nm were synthesized stability of the NPs was studied. The fresh sample of nanofluids has more stability (time-dependent parameter) whereas with time, they become less stable due to nanoparticle agglomeration. The kinetic parameters, such as moles of gas consumed, rate of hydrate formation and storage capacity were determined at ~275.15 K temperatures and ~3.5 MPa. The following are the salient conclusions.

- a) As the NPs concentration in the nanofluid increases up to a certain optimum concentration (1 wt% for the present study), the enhanced CO₂ capture capacity of the nanofluid is due to the high available surface area for CO₂ absorption, higher interfacial area for mass transfer through the gas-liquid interface.

- b) At the same optimum NPs concentration, the CO₂ hydrate formation kinetics is enhanced due to enhanced heat-mass transfer, surface area and homogeneity in the system.
- c) As the concentration of NPs increases further (> 1 wt%), agglomeration of nanoparticles hinders the further enhancement in hydrate formation kinetics due to the development of heterogeneity in the system.

It can be concluded from this study that nanofluids with a higher (optimum) concentration of single-step SiO₂ are more effective, concerning CO₂ hydrate formation kinetics and storage potential. They can be used as effective promoters for enhancing CO₂ hydrate growth and storage applications. Developed and synthesized a new type of nanoparticle that can promote hydrate more effectively. This includes exploring different oxide and their surface modification to enhance hydrate formation and storage. Moreover, combine this nanoparticle with a surfactant to improve nanoparticle effectiveness.

7.1. Conclusion and Summary

This chapter concludes the thesis by reporting both experimental and simulation results of hydrate formation and dissociation. The conclusion is summarized below:

- MD simulation is an excellent tool to explain the molecular-level interaction. MD simulation helps in quantitative analysis using RDF and, diffusion coefficient. The increase in concentration decreases the RDF value of carbon of methane, and oxygen of water, indicating faster dissociation. Increasing the concentration of EGY from 0wt% to 5wt% increases RDF of carbon of methane, and oxygen of ethylene glycol. Similarly, the diffusion coefficient also increases from $0.2532 \times 10^{-9} \text{ m}^2/\text{s}$ to $2.9031 \times 10^{-9} \text{ m}^2/\text{s}$ for 5 wt%, $0.2396 \times 10^{-9} \text{ m}^2/\text{s}$ to $2.8675 \times 10^{-9} \text{ m}^2/\text{s}$ for 3.5 wt% and $0.1570 \times 10^{-9} \text{ m}^2/\text{s}$ to $2.8049 \times 10^{-9} \text{ m}^2/\text{s}$ for 2.5 wt%. The total energy increases as the concentration increases, showing a similar trend when the temperature.
- When both CO_2 and CH_4 hydrate as present in a system along with EGY, the dissociation of both hydrate takes place faster at 1.0 wt% of concentration. This is the optimum concentration for the given system. RDF and MSD follow the trends that is given in the literature.
- Hydrate formation is an exothermic reaction i.e. release energy during the nucleation formation. Hence, heat and mass transfer is an important parameter in formation and dissociation. Here, Nps comes into picture. NPs are a good thermal conductor; size of the nanoparticles is nano (<100nm). Due to the presence of these nanoparticles in the system, the system becomes heterogeneous, that helps in more nucleation sites for hydrate growth. Hence, faster hydrate growth. Therefore, these Nps can be used as a hydrate promoter. As the concentration of these nanoparticles increases, it promotes faster hydrate formation. So, the concentration of these nanoparticles plays an important role in hydrate growth.
- The Nps (SiO_2) used in this study are synthesized in the lab, with average size of 35nm to 150 nm. As the concentration increases form 0.5 wt% to 1.5 wt%, the induction time increase and then decreases, indicating that 1.0 wt% is the optimum concentration in the given system (100 mins lesser than DI water). 1.0 wt% is the optimum concentration for storage capacity, CO_2 consumption, rate of hydrate formation.

7.2. Future Direction

The experimental and simulation work for gas hydrate can be used for other gas storage like hydrogen. As the experiments are not cost-effective, simulation can be performed for various promoters and inhibitors. The simulation will give a better understanding of the role of various promoters and inhibitors. Further, more studies can be based on hydrate formation in porous media. Various low-cost alternative chemicals can be used on an industry scale to maximize CO₂ capture and storage. This way, a wider scale applicability can be explored

References

- [1] Sloan ED. Natural Gas Hydrates. *J Pet Technol* 1991;43:1414–7. <https://doi.org/10.2118/23562-PA>.
- [2] Demirbas A. Methane Gas Hydrate. London: Springer London; 2010. <https://doi.org/10.1007/978-1-84882-872-8>.
- [3] Sloan ED. Gas hydrates: Review of physical/chemical properties. *Energy and Fuels* 1998;12:191–6. <https://doi.org/10.1021/ef970164+>.
- [4] Ripmeester J, Tse JS, Ratcliffe CI, Powell BM. A new clathrate hydrate structure. *Nature* 1987;325:135–6. <https://doi.org/10.1038/325135a0>.
- [5] Sloan ED. Fundamental principles and applications of natural gas hydrates. *Nature* 2003;426:353–9. <https://doi.org/10.1038/nature02135>.
- [6] Longinos SN. THE EFFECT OF EXPERIMENTAL CONDITIONS ON NATURAL GAS HYDRATE FORMATION. MIDDLE EAST TECHNICAL UNIVERSITY, 2020.
- [7] Mihama-ku H, Cho B, Ikegami T, Sugiyama H, Imasato Y, Dallimore SR, et al. DEVELOPMENT OF A MONITORING SYSTEM FOR THE JOGMEC / NRCAN / AURORA MALLIK GAS HYDRATE PRODUCTION TEST PROGRAM Kasumi Fujii * and Masato Yasuda. Differences 2008.
- [8] Ikegawa Y, Miyakawa K, Suzuki K, Masuda Y, Narita H, Ebinuma T. SS: Hydrates: Experimental results for long term CO₂ injection near methane hydrate formations. *All Days*, vol. 2, OTC; 2010, p. 1081–8. <https://doi.org/10.4043/20575-MS>.
- [9] Fujii K, Yasuda M, Mihama-ku H, Cho B, Ikegami T, Sugiyama H, et al. DEVELOPMENT OF A MONITORING SYSTEM FOR THE JOGMEC / NRCAN / AURORA MALLIK GAS HYDRATE PRODUCTION TEST PROGRAM, Vancouver, British Columbia, CANADA: 2008.

- [10] Jadhawar P. Subsurface Decarbonization Options as CO₂ Hydrates with Clean Methane Energy Recovery from Natural Gas Hydrate Reservoirs, 2022, p. 207–34. https://doi.org/10.1007/978-981-16-4505-1_11.
- [11] Makogon TY, Sloan ED. Phase Equilibrium for Methane Hydrate from 190 to 262 K. *J Chem Eng Data* 1994;39:351–3. <https://doi.org/https://doi.org/10.1021/je00014a035>.
- [12] Makogon YF. Hydrates of hydrocarbons. Tulsa, Okla. : PennWell Books; 1997.
- [13] Waite WF, Winters WJ, Mason DH. Methane hydrate formation in partially water-saturated Ottawa sand. *Am Mineral* 2004;89:1202–7. <https://doi.org/10.2138/am-2004-8-906>.
- [14] Durham WB, Kirby SH, Stern LA, Zhang W. The strength and rheology of methane clathrate hydrate. *J Geophys Res Solid Earth* 2003;108. <https://doi.org/10.1029/2002JB001872>.
- [15] Merey S. Instrumental Geochemical Analysis. Middle East Technical University, 2014.
- [16] Sloan Jr. ED, Koh CA. Clathrate Hydrates of Natural Gases. CRC Press; 2007. <https://doi.org/10.1201/9781420008494>.
- [17] Sloan ED, Koh CA. Clathrate Hydrates of Natural Gases. CRC Press; 2007. <https://doi.org/10.1201/9781420008494>.
- [18] Koh CA, Sloan ED, Sum AK, Wu DT. Fundamentals and Applications of Gas Hydrates. *Annu Rev Chem Biomol Eng* 2011;2:237–57. <https://doi.org/10.1146/annurev-chembioeng-061010-114152>.
- [19] Miller S. Clathrate Hydrates of Air in Antarctic Ice. *Sci New Ser* 1969;165:489–90. <https://doi.org/10.1126/science.165.3892.489>.
- [20] Birchwood R, Dai J, Shelander D, Boswell R, Collett T, Cook A, et al. Developments

- in gas hydrates. *Oilf Rev* 2010;22:18–33.
- [21] Claypool GE, Kaplan IR. The Origin and Distribution of Methane in Marine Sediments. *Nat. Gases Mar. Sediments*, Boston, MA: Springer US; 1974, p. 99–139. https://doi.org/10.1007/978-1-4684-2757-8_8.
- [22] Makogon Y. Features of Natural Gas Fields Exploitation in Permafrost Zone. *Gazov Promyshlennost* 1966;9:1–17.
- [23] Milkov A. Worldwide distribution of submarine mud volcanoes and associated gas hydrates. *Mar Geol* 2000;167:29–42. [https://doi.org/10.1016/S0025-3227\(00\)00022-0](https://doi.org/10.1016/S0025-3227(00)00022-0).
- [24] Milkov A., Sassen R. Thickness of the gas hydrate stability zone, Gulf of Mexico continental slope. *Mar Pet Geol* 2000;17:981–91. [https://doi.org/10.1016/S0264-8172\(00\)00051-9](https://doi.org/10.1016/S0264-8172(00)00051-9).
- [25] Merey Ş. Drilling of gas hydrate reservoirs. *J Nat Gas Sci Eng* 2016;35:1167–79. <https://doi.org/10.1016/j.jngse.2016.09.058>.
- [26] Max MD, editor. *Natural Gas Hydrate In Oceanic and Permafrost Environments*. vol. 5. Dordrecht: Springer Netherlands; 2000. <https://doi.org/10.1007/978-94-011-4387-5>.
- [27] Milkov A V. Molecular and stable isotope compositions of natural gas hydrates: A revised global dataset and basic interpretations in the context of geological settings. *Org Geochem* 2005;36:681–702. <https://doi.org/10.1016/j.orggeochem.2005.01.010>.
- [28] Sassen R, MacDonald IR. Evidence of structure H hydrate, Gulf of Mexico continental slope. *Org Geochem* 1994;22:1029–32. [https://doi.org/10.1016/0146-6380\(94\)90036-1](https://doi.org/10.1016/0146-6380(94)90036-1).
- [29] Makogon YF. Natural gas hydrates – A promising source of energy. *J Nat Gas Sci*

- Eng 2010;2:49–59. <https://doi.org/10.1016/j.jngse.2009.12.004>.
- [30] Englezos P, Lee JD. Gas hydrates: A cleaner source of energy and opportunity for innovative technologies. *Korean J Chem Eng* 2005;22:671–81. <https://doi.org/10.1007/BF02705781>.
- [31] Makogon YF, Holditch SA, Makogon TY. Natural gas-hydrates - A potential energy source for the 21st Century. *J Pet Sci Eng* 2007;56:14–31. <https://doi.org/10.1016/j.petrol.2005.10.009>.
- [32] Lee S-Y, Holder GD. Methane hydrates potential as a future energy source. *Fuel Process Technol* 2001;71:181–6. [https://doi.org/10.1016/S0378-3820\(01\)00145-X](https://doi.org/10.1016/S0378-3820(01)00145-X).
- [33] Houghton JT, Jenkins GJ, Ephraums JJ. *Climate Change; The IPCC Scientific Assessment*. vol. 1. Cambridge University Press; 1990. <https://doi.org/10.5771/9781666902006-23>.
- [34] Taylor AE, Dallimore SR, Hyndman RD, Wright F. Comparing the sensitivity of terrestrial and marine gas hydrates to climate warming at the end of the last ice age. *Fourth Int. Conf. Gas Hydrates*, 2002, p. 63–70.
- [35] Kennett JP, Cannariato KG, Hendy IL, Behl RJ. Carbon Isotopic Evidence for Methane Hydrate Instability During Quaternary Interstadials. *Science* (80-) 2000;288:128–33. <https://doi.org/10.1126/science.288.5463.128>.
- [36] Pauli CK, Ussler W, Dillon WP. Potential Role of Gas Hydrate Decomposition in Generating Submarine Slope Failures, 2003, p. 149–56. https://doi.org/10.1007/978-94-011-4387-5_12.
- [37] Kayen RE, Lee HJ. Slope stability in regions of sea-floor gas hydrate; Beaufort Sea continental slope. 1993.
- [38] Nimblett JN, Shipp RC, Strijbos F. Gas Hydrate As A Drilling Hazard: Examples From Global Deepwater Settings. *Offshore Technol. Conf., Offshore Technology*

- Conference; 2005. <https://doi.org/10.4043/17476-MS>.
- [39] Birchwood R, Noeth S, Jones E. Safe Drilling in Gas-Hydrate Prone Sediments : Findings from the 2005 Drilling Campaign of the Gulf of Mexico Gas Hydrates Joint Industry Project (JIP) 2005;8:1–20.
- [40] Dallimore S, Fisher D, Alavi S, Bellefleur G, Boswell R, Brody H. Energy From Gas Hydrates : ASSESSING THE OPPORTUNITIES & CHALLENGES FOR CANADA. 2008.
- [41] Yamamoto K, Dallimore S. Geologic and porous media factors affecting the 2007 production response characteristics of the JOGMEC/NRCAN/AURORA Mallik Gas Hydrate Production Research Well. 6th Int Conf Gas Hydrates 2008;8:1–20.
- [42] Power D, Slater K, Aldea C, Lattanzi S. Gas Hydrate Inhibited Water-Based Muds for Ultra-Deepwater Drilling. Design 2003:1–10.
- [43] Pakulski M, Qu Q, Percy R. Gulf of Mexico Deepwater Well Completion with Hydrate Inhibitors. All Days, SPE; 2005. <https://doi.org/10.2118/92971-MS>.
- [44] Nelson RD, Fleyfall F, Dubois R, Vitthal S, Spies BK. A Novel Gas-Hydrate Inhibitor for Deepwater Frac-Pack and Subsea Environments. All Days, SPE; 2000. <https://doi.org/10.2118/58764-MS>.
- [45] Talley LD, Mitchell GF. Application of Proprietary Kinetic Hydrate Inhibitors in Gas Flowlines. All Days, vol. 3, OTC; 1999, p. 681–9. <https://doi.org/10.4043/11036-MS>.
- [46] Sira JH, Patil SL, Kamath VA. Study of Hydrate Dissociation by Methanol and Glycol Injection. SPE Annu. Tech. Conf. Exhib., SPE; 1990. <https://doi.org/10.2118/20770-MS>.
- [47] Pakulski M, Qu Q. Hydrate Protection with Heat Producing Three – Component Gas Hydrate Inhibitor. ICGH, Edinburgh, Scotland, United Kingdom: 2011.

- [48] Elgibaly AA, Elkamel AM. A new correlation for predicting hydrate formation conditions for various gas mixtures and inhibitors. *Fluid Phase Equilib* 1998;152:23–42. [https://doi.org/10.1016/S0378-3812\(98\)00368-9](https://doi.org/10.1016/S0378-3812(98)00368-9).
- [49] Katz DL. Prediction of Conditions for Hydrate Formation in Natural Gases. *Trans AIME* 1945;160:140–9. <https://doi.org/10.2118/945140-G>.
- [50] Holder GD, Zetts SP, Pradhan N. Phase Behavior in Systems Containing Clathrate Hydrates: A Review. *Rev Chem Eng* 1988;5:1–70. <https://doi.org/10.1515/REVCE.1988.5.1-4.1>.
- [51] Makogon YF. Perspectives for the Development of Gas-Hydrate Deposits. 1982:299–304.
- [52] Katz DL. A Look Ahead in Gas Storage Technology, 1981, p. 283–9.
- [53] Waals JH van der, Platteeuw JC. Clathrate Solutions, 1958, p. 1–57. <https://doi.org/10.1002/9780470143483.ch1>.
- [54] Østergaard KK, Tohidi B, Danesh A, Todd AC, Burgass RW. A General Correlation for Predicting the Hydrate-Free Zone of Reservoir Fluids. *SPE Prod Facil* 2000;15:228–33. <https://doi.org/10.2118/66523-PA>.
- [55] Tahir AN. EFFECT OF POLYGLYCOLS ON HYDRATE FORMATION DURING drilling operations 2005.
- [56] Sum AK. Controlling Hydrate Formation in Production Lines. JEM 2015 Campinas, SP-Brazil: Colorado School of Mines; 2015.
- [57] Fu B, Neff S, Mathur A, Bakeev K. Application of Low-Dosage Hydrate Inhibitors in Deepwater Operations. *SPE Prod Facil* 2002;17:133–7. <https://doi.org/10.2118/78823-PA>.
- [58] Li G, Li X-S, Tang L-G, Zhang Y. Experimental Investigation of Production Behavior of Methane Hydrate under Ethylene Glycol Injection in Unconsolidated

- Sediment. *Energy & Fuels* 2007;21:3388–93. <https://doi.org/10.1021/ef060644d>.
- [59] Mohammadi AH, Afzal W, Richon D. Gas hydrates of methane, ethane, propane, and carbon dioxide in the presence of single NaCl, KCl, and CaCl₂ aqueous solutions: Experimental measurements and predictions of dissociation conditions. *J Chem Thermodyn* 2008;40:1693–7. <https://doi.org/10.1016/j.jct.2008.06.015>.
- [60] Kelland MA. History of the Development of Low Dosage Hydrate Inhibitors. *Energy & Fuels* 2006;20:825–47. <https://doi.org/10.1021/ef050427x>.
- [61] Villano L Del, Kommedal R, Fijten MWM, Schubert US, Hoogenboom R, Kelland MA. A Study of the Kinetic Hydrate Inhibitor Performance and Seawater Biodegradability of a Series of Poly(2-alkyl-2-oxazoline)s. *Energy & Fuels* 2009;23:3665–73. <https://doi.org/10.1021/ef900172f>.
- [62] Karaaslan U, Parlaktuna M. Surfactants as Hydrate Promoters? *Energy & Fuels* 2000;14:1103–7. <https://doi.org/10.1021/ef000069s>.
- [63] Chueh PL, Prausnitz JM. Vapor-liquid equilibria at high pressures: Calculation of partial molar volumes in nonpolar liquid mixtures. *AIChE J* 1967;13:1099–107. <https://doi.org/10.1002/aic.690130612>.
- [64] Fadnes FH, Jakobsen T, Bylov M, Holst A, Downs JD. Studies on the Prevention of Gas Hydrates Formation in Pipelines Using Potassium Formate as a Thermodynamic Inhibitor. All Days, SPE; 1998. <https://doi.org/10.2118/50688-MS>.
- [65] Kan AT, Fu G, Watson MA, Tomson MB. Effect Of Hydrate Inhibitors On Oilfield Scale Formation And Inhibition. All Days, SPE; 2002. <https://doi.org/10.2118/74657-MS>.
- [66] Hale AH, Dewan AKR. Inhibition of Gas Hydrates in Deepwater Drilling. All Days, SPE; 1989. <https://doi.org/10.2118/18638-MS>.
- [67] Quigley MS, Hubbard J. Gas Hydrates Formation in Drilling Fluids. Present. 1990

- Drill. Manag. Tech. Meet. Mob. Res. Dev. Corp., Dallas Res. Lab., 1990.
- [68] Kotkoskie TS, Al-Ubaidi B, Wildeman TR, Sloan ED. Inhibition of Gas Hydrates in Water-Based Drilling Muds. SPE Drill Eng 1992;7:130–6. <https://doi.org/10.2118/20437-PA>.
- [69] Ebeltoft H, Majeed Y, Særgård E. Hydrate Control During Deepwater Drilling: Overview and New Drilling-Fluids Formulations. SPE Drill Complet 2001;16:19–26. <https://doi.org/10.2118/68207-PA>.
- [70] Mohammadi AH, Kraouti I, Richon D. Methane hydrate phase equilibrium in the presence of NaBr, KBr, CaBr₂, K₂CO₃, and MgCl₂ aqueous solutions: Experimental measurements and predictions of dissociation conditions. J Chem Thermodyn 2009;41:779–82. <https://doi.org/10.1016/j.jct.2009.01.004>.
- [71] Kelland MA, Svartaas TM, Dybvik LA. Control of Hydrate Formation by Surfactants and Polymers. SPE Annu. Tech. Conf. Exhib., SPE; 1994. <https://doi.org/10.2118/28506-MS>.
- [72] Menendez CM, Jardine J, Mok WY, Ramachandran S, Jovancicevic V, Bhattacharya A. New Sour Gas Corrosion Inhibitor Compatible with Kinetic Hydrate Inhibitor. All Days, IPTC; 2014. <https://doi.org/10.2523/IPTC-17440-MS>.
- [73] Makogon TY, Larsen R, Knight CA, Dendy Sloan E. Melt growth of tetrahydrofuran clathrate hydrate and its inhibition: method and first results. J Cryst Growth 1997;179:258–62. [https://doi.org/10.1016/S0022-0248\(97\)00118-8](https://doi.org/10.1016/S0022-0248(97)00118-8).
- [74] Klomp U. The World of LDHI: From Conception to Development to Implementation. 6th Int. Conf. Gas Hydrates (ICGH 2008), 2008.
- [75] Nazari K, Moradi MR, Ahmadi AN. Kinetic Modeling of Methane Hydrate Formation in the Presence of Low-Dosage Water-Soluble Ionic Liquids. Chem Eng Technol 2013;36:1915–23. <https://doi.org/10.1002/ceat.201300285>.

- [76] Del Villano L, Kelland MA. An investigation into the kinetic hydrate inhibitor properties of two imidazolium-based ionic liquids on Structure II gas hydrate. *Chem Eng Sci* 2010;65:5366–72. <https://doi.org/10.1016/j.ces.2010.06.033>.
- [77] Ohno H, Susilo R, Gordienko R, Ripmeester J, Walker VK. Interaction of Antifreeze Proteins with Hydrocarbon Hydrates. *Chem – A Eur J* 2010;16:10409–17. <https://doi.org/10.1002/chem.200903201>.
- [78] Gordienko R, Ohno H, Singh VK, Jia Z, Ripmeester JA, Walker VK. Towards a Green Hydrate Inhibitor: Imaging Antifreeze Proteins on Clathrates. *PLoS One* 2010;5:e8953. <https://doi.org/10.1371/journal.pone.0008953>.
- [79] Herslund PJ, Thomsen K, Abildskov J, von Solms N, Galfré A, Brântuas P, et al. Thermodynamic promotion of carbon dioxide–clathrate hydrate formation by tetrahydrofuran, cyclopentane and their mixtures. *Int J Greenh Gas Control* 2013;17:397–410. <https://doi.org/10.1016/j.ijggc.2013.05.022>.
- [80] O’Reilly R, Jeong NS, Chua PC, Kelland MA. Missing Poly(N -vinyl lactam) Kinetic Hydrate Inhibitor: High-Pressure Kinetic Hydrate Inhibition of Structure II Gas Hydrates with Poly(N -vinyl piperidone) and Other Poly(N -vinyl lactam) Homopolymers. *Energy & Fuels* 2011;25:4595–9. <https://doi.org/10.1021/ef2009953>.
- [81] Chua PC, Kelland MA. Poly(N -vinyl azacyclooctanone): A More Powerful Structure II Kinetic Hydrate Inhibitor than Poly(N -vinyl caprolactam). *Energy & Fuels* 2012;26:4481–5. <https://doi.org/10.1021/ef300688x>.
- [82] Chua PC, Sæbø M, Lunde A, Kelland MA. Dual Kinetic Hydrate Inhibition and Scale Inhibition by Polyaspartamides. *Energy & Fuels* 2011;25:5165–72. <https://doi.org/10.1021/ef201007c>.
- [83] Chua PC, Kelland MA, Ishitake K, Satoh K, Kamigaito M, Okamoto Y. Kinetic

- Hydrate Inhibition of Poly(N -isopropylmethacrylamide)s with Different Tacticities. *Energy & Fuels* 2012;26:3577–85. <https://doi.org/10.1021/ef3006355>.
- [84] Sa J-H, Lee BR, Park D-H, Han K, Chun HD, Lee K-H. Amino Acids as Natural Inhibitors for Hydrate Formation in CO₂ Sequestration. *Environ Sci Technol* 2011;45:5885–91. <https://doi.org/10.1021/es200552c>.
- [85] Sa J-H, Kwak G-H, Han K, Ahn D, Cho SJ, Lee JD, et al. Inhibition of methane and natural gas hydrate formation by altering the structure of water with amino acids. *Sci Rep* 2016;6:31582. <https://doi.org/10.1038/srep31582>.
- [86] Tse JS, Klein ML, McDonald IR. Dynamical properties of the structure I clathrate hydrate of xenon). *J Chem Phys* 1983;78:2096–7. <https://doi.org/10.1063/1.444921>.
- [87] van der Waals JH. The statistical mechanics of clathrate compounds. *Trans Faraday Soc* 1956;52:184–93. <https://doi.org/10.1039/TF9565200184>.
- [88] Wierzchowski SJ, Monson PA. Calculation of Free Energies and Chemical Potentials for Gas Hydrates Using Monte Carlo Simulations. *J Phys Chem B* 2007;111:7274–82. <https://doi.org/10.1021/jp068325a>.
- [89] Rodger PM. Stability of gas hydrates. *J Phys Chem* 1990;94:6080–9. <https://doi.org/10.1021/j100378a082>.
- [90] Walsh MR, Koh CA, Sloan ED, Sum AK, Wu DT. Microsecond Simulations of spontaneous methane hydrate nucleation and growth. *Science* (80-) 2009;326:1095–8. <https://doi.org/10.1126/science.1174010>.
- [91] Santra M, Singh RS, Chakrabarty S, Bagchi B. Understanding Nucleation Phenomena at Large Metastability: From Gas-Liquid Transition to Metastable Solids and Polymers 2008;206104:234704.
- [92] Bouzidi A, Bouazzi AS, Amlouk M. Modelling, Simulation and Optimization of n-

- p-n-p Silicon Multilayer Solar Cells. *Open J Microphys* 2012;02:27–32.
<https://doi.org/10.4236/ojm.2012.23004>.
- [93] Haile JM. *Molecular dynamics simulation: elementary methods*. 1997.
- [94] Frenkel D, Smit B. *Understanding Molecular Simulation: From Algorithms to Applications*. Elsevier; 2023. <https://doi.org/10.1016/C2009-0-63921-0>.
- [95] Ewald PP. Die Berechnung optischer und elektrostatischer Gitterpotentiale. vol. 369. 1921. <https://doi.org/10.1002/andp.19213690304>.
- [96] Ciccotti G, Frenkel D, McDonald IR. *Simulation of liquids and solids : molecular dynamics and Monte Carlo methods in statistical mechanics*. 1987.
- [97] Buffett BA. Clathrate Hydrates. *Annu Rev Earth Planet Sci* 2000;28:477–507.
<https://doi.org/10.1146/annurev.earth.28.1.477>.
- [98] Grauls D. Gas hydrates: importance and applications in petroleum exploration. *Mar Pet Geol* 2001;18:519–23. [https://doi.org/10.1016/S0264-8172\(00\)00075-1](https://doi.org/10.1016/S0264-8172(00)00075-1).
- [99] Taylor CE, Link DD, Elsen HA, Ladner EP. *Enhancement in the Storage of Methane in Hydrates*. *Adv. Study Gas Hydrates*, Boston: Kluwer Academic Publishers; 2006, p. 199–211. https://doi.org/10.1007/0-306-48645-8_13.
- [100] Kang SP, Lee H. Recovery of CO₂ from Flue Gas Using Gas Hydrate: Thermodynamic Verification through Phase Equilibrium Measurements. *Environ Sci Technol* 2000;34:4397–400. <https://doi.org/10.1021/es001148l>.
- [101] Javanmardi J, Moshfeghian M. Energy consumption and economic evaluation of water desalination by hydrate phenomenon. *Appl Therm Eng* 2003;23:845–57.
[https://doi.org/10.1016/S1359-4311\(03\)00023-1](https://doi.org/10.1016/S1359-4311(03)00023-1).
- [102] Koh CA. Towards a fundamental understanding of natural gas hydrates. *Chem Soc Rev* 2002;31:157–67. <https://doi.org/10.1039/b008672j>.
- [103] Muller RA, Muller EA. Fugitive Methane and the Role of Atmospheric Half-Life.

- Geoinformatics Geostatistics An Overv 2017;05. <https://doi.org/10.4172/2327-4581.1000162>.
- [104] Nair VC, Prasad SK, Kumar R, Sangwai JS. High-Pressure Rheology of Methane Hydrate Sediment Slurry Using a Modified Couette Geometry. *Ind Eng Chem Res* 2020;59:4079–92. <https://doi.org/10.1021/acs.iecr.9b04390>.
- [105] Allen SK, Barros V, Burton I, Campbell-Lendrum D, Cardona O-D, Cutter SL, et al. Climate Change 2014 Synthesis Report Summary for Policymakers. In: Field CB, Barros V, Stocker TF, Dahe Q, editors. *Manag. Risks Extrem. Events Disasters to Adv. Clim. Chang. Adapt.*, vol. 9781107025, Cambridge: Cambridge University Press; 2014, p. 3–22. <https://doi.org/10.1017/CBO9781139177245.003>.
- [106] Wang Y, Feng J-C, Li X-S, Zhan L, Li X-Y. Pilot-scale experimental evaluation of gas recovery from methane hydrate using cycling-depressurization scheme. *Energy* 2018;160:835–44. <https://doi.org/10.1016/j.energy.2018.07.054>.
- [107] Zhan L, Wang Y, Li X-S. Experimental study on characteristics of methane hydrate formation and dissociation in porous medium with different particle sizes using depressurization. *Fuel* 2018;230:37–44. <https://doi.org/10.1016/j.fuel.2018.05.008>.
- [108] Stanwix PL, Rathnayake NM, de Obanos FPP, Johns ML, Aman ZM, May EF. Characterising thermally controlled CH₄–CO₂ hydrate exchange in unconsolidated sediments. *Energy Environ Sci* 2018;11:1828–40. <https://doi.org/10.1039/C8EE00139A>.
- [109] Xu C-G, Cai J, Yu Y-S, Yan K-F, Li X-S. Effect of pressure on methane recovery from natural gas hydrates by methane-carbon dioxide replacement. *Appl Energy* 2018;217:527–36. <https://doi.org/10.1016/j.apenergy.2018.02.109>.
- [110] Feng J-C, Wang Y, Li X-S. Hydrate dissociation induced by depressurization in conjunction with warm brine stimulation in cubic hydrate simulator with silica sand.

- Appl Energy 2016;174:181–91. <https://doi.org/10.1016/j.apenergy.2016.04.090>.
- [111] Li Z, Jiang F, Qin H, Liu B, Sun C, Chen G. Molecular dynamics method to simulate the process of hydrate growth in the presence/absence of KHIs. Chem Eng Sci 2017;164:307–12. <https://doi.org/10.1016/j.ces.2017.02.029>.
- [112] Feng J-C, Wang Y, Li X-S. Dissociation characteristics of water-saturated methane hydrate induced by huff and puff method. Appl Energy 2018;211:1171–8. <https://doi.org/10.1016/j.apenergy.2017.12.004>.
- [113] Nair VC, Prasad SK, Kumar R, Sangwai JS. Energy recovery from simulated clayey gas hydrate reservoir using depressurization by constant rate gas release, thermal stimulation and their combinations. Appl Energy 2018;225:755–68. <https://doi.org/10.1016/j.apenergy.2018.05.028>.
- [114] Khairkhan D, M PD, Bishnoi PR, Collett TS, Dallimore SR. Production potential of the mallik field reservoir. Bull Geol Surv Canada 2003:377–90.
- [115] Ahmadi G, Ji C, Smith DH. Numerical solution for natural gas production from methane hydrate dissociation. J Pet Sci Eng 2004;41:269–85. <https://doi.org/10.1016/j.profnurs.2003.09.004>.
- [116] Windmeier C, Oellrich LR. Theoretical Study of Gas Hydrate Decomposition Kinetics—Model Development. J Phys Chem A 2013;117:10151–61. <https://doi.org/10.1021/jp403471b>.
- [117] Clarke M, Bishnoi PR. Determination of the intrinsic rate of ethane gas hydrate decomposition. Chem Eng Sci 2000;55:4869–83. [https://doi.org/10.1016/S0009-2509\(00\)00137-8](https://doi.org/10.1016/S0009-2509(00)00137-8).
- [118] Gupta P, Chandrasekharan Nair V, Sangwai JS. Phase Equilibrium of Methane Hydrate in the Presence of Aqueous Solutions of Quaternary Ammonium Salts. J Chem Eng Data 2018;63:2410–9. <https://doi.org/10.1021/acs.jced.7b00976>.

- [119] Bavoh CB, Partoon B, Lal B, Gonfa G, Foo Khor S, Sharif AM. Inhibition effect of amino acids on carbon dioxide hydrate. *Chem Eng Sci* 2017;171:331–9. <https://doi.org/10.1016/j.ces.2017.05.046>.
- [120] Hu Y, Wang S, Yang X, He Y. Examination of amino acid inhibitor effect in methane hydrate dissociation via molecular dynamics simulation. *J Mol Liq* 2021;325:115205. <https://doi.org/10.1016/j.molliq.2020.115205>.
- [121] Zhu J, Li X, Liu Z, Sun X, Zhao L, Shi Y, et al. Effect of biofriendly amino acids on methane hydrate decomposition: Insights from molecular dynamics simulations. *Fuel* 2022;325:124919. <https://doi.org/10.1016/j.fuel.2022.124919>.
- [122] Xing D, Qind X, Qiub H, Lu H, Fane Y, Gee X, et al. Nuclear magnetic resonance study of the formation and dissociation process of nature gas hydrate in sandstone. *China Geol* 2022;5:1–2. <https://doi.org/10.31035/cg2022010>.
- [123] Porgar S, Saleh Fekr S, Ghiassi M, Hashemi Hosseini B. Methanol and sodium chloride inhibitors impact on carbon dioxide hydrate formation. *South African J Chem Eng* 2018;26:1–10. <https://doi.org/10.1016/j.sajce.2018.03.001>.
- [124] Zhang J, Pan Z. Effect of potential energy on the formation of methane hydrate. *J Pet Sci Eng* 2011;76:148–54. <https://doi.org/10.1016/j.petrol.2011.01.004>.
- [125] Okano Y, Yasuoka K. Free-energy calculation of structure-H hydrates. *J Chem Phys* 2006;124:024510. <https://doi.org/10.1063/1.2150430>.
- [126] Sarupria S, Debenedetti PG. Homogeneous Nucleation of Methane Hydrate in Microsecond Molecular Dynamics Simulations. *J Phys Chem Lett* 2012;3:2942–7. <https://doi.org/10.1021/jz3012113>.
- [127] Wei C, Hong-Yu Z. Molecular Dynamics Simulation of the Structure I Empty Gas Hydrate. *Chinese Phys Lett* 2002;19:301. <https://doi.org/10.1088/0256-307X/19/5/301>.

- [128] Li-Hua W, Ke-Feng Y, Xiao-Sen L, Shuan-Shi F. Molecular Dynamics Simulation of Methane Hydrate Dissociation Process in the Presence of Thermodynamic Inhibitor. *Acta Physico-Chimica Sin* 2009;25:486–94. <https://doi.org/10.3866/PKU.WHXB20090315>.
- [129] English NJ, MacElroy JMD. Theoretical studies of the kinetics of methane hydrate crystallization in external electromagnetic fields. *J Chem Phys* 2004;120:10247–56. <https://doi.org/10.1063/1.1730092>.
- [130] Yagasaki T, Matsumoto M, Andoh Y, Okazaki S, Tanaka H. Dissociation of methane hydrate in aqueous NaCl solutions. *J Phys Chem B* 2014;118:11797–804. <https://doi.org/10.1021/jp507978u>.
- [131] Sakemoto R, Sakamoto H, Shiraiwa K, Ohmura R, Uchida T. Clathrate Hydrate Crystal Growth at the Seawater/Hydrophobic–Guest–Liquid Interface. *Cryst Growth Des* 2010;10:1296–300. <https://doi.org/10.1021/cg901334z>.
- [132] Sun X, Zhou G, Zhu J, Wu H, Lu G, Bai D. Molecular Dynamics Simulation of Methane Hydrate Decomposition in the Presence of Alcohol Additives. *ChemPhysChem* 2019;20:2553–65. <https://doi.org/10.1002/cphc.201900742>.
- [133] Myshakin EM, Jiang H, Warzinski RP, Jordan KD. Molecular Dynamics Simulations of Methane Hydrate Decomposition. *J Phys Chem A* 2009;113:1913–21. <https://doi.org/10.1021/jp807208z>.
- [134] English NJ, Johnson JK, Taylor CE. Molecular-dynamics simulations of methane hydrate dissociation. *J Chem Phys* 2005;123:244503. <https://doi.org/10.1063/1.2138697>.
- [135] Qi Y, Wu W, Liu Y, Xie Y, Chen X. The influence of NaCl ions on hydrate structure and thermodynamic equilibrium conditions of gas hydrates. *Fluid Phase Equilib* 2012;325:6–10. <https://doi.org/10.1016/j.fluid.2012.04.009>.

- [136] Zhang J, Piana S, Freij-Ayoub R, Rivero M, Choi SK. Molecular dynamics study of methane in water: diffusion and structure. *Mol Simul* 2006;32:1279–86. <https://doi.org/10.1080/08927020601039598>.
- [137] Takeuchi F, Hiratsuka M, Ohmura R, Alavi S, Sum AK, Yasuoka K. Water proton configurations in structures I, II, and H clathrate hydrate unit cells. *J Chem Phys* 2013;138:124504. <https://doi.org/10.1063/1.4795499>.
- [138] Lindahl E, Hess B, van der Spoel D. GROMACS 3.0: a package for molecular simulation and trajectory analysis. *J Mol Model* 2001;7:306–17. <https://doi.org/10.1007/s008940100045>.
- [139] Berendsen HJC, Postma JPM, van Gunsteren WF, Hermans J. Interaction Models for Water in Relation to Protein Hydration, 1981, p. 331–42. https://doi.org/10.1007/978-94-015-7658-1_21.
- [140] Jorgensen WL, Chandrasekhar J, Madura JD, Impey RW, Klein ML. Comparison of simple potential functions for simulating liquid water. *J Chem Phys* 1983;79:926–35. <https://doi.org/10.1063/1.445869>.
- [141] Jorgensen WL, Madura JD. Temperature and size dependence for monte carlo simulations of TIP4P water. *Mol Phys* 1985;56:1381–92. <https://doi.org/10.1080/00268978500103111>.
- [142] Jorgensen WL, Tirado-Rives J. The OPLS [optimized potentials for liquid simulations] potential functions for proteins, energy minimizations for crystals of cyclic peptides and crambin. *J Am Chem Soc* 1988;110:1657–66. <https://doi.org/10.1021/ja00214a001>.
- [143] Kaiser A, Ismailova O, Koskela A, Huber SE, Ritter M, Cosenza B, et al. Ethylene glycol revisited: Molecular dynamics simulations and visualization of the liquid and its hydrogen-bond network. *J Mol Liq* 2014;189:20–9.

- <https://doi.org/10.1016/j.molliq.2013.05.033>.
- [144] Berendsen HJC, Postma JPM, van Gunsteren WF, DiNola A, Haak JR. Molecular dynamics with coupling to an external bath. *J Chem Phys* 1984;81:3684–90. <https://doi.org/10.1063/1.448118>.
- [145] Bussai C, Fritzsche S, Haberlandt R, Hannongbua S. A molecular dynamics (MD) study of methane in silicalite-1: A novel Møller-Plesset potential energy surface. *Stud. Surf. Sci. Catal.*, vol. 154 B, 2004, p. 2104–9. [https://doi.org/10.1016/S0167-2991\(04\)80752-3](https://doi.org/10.1016/S0167-2991(04)80752-3).
- [146] Xu J, Gu T, Sun Z, Li X, Wang X. Molecular dynamics study on the dissociation of methane hydrate via inorganic salts. *Mol Phys* 2016;114:34–43. <https://doi.org/10.1080/00268976.2015.1081708>.
- [147] Allen MP, Tildesley DJ. *Computer simulation of liquids*. vol. 1. Oxford University Press; 2017. <https://doi.org/10.1093/oso/9780198803195.003.0001>.
- [148] Liu Y, Chen C, Hu W, Li W, Dong B, Qin Y. Molecular Dynamics Simulation Studies of Gas Hydrate Growth with Impingement. *Chem Eng J* 2021;426:130705. <https://doi.org/10.1016/j.cej.2021.130705>.
- [149] Alavi S, Ripmeester JA. Nonequilibrium adiabatic molecular dynamics simulations of methane clathrate hydrate decomposition. *J Chem Phys* 2010;132. <https://doi.org/10.1063/1.3382341>.
- [150] Bagherzadeh SA, Englezos P, Alavi S, Ripmeester JA. Molecular simulation of non-equilibrium methane hydrate decomposition process. *J Chem Thermodyn* 2012;44:13–9. <https://doi.org/10.1016/j.jct.2011.08.021>.
- [151] Yagasaki T, Matsumoto M, Tanaka H. Effects of thermodynamic inhibitors on the dissociation of methane hydrate: a molecular dynamics study. *Phys Chem Chem Phys* 2015;17:32347–57. <https://doi.org/10.1039/C5CP03008K>.

- [152] Sun X, Zhou G, Liu Z, Zhu J, Guo F, Chen J, et al. Effect of ethanol concentration on methane hydrate decomposition: MD simulation insights. *J Mater Res Technol* 2021;13:1722–31. <https://doi.org/10.1016/j.jmrt.2021.06.004>.
- [153] Guo Q, Wang H, Liu X, Yuan X, Dong X, Li Y, et al. Computational Analysis of Vibrational Spectra of Hydrogen Bonds in sII and sH Gas Hydrates 2023. <https://doi.org/10.1021/acsomega.3c01237>.
- [154] Liao B, Wang J, Li M-C, Lv K, Wang Q, Li J, et al. Microscopic molecular and experimental insights into multi-stage inhibition mechanisms of alkylated hydrate inhibitor. *Energy* 2023;279:128045. <https://doi.org/10.1016/j.energy.2023.128045>.
- [155] Liao B, Wang J, Sun J, Lv K, Liu L, Wang Q, et al. Microscopic insights into synergism effect of different hydrate inhibitors on methane hydrate formation: Experiments and molecular dynamics simulations. *Fuel* 2023;340:127488. <https://doi.org/10.1016/j.fuel.2023.127488>.
- [156] Wang J, Liao B, Liu L, Chen L, Huang Y, Zhao K, et al. The effect of multi-component Inhibitor systems on hydrate formation. *Gas Sci Eng* 2024;122:205214. <https://doi.org/10.1016/j.jgsce.2024.205214>.
- [157] Su Z, Alavi S, Ripmeester JA, Wolosh G, Dias CL. Methane Clathrate Formation is Catalyzed and Kinetically Inhibited by the Same Molecule: Two Facets of Methanol. *J Phys Chem B* 2021;125:4162–8. <https://doi.org/10.1021/acs.jpcc.1c01274>.
- [158] Shin K, Udachin KA, Moudrakovski IL, Leek DM, Alavi S, Ratcliffe CI, et al. Methanol incorporation in clathrate hydrates and the implications for oil and gas pipeline flow assurance and icy planetary bodies. *Proc Natl Acad Sci* 2013;110:8437–42. <https://doi.org/10.1073/pnas.1302812110>.
- [159] Liao B, Wang J, Li M-C, Lv K, Wang Q, Li J, et al. Microscopic molecular and experimental insights into multi-stage inhibition mechanisms of alkylated hydrate

- inhibitor. *Energy* 2023;279:128045. <https://doi.org/10.1016/j.energy.2023.128045>.
- [160] Bai Y, Bai Q. *Engineering Handbook*. 2004.
- [161] Su Z, Alavi S, Ripmeester JA, Wolosh G, Dias CL. Methane Clathrate Formation is Catalyzed and Kinetically Inhibited by the Same Molecule: Two Facets of Methanol. *J Phys Chem B* 2021;125:4162–8. <https://doi.org/10.1021/acs.jpcc.1c01274>.
- [162] Swank L, Kapadia KP, Webber PA, Jones R. Mitigation of hydrates using continuous KHI injection in deepwater GoM. *Proc Annu Offshore Technol Conf* 2017;2:1440–51. <https://doi.org/10.4043/27791-ms>.
- [163] de Oliveira IA, Barreto AG, Tavares FW, Sum AK. Phase Equilibria Data and Thermodynamic Analysis for Liquid–Hydrate–Vapor (LHV) with High Ethanol Concentrations. *J Chem Eng Data* 2020;65:349–59. <https://doi.org/10.1021/acs.jced.9b00691>.
- [164] Hemmingsen P V., Burgass R, Pedersen KS, Kinnari K, Sørensen H. Hydrate temperature depression of MEG solutions at concentrations up to 60wt%. Experimental data and simulation results. *Fluid Phase Equilib* 2011;307:175–9. <https://doi.org/10.1016/j.fluid.2011.05.010>.
- [165] Haghghi H, Chapoy A, Burgess R, Tohidi B. Experimental and thermodynamic modelling of systems containing water and ethylene glycol: Application to flow assurance and gas processing. *Fluid Phase Equilib* 2009;276:24–30. <https://doi.org/10.1016/j.fluid.2008.10.006>.
- [166] Cha M, Shin K, Kim J, Chang D, Seo Y, Lee H, et al. Thermodynamic and kinetic hydrate inhibition performance of aqueous ethylene glycol solutions for natural gas. *Chem Eng Sci* 2013;99:184–90. <https://doi.org/10.1016/j.ces.2013.05.060>.
- [167] Abay HK, Svartaas TM. Effect of Ultralow Concentration of Methanol on Methane Hydrate Formation. *Energy & Fuels* 2010;24:752–7.

- <https://doi.org/10.1021/ef9009422>.
- [168] Yousif MH. Effect of Underinhibition With Methanol and Ethylene Glycol on the Hydrate-Control Process. *SPE Prod Facil* 1998;13:184–9. <https://doi.org/10.2118/50972-PA>.
- [169] Di Lorenzo M, Aman ZM, Kozielski K, Norris BWE, Johns ML, May EF. Underinhibited Hydrate Formation and Transport Investigated Using a Single-Pass Gas-Dominant Flowloop. *Energy & Fuels* 2014;28:7274–84. <https://doi.org/10.1021/ef501609m>.
- [170] Bi Y, Guo T, Zhang L, Zhang H, Chen L. Experimental study on cool release process of gas-hydrate with additives. *Energy Build* 2009;41:120–4. <https://doi.org/10.1016/j.enbuild.2008.08.004>.
- [171] Fazlali A, Kazemi S, Keshavarz-Moraveji M, Mohammadi AH. Impact of Different Surfactants and their Mixtures on Methane-Hydrate Formation. *Energy Technol* 2013;1:471–7. <https://doi.org/10.1002/ente.201300041>.
- [172] Kumar A, Sakpal T, Linga P, Kumar R. Influence of contact medium and surfactants on carbon dioxide clathrate hydrate kinetics. *Fuel* 2013;105:664–71. <https://doi.org/10.1016/j.fuel.2012.10.031>.
- [173] Ganji H, Manteghian M, Rahimi Mofrad H. Effect of mixed compounds on methane hydrate formation and dissociation rates and storage capacity. *Fuel Process Technol* 2007;88:891–5. <https://doi.org/10.1016/j.fuproc.2007.04.010>.
- [174] Ganji H, Manteghian M, Sadaghiani zadeh K, Omidkhah MR, Rahimi Mofrad H. Effect of different surfactants on methane hydrate formation rate, stability and storage capacity. *Fuel* 2007;86:434–41. <https://doi.org/10.1016/j.fuel.2006.07.032>.
- [175] Karimi R, Varaminian F, Izadpanah AA, Mohammadi AH. Effects of Different Surfactants on the Kinetics of Ethane-Hydrate Formation: Experimental and

- Modeling Studies. Energy Technol 2013;1:530–6.
<https://doi.org/10.1002/ente.201300064>.
- [176] Yoslim J, Linga P, Englezos P. Enhanced growth of methane–propane clathrate hydrate crystals with sodium dodecyl sulfate, sodium tetradecyl sulfate, and sodium hexadecyl sulfate surfactants. J Cryst Growth 2010;313:68–80.
<https://doi.org/10.1016/j.jcrysgro.2010.10.009>.
- [177] Park SS, Lee SB, Kim NJ. Effect of multi-walled carbon nanotubes on methane hydrate formation. J Ind Eng Chem 2010;16:551–5.
<https://doi.org/10.1016/j.jiec.2010.03.023>.
- [178] Arjang S, Manteghian M, Mohammadi A. Effect of synthesized silver nanoparticles in promoting methane hydrate formation at 4.7MPa and 5.7MPa. Chem Eng Res Des 2013;91:1050–4. <https://doi.org/10.1016/j.cherd.2012.12.001>.
- [179] Chari VD, Sharma DVSGK, Prasad PSR, Murthy SR. Methane hydrates formation and dissociation in nano silica suspension. J Nat Gas Sci Eng 2013;11:7–11.
<https://doi.org/10.1016/j.jngse.2012.11.004>.
- [180] Najibi H, Mirzaee Shayegan M, Heidary H. Experimental investigation of methane hydrate formation in the presence of copper oxide nanoparticles and SDS. J Nat Gas Sci Eng 2015;23:315–23. <https://doi.org/10.1016/j.jngse.2015.02.009>.
- [181] Li J, Liang D, Guo K, Wang R, Fan S. Formation and dissociation of HFC134a gas hydrate in nano-copper suspension. Energy Convers Manag 2006;47:201–10.
<https://doi.org/10.1016/j.enconman.2005.03.018>.
- [182] Mohammadi M, Haghtalab A, Fakhroueian Z. Experimental study and thermodynamic modeling of CO₂ gas hydrate formation in presence of zinc oxide nanoparticles. J Chem Thermodyn 2016;96:24–33.
<https://doi.org/10.1016/j.jct.2015.12.015>.

- [183] Dongliang L, Hao P, Deqing L. Thermal conductivity enhancement of clathrate hydrate with nanoparticles. *Int J Heat Mass Transf* 2017;104:566–73. <https://doi.org/10.1016/j.ijheatmasstransfer.2016.08.081>.
- [184] Javidani AM, Abedi-Farizhendi S, Mohammadi A, Hassan H, Mohammadi AH, Manteghian M. The effects of graphene oxide nanosheets and Al₂O₃ nanoparticles on the kinetics of methane + THF hydrate formation at moderate conditions. *J Mol Liq* 2020;316:113872. <https://doi.org/10.1016/j.molliq.2020.113872>.
- [185] Zhou S, Yu Y, Zhao M, Wang S, Zhang G-Z. Effect of Graphite Nanoparticles on Promoting CO₂ Hydrate Formation. *Energy & Fuels* 2014;28:4694–8. <https://doi.org/10.1021/ef5000886>.
- [186] Pahlavanzadeh H, Rezaei S, Khanlarkhani M, Manteghian M, Mohammadi AH. Kinetic study of methane hydrate formation in the presence of copper nanoparticles and CTAB. *J Nat Gas Sci Eng* 2016;34:803–10. <https://doi.org/10.1016/j.jngse.2016.07.001>.
- [187] Nashed O, Partoon B, Lal B, Sabil KM, Shariff AM. Review the impact of nanoparticles on the thermodynamics and kinetics of gas hydrate formation. *J Nat Gas Sci Eng* 2018;55:452–65. <https://doi.org/10.1016/j.jngse.2018.05.022>.
- [188] Abedi-Farizhendi S, Rahmati-Abkenar M, Manteghian M, Salehzadeh Yekshaveh J, Zahmatkeshan V. Kinetic study of propane hydrate in the presence of carbon nanostructures and SDS. *J Pet Sci Eng* 2019;172:636–42. <https://doi.org/10.1016/j.petrol.2018.04.075>.
- [189] Kakati H, Mandal A, Laik S. Promoting effect of Al₂O₃/ZnO-based nanofluids stabilized by SDS surfactant on CH₄+C₂H₆+C₃H₈ hydrate formation. *J Ind Eng Chem* 2016;35:357–68. <https://doi.org/10.1016/j.jiec.2016.01.014>.
- [190] Zhou S, Jiang K, Zhao Y, Chi Y, Wang S, Zhang G. Experimental Investigation of

- CO₂ Hydrate Formation in the Water Containing Graphite Nanoparticles and Tetra-
n-butyl Ammonium Bromide. *J Chem Eng Data* 2018;63:389–94.
<https://doi.org/10.1021/acs.jced.7b00785>.
- [191] Chaturvedi KR, Sharma T. Rheological analysis and EOR potential of surfactant
treated single-step silica nanofluid at high temperature and salinity. *J Pet Sci Eng*
2021;196:107704. <https://doi.org/10.1016/j.petrol.2020.107704>.
- [192] Bailey JK, Mecartney ML. Formation of colloidal silica particles from alkoxides.
Colloids and Surfaces 1992;63:151–61. [https://doi.org/10.1016/0166-
6622\(92\)80081-C](https://doi.org/10.1016/0166-6622(92)80081-C).
- [193] Vajihinejad V, Gumfekar SP, Bazoubandi B, Rostami Najafabadi Z, Soares JBP.
Water Soluble Polymer Flocculants: Synthesis, Characterization, and Performance
Assessment. *Macromol Mater Eng* 2019;304.
<https://doi.org/10.1002/mame.201800526>.
- [194] Kvamme B, Kuznetsova T, Aasoldsen K. Molecular dynamics simulations for
selection of kinetic hydrate inhibitors. *J Mol Graph Model* 2005;23:524–36.
<https://doi.org/10.1016/j.jmgm.2005.04.001>.
- [195] Kumar RS, Narukulla R, Sharma T. Comparative Effectiveness of Thermal Stability
and Rheological Properties of Nanofluid of SiO₂–TiO₂ Nanocomposites for Oil
Field Applications. *Ind Eng Chem Res* 2020;59:15768–83.
<https://doi.org/10.1021/acs.iecr.0c01944>.
- [196] Prasad SK, Nair VC, Sangwai JS. Effect of Asphaltenes on the Kinetics of Methane
Hydrate Formation and Dissociation in Oil-in-Water Dispersion Systems Containing
Light Saturated and Aromatic Hydrocarbons. *Energy & Fuels* 2021;35:17410–23.
<https://doi.org/10.1021/acs.energyfuels.1c02252>.
- [197] Prasad SK, Sangwai JS. Impact of lighter alkanes on the formation and dissociation

- kinetics of methane hydrate in oil-in-water dispersions relevant for flow assurance. *Fuel* 2023;333:126500. <https://doi.org/10.1016/j.fuel.2022.126500>.
- [198] Mohammadi A, Manteghian M, Haghtalab A, Mohammadi AH, Rahmati-Abkenar M. Kinetic study of carbon dioxide hydrate formation in presence of silver nanoparticles and SDS. *Chem Eng J* 2014;237:387–95. <https://doi.org/10.1016/j.cej.2013.09.026>.
- [199] Mohammadi A, Manteghian M, Mohammadi AH, Jahangiri A. Induction time, storage capacity, and rate of methane hydrate formation in the presence of SDS and silver nanoparticles. *Chem Eng Commun* 2017;204:1420–7. <https://doi.org/10.1080/00986445.2017.1366903>.
- [200] Prasad PSR, Kiran BS, Sowjanya K. Enhanced methane gas storage in the form of hydrates : role of the confined water molecules in silica powders † 2020:17795–804. <https://doi.org/10.1039/d0ra01754j>.
- [201] Zhai J, Shang L, Zhou L, Yao X, Bai J, Lv Z. Kinetics of Methane Hydrate Formation in the Presence of Silica Nanoparticles and Cetyltrimethylammonium Bromide 2022;202200215:1–6. <https://doi.org/10.1002/slct.202200215>.
- [202] Kumar A, Kushwaha OS, Rangsunvigit P, Linga P, Kumar R. Effect of additives on formation and decomposition kinetics of methane clathrate hydrates: Application in energy storage and transportation. *Can J Chem Eng* 2016;94:2160–7. <https://doi.org/10.1002/cjce.22583>.
- [203] Li X-S, Xu C-G, Zhang Y, Ruan X-K, Li G, Wang Y. Investigation into gas production from natural gas hydrate: A review. *Appl Energy* 2016;172:286–322. <https://doi.org/10.1016/j.apenergy.2016.03.101>.
- [204] Chaturvedi KR, Pandey A, Kumar R, Sharma T. Role of hydrogen to promote hydrate formation of flue gas mixture of CO₂ and N₂ in silica nanofluid of single-

- step origin. *J Environ Chem Eng* 2021;9:106591.
<https://doi.org/10.1016/j.jece.2021.106591>.
- [205] DuQuesnay JR, Diaz Posada MC, Beltran JG. Novel gas hydrate reactor design: 3-in-1 assessment of phase equilibria, morphology and kinetics. *Fluid Phase Equilib* 2016;413:148–57. <https://doi.org/10.1016/j.fluid.2015.11.006>.
- [206] Lederhos JP, Long JP, Sum A, Christiansen RL, Sloan ED. Effective kinetic inhibitors for natural gas hydrates. *Chem Eng Sci* 1996;51:1221–9. [https://doi.org/10.1016/0009-2509\(95\)00370-3](https://doi.org/10.1016/0009-2509(95)00370-3).
- [207] Sun S, Gu L, Yang Z, Lin H, Li Y. Thermophysical properties of natural gas hydrates: A review. *Nat Gas Ind B* 2022;9:246–63. <https://doi.org/10.1016/j.ngib.2022.04.003>.
- [208] Chaturvedi KR, Fogat M, Sharma T. Low Temperature rheological characterization of single-step silica nanofluids: An additive in refrigeration and gas hydrate drilling applications. *J Pet Sci Eng* 2021;204:108742. <https://doi.org/10.1016/j.petrol.2021.108742>.
- [209] Li G, Liu D, Xie Y, Xiao Y. Study on Effect Factors for CO₂ Hydrate Rapid Formation in a Water-Spraying Apparatus. *Energy & Fuels* 2010;24:4590–7. <https://doi.org/10.1021/ef100417y>.
- [210] Luo YT, Zhu JH, Fan SS, Chen GJ. Study on the kinetics of hydrate formation in a bubble column. *Chem Eng Sci* 2007;62:1000–9. <https://doi.org/10.1016/j.ces.2006.11.004>.
- [211] Kang SP, Lee H, Lee CS, Sung WM. Hydrate phase equilibria of the guest mixtures containing CO₂, N₂ and tetrahydrofuran. *Fluid Phase Equilib* 2001;185:101–9. [https://doi.org/10.1016/S0378-3812\(01\)00460-5](https://doi.org/10.1016/S0378-3812(01)00460-5).
- [212] Hassan H, Pahlavanzadeh H. Thermodynamic modeling and experimental

- measurement of semi-clathrate hydrate phase equilibria for CH₄ in the presence of cyclohexane (CH) and tetra-n-butyl ammonium bromide (TBAB) mixture. *J Nat Gas Sci Eng* 2020;75:103128. <https://doi.org/10.1016/j.jngse.2019.103128>.
- [213] Stoporev AS, Svarovskaya LI, Strelets LA, Altunina LK, Manakov AY. Effect of reactor wall material on the nucleation of methane hydrate in water-in-oil emulsions. *Mendeleeev Commun* 2018;28:343–4. <https://doi.org/10.1016/j.mencom.2018.05.039>.
- [214] Gootam D, Gaikwad N, Kumar R, Kaisare N. Modeling Growth Kinetics of Methane Hydrate in Stirred Tank Batch Reactors. *ACS Eng Au* 2021;1:148–59. <https://doi.org/10.1021/acsengineeringau.1c00012>.
- [215] Linga P, Kumar R, Lee JD, Ripmeester J, Englezos P. A new apparatus to enhance the rate of gas hydrate formation: Application to capture of carbon dioxide. *Int J Greenh Gas Control* 2010;4:630–7. <https://doi.org/10.1016/j.ijggc.2009.12.014>.
- [216] Ganji H, Manteghian M, Sadaghiani zadeh K, Omidkhah MR, Rahimi Mofrad H. Effect of different surfactants on methane hydrate formation rate, stability and storage capacity. *Fuel* 2007;86:434–41. <https://doi.org/10.1016/j.fuel.2006.07.032>.
- [217] Yoslim J, Linga P, Englezos P. Enhanced growth of methane–propane clathrate hydrate crystals with sodium dodecyl sulfate, sodium tetradecyl sulfate, and sodium hexadecyl sulfate surfactants. *J Cryst Growth* 2010;313:68–80. <https://doi.org/10.1016/j.jcrysgro.2010.10.009>.
- [218] Zhong Y, Rogers RE. Surfactant effects on gas hydrate formation. *Chem Eng Sci* 2000;55:4175–87. [https://doi.org/10.1016/S0009-2509\(00\)00072-5](https://doi.org/10.1016/S0009-2509(00)00072-5).
- [219] Kaczerewska O, Martins R, Figueiredo J, Loureiro S, Tedim J. Environmental behaviour and ecotoxicity of cationic surfactants towards marine organisms. *J Hazard Mater* 2020;392:122299. <https://doi.org/10.1016/j.jhazmat.2020.122299>.

- [220] Nahri SY, Nielsen JL, Chen Y. Effect of nanoparticles on the nucleation and agglomeration rates of hydrate growth using THF–water clathrates. *Pet Sci* 2020;17:467–76. <https://doi.org/10.1007/s12182-019-00390-4>.
- [221] Su X, Gao Y, Yin F, Li S. Investigation on the Influence of Different Coating Surfaces on the Adhesive Force of Hydrate Particles. *J Mar Sci Eng* 2024;12:232. <https://doi.org/10.3390/jmse12020232>.
- [222] Filarsky F, Schmuck C, Schultz HJ. Impact of Modified Silica Beads on Methane Hydrate Formation in a Fixed-Bed Reactor. *Ind Eng Chem Res* 2019;58:16687–95. <https://doi.org/10.1021/acs.iecr.9b01952>.
- [223] Beltrán JG, Servio P. Morphological Investigations of Methane–Hydrate Films Formed on a Glass Surface. *Cryst Growth Des* 2010;10:4339–47. <https://doi.org/10.1021/cg1003098>.
- [224] Em Y, Stoporev A, Semenov A, Glotov A, Smirnova E, Villevald G, et al. Methane Hydrate Formation in Halloysite Clay Nanotubes. *ACS Sustain Chem Eng* 2020;8:7860–8. <https://doi.org/10.1021/acssuschemeng.0c00758>.
- [225] Linga P, Haligva C, Nam SC, Ripmeester JA, Englezos P. Gas Hydrate Formation in a Variable Volume Bed of Silica Sand Particles. *Energy & Fuels* 2009;23:5496–507. <https://doi.org/10.1021/ef900542m>.
- [226] Esmail S, Beltran JG. Methane hydrate propagation on surfaces of varying wettability. *J Nat Gas Sci Eng* 2016;35:1535–43. <https://doi.org/10.1016/j.jngse.2016.06.068>.
- [227] Kumar A, Veluswamy HP, Kumar R, Linga P. Kinetic promotion of mixed methane-THF hydrate by additives: Opportune to energy storage. *Energy Procedia* 2019;158:5287–92. <https://doi.org/10.1016/j.egypro.2019.01.647>.
- [228] Kumar RS, Al-Arbi Ganat T, Sharma T. Performance evaluation of silica nanofluid

- for sand column transport with simultaneous wettability alteration: An approach to environmental issue. *J Clean Prod* 2021;303:127047. <https://doi.org/10.1016/j.jclepro.2021.127047>.
- [229] Chaturvedi KR, Narukulla R, Sharma T. CO₂ capturing evaluation of single-step silica nanofluid through rheological investigation for nanofluid use in carbon utilization applications. *J Mol Liq* 2020;304:112765. <https://doi.org/10.1016/j.molliq.2020.112765>.
- [230] Filarsky F, Hagelstein M, Schultz HJ. Influence of different stirring setups on mass transport, gas hydrate formation, and scale transfer concepts for technical gas hydrate applications. *Appl Res* 2023;2. <https://doi.org/10.1002/appl.202200050>.
- [231] Wu Y, Shang L, Pan Z, Xuan Y, Baena-Moreno FM, Zhang Z. Gas hydrate formation in the presence of mixed surfactants and alumina nanoparticles. *J Nat Gas Sci Eng* 2021;94:104049. <https://doi.org/10.1016/j.jngse.2021.104049>.
- [232] Sharifi Dehsari H, Halda Ribeiro A, Ersöz B, Tremel W, Jakob G, Asadi K. Effect of precursor concentration on size evolution of iron oxide nanoparticles. *CrystEngComm* 2017;19:6694–702. <https://doi.org/10.1039/C7CE01406F>.
- [233] Tantra R, Schulze P, Quincey P. Effect of nanoparticle concentration on zeta-potential measurement results and reproducibility. *Particuology* 2010;8:279–85. <https://doi.org/10.1016/j.partic.2010.01.003>.
- [234] Lv XF, Shi BH, Wang Y, Tang YX, Wang LY, Gong J. Experimental Study on Hydrate Induction Time of Gas-Saturated Water-in-Oil Emulsion using a High-Pressure Flow Loop. *Oil Gas Sci Technol – Rev d'IFP Energies Nouv* 2015;70:1111–24. <https://doi.org/10.2516/ogst/2014032>.
- [235] Rajabi Firoozabadi S, Bonyadi M. A comparative study on the effects of Fe₃O₄ nanofluid, SDS and CTAB aqueous solutions on the CO₂ hydrate formation. *J Mol*

- Liq 2020;300:112251. <https://doi.org/10.1016/j.molliq.2019.112251>.
- [236] Said S, Govindaraj V, Herri J-M, Ouabbas Y, Khodja M, Belloum M, et al. A study on the influence of nanofluids on gas hydrate formation kinetics and their potential: Application to the CO₂ capture process. *J Nat Gas Sci Eng* 2016;32:95–108. <https://doi.org/10.1016/j.jngse.2016.04.003>.
- [237] Wang F, Luo SJ, Fu SF, Jia ZZ, Dai M, Wang CS, et al. Methane hydrate formation with surfactants fixed on the surface of polystyrene nanospheres. *J Mater Chem A* 2015;3:8316–23. <https://doi.org/10.1039/C5TA01101A>.
- [238] Peng DY, Robinson DB. A New Two-Constant Equation of State. *Ind Eng Chem Fundam* 1976;15:59–64. <https://doi.org/10.1021/i160057a011>.
- [239] Javidani AM, Abedi-Farizhendi S, Mohammadi A, Mohammadi AH, Hassan H, Pahlavanzadeh H. Experimental study and kinetic modeling of R410a hydrate formation in presence of SDS, tween 20, and graphene oxide nanosheets with application in cold storage. *J Mol Liq* 2020;304:112665. <https://doi.org/10.1016/j.molliq.2020.112665>.
- [240] Lv X, Shi B, Zhou S, Peng H, Lei Y, Yu P. Study on the growth rate of natural gas hydrate in water-in-oil emulsion system using a high-pressure flow loop. *RSC Adv* 2018;8:36484–92. <https://doi.org/10.1039/C8RA07571A>.
- [241] Gonçalves I, Souza R, Coutinho G, Miranda J, Moita A, Pereira JE, et al. Thermal Conductivity of Nanofluids: A Review on Prediction Models, Controversies and Challenges. *Appl Sci* 2021;11:2525. <https://doi.org/10.3390/app11062525>.
- [242] Aliabadi M, Rasoolzadeh A, Esmailzadeh F, Alamdari AM. Experimental study of using CuO nanoparticles as a methane hydrate promoter. *J Nat Gas Sci Eng* 2015;27:1518–22. <https://doi.org/10.1016/j.jngse.2015.10.017>.
- [243] Das A, Saini V, Parikh K, Parikh J, Ghosh P, Tot M. Pathways to net zero emissions

- for the Indian power sector. *Energy Strateg Rev* 2023;45:101042. <https://doi.org/10.1016/j.esr.2022.101042>.
- [244] Stern N, Valero A. Innovation, growth and the transition to net-zero emissions. *Res Policy* 2021;50:104293. <https://doi.org/10.1016/j.respol.2021.104293>.
- [245] Hirohama S, Shimoyama Y, Wakabayashi A, Tatsuta S, Nishida N. Conversion of CH₄-Hydrate to CO₂-Hydrate in Liquid CO₂. *J Chem Eng JAPAN* 1996;29:1014–20. <https://doi.org/10.1252/jcej.29.1014>.
- [246] Zhao J, Cheng C, Song Y, Liu W, Liu Y, Xue K, et al. Heat Transfer Analysis of Methane Hydrate Sediment Dissociation in a Closed Reactor by a Thermal Method. *Energies* 2012;5:1292–308. <https://doi.org/10.3390/en5051292>.
- [247] Boswell R, Collett TS. Current perspectives on gas hydrate resources. *Energy Environ Sci* 2011;4:1206–15. <https://doi.org/10.1039/C0EE00203H>.
- [248] Copard Y, Amiotte-Suchet P, Di-Giovanni C. Storage and release of fossil organic carbon related to weathering of sedimentary rocks. *Earth Planet Sci Lett* 2007;258:345–57. <https://doi.org/10.1016/j.epsl.2007.03.048>.
- [249] Goel N. In situ methane hydrate dissociation with carbon dioxide sequestration: Current knowledge and issues. *J Pet Sci Eng* 2006;51:169–84. <https://doi.org/10.1016/j.petrol.2006.01.005>.
- [250] Boswell R, Schoderbek D, Collett TS, Ohtsuki S, White M, Anderson BJ. The Iñiuk Sikumi Field Experiment, Alaska North Slope: Design, Operations, and Implications for CO₂–CH₄ Exchange in Gas Hydrate Reservoirs. *Energy & Fuels* 2017;31:140–53. <https://doi.org/10.1021/acs.energyfuels.6b01909>.
- [251] Cha M, Shin K, Lee H, Moudrakovski IL, Ripmeester JA, Seo Y. Kinetics of Methane Hydrate Replacement with Carbon Dioxide and Nitrogen Gas Mixture Using in Situ NMR Spectroscopy. *Environ Sci Technol* 2015;49:1964–71.

- <https://doi.org/10.1021/es504888n>.
- [252] Zhou X, Liang D, Liang S, Yi L, Lin F. Recovering CH₄ from Natural Gas Hydrates with the Injection of CO₂–N₂ Gas Mixtures. *Energy & Fuels* 2015;29:1099–106. <https://doi.org/10.1021/ef5025824>.
- [253] Liang S, Kusalik PG. Crystal Growth Simulations of H₂S Hydrate. *J Phys Chem B* 2010;114:9563–71. <https://doi.org/10.1021/jp102584d>.
- [254] Ji H, Chen D, Zhao C, Wu G. Molecular Dynamics Simulation of Methane Hydrate Formation and Dissociation in the Clay Pores with Fatty Acids. *J Phys Chem C* 2018;122:1318–25. <https://doi.org/10.1021/acs.jpcc.7b08808>.
- [255] Tariq M, Soromenho MRC, Rebelo LPN, Esperança JMSS. Insights into CO₂ hydrates formation and dissociation at isochoric conditions using a rocking cell apparatus. *Chem Eng Sci* 2022;249:117319. <https://doi.org/10.1016/j.ces.2021.117319>.
- [256] Kelemen P, Benson SM, Pilorgé H, Psarras P, Wilcox J. An Overview of the Status and Challenges of CO₂ Storage in Minerals and Geological Formations. *Front Clim* 2019;1. <https://doi.org/10.3389/fclim.2019.00009>.
- [257] Ketzer M, Praeg D, Rodrigues LF, Augustin A, Pivel MAG, Rahmati-Abkenar M, et al. Gas hydrate dissociation linked to contemporary ocean warming in the southern hemisphere. *Nat Commun* 2020;11:3788. <https://doi.org/10.1038/s41467-020-17289-z>.
- [258] Long Z, Zhou X, He Y, Li D, Liang D. Performance of mixture of ethylene glycol and glycine in inhibiting methane hydrate formation. *J Nat Gas Sci Eng* 2018;56:134–40. <https://doi.org/10.1016/j.jngse.2018.05.034>.
- [259] Lim VWS, Metaxas PJ, Johns ML, Aman ZM, May EF. The impact of mono-ethylene glycol and kinetic inhibitors on methane hydrate formation. *Chem Eng J*

- 2022;427:131531. <https://doi.org/10.1016/j.cej.2021.131531>.
- [260] Chialvo AA, Houssa M, Cummings PT. Molecular Dynamics Study of the Structure and Thermophysical Properties of Model sI Clathrate Hydrates. *J Phys Chem B* 2002;106:442–51. <https://doi.org/10.1021/jp012735b>.
- [261] Zhang J, Hawtin RW, Yang Y, Nakagawa E, Rivero M, Choi SK, et al. Molecular Dynamics Study of Methane Hydrate Formation at a Water/Methane Interface. *J Phys Chem B* 2008;112:10608–18. <https://doi.org/10.1021/jp076904p>.
- [262] Bai D, Chen G, Zhang X, Wang W. Microsecond Molecular Dynamics Simulations of the Kinetic Pathways of Gas Hydrate Formation from Solid Surfaces. *Langmuir* 2011;27:5961–7. <https://doi.org/10.1021/la105088b>.
- [263] Cheng L, Cui J, Li Z, Liu B, Ban S, Chen G. Molecular dynamics simulation of the formation of methane hydrates in the presence of KHIs. *Chem Eng Sci* 2021;236:116508. <https://doi.org/10.1016/j.ces.2021.116508>.
- [264] Bai D, Zhang X, Chen G, Wang W. Replacement mechanism of methane hydrate with carbon dioxide from microsecond molecular dynamics simulations. *Energy Environ Sci* 2012;5:7033. <https://doi.org/10.1039/c2ee21189k>.
- [265] Dashti H, Thomas D, Amiri A. Modeling of hydrate-based CO₂ capture with nucleation stage and induction time prediction capability. *J Clean Prod* 2019;231:805–16. <https://doi.org/10.1016/j.jclepro.2019.05.240>.
- [266] Gambelli AM. Variations in terms of CO₂ capture and CH₄ recovery during replacement processes in gas hydrate reservoirs, associated to the “memory effect.” *J Clean Prod* 2022;360:132154. <https://doi.org/10.1016/j.jclepro.2022.132154>.
- [267] Tian H, Yu Z, Xu T, Xiao T, Shang S. Evaluating the recovery potential of CH₄ by injecting CO₂ mixture into marine hydrate-bearing reservoirs with a new multi-gas hydrate simulator. *J Clean Prod* 2022;361:132270.

- <https://doi.org/10.1016/j.jclepro.2022.132270>.
- [268] Liang S, Liang D, Wu N, Yi L, Hu G. Molecular Mechanisms of Gas Diffusion in CO₂ Hydrates. *J Phys Chem C* 2016;120:16298–304. <https://doi.org/10.1021/acs.jpcc.6b03111>.
- [269] Geng C-Y, Wen H, Zhou H. Molecular Simulation of the Potential of Methane Reoccupation during the Replacement of Methane Hydrate by CO₂. *J Phys Chem A* 2009;113:5463–9. <https://doi.org/10.1021/jp811474m>.
- [270] Chen L, Yamada H, Kanda Y, Okajima J, Komiya A, Maruyama S. Investigation on the dissociation flow of methane hydrate cores: Numerical modeling and experimental verification. *Chem Eng Sci* 2017;163:31–43. <https://doi.org/10.1016/j.ces.2017.01.032>.
- [271] Hembram BK, Mahmud M, Tripathi R, Nair VC, Sharma T. Insights of Molecular Dynamics Simulation To Investigate the Impact of Ethylene Glycol on Methane Hydrate Dissociation. *Energy & Fuels* 2024;38:1923–33. <https://doi.org/10.1021/acs.energyfuels.3c03854>.
- [272] Berendsen HJC, van der Spoel D, van Drunen R. GROMACS: A message-passing parallel molecular dynamics implementation. *Comput Phys Commun* 1995;91:43–56. [https://doi.org/10.1016/0010-4655\(95\)00042-E](https://doi.org/10.1016/0010-4655(95)00042-E).
- [273] Martínez L, Andrade R, Birgin EG, Martínez JM. P <sc>ACKMOL</sc> : A package for building initial configurations for molecular dynamics simulations. *J Comput Chem* 2009;30:2157–64. <https://doi.org/10.1002/jcc.21224>.
- [274] Park SH, Sposito G. Monte Carlo Simulation of Total Radial Distribution Functions for Interlayer Water in Li-, Na-, and K-Montmorillonite Hydrates. *J Phys Chem B* 2000;104:4642–8. <https://doi.org/10.1021/jp993017g>.
- [275] Alavi S, Shin K, Ripmeester JA. Molecular Dynamics Simulations of Hydrogen

- Bonding in Clathrate Hydrates with Ammonia and Methanol Guest Molecules. *J Chem Eng Data* 2015;60:389–97. <https://doi.org/10.1021/je5006517>.
- [276] Katayama Y, Hattori T, Saitoh H, Ikeda T, Aoki K, Fukui H, et al. Structure of liquid water under high pressure up to 17 GPa. *Phys Rev B* 2010;81:014109. <https://doi.org/10.1103/PhysRevB.81.014109>.
- [277] Liang S, Kusalik PG. Explorations of gas hydrate crystal growth by molecular simulations. *Chem Phys Lett* 2010;494:123–33. <https://doi.org/10.1016/j.cplett.2010.05.088>.
- [278] Dyupina E, van Amstel A. Arctic methane. *J Integr Environ Sci* 2013;10:93–105. <https://doi.org/10.1080/1943815X.2013.816749>.
- [279] Liu N, Zhou J, Hong C. Molecular dynamics simulations on dissociation of CO₂ hydrate in the presence of inhibitor. *Chem Phys* 2020;538:110894. <https://doi.org/10.1016/j.chemphys.2020.110894>.
- [280] Mukherjee S, Kumar A, Zaworotko MJ. Metal-organic framework based carbon capture and purification technologies for clean environment. *Met. Fram. Environ. Appl.*, Elsevier; 2019, p. 5–61. <https://doi.org/10.1016/B978-0-12-814633-0.00003-X>.
- [281] Lindsey R. Climate Change: Atmospheric Carbon Dioxide. *Natl Ocean Atmos Adm* 2024. <https://www.climate.gov/news-features/understanding-climate/climate-change-atmospheric-carbon-dioxide>.
- [282] Wright VP. *World Energy Outlook*. 1986:23–8.
- [283] Liu PR, Raftery AE. Country-based rate of emissions reductions should increase by 80% beyond nationally determined contributions to meet the 2 °C target. *Commun Earth Environ* 2021;2:29. <https://doi.org/10.1038/s43247-021-00097-8>.
- [284] Åhlén M, Cheung O, Xu C. Low-concentration CO₂ capture using metal–organic

- frameworks – current status and future perspectives. *Dalt Trans* 2023;52:1841–56.
<https://doi.org/10.1039/D2DT04088C>.
- [285] Canadell JG, Poulter B, Bastos A, Ciais P, Hayes DJ, Thompson RL, et al. Balancing greenhouse gas sources and sinks: Inventories, budgets, and climate policy. *Balanc. Greenh. Gas Budgets*, Elsevier; 2022, p. 3–28. <https://doi.org/10.1016/B978-0-12-814952-2.00024-1>.
- [286] Gao Y, Gao X, Zhang X. The 2 °C Global Temperature Target and the Evolution of the Long-Term Goal of Addressing Climate Change—From the United Nations Framework Convention on Climate Change to the Paris Agreement. *Engineering* 2017;3:272–8. <https://doi.org/10.1016/J.ENG.2017.01.022>.
- [287] IPCC. *Global Warming of 1.5°C*. Cambridge University Press; 2022. <https://doi.org/10.1017/9781009157940>.
- [288] Bashir A, Ali M, Patil S, Aljawad MS, Mahmoud M, Al-Shehri D, et al. Comprehensive review of CO₂ geological storage: Exploring principles, mechanisms, and prospects. *Earth-Science Rev* 2024;249:104672. <https://doi.org/10.1016/j.earscirev.2023.104672>.
- [289] Prasad SK, Sangwai JS, Byun H-S. A review of the supercritical CO₂ fluid applications for improved oil and gas production and associated carbon storage. *J CO₂ Util* 2023;72:102479. <https://doi.org/10.1016/j.jcou.2023.102479>.
- [290] Kim S, Ko Y, Lee GJ, Lee JW, Xu R, Ahn H, et al. Sustainable energy harvesting from post-combustion CO₂ capture using amine-functionalized solvents. *Energy* 2023;267:126532. <https://doi.org/10.1016/j.energy.2022.126532>.
- [291] Kumar S, Srivastava R, Koh J. Utilization of zeolites as CO₂ capturing agents: Advances and future perspectives. *J CO₂ Util* 2020;41:101251. <https://doi.org/10.1016/j.jcou.2020.101251>.

- [292] Ding Y, Ma L, Zeng F, Zhao X, Wang H, Zhu X, et al. Synthesis and CO₂ adsorption kinetics of Aluminum Fumarate MOFs pellet with high recovery. *Energy* 2023;263:125723. <https://doi.org/10.1016/j.energy.2022.125723>.
- [293] Jung W, Lee J. Pseudo counter-current turbulent fluidized bed process with sensible heat recovery for energy-efficient CO₂ capture using an amine-functionalized solid sorbent. *Energy* 2022;240:122803. <https://doi.org/10.1016/j.energy.2021.122803>.
- [294] Alhosani A, Scanziani A, Lin Q, Raeini AQ, Bijeljic B, Blunt MJ. Pore-scale mechanisms of CO₂ storage in oilfields. *Sci Rep* 2020;10:8534. <https://doi.org/10.1038/s41598-020-65416-z>.
- [295] Nair VC, Prasad SK, Kumar R, Sangwai JS. High-Pressure Rheology of Methane Hydrate Sediment Slurry Using a Modified Couette Geometry. *Ind Eng Chem Res* 2020;59:4079–92. <https://doi.org/10.1021/acs.iecr.9b04390>.
- [296] Prasad SK, Kumar Y, Bhawangirkar DR, Gaikwad N, Sangwai JS. Direct Flue Gas Injection into Ocean for Simultaneous Energy Recovery and CO₂ Sequestration in Solid Hydrate Reservoirs. *Energy & Fuels* 2024;38:16622–37. <https://doi.org/10.1021/acs.energyfuels.4c02058>.
- [297] Raza W, Raza N, Agbe H, Kumar RV, Kim K-H, Yang J. Multistep sequestration and storage of CO₂ to form valuable products using forsterite. *Energy* 2018;155:865–73. <https://doi.org/10.1016/j.energy.2018.05.077>.
- [298] Duc NH, Chauvy F, Herri J-M. CO₂ capture by hydrate crystallization – A potential solution for gas emission of steelmaking industry. *Energy Convers Manag* 2007;48:1313–22. <https://doi.org/10.1016/j.enconman.2006.09.024>.
- [299] Khokhar AA, Gudmundsson JS, Sloan ED. Gas storage in structure H hydrates. *Fluid Phase Equilib* 1998;150–151:383–92. [https://doi.org/10.1016/S0378-3812\(98\)00338-0](https://doi.org/10.1016/S0378-3812(98)00338-0).

- [300] Circone S, Stern LA, Kirby SH, Durham WB, Chakoumakos BC, Rawn CJ, et al. CO₂ Hydrate: Synthesis, Composition, Structure, Dissociation Behavior, and a Comparison to Structure I CH₄ Hydrate. *J Phys Chem B* 2003;107:5529–39. <https://doi.org/10.1021/jp027391j>.
- [301] Anderson GK. Enthalpy of dissociation and hydration number of carbon dioxide hydrate from the Clapeyron equation. *J Chem Thermodyn* 2003;35:1171–83. [https://doi.org/10.1016/S0021-9614\(03\)00093-4](https://doi.org/10.1016/S0021-9614(03)00093-4).
- [302] Ripmeester JA, Ratcliffe CI. The Diverse Nature of Dodecahedral Cages in Clathrate Hydrates As Revealed by ¹²⁹Xe and ¹³C NMR Spectroscopy: CO₂ as a Small-Cage Guest. *Energy & Fuels* 1998;12:197–200. <https://doi.org/10.1021/ef970171y>.
- [303] Ratcliffe CI, Ripmeester JA. Proton and carbon-13 NMR studies on carbon dioxide hydrate. *J Phys Chem* 1986;90:1259–63. <https://doi.org/10.1021/j100398a012>.
- [304] Chazallon B, Kuhs WF. In situ structural properties of N₂-, O₂-, and air-clathrates by neutron diffraction. *J Chem Phys* 2002;117:308–20. <https://doi.org/10.1063/1.1480861>.
- [305] Henning RW, Schultz AJ, Thieu V, Halpern Y. Neutron Diffraction Studies of CO₂ Clathrate Hydrate: Formation from Deuterated Ice. *J Phys Chem A* 2000;104:5066–71. <https://doi.org/10.1021/jp0001642>.
- [306] Udachin KA, Ratcliffe CI, Ripmeester JA. Structure, Composition, and Thermal Expansion of CO₂ Hydrate from Single Crystal X-ray Diffraction Measurements. *J Phys Chem B* 2001;105:4200–4. <https://doi.org/10.1021/jp004389o>.
- [307] Zheng J, Yang M, Liu Y, Wang D, Song Y. Effects of cyclopentane on CO₂ hydrate formation and dissociation as a co-guest molecule for desalination. *J Chem Thermodyn* 2017;104:9–15. <https://doi.org/10.1016/j.jct.2016.09.006>.
- [308] Dufour T, Hoang HM, Oignet J, Osswald V, Clain P, Fournaison L, et al. Impact of

- pressure on the dynamic behavior of CO₂ hydrate slurry in a stirred tank reactor applied to cold thermal energy storage. *Appl Energy* 2017;204:641–52. <https://doi.org/10.1016/j.apenergy.2017.07.098>.
- [309] Cheng Z, Xu H, Wang S, Liu W, Li Y, Jiang L, et al. Effect of nanoparticles as a substitute for kinetic additives on the hydrate-based CO₂ capture. *Chem Eng J* 2021;424:130329. <https://doi.org/10.1016/j.cej.2021.130329>.
- [310] Yang M, Song Y, Jiang L, Zhao Y, Ruan X, Zhang Y, et al. Hydrate-based technology for CO₂ capture from fossil fuel power plants. *Appl Energy* 2014;116:26–40. <https://doi.org/10.1016/j.apenergy.2013.11.031>.
- [311] Rodriguez CT, Le Q Du, Focsa C, Pirim C, Chazallon B. Influence of crystallization parameters on guest selectivity and structures in a CO₂-based separation process using TBAB semi-clathrate hydrates. *Chem Eng J* 2020;382:122867. <https://doi.org/10.1016/j.cej.2019.122867>.
- [312] Xu CG, Xie WJ, Chen GS, Yan XX, Cai J, Chen ZY, et al. Study on the influencing factors of gas consumption in hydrate-based CO₂ separation in the presence of CP by Raman analysis. *Energy* 2020;198:117316. <https://doi.org/10.1016/j.energy.2020.117316>.
- [313] Li X Sen, Xia ZM, Chen ZY, Wu HJ. Precombustion Capture of Carbon Dioxide and Hydrogen with a One-Stage Hydrate/Membrane Process in the Presence of Tetra- n -butylammonium Bromide (TBAB). *Energy & Fuels* 2011;25:1302–9. <https://doi.org/10.1021/ef101559h>.
- [314] LI S, FAN S, WANG J, LANG X, WANG Y. Clathrate Hydrate Capture of CO₂ from Simulated Flue Gas with Cyclopentane/Water Emulsion. *Chinese J Chem Eng* 2010;18:202–6. [https://doi.org/10.1016/S1004-9541\(08\)60343-2](https://doi.org/10.1016/S1004-9541(08)60343-2).
- [315] Lin W, Chen G-J, Sun C-Y, Guo X-Q, Wu Z-K, Liang M-Y, et al. Effect of

- surfactant on the formation and dissociation kinetic behavior of methane hydrate. *Chem Eng Sci* 2004;59:4449–55. <https://doi.org/10.1016/j.ces.2004.07.010>.
- [316] Hembram BK, Yadav MK, Sharma T, Nair VC. Single-Step Silica Nanofluid for the Improved Thermodynamics and Kinetics of Methane Hydrate Stabilized by a Conventional Promoter. *Energy & Fuels* 2024;38:12741–53. <https://doi.org/10.1021/acs.energyfuels.4c01323>.
- [317] Chaturvedi KR, Sharma T. Enhanced carbon capture and storage in depleted sandstone reservoirs using silica nanofluids. *Mater Today Proc* 2021;46:5298–303. <https://doi.org/10.1016/j.matpr.2020.08.782>.
- [318] Haider MB, Hussain Z, Kumar R. CO₂ absorption and kinetic study in ionic liquid amine blends. *J Mol Liq* 2016;224:1025–31. <https://doi.org/10.1016/j.molliq.2016.10.044>.
- [319] El-sayed GM, Kamel MM, Morsy NS, Taher FA. Encapsulation of nano Disperse Red 60 via modified miniemulsion polymerization. I. Preparation and characterization. *J Appl Polym Sci* 2012;125:1318–29. <https://doi.org/10.1002/app.35102>.
- [320] Liang Z (Henry), Rongwong W, Liu H, Fu K, Gao H, Cao F, et al. Recent progress and new developments in post-combustion carbon-capture technology with amine based solvents. *Int J Greenh Gas Control* 2015;40:26–54. <https://doi.org/10.1016/j.ijggc.2015.06.017>.
- [321] Haider MB, Hussain Z, Kumar R. CO₂ absorption and kinetic study in ionic liquid amine blends. *J Mol Liq* 2016;224:1025–31. <https://doi.org/10.1016/j.molliq.2016.10.044>.
- [322] Bougie F, Iliuta MC. CO₂ Absorption in Aqueous Piperazine Solutions: Experimental Study and Modeling. *J Chem Eng Data* 2011;56:1547–54.

<https://doi.org/10.1021/je1012247>.

- [323] Liu N, Chen L, Liu C, Yang L, Liu D. Experimental study of carbon dioxide hydrate formation in the presence of graphene oxide. *Energy* 2020;211:118994. <https://doi.org/10.1016/j.energy.2020.118994>.
- [324] Veluswamy HP, Kumar S, Kumar R, Rangsunvigit P, Linga P. Enhanced clathrate hydrate formation kinetics at near ambient temperatures and moderate pressures: Application to natural gas storage. *Fuel* 2016;182:907–19. <https://doi.org/10.1016/j.fuel.2016.05.068>.
- [325] Krishnamurthy S, Bhattacharya P, Phelan PE, Prasher RS. Enhanced Mass Transport in Nanofluids. *Nano Lett* 2006;6:419–23. <https://doi.org/10.1021/nl0522532>.
- [326] Rezaei E, Manteghian M, Tamaddondar M. Kinetic study of ethylene hydrate formation in presence of graphene oxide and sodium dodecyl sulfate. *J Pet Sci Eng* 2016;147:857–63. <https://doi.org/10.1016/j.petrol.2016.10.008>.

PUBLICATION (IN THESIS)

1. **Hembram BK**, Mahmud M, Tripathi R, Nair VC, Sharma T. Insights of Molecular Dynamics Simulation To Investigate the Impact of Ethylene Glycol on Methane Hydrate Dissociation. **Energy & Fuels** 2024;38:1923–33. <https://doi.org/10.1021/acs.energyfuels.3c03854>.
2. **Hembram BK**, Yadav MK, Sharma T, Nair VC. Single-Step Silica Nanofluid for the Improved Thermodynamics and Kinetics of Methane Hydrate Stabilized by a Conventional Promoter. **Energy & Fuels** 2024;38:12741–53. <https://doi.org/10.1021/acs.energyfuels.4c01323>.
3. **Hembram BK**, Prasad SK, Abdullah MS.M., Sharma T, Trivedi J, Nair VC. Comparative Effectiveness of Ethylene Glycol and Silica Nanoparticles of Single-Step Method on Hydrate Formation for Storage/Transportation of Methane. **Energy & Fuels**. <https://doi.org/10.1021/acs.energyfuels.5c00848>.
4. **Hembram BK**, Abdullah MS.M., Chaturvedi K R, Nair VC, Sharma T, Examine the effect of ethylene glycol on the dissociation of hydrates (CH₄ & CO₂): A Molecular Dynamics Analysis. **Geoenergy Science and Engineering**. (Revision Submitted)
5. **Hembram BK**, Prasad S K., Sharma T, Nair VC, Impact of Silica Nanofluid on Formation Kinetics of CO₂ Hydrate: A Relevant Study for Carbon Capture and Storage Applications. **Journal of Chemical Thermodynamics** (Revision Submitted)

BIDESH KUMAR HEMBRAM

• [Rae Bareli, India](#) • [+91-7860988987](#) • bidesh2007@gmail.com

• [linkedin.com/in/bidesh-kumar-hembram-74405b7b/](https://www.linkedin.com/in/bidesh-kumar-hembram-74405b7b/)

• <https://scholar.google.co.in/citations?hl=en&user=MoklX64AAAAJ>

Results-oriented Research Scholar with expertise in both practical and theoretical domains. Proven ability to design and implement engaging curriculum strategies for optimal outcomes. Skilled in providing comprehensive support for positive corporate experiences. I am committed to continuous learning and contributing to organizational success.

PHD THESIS OVERVIEW

Title: “Mitigation of Methane and Carbon Dioxide Storage Issues for Transportation as well as Storage from the Gas Hydrate”

In this work, the role of single-step SiO₂ was investigated to form gas hydrate for both CH₄ and CO₂. The nanoparticles are synthesized in the lab. The primary focus of this study was on the formation, and dissociation of gas hydrate in the presence of SiO₂. Also, molecular dynamics simulation study of dissociation of hydrate was studied.

PUBLICATION AND CONFERENCE

-
1. **Hembram BK**, Mahmud M, Tripathi R, Nair VC, Sharma T. Insights of Molecular Dynamics Simulation To Investigate the Impact of Ethylene Glycol on Methane Hydrate Dissociation. *Energy & Fuels* 2024;38:1923–33. <https://doi.org/10.1021/acs.energyfuels.3c03854>.
 2. **Hembram BK**, Yadav MK, Sharma T, Nair VC. Single-Step Silica Nanofluid for the Improved Thermodynamics and Kinetics of Methane Hydrate Stabilized by a Conventional Promoter. *Energy & Fuels* 2024;38:12741–53. <https://doi.org/10.1021/acs.energyfuels.4c01323>.
 3. **Hembram BK**, Prasad SK, Abdullah MS.M., Sharma T, Trivedi J, Nair VC. Comparative Effectiveness of Ethylene Glycol and Silica Nanoparticles of Single-Step Method on Hydrate Formation for Storage/Transportation of Methane. *Energy & Fuels*. <https://doi.org/10.1021/acs.energyfuels.5c00848>
 4. Tripathi R, **Hembram BK**, Chaturvedi KR, Sharma T, Nair VC. Evaluating the role of salts on wettability alteration in dolomite rocks: Possibility of water based oil mobilization application. *J Mol Liq* 2023;388:122738. <https://doi.org/10.1016/j.molliq.2023.122738>
 5. Shukla H, **Hembram BK**, Vishal V, Trivedi J, Srivastava VC, Sharma T. Surface modified single-step nanofluid for improved CO₂ absorption and storage Prospects at pore-scale in micromodels: CO₂ utilization for saline porous media. *Energy* 2024;294:130808. <https://doi.org/10.1016/j.energy.2024.130808>.
 6. Mahmud M, **Hembram BK**, Tripathi R, Sakthivel S, Chandrasekharan Nair V. Development of Sulfate-Based Smart Water for Improving the Oil Recovery in the Calcite Formation: New Insights from Molecular Simulation. *J Mol Liq* 2023:122409. <https://doi.org/10.1016/j.molliq.2023.122409>.
 7. Singh A, **Hembram BK**, Iglauer S, Keshavarz A, Sharma T. Pore-scale micromodel experiments for performance evaluation of polymeric nanofluids in CO₂ flow through porous media for carbon utilization and storage. *J Mol Liq* 2025;426:127358. <https://doi.org/10.1016/j.molliq.2025.127358>.

8. Kumar P, Kumar R, **Hembram BK**, Murugan M, Arif A, Veerababu M. Study of microstructure and mechanical properties of aluminium alloy (AA-6351-T6) using friction stir welding. *Mater Today Proc* 2020;27:1733–7. <https://doi.org/10.1016/j.matpr.2020.03.650>.
9. **Hembram BK**, Sharma T. “Effect of Single-Step and Size-Controlled Silica Nanofluid as Promoter for Gas Hydrate Formation: Kinetic Studies” *IOGTC- Upstream 2024*. (Conference).

PROFESSIONAL EXPERIENCE

Research Scholar, Rajiv Gandhi Institute of Petroleum Technology, Jais; July 2020 – Present

Petroleum Engineering & Geoengineering

- Working on Gas Hydrates and mitigating methane recovery issues from hydrate reservoirs through CO₂ in the Gas Hydrate and Flow assurance laboratory. (Experimental and Simulation)
- Area of interest: Gas hydrate, Molecular dynamics simulation, Kinetics and thermodynamics of gas hydrate.

Assistant Professor, Aditya Engineering College, Surampalem; August 2018 – February 2020

Petroleum Engineering courses undertaken

- Reservoir Engineering
- Well-test analysis
- Production Engineering

Assistant Professor, Al Habeeb College of Engineering & Technology, Hyderabad; October 2015 – July 2018

Petroleum Engineering courses undertaken

- Production Engineering
- Reservoir Engineering
- Placement coordinator (2015-2016)
- Arrange and accompany three industrial visits. (February 2017; January 2017; January 2016)

EDUCATION

Indian Institute of Technology, Madras, Chennai, India; August 2012 – June 2014. **Master of Technology**, Major: **Petroleum Engineering** (8.79/10)

- Thesis: Study of the structural behavior of dolomite-loaded bentonite drilling fluid. It deals with the structural drilling fluid behavior of bentonite clay mixed in water with different ratios of dolomite in weight. Experiments are performed to find out the plastic viscosity, yield strength, density, pH of the sample, and shear rate.

Maulana Azad National Institute of Technology, Bhopal India; August 2006 – June 2010. **Bachelor of Technology**, Major: **Mechanical Engineering** (6.41/10)

- Thesis: Reduction of NO_x Emission with the help of Selective Catalytic Reduction (SCR) and the performance evaluation of SCR by varying exhaust temperature. Experiments are performed with various catalysts to see the reduction of NO_x from bike engine exhaust.

SKILLS & OTHER

Skills: Gromacs, Molecular Dynamics, OriginPro, Google Sheets, AutoCAD

Workshop on Fundamentals of **GeoFrame, Petrel, ECLIPSE & PIPESIM**, by

Schlumberger information solutions pvt ltd held at Gurgaon 31st Dec 2012 – 5th Jan 2013

Language: English (Fluent), Hindi (Fluent), Bengali (Native)

Internship: Oil and Natural Gas Corporation. (May 2013 - June 2013)
Indian Oil Corporation Limited. (May 2009 - June 2009)

REFERENCES

Dr. Tushar Sharma

Associate Professor, Rajiv Gandhi Institute of
Petroleum Technology, Jais, India
Email: tsharma@rgipt.ac.in

Dr. Vishnu C Nair

Assistant Professor, Indian Institute of
Technology Kharagpur, India
Email: vishnuc@iitkgp.ac.in

END
